Library

3. **Library loan and photocopying permit**

Title of thesis A STUDY OF CURRENTS IN THE SOUTHERN OCEAN USING SATELLITE ALTIMETER AND MODEL DATA

Candidate HELEN MARY SNAITH

Three copies of the above thesis are now formally submitted for the degree of

PhD. Should the Senate of the University award me either this degree or another higher degree in respect of this thesis, I hereby agree that from the date of the award the thesis may be made available for inter-library loan or for photocopying and that the abstract may be made available for publication.

Signature [redacted] Date 17-9-92

UNIVERSITY OF SOUTHAMPTON

A STUDY OF CURRENTS IN THE SOUTHERN OCEAN USING SATELLITE ALTIMETER AND MODEL DATA

HELEN MARY SNAITH

A Thesis Submitted in Candidature for the Degree of
Doctor of Philosophy
Department of Oceanography
September 1992

UNIVERSITY OF SOUTHAMPTON

ABSTRACT

FACULTY OF SCIENCE
OCEANOGRAPHY

Doctor of Philosophy

A STUDY OF CURRENTS IN THE SOUTHERN OCEAN USING SATELLITE ALTIMETER AND MODEL DATA

by Helen Mary Snaith

The aims of the project are outlined and the satellite altimeter is introduced as a new method for the physical oceanographer to study ocean dynamics. The principles of the satellite altimeter are explained and a description of the sources of error found in the data is given, together with two possible methods for removal of residual errors. The principles of primitive equation ocean circulation models are outlined and the Fine Resolution Antarctic Model (FRAM) is introduced. Methods of hydrographic data collection are discussed and historical data on the circulation of the Southern Ocean are reviewed.

The methods for Geosat data extraction, quality control and error correction used in the study are discussed. Data processed by collinear techniques have been used to obtain height profiles along tracks in two regions of the Southern Ocean; South of Africa and in the Central South Pacific. Mesoscale variability fields calculated from the along track altimeter data are presented and explained in terms of historical in situ current data and bottom topography. Geostrophic current speeds calculated from the residual height profiles yield velocity anomalies of the order of 20 cm s^{-1} for the Antarctic Circumpolar Current (ACC) and up to 1.38 m s^{-1} for the Agulhas Current System, similar to values obtained by in situ measurements. Autocorrelation function calculations show that the characteristic length scales of height anomalies in the ACC are smaller than those of the Agulhas Current System.

The FRAM data set is used as a source of artificial sea surface heights to give model altimeter data which are processed and analyzed for the Geosat study regions. The resultant variability fields are compared with the Geosat results. The effects of Geosat's sampling strategy and altimeter processing on the FRAM data are analyzed and are given as an indication of the possible reliability of Geosat variability fields. The results of feature recognition and autocorrelation function analyses are compared to those from Geosat both as a verification for the FRAM mesoscale circulation and as an aid to altimeter data interpretation.

CONTENTS

LIST OF FIGURES

ACKNOWLEDGEMENTS

I would like to thank my supervisor, Ian Robinson, for his invaluable comments and suggestions over the three years of research and for his unerring ability to make visits to his office a confidence boost not a cause for depression. To David Webb and Peter Challenor of IOSDL goes my appreciation for a different perspective and to Nick Ward, Claire Burren and Sigrid Gellers-Barkman goes my gratitude for aid in the unceasing battle to defeat the IBM mainframe.

This research was supported by the N.E.R.C. as a FRAM special topic studentship awarded to the University of Southampton.

Finally, my thanks to Paul for being my greatest support.

LIST OF ABBREVIATIONS

ACC	Antarctic Circumpolar Current
CTD	Conductivity Temperature Depth sensor
FGGE	First GARP Global Experiment
FNOC	Fleet Numerical Oceanographic Centre
FRAM	Fine Resolution Antarctic Model
GARP	Global Atmospheric Research Program
GDR	Geophysical Data Record
Geosat	GEOdetic SATellite
RMS	Root Mean Square
SMMR	Scanning Multichannel Microwave Radiometer
SSMI	Special Sensor Microwave Imager
SWH	Significant Wave Height
TOVS	TIROS Operational Vertical Sounder

Section I: INTRODUCTION

1 PROJECT OVERVIEW

In recent years the satellite altimeter has introduced a new method for ocean current determination to the physical oceanographer which makes possible the mapping of global ocean current activity, at a spatial resolution of the order of 100 km over time scales of a month. The long term, global, high accuracy data set from Geosat is a major contributor to the field, although there are considerable difficulties to be overcome in obtaining useful information, due to general difficulties with altimeter data and problems specific to Geosat.

This project was initiated to use the Geosat data set to study ocean current variability in the Southern Ocean, a region where more traditional data collection methods are hampered by inaccessibility. Especially difficult is the collection of year round data and it is hoped that the altimeter can provide continuous monitoring of ocean currents.

The work falls into several main areas of research;

I: Development of a processing system able to extract and correct any required Geosat track and display the results in a useful format.

To make use of the Geosat data set it is necessary to understand the principles of satellite altimetry and the peculiarities of the Geosat altimeter in order to apply the necessary corrections and realize the limitations of results. So far there is no single processing method which has proven to give better results than any other and although there is agreement on the cause of data errors, the corrections to be applied vary significantly between authors. Therefore it is necessary to experiment with the data to decide upon the most appropriate forms of quality control and error correction before any significant analysis is undertaken.

For the data to be analyzed successfully, they must be displayed in a format which shows the information clearly and in detail. To do this a series of display programs had to be written utilizing the graphics capabilities of the Southampton University IBM 3090 mainframe system, and the SUN workstation provided by the FRAM community project at Southampton University Oceanography department.

II: Examination of the Geosat data for specific regions to study aspects of the mesoscale activity.

A comparison between the altimetry results and historical *in situ* data sets in published works has been carried out for two regions of the Southern Ocean and the relationship between mesoscale variability and bathymetry has been examined. Time series of orbit repeats of particular tracks have been used to attempt to identify such features as eddies, frontal meanders and changes in frontal velocity structure. The evolution of such features in time can then be traced through the repeating orbit tracks. It has proved possible in some cases to determine both radial velocity and rate of advection of an eddy from individual orbit tracks.

The study of mesoscale features also includes an analysis of the scale of features seen using an autocorrelation function in order to determine whether changes of length scale occur within or between study regions.

III: Comparison of the results of the Geosat study with data from the Fine Resolution Antarctic Model (FRAM).

The project is part of the FRAM Community Research Program, based on a numerical model designed to resolve mesoscale activity in the Southern Ocean. Surface pressure fields from the model have been interpreted as dynamic heights and sampled as if by an altimeter along specified tracks. Once sampled in this way, the model data have been processed in the same manner as altimeter data and compared with the Geosat altimeter results to give an indication of the model's ability to realistically reproduce the mesoscale variability fields of the Southern Ocean.

The FRAM data have also allowed determination of some of the effects of sampling and processing on altimetric sea surface height data. Model altimeter data have been used to create dynamic height anomaly fields which are compared with the original fields. The effects of interpolation from discrete tracks onto a grid, the temporal sampling pattern of Geosat and long wave-length orbit corrections on the fields are all examined.

The residual height data obtained from the FRAM 'model altimetry' have been directly compared to the height fields from which they were produced. This gives an improved insight into feature recognition and tracking using real altimeter data.

2 SATELLITE ALTIMETRY

The satellite altimeter is a very new instrument for the study of the oceans and in principle is relatively simple, using a radar to measure the distance from a transmitter on the satellite to the sea surface. This value is then converted to sea surface height with respect to some reference ellipsoid. This is a tool which is of most obvious benefit to the geodesist as the shape of the mean sea surface is affected, and indeed dominated, by the gravity field of the earth, which produces 'topography' with 50 m or more relief over major sea-floor features, such as trenches and ridges, and more than 100 m at longer wavelengths. However, there is a much smaller signal in the sea surface topography due to surface currents, which can now be detected due to the development of high accuracy altimeters.

The altimeter has several advantages over more 'conventional' remote sensing instrumentation in the determination of ocean dynamics. As an active microwave sensor the altimeter is an 'all weather' instrument, unlike visible and infra-red sensors which are limited to operation in cloud-free conditions. Also the altimeter measures a parameter, sea surface slope, which can be directly linked to the dynamics of the ocean via the use of geostrophic flow calculations. Other sensors detect semi-passive tracers, heat and colour, which can only be used as qualitative indicators of flow.

Problems arise in extracting the part of the signal of interest to oceanographers; that due to ocean currents. 'Noise' from sources such as the transmission path and sea-state as well as instrumental error, are sufficient to completely swamp the current signal, quite apart from the problem of removing the large geoid trends. Most of these effects can be corrected to some extent but this requires that a large amount of pre-processing is applied to the data before useful results can be obtained.

2.1 HISTORY OF THE ALTIMETER

Use of an altimeter in the study of ocean dynamics was first proposed by Frey *et al.* (1966) and is discussed in McGoogan (1975). Leitao and McGoogan (1974) were the first to extract current information from altimeters, obtaining the Gulf Stream signature from the Skylab S-193 'proof of concept' sensor data, although this suffered heavily from sensor noise and a rather erratic orbit. Much better results were obtained from the GEOS-3 altimeter (April 1975 - December 1978) which gave the first data of sufficiently high quality for quantitative analysis, but continuous coverage was limited to the western North Atlantic. The altimeter flown aboard Seasat in 1978 had a precision of 20 cm and, despite its limited life-span, provided the first global altimetric coverage of the oceans. In March

1985 a dedicated altimetric satellite, known as Geosat, was launched. Although primarily designed to obtain a high accuracy geoid for the U.S. Navy (McConathy and Kilgus, 1987), after this classified mission was completed Geosat was manoeuvred into an exactly repeating orbit for oceanographic research, the sub-satellite track being maintained within the SEASAT orbit specifications in order to allow unclassified distribution of the data. This exact repeat mission (ERM), which began on November 8th 1986, produced a largely high accuracy data set before its failure on January 5th 1990, although increasing ionospheric activity in its final year caused data degradation. Two altimetric satellites are currently in operation, the European Remote-sensing Satellite 'ERS-1' (launched in July 1991) and the joint French/American 'TOPEX-Poseidon' mission (launched in August 1992).

2.2 THE ALTIMETER CONCEPT

In theory an altimeter is a relatively simple instrument operating by measuring the time taken for an emitted pulse of microwave radiation to be reflected from the sea surface back to the transmitter. If the speed of the pulse is known then the distance of the satellite from the sea surface can be calculated. In practice the development of an instrument capable of achieving this is far more difficult. There are several constraints on the design of an altimeter:

1. The frequency of the emitted pulse must be within one of the internationally agreed wave-bands.
2. The antenna size is restricted by practical constraints of engineering.
3. The power of the pulse is limited by the satellite power supply, a more powerful pulse or high repetition of pulsing will drain the supply and so limit the satellite life-span.

The length of the pulse is constrained by the accuracy of measurement required. For an accuracy of 1 cm, the time of the returning pulse must be measured to within 30 ps and so the leading edge of the emitted pulse must rise to full power in this time. To create a sharp pulse a wide frequency band of emission is required, around 30 GHz for 30 ps. This is obviously impractical and even if achievable the pulse is scattered, and so degraded, on reflection, 'stretching' the leading edge. Instead a longer pulse, typically around 3 ns, is used, and the return sampled approximately twice per ns to produce intensity data to which a model curve can be fitted. The altimeter measures the mid-point of the leading slope of this model curve as shown in figure 2.1. The readings of 1000 or more returns are averaged to reduce the errors of curve fitting, giving a much improved accuracy. For both Seasat and Geosat the pulse rate of approximately 1000 Hz gave one averaged height measurement per second. This extended pulse method can give accuracy of the order of 150 ps utilizing a band-width of only 300 MHz. The location of the sampling window

(the time interval over which samples are taken), is determined by a tracking algorithm which uses the previous few seconds of data to predict the time of the return pulse. If the return does not occur in the predicted window the altimeter is said to be 'out of lock', a model curve cannot be fitted and no height value is returned. This is a problem especially over land or ice where gradients change rapidly over short space scales.

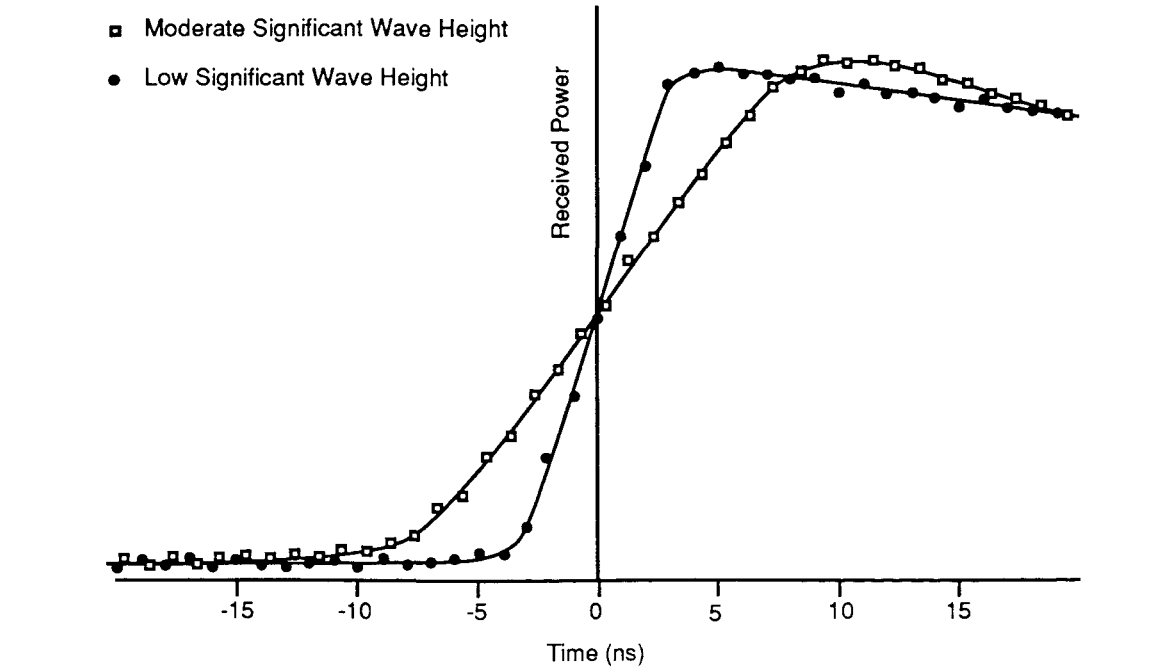

Figure 2.1 Smooth Curves Fitted Through Averaged Altimeter Pulse Shapes Corresponding to Two Different Sea-States (after Walsh *et al.*, 1978)

Further problems are encountered in designing an antenna which is capable of emitting sufficient power in a 3 ns pulse to give a measurable return. This is overcome by using a technique known as pulse compression. The emitted pulse is passed through a filter to create a long 'swept-frequency' pulse, for Geosat this gave an uncompressed pulse of 102.4 μs from a compressed pulse of just 3.125 ns. The return signal undergoes the reverse process so that the effect is that of the short pulse having been reflected, as propagation and reflection are linear processes.

The area of sea sampled by the altimeter in its footprint can theoretically be limited by one of two processes. The first is known as 'beam-limited geometry' and the size of the footprint is a function of the antenna size, as shown in figure 2.2. Unfortunately this requires a very large antenna. For Geosat, which had satellite height of approximately 800 km and radar wavelength of 2.2 cm, an antenna width of 2.5 m would have been needed to obtain a ground resolution of 7 km, which is unreasonable due to practical constraints. Further restrictions are imposed as the entire footprint must be illuminated at the same time and this requires that an antenna almost 10 m in diameter is used (see Rapley, 1990 for a derivation of this) and that the beam must be maintained exactly vertical.

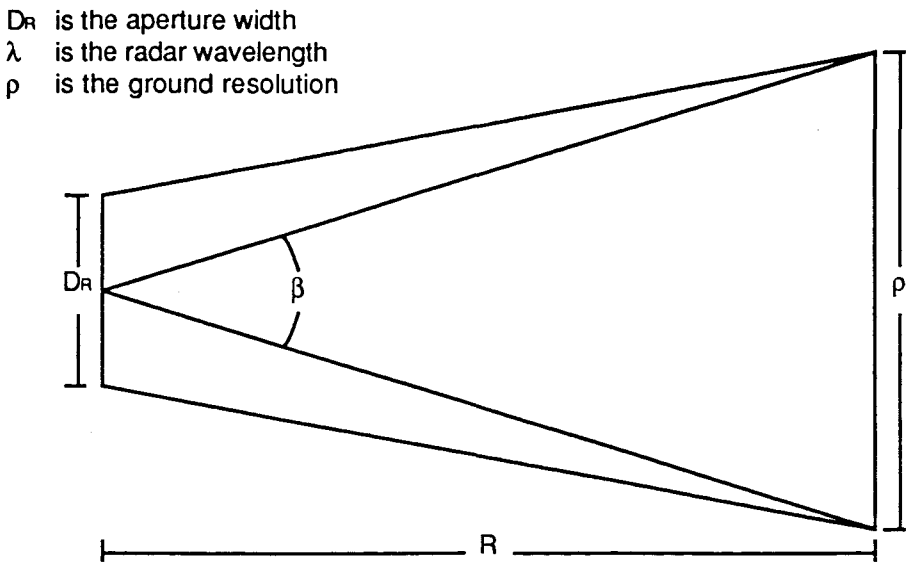

Beamwidth $\beta = \lambda/D_R$ far from the antenna (from antenna theory)
Hence $\rho = R\lambda/D_R$

Figure 2.2 Beam Limited Geometry for a Radar Altimeter Footprint.

All operational systems to date utilize what is termed 'pulse-limited geometry', a result of the geometric spreading of the emitted pulse. Provided that the sensor is within a few degrees of vertical, the leading edge of the pulse will be reflected first from the nadir point, and the area reflecting will increase as a circle until the pulse trailing edge is encountered. Assuming a square pulse waveform, the intensity of the return will increase linearly with the radius of the circle until the maximum is attained. The maximum radius of the pulse limited circle is determined by the backscatter of the sea surface and will increase with increasing roughness, for Geosat from 2 km in calm conditions to 12 km in heavy seas (Zlotnicki *et al*, 1989) as shown in figure 2.3. As it is the leading edge of the return which is used to determine the altimeter height, it is this radius which gives the resolution of the altimeter in the cross-track direction, whilst the pulse repeat rate and satellite ground speed combine to control the along-track resolution.

Once the maximum radius is reached the region of sea which gives a return to the altimeter will become an annulus of increasing radius, but of area equal to that of the circle from which it developed, until the signal return is beyond the range of the antenna beam width. Once the maximum intensity is reached, theoretically there should be constant intensity return, however the effects of scattering, antenna characteristics and mis-pointing combine to decrease the intensity with time, giving 'plateau droop'. This plateau droop can be used to determine the attitude of the sensor, important in calculating the effect of mis-pointing on the shape of the leading edge.

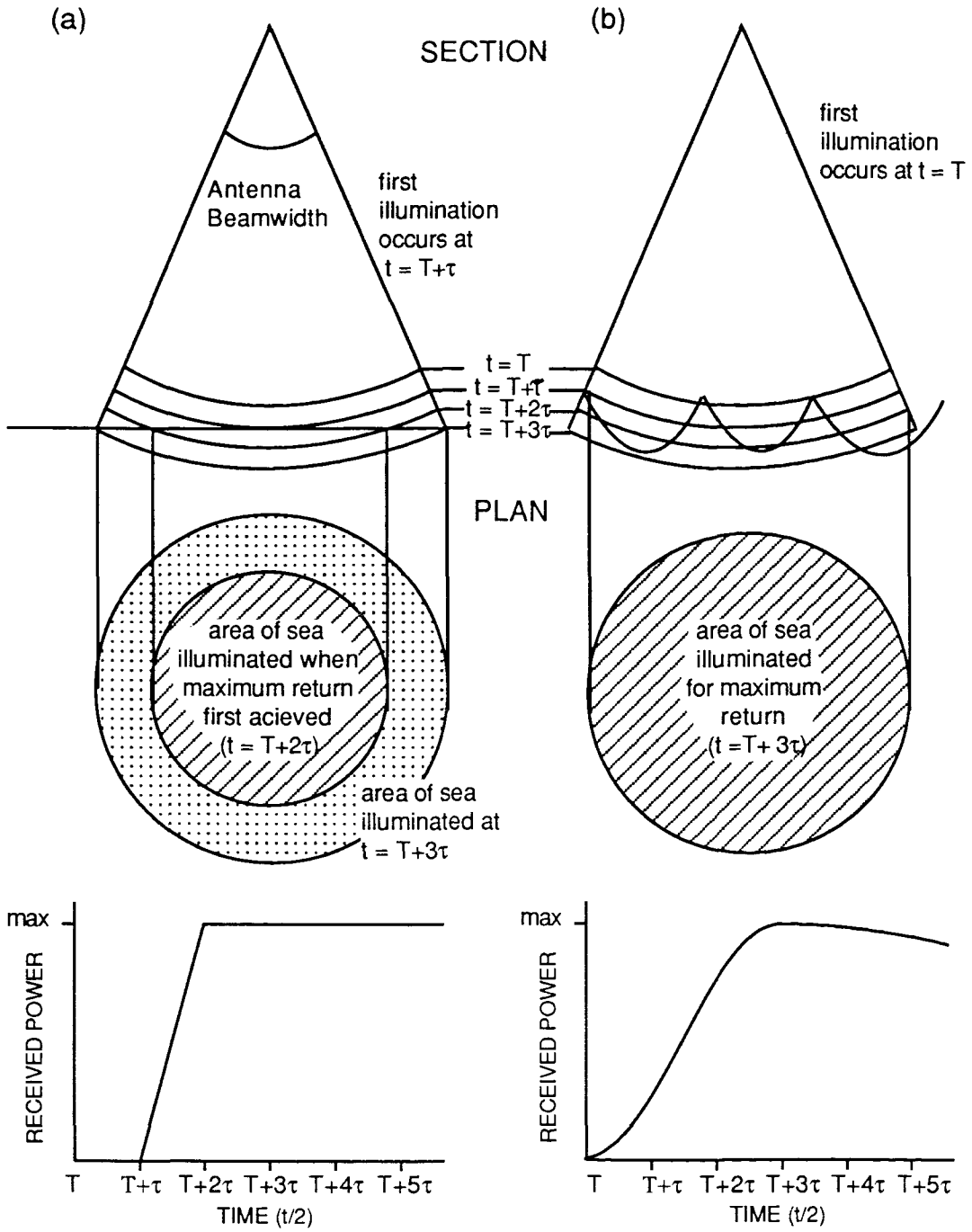

Figure 2.3 Interaction of a Radar Pulse with the Sea Surface
for a Smooth Surface (a) and for an Increased Sea-State (b).

Problems may arise if the footprint contains land or ice as well as sea, especially if there is high topography. In these cases the first return may be from the land or ice, not the sea at nadir, and the pulse shape is unlikely to be regular, influencing the curve fitting. The result may be that the sensor considers the area as one of very high sea-state and gives an anomalous sea surface height reading.

2.3 ERRORS IN THE DATA

The altimeter data contain errors from a number of sources, discussed below, including sensor limitations, signal transmission and a lack of supporting information. The magnitude of these errors is highly variable, from a few centimetres to several metres, but many can be corrected to a large extent. It is not the absolute scale of the errors which determines their effect on the accuracy of altimetric data but the scale of the residuals once corrections have been applied. The magnitude of this residual error is an indication of how closely we are able to reconstruct the processes causing the original error, in turn a function of our understanding of the physics involved, the additional information available and the complexity of modelling applied.

2.3.a Instrumental Errors

Perhaps the most obvious errors in the altimeter data are those due to operation of the instrument, such as clock timing and tracking of the leading edge of the return pulse. These errors are discussed in Chelton *et al.* (1989) and may be divided into random and systematic errors. Random errors are reduced by averaging of returns over one second to give an accuracy of approximately 4 cm (Fu *et al.*, 1988). Systematic instrument errors are not reduced by this along track averaging, but fortunately these errors are long wavelength compared with oceanic signals and so can be separated from them.

2.3.b Effects of the Transmission Path

Calculations performed on board the satellite to find the sea surface height assume that the speed of the radar wave is that of electromagnetic waves in a vacuum. This is not the case, as atmospheric components act to retard the wave, hence the calculated height of the satellite is increased and the sea surface is apparently depressed relative to a reference ellipsoid. The retardation effect is controlled by the composition of the atmosphere, which is the electron content of the ionosphere, the dry gas composition of the troposphere and its water content, both as vapour and in clouds (the most variable parameter). The ionospheric effect produces an error of only around 20 cm whilst the dry gases result in an error of order 2.3 m. The highly variable water vapour content can cause errors of between 5 and 40 cm.

The height error due to effects of the transmission path on the speed of the radar wave is;

$$\delta h = \tfrac{1}{2} t_T c - \tfrac{1}{2} t_T c_m$$

which can be written as;

$$\delta h = \tfrac{1}{2} t_T c_m \left(\frac{c - c_m}{c_m} \right) \qquad (2.1)$$
$$= h(n-1)$$

where;

δh is the overestimate of height

h is the true height of the satellite (the nominal orbit height of the satellite is sufficiently accurate in this equation)

c_m is the speed of the pulse through a medium

c is the speed of light in a vacuum

t_T is the measured pulse travel time

n is the refractive index of the medium $\left(n = \frac{c}{c_m} \right)$.

In order to include vertical structure of the atmosphere equation 2.1 can be written as;

$$\delta h = \int_0^h (n-1)\,dz \qquad (2.2)$$

(1) Ionospheric

When applied to the ionosphere the important consideration is the concentration of electrons, which is variable in both space and time. For frequencies around 10 Hz it is known that there is a relation such that;

$$(n-1) \approx \tfrac{1}{2} N a f^{-2} \qquad (2.3)$$

where;

N is the ion concentration

a is a constant = 80.5 $m^3 s^{-2}$

and so equation 2.2 becomes;

$$\delta h = \tfrac{1}{2} a f^{-2} \int_0^h N\,dz \qquad (2.4)$$

The influence of the frequency term in the above equation reduces the error as higher frequencies are used, at the frequency of the Geosat altimeter (13.5 GHz) the correction is only around 20 cm. For mid-latitudes diurnal and solar source (sun-spot) effects have been recorded as causing variation from approximately 5 to 100×10^{16} electrons m^{-2} (Callahan, 1984) with lower values occurring overnight and in the Summer. The frequency dependence of equation 2.4 can be utilized by means of a dual frequency altimeter such as TOPEX, for which comparison of the two measured heights determines

the local ionospheric effect. For previous altimeter missions this has not been possible and the electron content must be determined by an alternative method.

One method is to use ground station observations of electron content which are extrapolated onto the satellite tracks using geographical electron distribution fields. This approach was used for the Geophysical Data Record (GDR) of the Seasat altimeter (Lorell *et al.*, 1982), but the high spatial variability of ionospheric electron content can result in large errors in the estimate used. Some part of this error could be removed by use of the German PRARE system, a dual frequency system flown on board ERS-1. This system would give increased spatial and temporal information of the ionosphere but does not measure at nadir and so interpolation is still necessary. The accuracy of this system cannot yet be verified due to the failure of the PRARE system on ERS-1. A second approach, used for the Geosat GDR, is to model the physical processes of the ionosphere, using solar forcing parameters measured at fixed locations. Only long wavelength effects are modelled as these dominate the signal. This method is perfectly adequate in periods of low solar activity, such as that for the first two years of the Geosat ERM when it has an accuracy of 3-5 cm, but questionable during high ionospheric activity.

(2) Tropospheric

The tropospheric corrections are rather more complicated as the dry gas and water components must be considered independently to produce both dry and wet tropospheric corrections. The dry tropospheric correction uses model atmospheres, derived from empirical data on the vertical structure of the atmosphere, to give the input to equation 2.2 above. The Geosat GDR dry tropospheric correction is based on that of Saastamoinen (1972) which uses the surface pressure of the Fleet Numerical Oceanographic Centre (FNOC) weather model. The model output occurs only at 12 hour intervals on a 2.5° global grid and so values must be interpolated onto the satellite tracks. The dry tropospheric correction is then calculated using;

$$\mathbf{DRY(FNOC)} = -2.277\,p\left(1 + \left(0.0026\cos 2\phi\right)\right)$$

(Cheney *et al.*, 1987)

where;

p is surface atmospheric pressure (mbar)

ϕ is latitude

Despite being the largest transmission path correction at more than 2 m, it is estimated as being accurate to 2-3 cm and so is not a major contributor to residual errors.

The water content of the troposphere can be found in one of two ways. The first is to use a weather model output of surface air temperature and water vapour pressure. The wet tropospheric correction can then be produced using one of several proposed methods

(including those of Saastamoinen, 1972 and Tapley *et al.*, 1982) which use FNOC data and are incorporated into the GDR of the Geosat altimeter;

$$\mathbf{WET(FNOC) = -2.277}e\left(\mathbf{0.05} + \frac{\mathbf{1255}}{T + \mathbf{273.16}}\right)$$

(Cheney *et al.*, 1987)

where;

T is surface atmospheric temperature (°C)

e is surface water vapour pressure (mbar)

This correction is believed to have an accuracy of within 5 cm, limited by poor meteorological station coverage over large areas of the world's oceans and poor estimates of water vapour content in regions such as the inter-tropical convergence zone in the model. As for the DRY(FNOC) correction, the model grid is interpolated onto the satellite track.

An alternative method is available if a passive radiometer, such as the Scanning Multichannel Microwave Radiometer (SMMR), is flown aboard the same satellite as the altimeter. This occurred with the Seasat altimeter and direct measurement of water content was possible by comparison of the different channels of the SMMR along its ground track, parallel to that of the altimeter. For Seasat the resultant correction was found to vary by 25-30% from the FNOC derived value for the Northern hemisphere (Tapley *et al.*, 1982). Discrepancies in the Southern hemisphere were even larger due to the increased scarcity of meteorological data. Geosat did not incorporate a passive radiometer and so the wet tropospheric correction applied must come from an independent source. An alternative correction given in the Geosat GDR is based on those of Prabhakara *et al.* (1985) and Tapley *et al.* (1982), and is given as;

$$\mathbf{WET(SMMR) = -6.36}W$$

(Cheney *et al.*, 1987)

where;

W is the vertically integrated atmospheric water vapour (gm cm^{-2})

This correction uses a climatological data base of vertically integrated atmospheric water vapour collected from the SMMR flown aboard NIMBUS-7, prepared by C. Prabhakara in the form of a 3° lat. by 5° long. grid of monthly averages for 1979-1981. Near real-time water vapour corrections are now available for Geosat from contemporary radiometer data on an improved set of GDR data (see § 7.2.a, page 89).

(3) Rain Cells

There has been some concern for the effects of spatially non-uniform cloud and rain within an altimeter footprint which can cause degradation of the waveform. This results in

the tracker algorithm having difficulty in locating the leading edge of the return pulse and hence errors in the sea surface height measurement (Walsh *et al.*, 1984b; Monaldo *et al.*, 1986). The effect gives an error of less than 4 cm in a 1 s average at 13.5 GHz (Walsh *et al.*, 1984b), increasing with frequency, which although not great is still significant, especially for the proposed accuracy of future altimeters. Rain contamination is currently not flagged in the Geosat GDR data and is usually detected by associated anomalous standard deviations of height measurements.

2.3.c Sea-State Bias

Further errors are introduced by the sea-state in two ways. Oceanic waves have a tendency to become 'peaky', that is with a high, narrow peak and much broader trough. Radar reflections from the horizontal troughs are of a higher intensity than those from the peaks and consequently the radar returns will be dominated by the large area of depressed water (troughs). The result, as illustrated in figure 2.4, is that the apparent measured mean sea level is lower than the still water level. This is known as the electromagnetic effect and is proportional to the significant wave height (SWH), but is also a function of the wavelengths of the emitted pulse and of the wave field. This effect is not fully understood and many workers have attempted to determine the actual error involved, both theoretically and empirically.

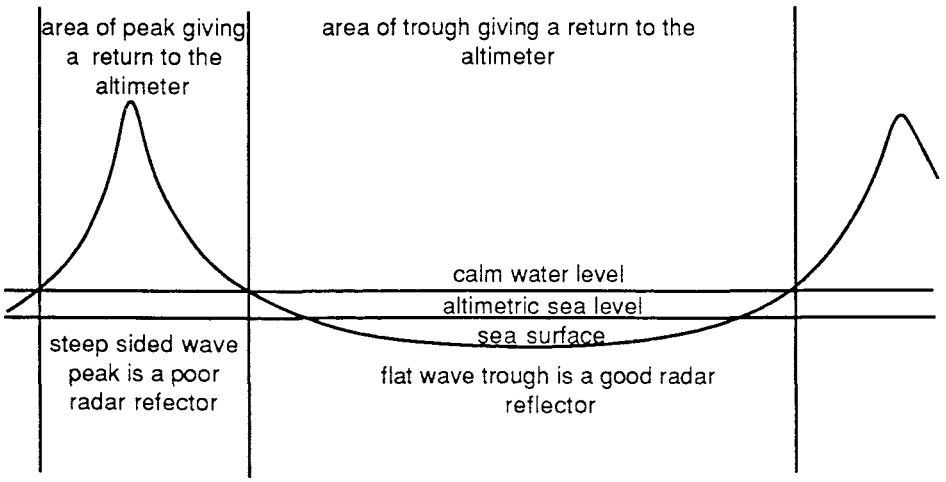

Figure 2.4 The Electromagnetic Effect.

In addition, the Seasat altimeter is known to have had an instrument specific error, also related to the sea-state, in the tracker algorithm which locates the leading edge of the return pulse. So far it is believed that no such error is present in the Geosat tracker. The total error is known as the sea-state bias.

Sea-state bias was first reported by Yaplee *et al.* (1971), using a fixed tower altimeter, and later by Choy and Uliana (1980), from an airborne sensor. Walsh *et al.* (1984a, using a 36 GHz altimeter) and Choy *et al.* (1984, using 10 GHz) both found a consistent proportional dependence on wave-height within frequency, greater at lower frequency (3% compared with 1.1% SWH), but with dependence on the wind speed and wavelength. Both wave-height and wind-speed can be derived from the altimeter data using the return waveform. This is in itself a very useful application of the data and many workers have concentrated on this aspect (for a review of the principles see Webb, 1983). Some of the most notable work in this field has been carried out by Mognard (1983; 1984, and with others, 1983; 1984), Queffeulou (1983) and Dobson *et al.* (1987).

Born *et al.* (1982) have reported on the sea-state bias effect from satellite altimeters and show a method for determining the error involving a comparison of the sea surface heights at the same location during different sea-states. They find an error of 1 to 4% SWH but have a standard deviation of the same order, most probably a result of the wavelength dependence noted previously. Prior to a mission the expected electromagnetic bias can be calculated from theory, or using airborne tests. The tracker error is instrument specific and can be found only during testing or after data collection by a method such as that of Born *et al.* (1982).

2.3.d Orbit Calculation

To calculate sea surface elevation with respect to a reference ellipsoid the satellite orbit must be known relative to this reference to the same accuracy as the data required. This is difficult as the orbit is dependent on many variables, and orbit uncertainty is the largest single residual error in the data. The orbit is also controlled to a large extent by long wavelength components of the gravity field and this field is still not accurately known for most regions of the world, indeed the primary aim of the Geosat mission was to produce an accurate geoid from which the gravity field could be determined.

Modelling the orbit path (termed creating an 'ephemeris') for the satellite is achieved by using the nominal orbit parameters, a model geoid and parameters for physical effects on the satellite, such as drag, and incorporating satellite tracking information. In the past this was mainly laser tracking data but more recent developments include the use of satellite based trackers, including the US Global Positioning System (GPS).

Modelling the orbit requires an accurate knowledge of the dynamic processes acting on the satellite. These are dominantly;

a. Gravity: As well as using a model of the geoid, or mean field, the effects of both solid earth and ocean tides must be considered.
b. Atmospheric drag and pressure forces: Mainly caused by ion content at the height of an altimetric satellite.
c. Pressure of direct and reflected solar radiation.

All these parameters vary with the satellite shape and mass distribution, in space and in time. In early 1989 ionic activity increased dramatically due to high solar activity and the resultant drag and pressure forces on the long boom of Geosat caused the loss of almost a third of its data by loss of attitude.

The geoid is highly variable over a range of space scales, but the long wavelength components dominate the orbit. In the most recent geoid models, including Goddard Earth Model (GEM) 10 (Lerch *et al.*, 1979, used in the Geosat GDR) and GEM T2 (Marsh *et al.*, 1989, used in the improved GDR), tracking data from a large number of satellites is used to greatly improve the long wavelength geoid resolution. Previous altimeter mission data provide the best currently available geoid models such as that of Won and Miller (1979), with the highest resolution and accuracy.

Relying on laser-tracking to maintain the ephemeris has associated problems as the tracking station locations relative to the reference ellipsoid must be known to within a few centimetres, often not possible in remote areas. Also, to obtain full earth coverage a very large number of ground stations would be required and so only a limited number of arcs can ever be tracked. Continuous tracking is now possible using systems such as DORIS and GPS, high global precision being possible with very few ground stations (Yunck *et al.*, 1985). Currently the most accurate orbit model available for Geosat is that of Haines *et al.* (1990), believed to have a radial accuracy of 35 cm global rms.

2.3.e Time-tag

The time taken for the signal to pass through the electronics of the altimeter from the receiver to the on board processor can cause another error known as a time-tag error. This time must be accurately known so that height values obtained are assigned to the correct section of the orbit. If the satellite is moving vertically relative to the reference ellipsoid, then the actual height of the satellite with respect to the sea surface will be changing with time. An altitude measurement assigned to the wrong portion of the orbit will give an incorrect apparent sea surface elevation calculation, as shown in figure 2.5. The initial Seasat time-tag bias estimation was in error by only approximately 80 ms but this gave a highly variable altitude error with a maximum of more than 1 m (Marsh and Williamson, 1982).

The time-tag bias of the altimeter is an instrument specific error which should remain constant with time. The value of this bias is found during the testing of an altimeter prior to its launch although revised values may be calculated later using the same data (Tapley *et al.*, 1979) or using sea surface height discrepancies at ground track intersections (Schutz *et al.*, 1982; Marsh and Williamson, 1982).

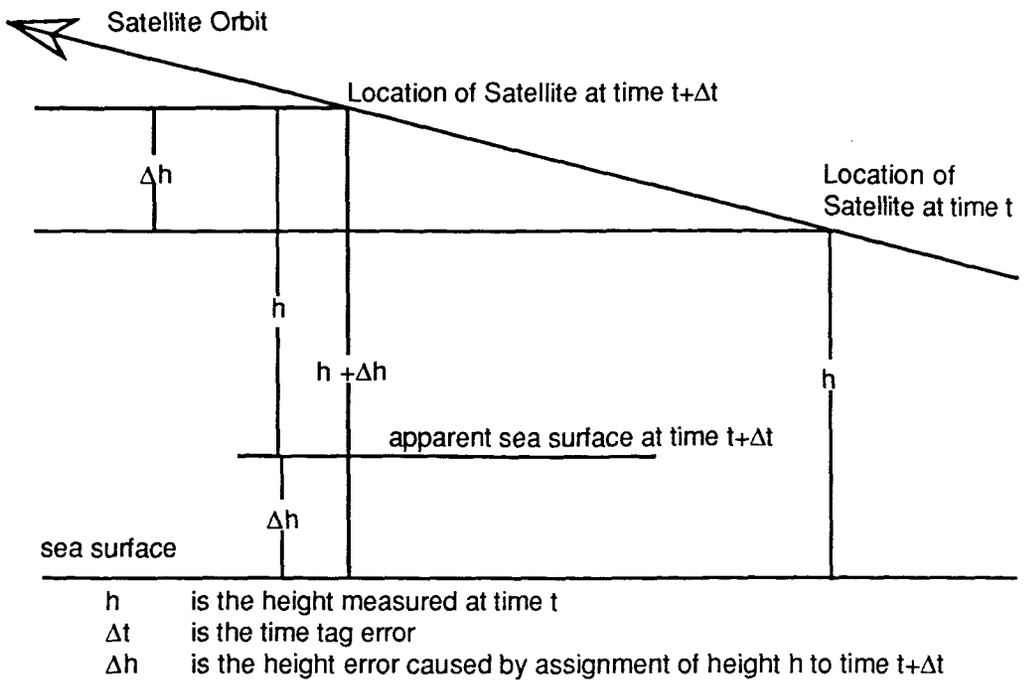

Figure 2.5 The Effect of Time-tag Error on Altimetric Heights.

2.4 EXTRACTION OF THE CURRENT SIGNAL

Even after the above corrections have been applied to the data there are still residual errors which are significantly larger than the oceanic current signal. The largest of these is the residual orbit error which was computed as approximately 3 m rms for the orbit supplied on the Geosat GDR (Born *et al.*, 1988). Fortunately much of this error occurs at very long wavelengths, of the order of 40,000 km, and so is readily separated from the shorter wavelength dynamic signal.

Linked with this are errors due to the un-modelled or incorrectly modelled sections of the geoid which are believed to be of the order of 2-3 m (Cheney and Marsh, 1981b). These errors not only contribute to the residual orbit error, but also cause significant problems when attempting to study the total dynamic field of the oceans. In order to study the time invariant flow, its resultant signal must be separated from the static (geoidal) topography. Unfortunately geoid errors are much greater than the decimetre signals associated with current activity. As stated previously the best geoid models currently available incorporate previous altimetric data, these models, however, suffer from contamination by the mean ocean currents. A further complication when attempting to resolve the geoid to better than a few metres internal accuracy, using satellite altimeter data, is that the ocean tides give an input to the total gravity field and some tidal frequencies are difficult to separate from the geoid signal.

The uncertainty in the geoid makes it impossible to separate the time-invariant current signal except in a few restricted areas such as the western North Atlantic where an accurate gravimetric model is available (Cheney and Marsh, 1981b). Information from gravimetric surveys has a very limited spatial coverage over the oceans because of the difficulty of ocean surveys, but even in such areas it must be realized that only mesoscale activity can be studied if orbit errors are to be ignored.

2.4.a The Tidal Component

If the satellite orbit is correctly chosen (see Parke *et al.*, 1987) then tidal data can be extracted via harmonic analysis of sea surface height data and much work has been done towards this end including that by Brown (1983) and Won and Miller (1979). In recent years Cartwright and Ray have made significant use of the Geosat data in determining aspects of the global ocean tides in a series of papers (1989; 1990a; 1990b; 1991).

However, when considering surface currents, tidal signals must be dealt with as noise and corrections applied, usually by use of a tidal model. Errors in the tidal model used are generally at longer wavelengths than the mesoscale activity for the open ocean, although the varying time dependence of tidal constituents and their associated residual model errors can introduce fictitious height variability at some frequencies, especially on the continental shelves. In the north-east Atlantic, Thomas and Woodworth (1990) have shown that apparent mesoscale variability can seen in the region of the Iceland-Faroes ridge by differencing the results of two tidal models and hence using an incorrect model may introduce apparent mesoscale variability in the altimeter data.

2.4.b Separation of Scales

Fortunately there is a difference in scale between the current signal to be studied and the major residual errors. The dominant orbit error occurs at a frequency of once per orbit (approximately 40,000 km wavelength), thereby only creating a problem for studying the basin scale current activity.

Included in the surface topography are the effects of atmospheric pressure loading, the 'inverse barometer' effect. The exact mechanism of transfer of pressure from the atmosphere to sea-level, and especially the frequency characteristics of the response, are not well understood and so the accuracy of any correction for this effect will be limited not only by the uncertainties of model atmospheric pressures but also by those of the transfer function used. Oceanic mesoscale features such as eddies have characteristic sizes of the order of 50-500 km whilst atmospheric features tend to occur with wavelengths of 1000 km or more. Mainly due to separation in scale between ocean and atmospheric effects, the inverse barometer error and residuals from the transmission path corrections are greatest at wavelengths greater than oceanic mesoscale activity. It must be noted however

that in the Southern Ocean the occurrence of intense, localised storms can produce short wavelength variations in atmospheric effects which cannot be properly resolved without use of a passive microwave sensor along the altimeter track, increasing the residual errors of Geosat data.

The time variant current signal is more readily obtainable for the majority of the worlds oceans, by finding the variability of the altimeter data. This gives a good indication of the eddy activity and meandering of current systems and sea surface variability data is relatively free of error due to the separation in scales between residual errors and mesoscale activity. Two principal methods are used to obtain the variability and these will be discussed in the following sections.

2.4.c Along Track Analysis of Collinear Altimeter Data

The Seasat orbit pattern was the first to give exact repeat overpasses (to within 2.5 km), repeating every 3 days for the last 25 days of its life, whilst the Geosat exact repeat mission gave repeated orbits (to within 1 km) every 17.05 days. Short arcs of this data, corrected for orbit, sensor and transmission path errors, will show dominantly the unresolved geoid signal and residual orbit error, as shown in figure 2.6. The method of collinear tracks aims to remove both the residual orbit errors and unresolved static topography. Once data have been filtered to remove any anomalous points, they are grouped into sets of collinear tracks and resampled onto consistent latitude longitude tracks to account for variation in the exact location of the sampled points (see figure 5.2, page 42).

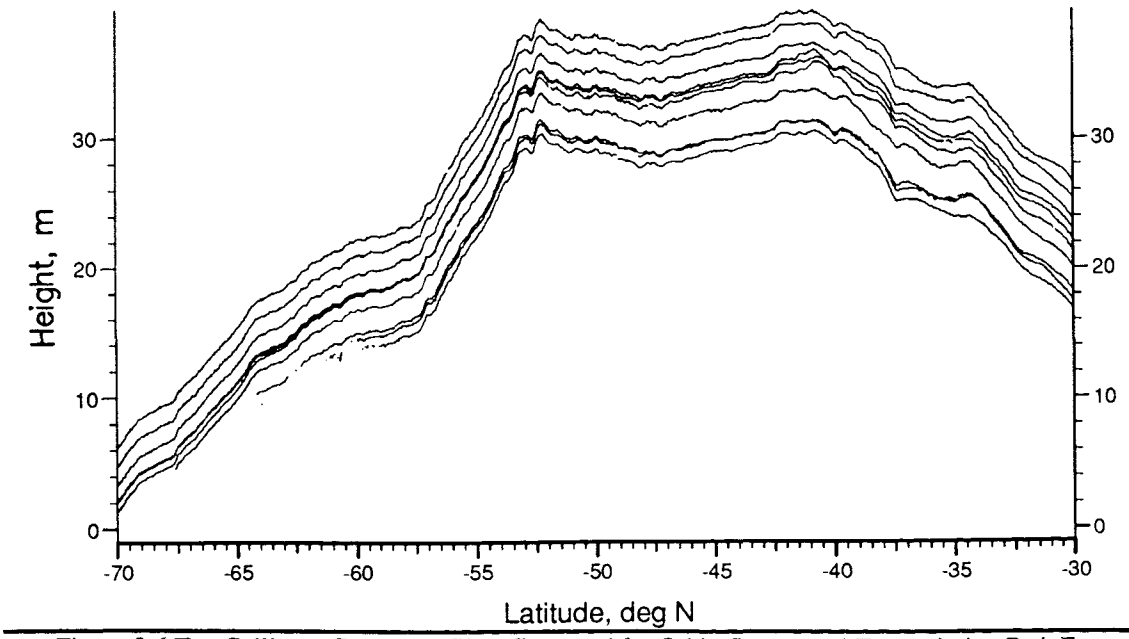

Figure 2.6 Ten Collinear Geosat Profiles, Corrected for Orbit, Sensor and Transmission Path Error.
Each Successive Orbit Repeat is Offset by 1 m.
Note: All figures Follow a 'South Latitude Negative' Convention as used on the Geosat GDR.

The mean of all repeats of any given orbit arc will give the time-invariant part of the signal, containing geoid and mean current data, and once this is removed from each individual track what remains is the sea surface height variability together with residual orbit errors and other residual errors such as tides (see figure 2.7). Over short arcs (less than 5000 km, Cheney *et al.*, 1983) the orbit residuals can be removed by applying a linear fit (tilt and bias of the data) to each track and reducing to zero. Over longer arcs the error is the difference between a computed ephemeris and the actual elliptical orbit, and the residual is best modelled by a quadratic fit to each track.

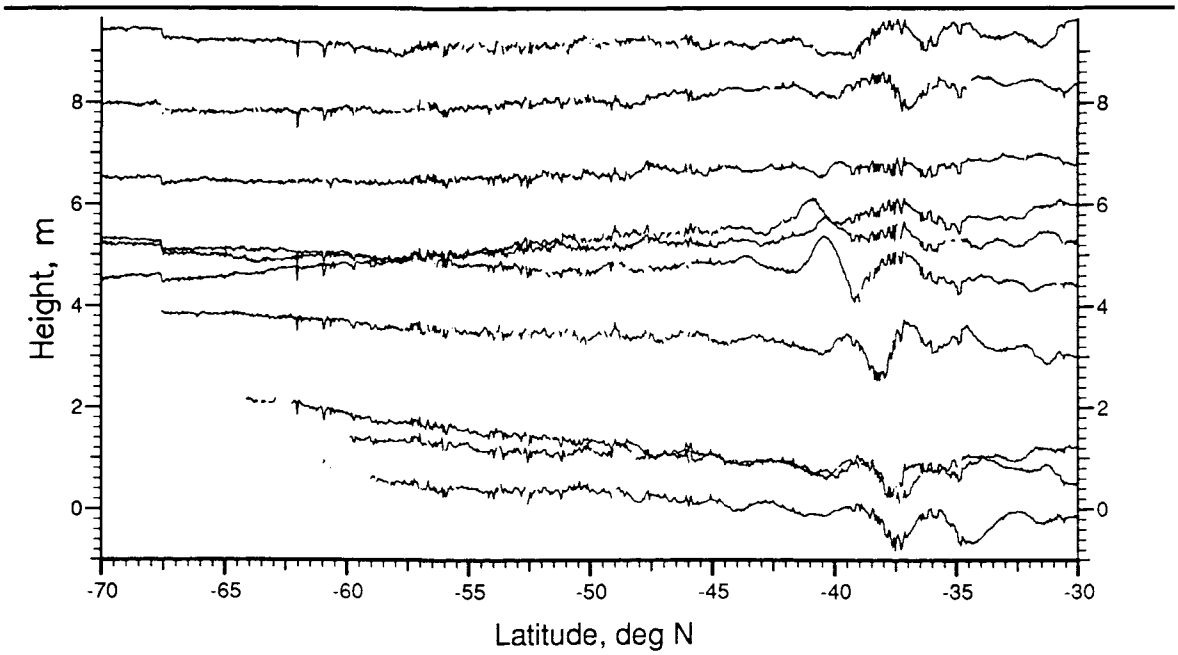

Figure 2.7 The Ten Geosat Profiles of figure 2.6 after Subtraction of the Group Mean at each Data Point. Each Successive Orbit is Offset by 1 m.

This approach has been used by many workers to great effect, amongst the earliest being Douglas and Gaborski (1979) using GEOS-3 near repeat data. A global study was carried out by Cheney *et al.* (1983) on the Seasat data to give maps of sea surface variability, which can then be related to the mesoscale current activity. From the sea surface height variability it is possible to calculate parameters such as the eddy kinetic energy of the oceans, statistics which can be compared with model output (Colton and Chase, 1983) or with other data sets such as that of Wyrtki *et al.* (1976). Similar studies have been carried out on smaller areas such as the Gulf of Mexico (Cheney and Marsh, 1981b; Robinson *et al.*, 1983) and on the Antarctic Circumpolar Current (Colton and Chase, 1983; Chelton *et al.*, 1990).

2.4.d Cross-Over Analysis

This approach, first applied to the non-collinear GEOS-3 data set, uses the height differences obtained at the cross-over points of ascending and descending passes of the

satellite. At these cross-overs, the sea surface height is measured by each of the two passes. The geoid and mean errors will be the same in the two height measurements, but the orbit errors and other time dependant signals and errors will contribute to the height differences. These height differences are minimized by solving a set of simultaneous equations for the orbit error of all the orbit arcs involved, the exact procedure used varying between researchers. This yields the orbit error along each orbit arc used which can be removed from the height profiles leaving the mean sea surface together with the time dependant signals. Unfortunately this is not quite true as the biasing of the orbit repeat times gives a 'once per revolution' orbit residual which cannot be removed in this way (Douglas *et al.*, 1984). Also the mean sea surface must be constrained in some manner prior to the minimization, usually by fixing two orbit arcs, resulting in the mean sea surface obtained having an unknown bias and tilt. The methods of cross-over analysis and their uses in oceanographic studies are discussed in Tai and Fu (1986).

This method of analysis has been very popular with the GEOS-3 and Seasat data sets (Marsh *et al.*, 1982; Cheney and Marsh, 1981a; Fu and Chelton, 1985) due to the absence of a large number of collinear tracks; GEOS-3 had a near repeat orbit pattern which gave an excellent ocean coverage but was not sufficiently close for true collinear analysis, whilst the Seasat repeat orbit mission was too short to accumulate a large data set.

This method also has the advantage of retaining the error reduced mean sea surface for the region of the analysis, important for those attempting to create an accurate geoid (Rapp, 1983). These mean sea surfaces can also be used in areas where good independent geoidal data is available to give the mean currents. The collinear method retains the mean sea surface along each track but this mean contains the mean orbit error of that arc and differences in the mean orbit errors between arcs may cause significant offsets in the mean sea surface between adjacent tracks.

The height residuals at each data point are a measure of the sea height variability and, as with the collinear analysis, give an indication of the current variability within the analysis area. Some recent work has applied this technique to Geosat data, including that of Wakker *et al.* (1990), analyzing data for the oceans around South Africa and Tai (1988), using a modified technique for the Tropical Pacific.

3 THE FINE RESOLUTION ANTARCTIC MODEL

The Fine Resolution Antarctic Model (FRAM) is a major program of the UK Physical Oceanography community. The objectives of the project were to develop the expertise and manpower for research of the oceans and climate using numerical models.

The primary scientific questions which FRAM was designed to answer are;

1: What are the physical processes which control the circulation of the Southern Ocean? Most particularly, what is the relative importance of topography and eddies in balancing wind stress?

2: What is the heat transport in the Southern Ocean? Of special interest is how important eddies are in transporting heat across the Antarctic Circumpolar Current (ACC).

3: How are water types created and transported?

4: What effect does the extensive sea-ice cover have on fluxes of heat, fresh water and momentum?

3.1 PRIMITIVE EQUATION MODELS

Models such as the FRAM are an attempt to understand the oceans' circulation by recreating that circulation using the laws of fluid dynamics. The basic laws of physics which govern the study of ocean dynamics are explained in Pond and Pickard1983, chapter 3. These laws are expressed as a series of equations relating fluid motions to a fixed reference frame, usually the earth. The governing equations usually used in primitive equation models are the horizontal components of the momentum equation;

$$\frac{\partial \underline{u}}{\partial t} + (\underline{u}.\nabla)\underline{u} - \underline{f} \wedge \underline{u} = \frac{-1}{\rho_0}\nabla_H p + A_H \nabla_H{}^2 \underline{u} + A_V \frac{\partial^2 \underline{u}}{\partial z^2}$$

the hydrostatic equation;

$$\frac{\partial p}{\partial z} = -\rho g$$

the continuity equation;

$$\nabla_H . \underline{u} + \frac{\partial w}{\partial z} = 0$$

and the advection-diffusion equation;

$$\frac{\partial(T,S)}{\partial t} + (\underline{u}.\nabla)(T,S) = K_H \nabla_H{}^2(T,S) + \frac{\partial^2(T,S)}{\partial z^2}$$

where;

$\underline{x}(x,y,z)$ is distance (east, north and upward positive)

$\underline{u}(u,v,w)$ is velocity in direction $\underline{x}$

f is the Coriolis parameter

p is pressure

A_H, A_V are horizontal and vertical diffusion coefficients of momentum

T,S are temperature and salinity

K_H, K_V are the horizontal and vertical diffusion coefficients of heat and salt

The analytical solution of these equations is not possible for any but strictly limited special cases (Pond and Pickard, 1983). Instead numerical models are used which attempt to solve approximations to the governing equations numerically by computer.

Most numerical models make use of the finite difference technique. In this method, instead of attempting to find the values of properties such as temperature, salinity and velocity for any point in the ocean, approximate solutions are found at points on a grid. The basic principle is to replace the gradient terms, for instance $\frac{\partial u}{\partial x}$, with approximate values, eg $\frac{u_{i+1} - u_{i-1}}{\Delta x}$ where Δx is the spatial grid spacing and u_i is the value of u at the i^{th} grid point. Such approximations must be made in time as well as space in order to find how these properties change. Finite difference schemes of many types have been produced, the exact scheme used depending on the space and time scales to be resolved. The time step of the model is constrained by stability criteria, such as $\Delta t \leq \Delta x / C_{\max}$ where $C_{\max}$ is the maximum wave propogation speed in the model (Pond and Pickard, 1983). As Δx decreases more spatial detail can be resolved but the computation time required increases as there will be a greater number of points in the grid and the length of the time step must be reduced to maintain stability. Many schemes give the depth integrated velocities in order to reduce the computation time necessary. Where depth dependant information is required, then the x-y grid is usually calculated at a series of levels determined by depth, or occasionally pressure.

Not all physical effects are incorporated into the governing equations, due to the neglect of some small terms, and the system of equations is not closed (see Pond and Pickard, 1983). In order to remedy this the effects of sub-grid scale, turbulent-like motions which may control friction and diffusivity are parameterized by the application of eddy viscosity and diffusivity terms. The values of these parameters are chosen to ensure numerical stability rather than from measurements of oceanic properties. Eddy resolving models require a very small grid scale, and hence short time step, but still require that sub-

grid scale processes are parameterized. For the FRAM the coefficients chosen for numerical stability were close to those observed in the real ocean.

In addition to the numerical solution within the bounds of a numerical model grid, considerable care must be taken with the boundary conditions. These include the wind stresses and atmospheric effects such as evaporation at the surface as well as lateral and bottom friction. A common boundary condition in ocean models is the 'rigid lid' approximation which disallows surface gravity waves. As such waves have high velocities, very short time steps would be needed to resolve the resultant motions and precluding them allows a much longer time step to be used, easing the computation requirements. Perhaps most difficult of all boundary conditions to implement are those at open sea boundaries of a model where the transfer of all properties in and out of the model confines must be determined.

The first large scale three dimensional primitive equation model for baroclinic ocean circulation was coded by Bryan and Cox (1967), the physics and numerics of which are described by Bryan (1969). This model followed work on geostrophic baroclinic models by Sarkisyan (1962) and Gormatyuk and Sarkisyan (1965) as well as the atmospheric general circulation model of Smagorinsky (1963). Such circulation models are more difficult to verify than the thermocline models of workers such as Wellander (1959) and Stommel and Webster (1962) which attempt to predict the density structure of the ocean, because mass transport is difficult to measure in the real ocean. However, by resolving the velocity field for an entire ocean basin, rather than for a region of open ocean, they do attempt to remove the problem of introducing unrealistic interactions between the study area and surrounding oceans.

Eddy resolving models have been created recently to try and improve our understanding of the part that eddies play in distribution and transport of properties such as heat and salt. Because of the small grid scale required, eddy resolving models are very intensive of computer time and only recently have advances in computer technology made the use of such models feasible for more than regional studies. Semtner and Chervin (1988) ran a global model with a horizontal resolution of $^1/_2^\circ$ and 20 vertical levels which showed how the mesoscale field acted to intensify surface gradients of temperature and salinity relative to the climatic mean fields, even though mesoscale features were still not fully resolved. As part of the World Ocean Circulation Experiment's Community Modelling Effort Bryan and Holland (1989) developed a model of the North Atlantic with a horizontal grid of resolution $^1/_3^\circ$ latitude by $^2/_5^\circ$ longitude and 30 vertical levels. This model recreated much of the circulation of the North Atlantic well but still showed problems with details such as the point of separation of the Gulf Stream from the coast of North America. The FRAM is a continuation and advancement of these studies to a large region where the circulation is less well studied, especially at mesoscales.

3.2 THE FRAM PROJECT

FRAM is a primitive equation model which covers the entire Southern Ocean from 24° S to 79° S. The FRAM was the first large scale ocean circulation model to attempt to resolve the mesoscale features of the Southern Ocean. The grid spacing is 1/4° latitude by 1/2° longitude, which gives an equal N-S and E-W spacing at 60° S of approximately 27 km. This value was chosen as it is close to the Rossby radius and hence the model would have a chance of resolving the main eddy features of the ocean. The model has 32 vertical levels, increasing in thickness with depth, the top level having a thickness of only 20.7 m whilst the deepest is 233 m thick and extends to 5499 m.

The model uses bottom topography based on the DBDB5 depth data set (U.S. Naval Oceanographic Office, 1983). This data was smoothed to a 1° grid at model depth levels to prevent topographic instabilities developing in the model (Killworth, 1987).

The model used is based on the models of Bryan (1969), Semtner (1974) and Cox (1984) with a Northern boundary using the open boundary conditions developed by Stevens (1990). Within the interior the viscosity coefficients were 200 m^2s^{-1} horizontally and 10^{-4} m^2s^{-1} vertically, the diffusion coefficients for temperature and salinity were 100 m^2s^{-1} horizontally and 5×10^{-5} m^2s^{-1} vertically and bottom friction was initially linear.

The model was started with a cold (-2°C), saline (36.69‰) ocean having zero velocity and was dynamically relaxed to the Levitus data set (Levitus, 1982) for the first six model years. The relaxation times were sufficiently long to allow eddies to form within the model. Forcing was by means of annual mean winds (Hellerman and Rosenstein, 1983) which were introduced over the first three years of the model run, increasing linearly from zero.

After 6 years the relaxation to Levitus was removed and seasonal winds replaced the annual mean winds for forcing. After 8 years 11 months the bottom friction was changed to a quadratic form and biharmonic diffusion and viscosity were introduced.

3.2.a Results Obtained from FRAM

The results of the model up to year six are reported in by the FRAM Group (1991) where they find good qualitative agreement with observations of the flow through the Drake Passage (Whitworth *et al*, 1982) and the Falklands current, Brazil Current, Agulhas current and Menard fracture zone regions. Topography seems to be the major control on the ACC, which appears to have difficulty crossing ocean ridges, resulting in the formation of instabilities and hence regions of high eddy energy.

After 6 years, the change in forcing and removal of relaxation resulted in an increase in the eddy energy of the ACC. Eddies generated in the Agulhas region became

less regular in form with more variation in propagation track and seasonal changes were noticed in the South Atlantic Gyre (the FRAM group, 1991).

The change in bottom friction, viscosity and diffusivity terms caused a further increase in eddy activity, especially in the ACC, again increasing the model kinetic energy. Killworth (1991) has compared five years of FRAM data (horizontal velocities and eddy kinetic energy) with those of Patterson (1985) for the FGGE drifting buoy arrays (see § 4.2 for a discussion of these data). Killworth found good surface correlation of the eastward velocity and eddy kinetic energy, but very poor correlation of the northward velocity, the reason for which is still not understood. Lutjeharms (1991) compared the results of the model in the Agulhas area with hydrographic information and found that although it is reasonably good at predicting the mesoscale activity, the FRAM underestimated the variability of some areas, especially where the topography was not accurately resolved.

4 GROUND TRUTH

The Southern Ocean is one of the most important regions of the world's oceans, being the source of the majority of bottom and intermediate waters and the only connection between the major ocean basins. Historical information on the currents of the Southern Ocean is scarce due to the harsh environment, with high wind and wave regimes making data collection difficult and expensive.

4.1 DATA COLLECTION METHODS

Measurements of the ocean currents can be made by two main methods:

1: Direct current measurement.

2: Indirect calculation from other hydrographic information.

4.1.a Direct Current Measurement

Measurement of currents can be made using one of two principles, a Eulerian method which aims to find the current direction and speed for all locations within an area for all times, or a Lagrangian method, which follows the flow of individual particles in the fluid and determines their velocity.

Measurement by current meters employs a Eulerian principal, determining the current at specific locations. Current meters may be deployed from ships, but this introduces major problems concerning the ship location and movement. Even where it is possible to anchor a ship, maintaining an exact location is not generally possible as the ship will drift slightly around its moorings and no fixed frame of reference for the measured currents will exist. An additional problem is the apparent current variation in the meters induced by vertical motions of the ship with surface waves. An alternative is to moor current meters in strings on a cable, supported by a buoy and anchored to a bottom weight. This limits the possible movement of the meters as the line is held close to vertical, and multiple deployments allow simultaneous measurements of currents from a range of depths and locations.

Two further methods of direct Eulerian current measurement are used which utilize the transmission of sound. Ocean Acoustic Velocity Tomography uses a pair of acoustic transmitters and receivers to measure the time for a sound signal to travel along a given path in two opposite directions. The travel time for sound travelling with a current is less than that against a current and so the current velocity component along the transmission path can

be found. A second, recent addition to hydrographic instrumentation is the Acoustic Doppler Current Profiler (ADCP). This instrument exploits the Doppler effect or shift in frequency induced by relative motion between a sound source and a reflector. Two narrow beam echo sounders are targeted at the same parcel of water and the frequency of sound backscattered by particles in the water is measured. The Doppler shift is proportional to the velocity of the ship relative to the water and so the ship's absolute velocity must be known to obtain the current speed.

An alternative method of direct current measurement is through the use of drifting buoys, a Lagrangian method of current determination. Surface buoys, often coupled to the ocean currents by sub-surface drogues, are released into the ocean and then tracked. The original method of tracking buoys was by visual location from ships, but the majority of buoys now emit radio signals allowing radio ranging of the buoys, by ships or shore stations, or Doppler shift calculation by satellite systems. The measurement of sub-surface currents is also possible with the use of neutrally buoyant floats, often known as 'Swallow floats' after their inventor John Swallow, which have pre-set densities to allow them to float at pre-determined depths. These floats emit signals which can be tracked by nearby ships or, via the SOFAR technique, by fixed 'listening stations'. All drifter data suffer from the possibility that the floats are not fully coupled to the ocean currents. For surface drifters the problem is increased by the likelihood of wind or surface waves modifying the buoys' motions.

Ship drift is a type of drifter measurement which has the advantage of being a by-product of all ship navigation. Ship drift is calculated by comparing the expected location of a ship (from speed and course) with its actual location, found by astronomical or chart observations, the difference being caused by the ocean currents. These data provide the most extensive form of historical current data, especially in areas where there are major shipping routes, although large regions of the Southern Ocean have very poor coverage.

4.1.b Indirect Methods of Current Determination

Because of the expense of ship time to deploy and recover instruments and the cost of the instruments themselves direct measurement is restricted to a limited number of locations and indirect methods of current measurement have been developed. The most common form of indirect current determination is by use of the geostrophic equation, which gives velocity characteristics from vertical density profiles of the ocean. The method neglects all friction and assumes that the region under analysis is far from any boundaries, which results in there being a balance between the horizontal pressure gradient and the Coriolis force.

If an isobaric (constant pressure) surface is not parallel to the local geoid surface there will be a resultant horizontal pressure gradient. A particle of water which exists in an area of horizontal pressure gradient will have a force (the pressure gradient force) exerted

upon it which will cause it to begin moving down the pressure slope. Once movement has begun however, the Coriolis force will act perpendicular to the motion (to the right in the Northern Hemisphere and the left in the Southern Hemisphere) tending to accelerate the particle to the right (or left) until it is moving perpendicular to the pressure gradient force. At this time the Coriolis force is equal and opposite to the pressure gradient force and there is a balance of forces which can be represented by the gradient equation;

$$fV = g\tan\theta \qquad (4.1)$$

where;

θ is the angle of the isobaric surface to the geoid

V is the velocity perpendicular to the gradient

f is the local Coriolis parameter, given by;

$$f = 2\Omega\sin\phi$$

where;

Ω is the earth's angular velocity of rotation (7.29×10^{-5} rad s^{-1})

ϕ is the latitude

In order to find the geostrophic current, V, the slope of the isobaric surface must be found. All ship measurements are made relative to the sea surface which is itself sloping due to the surface geostrophic currents and so θ can not be measured directly. Instead the distance between two isobaric surfaces is found to give the velocity at one level relative to the other, or the 'velocity shear'. From equation 4.1 the difference in velocity between isobaric surfaces 1 and 2 is given by;

$$(V_1 - V_2) = \frac{g}{f}(\tan\theta_1 - \tan\theta_2) \qquad (4.2)$$

and taking the height of surface 2 above surface 1 as h_A and h_B at two stations A and B distance L apart equation 4.2 becomes;

$$(V_1 - V_2) = \frac{g}{fL}(h_B - h_A) \qquad (4.3)$$

one form of the geostrophic equation.

The value of h_B-h_A is not measured directly but is calculated from the density structure of the ocean using the hydrostatic equation and equation 4.3 can be written as;

$$V_1 - V_2 = \frac{g}{fL}\left(\int_{p_1}^{p_2}\frac{1}{\rho_B}\mathrm{dp} - \int_{p_1}^{p_2}\frac{1}{\rho_A}\mathrm{dp}\right) \qquad (4.4)$$

In barotropic conditions density is controlled only by depth, not temperature and salinity. In this case isobaric surfaces will be parallel to the sea surface, θ will be constant with depth and flow will be equal through the entire depth of the ocean, i.e. there will be no current shear. In baroclinic conditions density is controlled by temperature and salinity as well as pressure. Geostrophic calculations will only yield the velocity shear and so only the baroclinic portion of flow is found.

Traditionally geostrophic current determinations are made relative to an assumed 'level of no motion', a depth at which no flow is assumed to occur, and isopycnal surfaces are found relative to this level. If this assumption of no motion is not true, due to barotropic tides for instance, then only the baroclinic component of currents can be determined. In the sub tropical gyres a depth of 1500 m is often used as this is usually a good approximation to a level of no motion. An alternative level of no motion is at great depth. The sea floor can not be used as a level of no motion, despite the fact that current flow here is usually zero, as friction is specifically omitted from the geostrophic approximation. If synchronous direct current measurements and density fields are found, then a 'level of known motion' can be used in the calculation.

Geopotential is the potential energy gained per unit mass in raising water through a given height z and so the difference in geopotential between two surfaces is given by;

$$\begin{aligned}\Phi_2 - \Phi_1 &= -\int_{p_1}^{p_2} \frac{1}{\rho}\,\mathrm{dp} \\ &= -\int_{p_1}^{p_2} \alpha_{35.0.p}\,\mathrm{dp} - \int_{p_1}^{p_2} \delta\,\mathrm{dp} \\ &= -\Delta\Phi_S - \Delta\Phi\end{aligned} \qquad (4.5)$$

where;

$\alpha_{35.0.p}$ is specific volume $\left(\frac{1}{\rho}\right)$ at standard temperature and salinity

δ is the specific volume anomaly

$\Delta\Phi_S$ is the standard geopotential

$\Delta\Phi$ is the geopotential anomaly

By substituting α and δ for ρ in the geostrophic equation 4.4 we have

$$\begin{aligned}V_1 - V_2 &= \frac{g}{fL}\left(\int_{p_1}^{p_2} \delta_B\,\mathrm{dp} - \int_{p_1}^{p_2} \delta_A\,\mathrm{dp}\right) \\ &= \frac{g}{fL}\left(\Delta\Phi_B - \Delta\Phi_A\right)\end{aligned} \qquad (4.6)$$

This concept is useful as it allows production of dynamic topography maps from the specific volume anomaly distribution. These give a visual representation of flow relative to the level of no motion with flow direction parallel to the topographic contours (high

regions to the left of flow in the Southern Hemisphere), and flow rate dependant on the slope steepness. The geopotential distance $\Phi_2 - \Phi_1$ (J kg^{-1}) is usually given in units of 'dynamic metres' (dyn m) where 1 dyn m = 10 J kg^{-1} and this dynamic height is numerically almost equal to the height difference (in metres) between isobaric surfaces.

In order to calculate the two dimensional flow characteristics of V over an area of ocean, a grid of hydrographic station data is needed. This takes time to collect and so the data is never totally synoptic even on a scale of 50 to 100 km, leading to some smoothing of the dynamic fields over time.

4.2 SOUTHERN OCEAN CIRCULATION

The dominant feature of Southern Ocean circulation is the Antarctic Circumpolar Current (ACC), a broad, easterly zonal flow which has been recognized since the beginning of this century. The ACC was originally known as the 'West Wind Drift' because it is primarily driven by the strong westerly winds of the Southern Ocean. Energy is transferred from the wind to the surface waters as a consequence of fluid friction, but the resultant motions are complicated by the effects of the Coriolis force and the latitudinal wind gradient (see Pond and Pickard, 1983, chapter 9 for an explanation of some of the theories of wind-driven circulation).

Hydrographic information from cruises, by *Discovery*, USNS *Eltanin* and USNS *Meteor* amongst others, have allowed the large scale dynamic topography of the Southern Ocean to be determined. Figure 4.1 shows the dynamic height anomaly of the Southern Ocean relative to the 1000 dbar level as determined by Gordon *et al.* (1978) from all available hydrographic data. The mean circulation is a continuous easterly flow with an axis varying in latitude from approximately 49°S in the South Atlantic to 52°S south of Australia and 57°S in the South Pacific. This mean flow is dominated by bathymetry and dynamic height contours are frequently influenced by sea floor features. South of New Zealand, where the geostrophic current crosses the Macquarie Ridge System (160°E), the dynamic height contours show strong deflection southward as discussed by Gordon (1972). The current then branches, with the southern arm continuing eastward whilst the northern branch veers northwards to 50°S before it too returns to a zonal flow.

In the Southwest Pacific the ACC breaches the Antarctic-Pacific Rise in the Udintsev fracture Zone (56-57°S) where there is an intensified flow. At 145°W the dynamic height slope of 48×10^{-7} dyn m km^{-1} gives a geostrophic velocity of 40 cm s^{-1} with respect to the 2500 dbar level (Gordon and Bye, 1972). Downstream of this feature Rossby waves are seen, which migrate westward with a velocity equal and opposite to the current resulting in standing waves of wavelength almost 1000 km (Gordon and Bye, 1972).

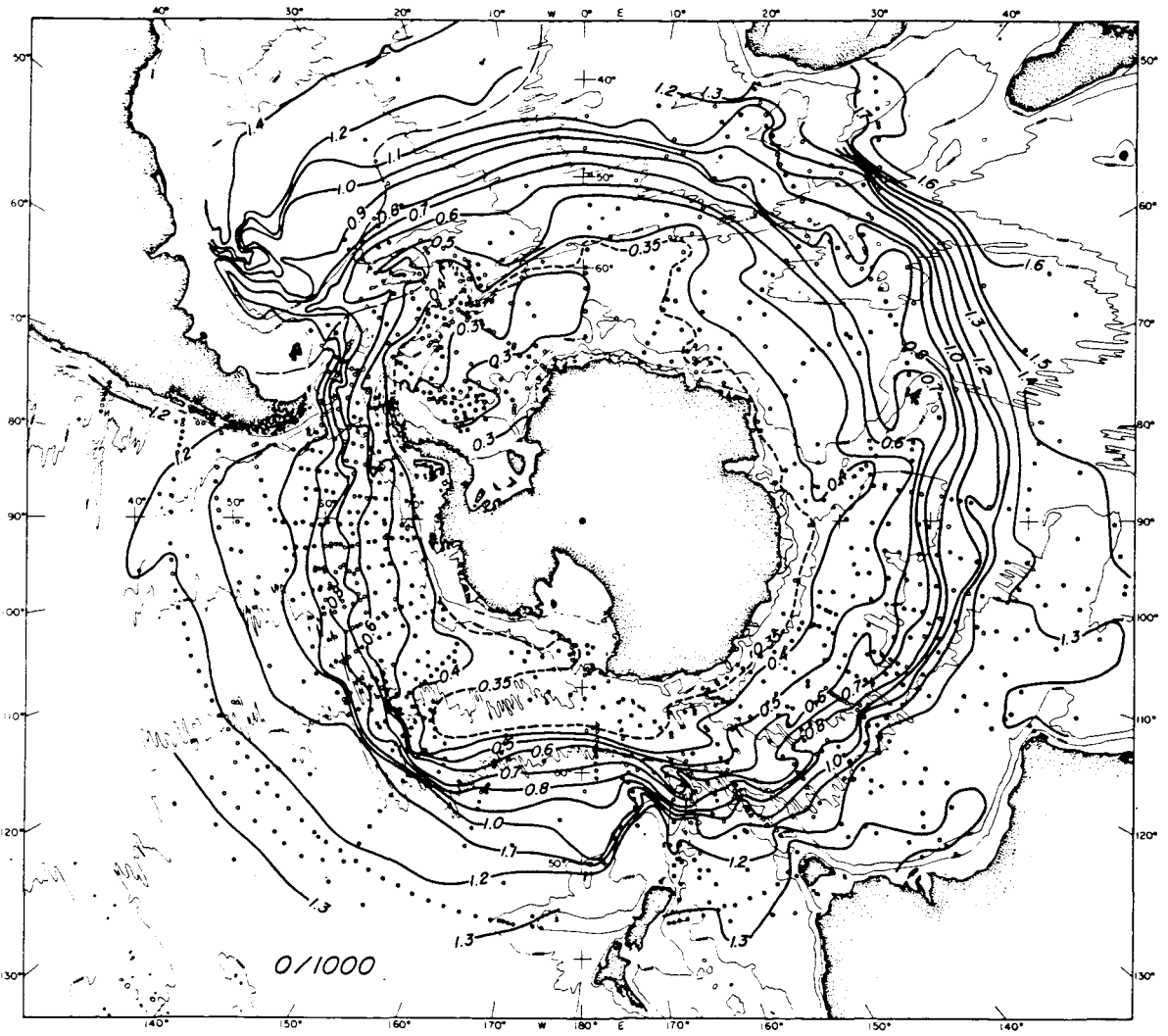

Figure 4.1 Anomaly of Geopotential Height of the Sea Surface Relative to the 1000 dbar Level, expressed in Dynamic Meters (from Gordon *et al.*, 1978).

The Agulhas current region to the south and east of Africa is not shown by the data set used by Gordon *et al.* but work, by Darbyshire (1964; 1972) and Lutjeharms (1972) amongst others, has shown the dynamics of this current system. The Agulhas current flows down the east coast of South Africa, turning west along the coast until 15-20°E where it abruptly reverses direction in an anticyclonic loop (the Agulhas Retroflection) to form the Agulhas Return Current at around 40°S. This current forms an arm of the ACC which intensifies on the Eastern edge of the South-West Indian Ridge (40°E).

There is also evidence from the dynamic height field of two cyclonic gyre systems existing in the Southern Ocean, the Weddell Sea Gyre, centred on 20°W 65°S, and the Ross Sea Gyre around 175°W 68°S. Hydrographic evidence for these gyres is poor however as they are within the seasonal ice extent of Antarctica making surveying difficult. Iceberg movements (Tchernia, 1974; Swithinbank *et al.*, 1977) and direct current

measurements (Sverdrup, 1953) together with drift of cruise ships (Deacon, 1937) form the basis of knowledge of the west and north flowing limbs of the Weddell Sea Gyre.

This mean geostrophic circulation is only an indication of the baroclinic portion of the Southern Ocean Circulation. The baroclinicity of the 1000 dbar level relative to 2500 dbar shows very similar features to that of figure 4.1 (Gordon *et al.*, 1978) indicating that the 1000 m level is not a true level of no motion and actual baroclinic flow may be greater than indicated by figure 4.1 This also indicates that surface currents may extend to several kilometres depth around most of the Southern Ocean.

From 1978-1979 316 satellite tracked drifting buoys were deployed in the Southern Hemisphere as part of the First GARP (Global Atmospheric Research Program) Global Experiment (FGGE), half of them in the Southern Ocean. Patterson (1985) calculated the mean buoy velocities in 5°×5° squares to give the mean surface circulation. This circulation agrees qualitatively with that of Gordon *et al.* (1978) but is less detailed due to the coarse resolution of the grid. Patterson also calculated the mean kinetic energy of the buoy velocity data on the same grid and this shows the ACC as a zone of high mean kinetic energy. The Agulhas Retroflection zone has one of the highest mean kinetic energy values at more than 1000 cm^2s^{-2}. Patterson also notes the apparent correlation of the highest mean kinetic energy areas with areas where the ACC crosses major bathymetric features.

The variability of the Southern Ocean at mesoscales is very important as much momentum and heat transfer is believed to be by eddies and other mesoscale features (Nowlin and Klink, 1986). The collection of data at the high spatial and temporal frequency required to study such motions requires extensive resources in time and money. Wyrtki *et al.* (1976) used ship drift data to find eddy kinetic energy for variations on time scales greater than 1 day and length scales of more than 400 km, restricted by the observation frequency of ship drift. These data do show higher mean and eddy kinetic energy in the ACC but observations are very limited this far south. The FGGE drifter data set shows mesoscale activity present all around the ACC, with eddy kinetic energy more than twice the mean kinetic energy almost everywhere south of 35°S (Patterson, 1985). The highest eddy kinetic energy values are in the Western boundary currents, with a maximum of 4000 cm^2s^{-2} in the Agulhas retroflection zone. Most of this energy is at time scales of less than 1 month.

Most of the hydrographic data available in the Southern Ocean are for the Drake Passage because the Southern Ocean is here limited to a narrow (800 km), relatively accessible zone. Volume transport estimates calculated for Drake Passage vary from 15 Sv (1 Sv = 10^6 m^3s^{-1}) westward by Foster (1972) to 237 Sv eastward by Reid and Nowlin (1971). The estimate by Foster uses only 10 days of data from 4 current meter strings, whilst that of Reid and Nowlin combines hydrographic and current meter measurements but requires the interpolation of current meter values to the hydrographic stations. As part of the International Southern Ocean Studies (ISOS) project, dense current meter arrays were deployed in the Drake Passage for up to 1 year, some coincident with hydrographic

stations. Using the short term current meter and hydrographic data, Nowlin *et al.* (1977) calculated transport rates over 3 weeks of 110-138 Sv with an average of 124 Sv. Bryden and Pillsbury (1977) calculated an average of 139 Sv over the whole year, but with variations of 28-290 Sv having typical time and space scales of 2 weeks and less than 80 km. This variability is associated with strong zonal jets at major fronts where surface velocities of 20-30 cm s^{-1} were recorded by Nowlin *et al.* (1977) separated by zones of low westerly or occasional easterly flow. These current cores move laterally up to 100 km in 10 days.

The flow of the ACC has been shown to be in approximate geostrophic balance (Whitworth and Peterson, 1985), with the mean flow being 70% baroclinic whilst fluctuations are dominantly barotropic. Little seasonal variability has been noted but maximum flow seems to occur in March and September, however, strong interannual variability is evident in the transport (Whitworth and Peterson, 1985). The surface ACC is wind driven and so there is a slight northerly component to the flow which is non geostrophic, however the velocity and eddy kinetic energy distributions found from FGGE drifters (Patterson, 1985) are very similar to those derived by Lutjeharms and Baker (1980) using geostrophic calculations. This tends to imply that the variation is due to changes in geostrophic flow.

The importance of mesoscale activity in the Southern Ocean and the geostrophic nature of much of this flow has led to an increasing interest in altimeter observations which can give long term, high resolution information on the surface circulation.

Section II: GEOSAT DATA

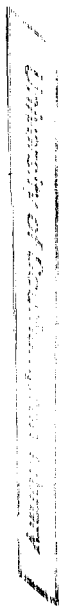

5 DATA PROCESSING

In order to process the Geosat Geophysical Data Record (GDR) data into a useful form, a suite of programs had to be written, adapted from those developed by Stephen Foale at the Institute of Oceanographic Sciences Deacon Laboratory (IOSDL) (Challenor *et al*, 1990). These programs were designed to extract data for the required orbit arcs from the GDR tapes held at the Natural Environment Research Council (NERC) computing centre at the Institute of Hydrology, Wallingford and to process the data using along-track, collinear techniques.

This suite of programs performs the following tasks:-

1: Locates and extracts the tracks required from the GDR tapes.

2: Draws maps of selected areas with the Geosat tracks available superimposed.

3: Processes the data to give the corrected heights, variability and corrections for each data point.

4: Displays the resultant data.

5.1 DATA EXTRACTION

The data used consists of a series of selected orbit arcs which are extracted from the global Geosat GDR tapes. The tapes each contain approximately 34 days, or 2 orbit repeat cycles, of data. To locate the required orbit arcs in each tape, the program requires the expected time of the start of each overpass. This time must be calculated using an average repeat orbit time and the start time of the first overpass of any specified arc, taken from a printout of all data points within the area of interest.

There are some problems with extracting data from the study region, especially on the ascending passes (south to north). These tracks begin over the Southern sea-ice areas and the tracking algorithm has difficulty in retaining lock, especially where the ice surface has high, broken topography.

Originally the start of each arc was located using the latitude and longitude of the start point. This point was then searched for and only data within 8 km of the required location would be accepted. Although it is simpler to extract data in this way, if the first data point is absent due to data dropout, the entire arc is lost for that repeat. This is a serious problem on the ascending overpasses where ice may cause data loss.

Once the arc is located the following 1000 data records are copied directly to disk file and all repeats of the same track are appended to form a single file. The same number of records are read for each arc so that all tracks are of the same length. Extracting only data

points within a specified region is a simpler task and requires less data storage space, but arcs will be of different lengths creating problems later when applying the orbit corrections.

5.2 CHECKS ON DATA QUALITY AND CORRECTIONS APPLIED

The Geosat GDRs are produced from the sensor records telemetered by Geosat, and they contain many errors either from the sensor, or due to the telemetry system. The majority of these errors are located during production of the GDRs and poor or doubtful quality data are assigned appropriate flags. In addition some data values are missing and other poor quality data are not flagged but must be tested for. The format of each record on the data tapes is given in table I.

5.2.a Data Quality Checks

Poor data were found either by using the data flags (item 24 in the GDR) or by testing for certain criteria in the other items. Data values were rejected if they failed any of the following tests.

1: If any value for items 1-18, 26-28, 30 or 31 is set to 32767. These represent data values rejected during creation of the GDR from the sensor records or correction values which are not available and account for less than 0.05% of data.

2: $\sigma_H = 0$. This test precludes any data for which the variation in height measurements for an entire second is zero, an unlikely occurrence in the open ocean, probably indicating a sensor malfunction. This test eliminates less than 0.1% of the data.

3: $\sigma_{SWH} = 0$. This test for zero SWH variability was included to remove some clearly anomalous data which passed all other checks. By inspection of the GDRs it was seen that non-zero SWH values occasionally had zero associated variability, suggesting that the sensor was behaving abnormally, perhaps a fault in the tracking algorithm. Very few data points are lost by this test, most tracks having no data lost. The program originally included far more severe SWH quality tests as it was developed from one designed to look solely at the SWH. These earlier tests seemed to eliminate large amounts of data for which the SWH was very variable but the sea surface height was not and as a consequence are not currently being used.

4: $\sigma_0 = 0$. As this would imply that there was no return the sensor was clearly malfunctioning and any associated height data is probably erroneous. On some tracks as much as 2.5% of data was lost by this check, but the average was only 1%.

ITEM	PARAMETER	DESCRIPTION	UNITS	RANGE	BYTES
1	UTC	universal time coordinated in seconds from 00:00 01-01-1985	s	0 to 2E31	4
2	UTC(cont.)		μs	0 to 1E6	4
3	LATITUDE		μ°	± 7.21E7	4
4	LONGITUDE		μ°	0 to 3.60E8	4
5	ORBIT	satellite height.	mm	7E8 to 9E8	4
6	H	one second average sea surface height (ORBIT-measured height) corrected for FM cross-talk, spacecraft centre of gravity, pre-launch sensor calibration and ATTITUDE/SWH bias. Calculated from a straight line fit of the 10 Hz averages (items 9-18) using the method described in Cheney *et al*, 1987.	cm	± 32766	2
7	σ_H	standard deviation of the 10 Hz height values from the best fit line.	cm	0 to 32766	2
8	GEOID	model geoid height.	cm	± 1.5E5	2
9	H(1)	first 10 Hz sea surface height value	cm	± 32766	2
10	H(2)	second 10 Hz sea surface height value	cm	± 32766	2
11	H(3)	third 10 Hz sea surface height value	cm	± 32766	2
12	H(4)	fourth 10 Hz sea surface height value	cm	± 32766	2
13	H(5)	fifth 10 Hz sea surface height value	cm	± 32766	2
14	H(6)	sixth 10 Hz sea surface height value	cm	± 32766	2
15	H(7)	seventh 10 Hz sea surface height value	cm	± 32766	2
16	H(8)	eighth 10 Hz sea surface height value	cm	± 32766	2
17	H(9)	ninth 10 Hz sea surface height value	cm	± 32766	2
18	H(10)	last 10 Hz sea surface height value	cm	± 32766	2
19	SWH	one second average of the 10 Hz significant wave-heights, corrected for ATTITUDE/SWH bias and found as for H.	cm	0 to 2E3	2
20	σ_{SWH}	standard deviation of 10 Hz SWH values	cm	0 to 2E3	2
21	σ_0	backscatter coefficient, corrected for satellite height, receiver temperature, ATTITUDE/SWH effect, on-board and pre-launch calibration.	.01 db	0 to 6.4E3	2
22	AGC	one second average of the 10 Hz values of automatic gain control, found as for H.	.01 db	0 to 6.4E3	2
23	σ_{AGC}	standard deviation of 10 Hz AGC values	.01 db	0 to 6.4E3	2
24	FLAGS				2
25	H OFFSET	supplied for land use.	m	0 to 5.0E4	2
26	SOLID TIDE	solid earth tidal correction based on Cartwright and Taylor (1971) and Cartwright and Edden (1973)	mm	± 1000	2
27	OCEAN TIDE	surface ocean tidal correction based on Schwiderski (1980).	mm	± 10000	2
28	WET (FNOC)	FNOC wet tropospheric correction.	mm	0 to -1000	2
29	WET (SMMR)	SMMR wet tropospheric correction.	mm	0 to -1000	2
30	DRY (FNOC)	FNOC dry tropospheric correction.	mm	-2E3 to -3E3	2
31	IONO (GPS)	ionospheric correction.	mm	0 to -500	2
32	dh(SWH/ATT)	height bias caused by attitude-wave-height interaction.	mm	± 9999	2
33	dh(FM)	height bias caused by linear pulse compression of the radar signal.	mm	± 999	2
34	ATTITUDE	spacecraft off-nadir orientation angle, found from the return waveform trailing edge.	.01°	0 to 200	2

Table I Geophysical Data Record Content (after Cheney *et al*, 1987).
All height measurements are given relative to the reference ellipsoid.

5: $\sigma_H > 0.1$ m. This is to try and remove those data contaminated by the effects of rain cells. H, σ_H and AGC are all affected but σ_H has proved to be the most reliable parameter for editing Seasat data (Cheney *et al*, 1987). This test removes up to 7.5% of all data.

6: $\sigma_0 > 20$ dbar. In this case the data may be contaminated by land in the footprint, or be a specular return from a calm sea, as normal oceanic backscatter rarely exceeds 15 dbar, in either case the data is likely to be unreliable. Between 1 and 2% of data on most tracks was removed by this check.

7: Flags

a. flag(0) = 0. This flag indicates the sensor footprint includes land and is set according to a land mask. Small islands and ice areas, which may contaminate the signal, are not included in this mask and so the σ_0 test must still be made.

b. flag(2) = 1. This flag is set if dh(SWH/ATT) or dh(FM) are out of their normal range, indicating that the satellite was not operating normally. Less than 1% of data was eliminated by this test.

8: An additional test which rejects the first two data points after leaving a flagged land area. This is a further safeguard against land contamination and also potential problems with loss of lock.

In all the above cases the latitude and longitude data are still used, if present, but the height values are substituted by an 'absent-data' value.

These checks do not eliminate all poor quality data points. Some may be caused by the waveform tracker of the altimeter, which switches to a wider search window if the waveform is located in the centre of its window. Incorrect summation of the wave-forms then produces a waveform offset resulting in erroneous height calculations.

In addition to these data value quality checks a further test had to be included to allow for gaps in the data set. These gaps are created by NOAA in preparation of the GDRs, either due to the removal of land and ice records or absent and irretrievable data points, particularly those due to loss of attitude as ionic activity increased. The method of testing for such absent data involved comparing the actual time of a record with the expected time of that record, using the sample interval of 0.97992165 s. Any missing data are 'padded' using absent-data values and these may make up 25% of some track repeats although this is rare, with less than 1% of data normally absent.

5.2.b The Corrections Applied

Corrected sea surface height data are obtained from the GDR using;

H_c = SOLID TIDE–OCEAN TIDE–IONO(GPS)–DRY(FNOC)–WET(FNOC)–INV BARO

where;

H_c is the corrected sea surface height

INV BARO is the inverse barometer correction

This formula does not include the model geoid correction given on the GDR due to a problem with the interpolation method used whilst creating the records. The result was to introduce undulations of up to 1 m amplitude and space scales of around 150 km (as shown in figure 5.1). Such large variations almost totally mask the current signals and are at almost identical space scales. This problem was reported in Cheney *et al.* (1988) and consequently an alternative method of geoid removal must be used.

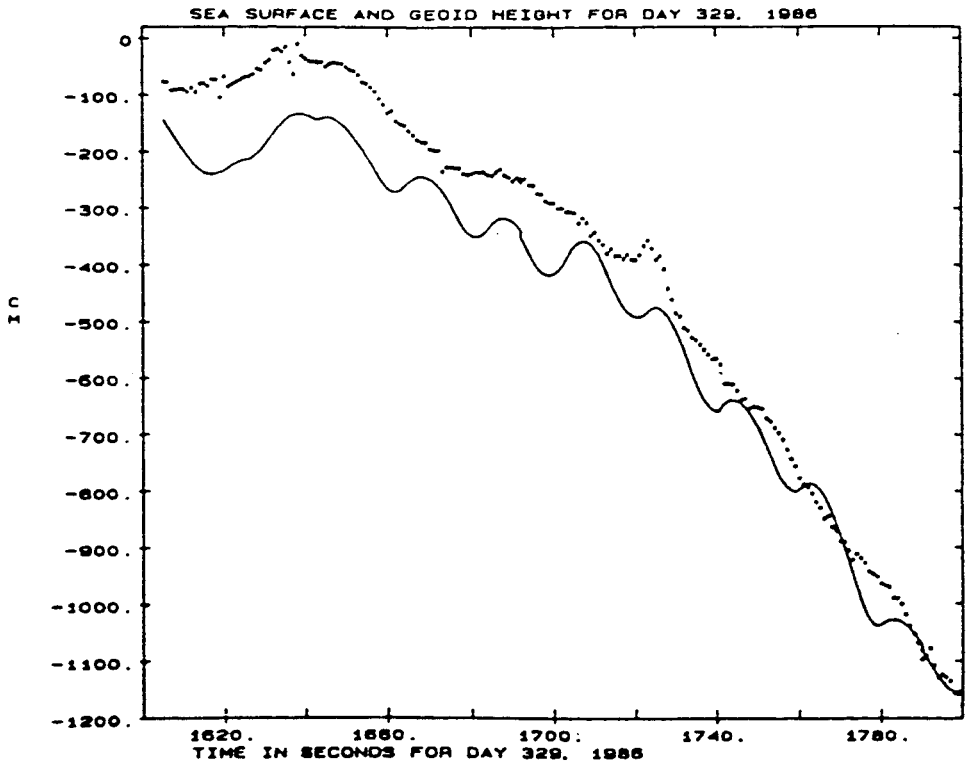

Figure 5.1 Comparison of Geosat Height and GDR Geoid Height for a North Pacific Segment (from Cheney *et al.*, 1988).

The Ocean Tide correction supplied on the GDR tapes was altered according to a recommendation by P. Woodworth of the Proudman Oceanographic Laboratory for all records after the start of 23rd October 1988 (Doyle *et al.*, 1989). This change was to ammend some tidal constituents of the Schwiderski model tide which resulted in a global change of 1.5 cm rms for the tidal correction and so data after the 41st repeat will vary slightly from the first 23 months of data. Applying the changed correction to all the repeats would have involved obtaining the new constituents, calculating the altered correction for all previous repeats and then re-working all the processing. It was decided that the residual

increase in error over an orbit arc after a quadratic long wavelength adjustment had been applied was too small at mesoscales to warrant the additional work.

The FNOC wet tropospheric range correction is a real time correction rather than a monthly average and should account for any unusual weather during the time of overpasses. Work done by Emery *et al.* (1990) shows that the SMMR correction is closer to water vapour measurements obtained by satellite atmospheric sounders than the FNOC value, especially in the Southern Ocean. Unfortunately it was found that the SMMR data set was incomplete for some of the areas under study and so no SMMR correction was available and the FNOC correction had to be used. This should not effect the short time scale however, as Ray *et al.* (1991) show that the two corrections give the same reduction in rms height residual when comparing two consecutive orbit repeats.

The GDR users handbook suggests the use of a 2% SWH correction to account for sea-state bias, however, recent work seems to show that this is too simplified. Witter and Chelton (1991) show that the proportional correction to be applied is SWH dependant, being approximately 3.5% for SWH values less that 4 m but decreasing linearly to 1.5% for 6 m SWH. They suggest that this change may be due to the effects of antenna mis-pointing on the tracker explained by Hayne and Hancock (1990), as the largest SWH values occur in the Southern Ocean where Geosat attitude errors are worst. So far no analysis of this possibility has been carried out. The change may also be due to unusual wave field characteristics in the Southern Ocean which has unique basin morphology. Fu and Glazman (1991) show that there is a correlation between sea-state bias and wave age, possibly due to swell waves being less 'peaky' in form. Although wind speeds are generally high in the Southern Ocean, and so many of the waves are young, there is also a significant swell contribution. As the change in SWH is generally over long wavelengths it was felt unnecessary to apply any correction.

The inverse barometer effect is also corrected. This correction is determined from the GDR using;

$$\mathbf{INV\ BARO} = -9.948(p - 1013.3)$$

where;

p is the surface atmospheric pressure (mbar) given by:

$$p = \frac{\mathbf{DRY(FNOC)}}{-2.277(1 + 0.0026\cos 2\phi)}$$

where;

ϕ is latitude.

This correction does not allow for the time response of the ocean to atmospheric pressure changes, which is not fully understood and this may introduce error although Ray

et al (1991) have shown that including this correction reduces the global rms variation of height residuals over the ocean, indicating that its inclusion reduces residual errors.

5.3 THE PROCESSING TECHNIQUE

One of two possible methods of processing could have been used for the Geosat data, a collinear method or a cross-over differences method (see chapter 2). The choice of a collinear method of data processing for this project was influenced by several considerations.

The primary factor was the constraint of available computing facilities. In order to process Geosat data using a cross-over technique the rms difference at all crossing points for a particular repeat within a given area must be minimized. In order to achieve this simultaneous orbit corrections must be calculated for every track included. This technique requires extensive facilities in terms of computational time and memory, as well as programming. A collinear technique has much less stringent demands on computing facilities.

A second factor was concern for the problems of residual orbit error. A cross-over technique attempts to minimize orbit errors by minimizing the height differences at intersections of ascending and descending orbit arcs. Height measurements at these cross-overs are separated in time and the time separations occur at discreet intervals determined by the orbit ground pattern (see Douglas *et al*, 1984, for a discussion). The matrix inversion to calculate the orbit error in cross-over analysis is only capable of removing the frequencies of orbit errors which are resolved by these discreet time separations. Unfortunately the main orbit residual error is at a frequency of almost once per orbit revolution and this is not a resolved frequency, leaving a 'once per orbit' radial error in the data. This is not the case for collinear methods as the orbit error calculation is specific to a single orbit arc repeat. Compounding the problem for cross-over techniques are the orbit 'jumps' which occur mainly over polar regions, due to actual satellite adjustments and also as part of the NAG orbit calculation.

A final factor in the decision to use a collinear technique was the scale of features which can be resolved. For cross-over methods data must be gridded to the scale of the orbit cross-overs, a much coarser grid than the 6.7 km possible along track, resulting in a loss of some of the fine scale detail of the data.

5.3.a Resampling Along Track

During the ERM mission objectives required the maximum cross-track ground separation of repeat Geosat orbits to be within 1 km, maintained by firing of the boosters

on board if the orbit drifts too far. This was maintained for the first year of the ERM but increased to 1.5 km during 1988 due to increased drag caused by the high solar activity (Doyle *et al*, 1989). However, the exact location of any sample point along the track was not constrained, as shown in figure 5.2, and this will introduce apparent sea surface height variability for a sloping surface if not allowed for.

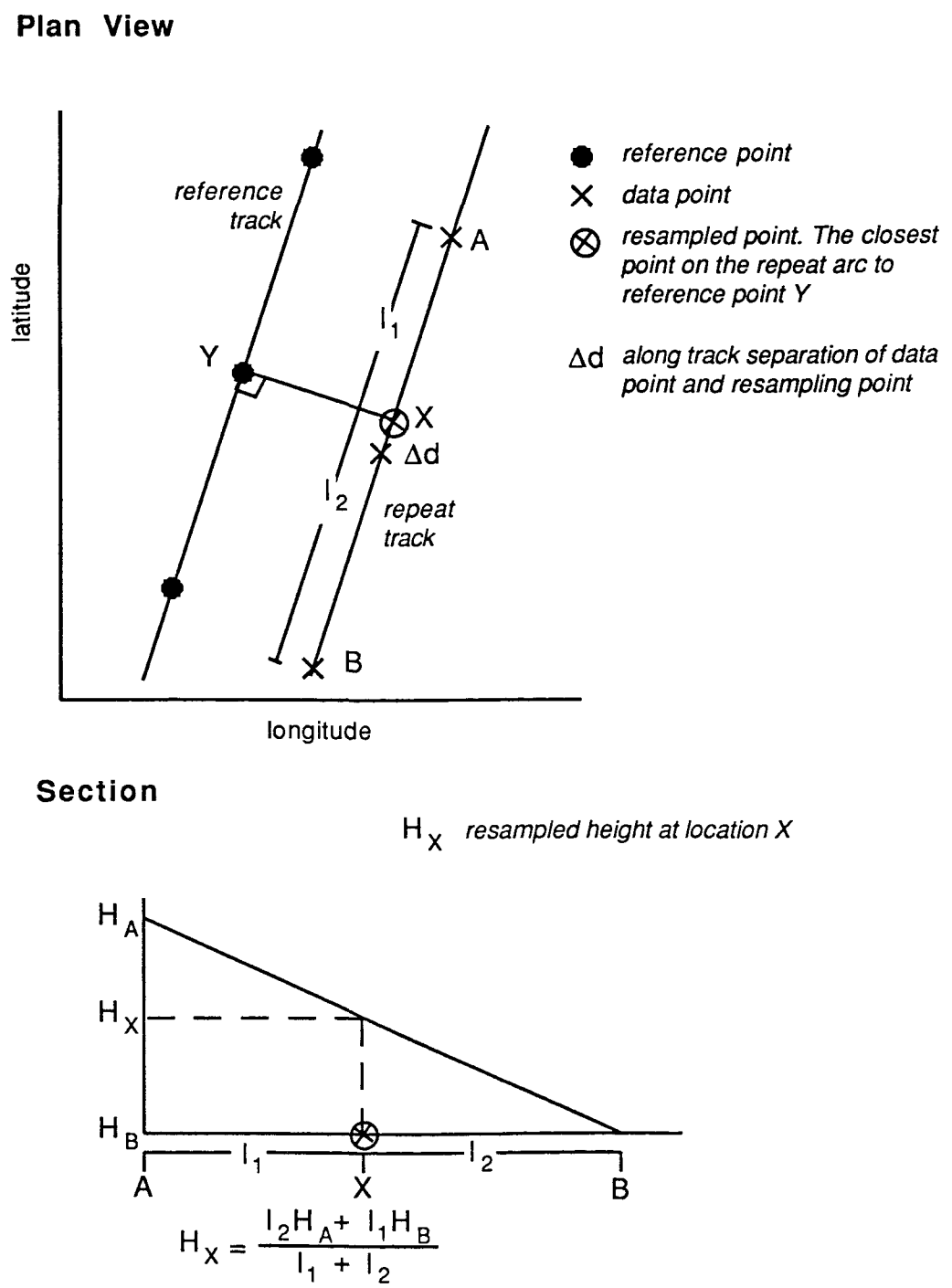

Figure 5.2 A Representation of the Ground Tracks of Two Repeats of the Same Orbit Arc Showing the Along Track Separation of Data Points and the Method of Correction.

A reference track was found for each orbit arc using the most complete available repeat of that arc. Where possible the actual GDR latitude and longitude values of this track were used as the reference, but where dummy values had been assigned due to gaps in the data, linear interpolation was carried out to give expected locations for the reference.

The processing program used applied a simple linear, along-track interpolation method to give sea surface height at the closest location on each repeat to the data point on the reference track (see figure 5.2). Interpolation was only carried out if height values for the two data points to be used in the interpolation differed by less than 20 cm, eliminating some data points which were suspect but not removed by the data quality checks.

This technique was designed to introduce the least possible smoothing along-track and hence preserve any small scale features in the data. It also has the advantage of eliminating isolated data points, sometimes seen amongst rejected data, which pass all quality controls but are clearly erroneous, such as that shown in table II.

Record Number	SWH (m)	σ_{SWH} (m)	Height (m)	σ_H (m)	Rejected
1	3.64	0.13	0.64	0.03	
2	3.97	0.24	0.57	0.08	
3	4.39	0.56	99.99	2.22	*
4	18.49	0.79	99.99	0.58	*
5	17.88	2.66	-45.9	0.04	
6	99.99	99.99	99.99	99.99	*
7	99.99	99.99	99.99	99.99	*

Table II Sample of GDR Data Showing the Problem of Isolated Data Values(99.99 represents absent data).

5.3.b Removing the Geoid and Orbit errors

As has been mentioned previously, an error in the interpolation scheme for the geoid model given on the GDR tapes resulted in the correction being unusable. Instead the mean sea surface height profile along any track was taken to be an approximation to the geoid. In practice this mean sea surface height contains the mean current signature and any tidal aliasing in addition to the geoid, prohibiting calculation of the absolute currents.

This mean also contains the mean orbit error, however this still leaves a significant portion of the orbit error in any given repeat. To remove this residual error a quadratic curve is fitted to, and removed, from each arc repeat.

In theory it would be preferable to remove the orbit error from each track before the mean is calculated as this would remove some of the problems noted below. In practice however this has proved impossible as the orbit error is very much smaller than the geoid height in each track and a quadratic curve will approximate the geoid, with slight modification by the orbit error. Where data gaps occur, especially at the ends of arcs, the difference between the resultant quadratic and that for a complete track is much larger than the orbit errors and can introduce long wavelength error of several metres amplitude.

(1) Finding a Working Mean

The mean, $\bar{h}$, of all non-rejected data values, h, from N_{max} orbit repeats, was found at each data point, as defined in the along-track resampling process, using;

$$\bar{h}_j = \frac{1}{N_j}\sum_{i=1}^{N_j} h_{ij}$$

where;

i is the orbit repeat number

j is the along track data point number

N_j is the number of non-rejected data points at j

At least 10 data values had to be found at a point for the mean to be calculated, if less were available then $\bar{h}_j$ was undefined and all height values at that point were ignored in subsequent work. Where a mean was found, this mean was then subtracted from each valid data value to give corrected heights $h^{(1)}$ such that;

$$h^{(1)}_{ij} = h_{ij} - \bar{h}_j$$

(2) Removing a Quadratic Orbit Correction

After removal of the working mean the data was still dominated by random ephemeris errors, as seen in figure 2.7 (page 19) although the mean orbit error was removed. The residual error was modelled as a quadratic curve, fitted to and removed from each track repeat in order to minimize the along track rms height residual. This gave height residuals $h^{(2)}$ as;

$$h^{(2)}_{ij} = h^{(1)}_{ij} - \left(a_i + jb_i + j^2 c_i\right)$$

where;

a_i, b_i and c_i are orbit specific constants.

The quadratic correction not only removes the dominant long wavelength orbit error, but also some part of other long wavelength errors such as the inverse barometer and tidal residuals. The correction will not however remove any small scale residual errors.

(3) Improvement of the Mean

At this stage of the processing, height residuals such as those shown in figure 5.3 have been obtained, which could be used as an indication of the mesoscale variability of the ocean.

Unfortunately, when the data set is as sparse as that for Geosat can be, the working mean is contaminated by the difference in residual orbit errors between repeats. Where mean values at all data points do not use the same number of values, from the same repeats, then it is possible to introducing artificial jumps in the resultant sea surface height values

such as those shown in figure 5.3, due to the random orbit error residuals. At A in figure 5.3 the fourth repeat of this arc ends and a corresponding step can be seen in all the other repeats, where it is not masked by other signals. At B a very short section of the first repeat is included and there is a corresponding square step in the other repeats. The introduced feature at C is more complicated, being formed by data dropout from several repeats in a small area where there is also a strong oceanographic signal. This is a well known problem with the Geosat data set and several solutions have been applied, including use of an integrated mean slope (Sandwell and Zhang, 1989) and simultaneous reduction of the orbit error (Chelton *et al.*, 1990).

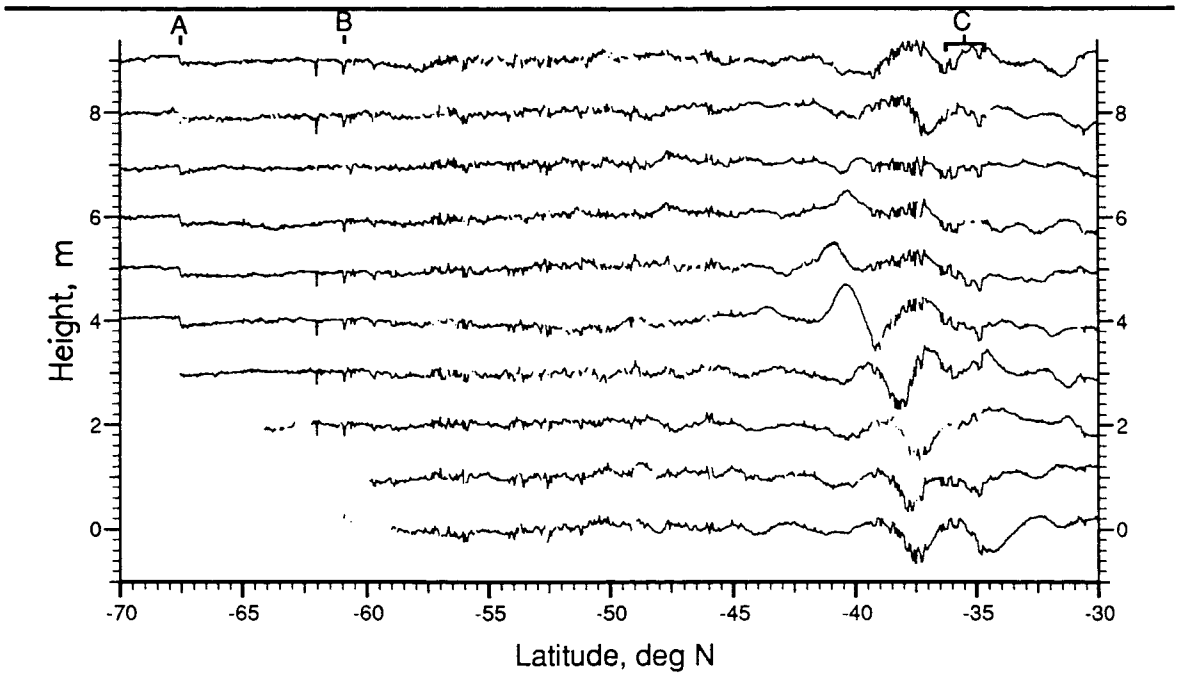

Figure 5.3 The Ten Geosat Profiles of figure 2.7 after Removal of Repeat Specific Orbit Errors. Letters A-C Mark Introduced Short Wavelength Features.

In order to reduce the effects of random jumps a simple iteration of the mean calculation was introduced. The working mean was added back to height residuals $h^{(2)}$ to give height residuals $h^{(3)}$ where;

$$h^{(3)}_{ij} = h^{(2)}_{ij} + \overline{h}_j = h_{ij} - \left(a_i + jb_i + j^2 c_i\right)$$

effectively giving corrected height data less a repeat specific quadratic orbit correction. As can be seen from figure 5.4 the difference between arc repeats has now been much reduced compared to the original corrected data (figure 2.6, page 18).

A new mean, $\overline{h^{(3)}}$, was calculated from $h^{(3)}$ using;

$$\overline{h^{(3)}}_j = \frac{1}{N_j} \sum_{i=1}^{N_j} h^{(3)}_{ij}$$

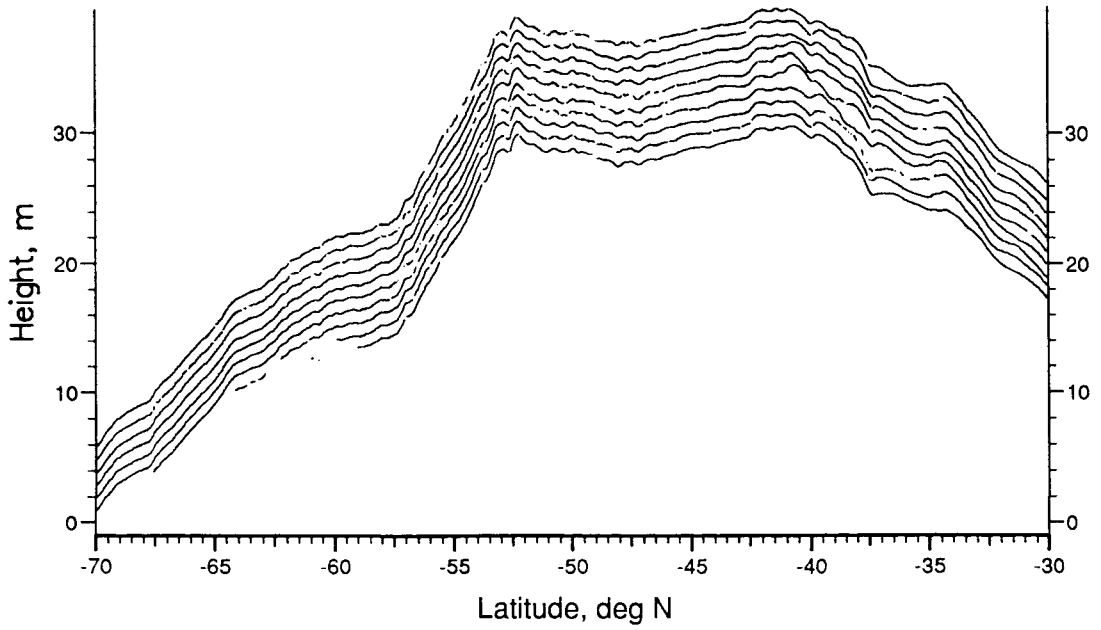

Figure 5.4 The Ten Geosat Profiles of figure 5.3 after Restoring the Working Mean.

Due to a specific long wavelength error having been removed from each repeat this new mean does not have the data 'spikes' of the working mean, and the difference between the two mean curves is shown in figure 5.5.

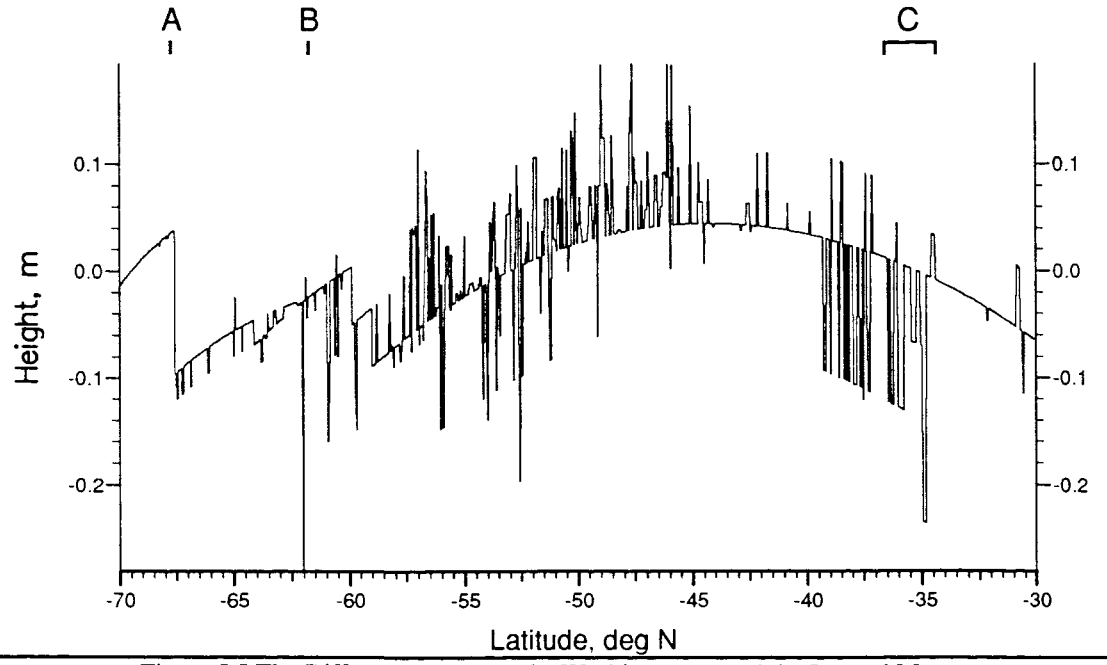

Figure 5.5 The Difference Between the Working mean and the Iterated Mean.
A-C Mark Features Shown in figure 5.3.

Removal of this iterated mean gives the final height residuals, $h^{(4)}$, as;

$$h^{(4)}_{ij} = h^{(3)}_{ij} - \overline{h^{(3)}}_j$$

This iteration reduces the short wavelength signal to noise ratio of the mean curve and of the final height residual profiles (see figure 5.6). The root mean square height variability at any point will not be altered by this process as the introduced data jumps affect all existing data points equally.

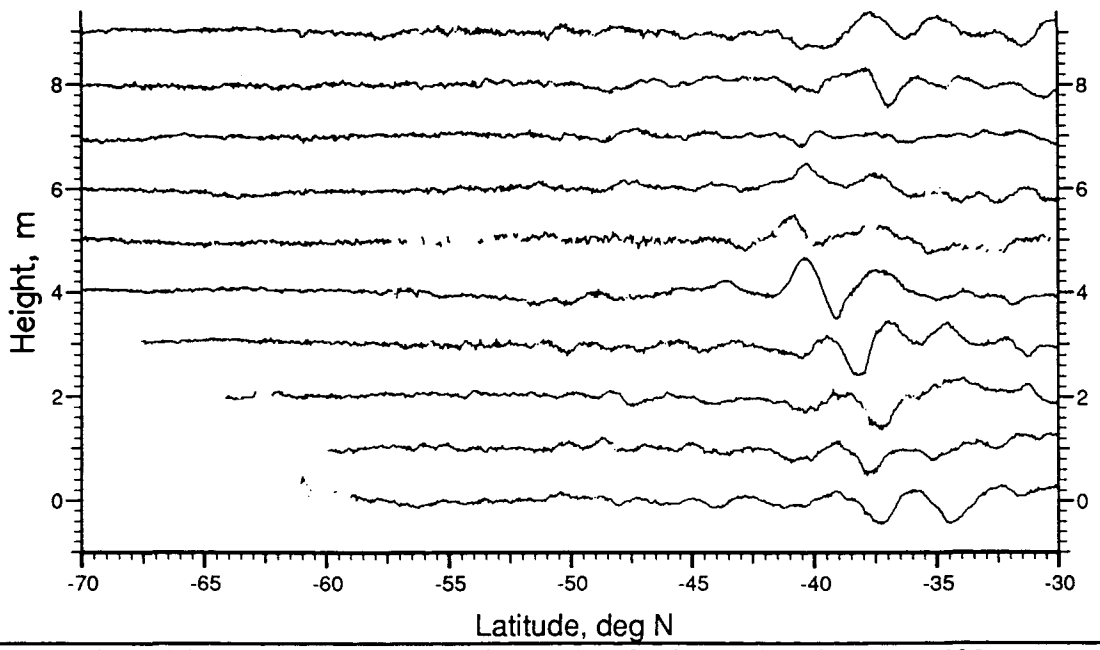

Figure 5.6 The Ten Geosat Profiles of figure 5.4 After Subtraction of the Iterated Mean.

5.3.c Cross Track Corrections

Although removal of the track mean should account for along track geoidal components, there is concern that cross track geoid slope may introduce apparent sea surface height variability where the repeat is not exact. If the geoid slope is parallel to the track but of constant form, or only differing at long wavelengths, any cross track slope will be removed by the quadratic orbit correction. If the slope is crossed obliquely by the orbit arc there may be some residual cross slope effects. Any such effects should be minimal as the altimeter footprint size is larger than the separation of repeat orbits. However, they may prove to be important in areas of large amplitude, small spatial scale geoid variability.

Cross track slope has been examined by comparing data from orbit repeats output from the processing program. To make this analysis somewhat simpler it was hoped to remove gross geoid variation using the GDR geoid data, but this is not possible due to the model errors mentioned previously. The cross track slopes determined from output file 5 (see following section) are generally small, of the same order as residual sea height variability slope along track. Brenner *et al.* (1990) have calculated a method of reducing the geoidal cross track slope errors but this only reduces the overall rms of the height residuals by 0.2 cm.

5.4 OUTPUT FORMAT

Output from the processing program is in the form of five files for each track containing;

1: Latitude and longitude of the reference track, and hence of each data point.

2: The mean sea surface height and rms variability at each data point. This file essentially contains the geoid and current variability for each track.

3: The corrected height values for each repeat of the track together with the orbit repeat numbers.

4: The value of the along-track height correction applied to each data value (the difference between the raw data value and the resampled data value) and the associated distance correction (Δd in figure 5.2).

5: The difference between the reference track height and the corrected height for each data point together with the perpendicular track separation.

6. THE AGULHAS REGION

It was decided to begin analysis of the Geosat data by looking at a region of the Southern Ocean which appeared to be showing interesting features in the FRAM data, and accordingly an area to the South and East of Africa was chosen, which includes the Agulhas current and associated features. All Geosat orbits which cross this area have been located and extracted for analysis. The descending passes (northeast to southwest) begin at 30°S and in order to avoid severe problems with ice contamination, the ascending passes (southeast to northwest) begin at 60°S. Figure 6.1 shows the region under investigation, and the set of Geosat tracks extracted within the region. As can be seen, the separation of tracks in the same sense (ascending or descending passes) is of the order of only 100 km or less in this region.

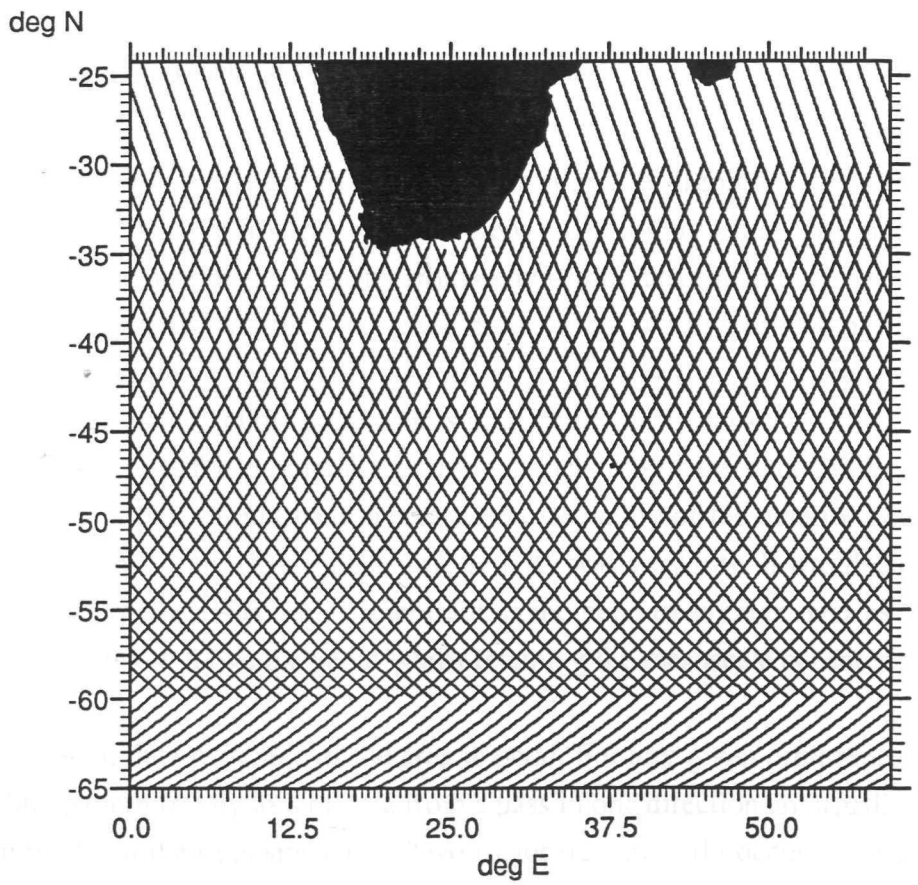

Figure 6.1 A Map of the Agulhas Study Area Showing the Location of Geosat Tracks Extracted from the GDR Tapes.

In order to use the data to study mesoscale variability a series of graphical display programs has been developed. These routines utilize the UNIRAS graphics package

installed on the Southampton IBM 3090 main-frame and the FRAM project Sun workstation. This system allows far more flexibility in display procedures and enhancement of displays than other packages available, although use of UNIRAS at Southampton has been very limited until recently and involved much development work.

6.1. MAPPING THE GEOSAT TRACKS

In order to show the location of extracted Geosat tracks a routine was created to remove the track location data from the GDR and plot this onto a world map. Latitude and longitude can be found either from the output file of the processing program or from raw data, allowing display of the reference tracks as well as the actual locations of data points. The latter is a useful check that the correct track has been found, and gives an indication of the areas of data loss in any given repeat.

6.2. THE DATA TIME SERIES

Data were extracted for all the orbit arcs shown in figure 6.1 (using the method described in § 5.1) for the first two years of Geosat data (43 repeats). Towards the end of the second year the data began to suffer from extreme degradation in quality. This was due to increasing solar activity which increased drag on the satellite, producing frequent off-pointing and subsequent loss of lock and making orbit calculations more difficult. Two years was chosen as the cut off point as it is preferable to use an exact number of years of data to minimize possible problems of seasonal variation of the data aliasing the mean. Using one year of data would have increased the accuracy of the data measurements by restricting them to a time when ionospheric activity was very low. It was decided that the decrease in data quality was not as important as the need to average over as long a time period as possible to remove the geoid whilst retaining the mesoscale oceanographic signal (see chapter 5).

In general data coverage of the area is good. For any given orbit repeat, spaces in the sampling pattern left by loss of data from a pass in one direction are usually crossed by data from tracks in the opposite sense. Two major data gaps do occur during the second year of data. The first loss occurred in November 1987 (orbit repeat 23) when no data were received for a week due to the altimeter not maintaining a vertical attitude and the second was for 8 days in August 1988 (repeat 39) whilst Geosat's batteries were reconditioned (Doyle *et al.*, 1989).

In the first two reports on Geosat GDR data released (Cheney *et al.*, 1988 and Doyle *et al.* , 1989) it has been noted that there are more observations in boreal winter than

summer. This may be a result of the extensive Southern ice-sheets causing more frequent loss of lock. It has also been noted that there are regional data gaps, caused by large excursions of space craft attitude, which tend to migrate eastward with time.

6.3. ROOT MEAN SQUARE HEIGHT VARIABILITY

From the geostrophic current relationship (see § 4.1.b) changes in sea surface height can be related to changes in geostrophic surface currents and the height variability is therefore a measure of surface current variability. The root mean square (rms) of sea surface height variations from the two year mean calculated during processing can therefore be used to locate areas of surface current variability. This allows comparisons of altimeter results with current data from different sources in published work.

6.3.a. Individual Tracks

The rms variability for an individual track can be plotted against latitude together with the mean and longitude curve as shown in figure 6.2, in order to show the amplitude and wavelength of the main variability regions along track.

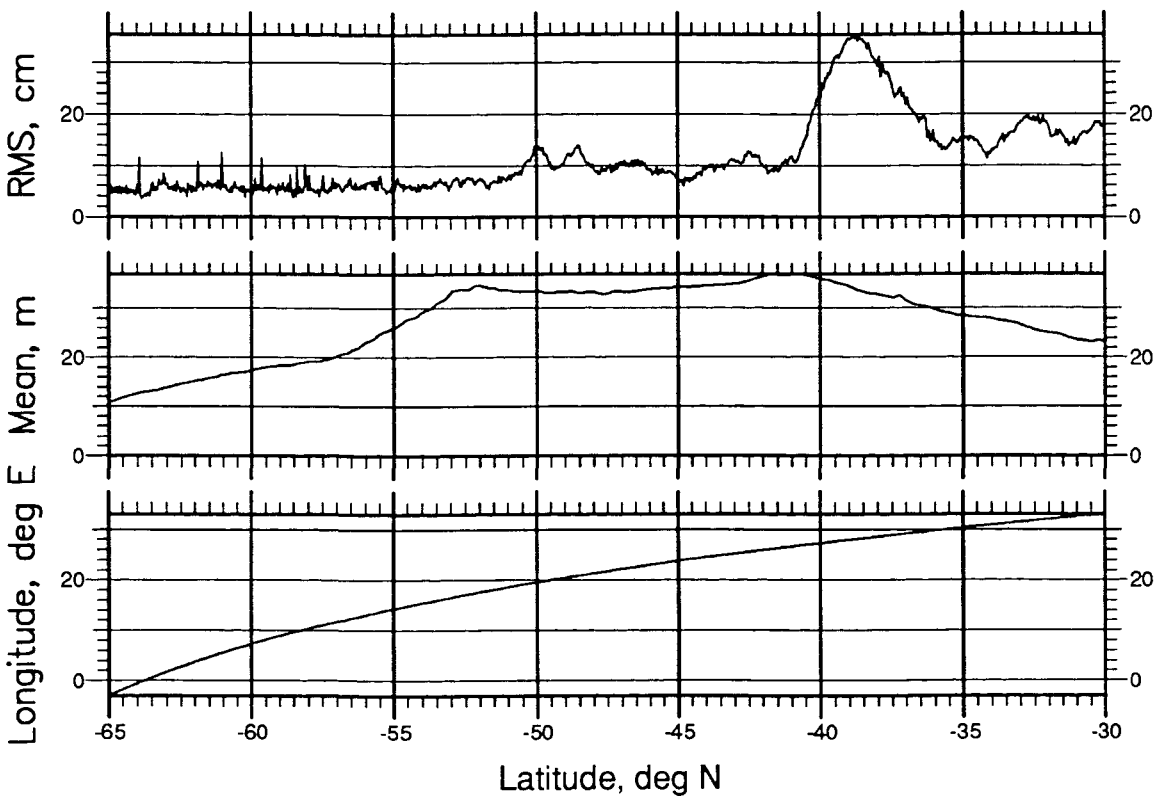

Figure 6.2 The Root Mean Square Sea Surface Height Variability along a Descending Track.

Figure 6.2 shows the rms variability for a descending pass (north-east to south-west direction) which starts just east of South Africa and it can be seen from this figure that the rms height variability rarely falls below 5 cm along track. This is the case for the majority of tracks analyzed and seems to indicate that the sensor accuracy and corrections applied give a background 'noise' level of around 5 cm rms, although a portion of this is probably due to real oceanographic variability. Hence only rms values greater than this may be considered as significant sea surface height variability. North of 36°S the variability is relatively high, generally 15-20 cm rms, in the area corresponding to the Agulhas current. South of this, from 36-41°S is a broad peak of rms variability, reaching a maximum of more than 35 cm, in an area which corresponds to the region of the Agulhas Retroflection. South along the track, variability remains around 10 cm rms until the track crosses the ACC at 48-50°S, where there is an increase to more than 14 cm before dropping to a background level of 5-6 cm. This track has features which are typical of many of the rms curves of the region although the exact form and location of the rms peaks vary.

6.3.b. Variability Field

The rms variability values of all the tracks shown in figure 6.1 have been interpolated onto a grid of the area. The grid has a resolution of $^1/_2$° longitude by $^1/_4$° latitude giving a resolution of approximately 27 km in both directions at 60°S. This is the same resolution as the FRAM grid and was chosen to facilitate comparisons between the data sets.

The interpolation used is the simple scheme of UNIRAS routine GEOINT1. The data is first sorted to the closest grid node. If more than one data point is assigned to a single node then the arithmetic mean of these data is taken with no weighting. If no data value is assigned to a node then nodes in the four surrounding quadrants (north-east, south-east, south-west and north-west) are searched to a maximum radius (set at 1° latitude, 2° longitude) and the closest data values found in each of the four quadrants are then used in a distance weighted mean to calculate the node value. If no data values are found within the search radius the node is set to the undefined data value. The resultant rms variability field is shown in figure 6.3.

There are several features noticeable in the variability field. The peak rms value of just over 51 cm occurs at 39.5°S 23°E in a zonal band of generally high rms values approximately 5° wide, which extends from around 10°E to the eastern edge of the region. Within this band the highest rms values (greater than 35 cm) occur to the south and west of the Cape of Good Hope from 38 to 41°S and from 14 to 26°E. At its western limit the band broadens in extent but reduces in amplitude. East of South Africa the band exists as a series of local variability maxima centred on 38°S with two distinct northward loops at 26 and 32°E and a southward loop at 45°E before the high variability core turns south-east.

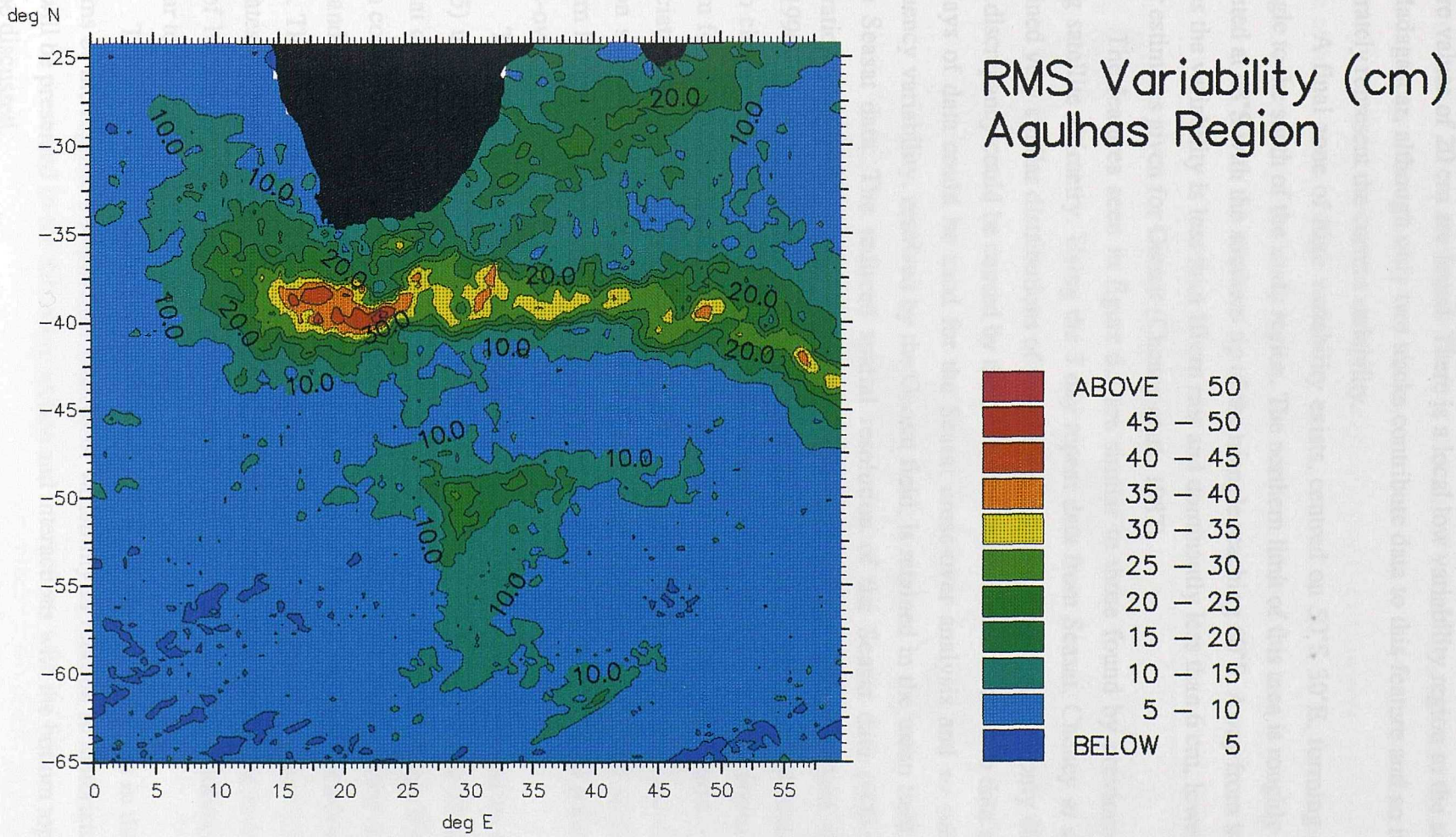

Figure 6.3 RMS Sea Surface Height Variability of the Agulhas Region from Two Years of Geosat Data.

The area immediately east of Africa also has variability of more than 10 cm rms, especially in a band stretching from the tip of South Africa to just South of Madagascar where values of 20 cm are found. There is a local low variability region to the south-west of Madagascar, although only two tracks contribute data to this feature and so it may not accurately represent the current variability.

A final zone of high variability exists, centred on 50°S 30°E, forming a distinct triangle to the south of the study region. The northern limit of this area is roughly east-west oriented at 48°S with the southern tip of the triangle reaching 60°S. Away from these three zones the variability is less than 10 cm rms and dominantly less than 6 cm, lower than the error estimates given for Geosat (Cheney *et al.*, 1987).

The features seen in figure 6.3 are similar to those found by previous workers using satellite altimetry. Using the 3 day repeat data from Seasat, Cheney *et al.* (1983) obtained very similar distributions of variability, but with a maximum of only 40 cm rms. This discrepancy could be caused by the difference in time scale of the two data sets. Only 25 days of data could be used for the Seasat cross-over analysis and so some lower frequency variability, resolved by the Geosat field, is retained in the mean field obtained from Seasat data. The reduced spatial resolution of the Seasat data (600 km track separation) also results in a somewhat smoothed version of the variability field. Chelton *et al.* (1990) use two years of the Geosat data in an along-track technique and obtain results much closer to those of the present study. Their peak variability is 6 cm lower than the 51 cm found here but this may be due to their regridding of data to a 2° grid with some associated smoothing. Wakker *et al.* (1990) also note the presence of a low variability region south-west of Madagascar but high variability patches along the southern and eastern limits of their study area seem to be a result of the inclusion of short tracks in their cross-over analysis.

The high variability of currents in the Agulhas region was also noted by Patterson (1985) using FGGE drifting buoy data with all the high variability areas found in the Geosat data being represented in the eddy kinetic energy field of the buoys. Patterson's much coarser grid of 5° gives a smoothed result compared to figure 6.3 and the absence of the band of lower variability along 45°S may be due to the difference in resolved spatial scale. The statistical analysis of hydrographic data by Lutjeharms and Baker (1980) also indicates the high current variability of the region as a whole and despite the even coarser grid of 10° the distribution of high and low variability within the region is qualitatively very similar to that found from the Geosat data.

The variability field as measured by Geosat is the result of changes in the current systems of the region. The possible sources of variability in relation to historical current data will be presented in the following section and interactions with the bottom topography will be discussed.

(1) Comparison With Historical Current Data

The general current flow of the region as determined from historical current information, including hydrographic data, drifting buoy tracks and infra-red imagery, is given in figure 6.4. Comparisons of the variability field with this data show a close correlation between the areas of highest variability and the strongest currents. The main areas of high variability are coincident with the East Madagascar Current, the Agulhas Current and the Agulhas Return Current, with maximum variability in the Agulhas Retroflection area.

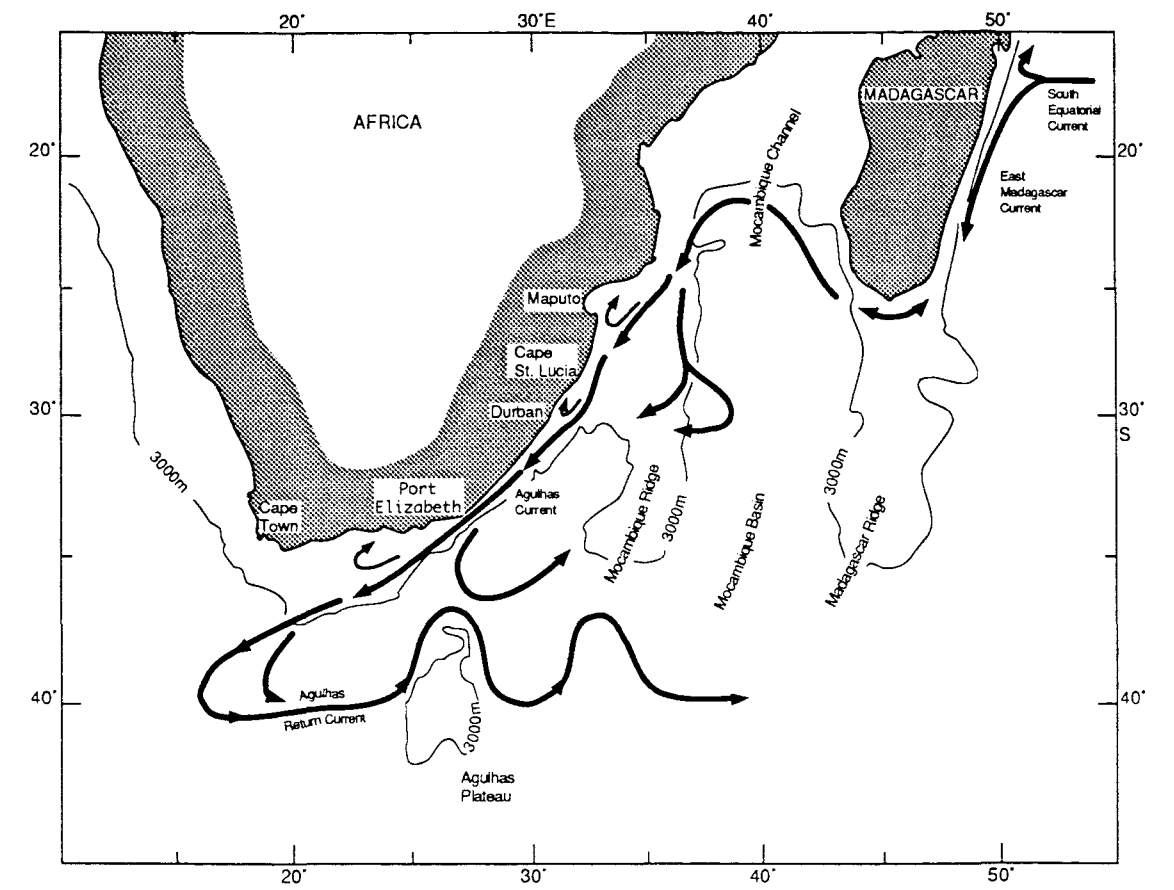

Figure 6.4 The Characteristic Flow Pattern in the Agulhas Current Region (after Gründlingh, 1982).

Chelton *et al.* (1990) compare Geosat variability for the whole Southern Ocean with dynamic heights from Gordon and Molinelli (1982) and show that variability maxima generally occur along the cores of major currents. The exact relationship of the sea surface height variability observed by Geosat to the current systems is dependant on the system dynamics. The correlation of regions of high variability with the cores of the major currents implies that these systems are not steady but that some form of instability exists.

The core of the Agulhas Current occurs very close to the coast, in a band only 100 km wide (Pearce, 1977) and although variability seen in the Geosat data along the east coast of Africa is above the noise level, the main increase is 300 to 400 km off-shore. This

seems to indicate that the location of the core of the current is relatively stable with time. Pearce and Gründlingh (1982) show that there is little variation with time in the intensity of the Agulhas Current at the surface to account for the small increase in variability seen. The large current velocities (over 200 cm s^{-1}, Pearce, 1977) should produce correspondingly large anomalies in the Geosat data if meandering occurs and so the small variability signal implies that the current core must have a fairly constant location. This is consistent with the report of Pearce (1977) who found the core at the same position off Durban for 90% of the time. At two locations, near 25°S and again near 28°S, the coastal variability is above 15 cm rms and these could be indicative of the small coastal eddies seen to exist in-shore of the Agulhas Current in the lee of headlands (Pearce *et al.*, 1978). Similarly the East Madagascar Current is not represented by high variability close to the coast where the current core is thought to exist. It must be noted that the lack of variability close to the coast may be an artefact of the Geosat processing as only ascending tracks are included north of 30°S and there is significant data loss from these tracks close to the coast which may artificially reduce the observed variability. Both currents do however exhibit strong variability off-shore of the current cores, forming the continuous strip noted in section 6.3.b above. These systems are both known to spawn eddies (Gründlingh, 1982) which have been recognized in hydrographic data, infra-red imagery and drifting buoy tracks (Lutjeharms *et al.*, 1981; Gründlingh, 1977). These eddies are believed to allow the exchange of water from the East Madagascar Current to the Agulhas Current (Lutjeharms *et al.*, 1981) a theory supported by the continuous nature of the observed variability implying mesoscale activity linking the two currents.

The small peak in variability at 35.5°S 24.5°E is interesting as it is almost coincident with the location of a loop in the Agulhas Current noted by Harris and Bang (1974), Harris *et al.* (1978) and Gründlingh (1979) in hydrographic data and infra-red imagery. This meander is believed to move south-west along the African coast from 25 or 30°S, increasing in amplitude to form a loop in the current south of Port Elizabeth which is where the peak in variability is seen.

Variability associated with the Agulhas Retroflection and Return Current is somewhat different in nature to that of the Agulhas Current, with peak values occurring along the axis of maximum current, reducing away from the core. This tends to imply that the variability is caused by changes in the core of the current, not only by generation of eddies by the system. In the Retroflection, the maximum variability occurs within the range of locations for the main return flow, given by Gründlingh as being from 15 to 20°E. This is compatible with infra-red imagery which shows that large anticyclonic eddies or 'rings' are pinched off from the Retroflection (Lutjeharms, 1981). After a ring has separated from the Retroflection, the point of return will have retreated eastward and so maximum variability will occur where the Retroflection alternately advances westward and retreats eastward. Once the rings have detached from the Retroflection, they follow paths generally

westward but ranging from south-west to north-west into the Atlantic. The curve of the variability maxima to the north-west around the coast of South Africa indicates that this is the preferred direction of transport of these rings. Current speeds within the rings are similar to those of the Agulhas Current at the point of separation (Gründlingh, 1982) and so they should have large surface height signatures which it should be possible to detect in the height profiles (see § 6.2).

East of the point of retroflection, the observed variability seems concentrated close to the core of the Return Current with each of the two northward deflections of the peak variability location noted above seen in the mean flow diagram of Gründlingh (figure 6.4). The location of these loops relative to topography will be discussed further in the following section. Local maxima of variability are coincident with these loops, where many eddies have been detected by drifting buoys and infra-red imagery (Gründlingh, 1978; Lutjeharms and Valentine, 1988). Lutjeharms and Valentine (1988) use infra-red imagery to characterize five groups of eddies seen in the region of the Retroflection and Return Currents, all caused by local shearing of current meanders. The concentrated nature of variability in the Return Current makes it probable that meandering of the current core is a dominant cause of mesoscale activity, with the production of eddies spreading variability away from the core.

East of 40°E the location of the Agulhas Return Current is not well determined in historical data and the southward loop of variability near 45°E does not appear correlated with the direction of current as determined by Gordon *et al.* (1978) and given in figure 4.1 (page 31). The cause of this loop, and the associated peaks in variability is unclear but it is likely to be linked to the topography (see below). The southward deflection of variability from 50°E is reflected in a corresponding southward bend in the current direction shown by Gordon *et al.*, although the current here is much less intense than further west. It seems unlikely that meandering of this much smaller current would be sufficient to account for the observed level of variability (over 35 cm rms) and some eddy activity would be expected.

The southern region of high variability is coincident with the ACC in this region, although dynamic height contours of Gordon *et al.* show the ACC is here rather broad and slow flowing when compared to other regions. There are, however, several notable features in the dynamic height data which all occur within the region of increased variability. There is a marked convergence of dynamic height contours at 30°E, close to the area of greatest variability, and there is also a southward deflection by almost five degrees of latitude of the 0.6 dyn m contour between 20 and 30°E. Bowen and Stommel (1974) located the core of the ACC at 50°S on cruise tracks along 0° and 20° longitude, with the current axis running west-east, whilst data collected by Khimitsa (1976) in austral summer shows the southern edge of the ACC at 60°S between 30 and 50°E with meanders and eddies existing south of this. These data are consistent with some part of the ACC shifting south around 20-30°E, corresponding to the southern extension of the area of increased Geosat variability. This southern shift is associated with the eastern limit of the Weddell

Sea Gyre, although the westerly flowing limb is not apparent this far east, and changes further west in this Gyre could account for some of the variability seen south of 50°S. The dynamic height data of Gordon *et al.* (1978) also show a wave like feature in the 0.8 dyn m contour between 40 and 50°E which is closely linked to the eastern extension of the increased variability area. At 50°E a second branch of the ACC is deflected northwards to coalesce with the Agulhas Return Current between 40 and 45°S. This area of convergence of the two currents is close to the peak in variability seen in the Agulhas Return Current and it is likely that interaction between the two currents is the cause of instability here.

Variability associated with the ACC seems to be more restricted zonally than that of the Agulhas Return Current, not following the complete path of the current but concentrating in the region where the ACC is seen to intensify and shift direction. Few data are available for the ACC in this region but it would appear that the current must be rather stable west of 25°E. East of here it appears that the ACC divides with branches deflecting both north and south, the point of division and local intensification apparently controlled by the bottom topography (see below). As with the main Agulhas system it appears that instabilities are formed at locations where branches of the ACC change direction, the observed variability being caused by these instabilities. The evidence of eddies seen in the data of Khimitsa (1976) is consistent with eddy formation in the southward branch of the ACC.

(2) Comparison With Bottom Topography

The bottom topography of the Agulhas area is shown in figure 6.5, with the major sea-floor features named. The area of maximum sea surface height variability occurs in the deep water south of the African continental shelf at the tip of South Africa, flanked to the south-west by the northern limit of the Agulhas Ridge and to the east by the Agulhas Plateau. Tracing the high variability region to the East along the Agulhas Return Current, it appears to be quite strongly correlated with the topography. The northward loop at 26°E passes around the northern half of the Agulhas Plateau, with the maximum variability occurring on the western slope. Darbyshire (1972) was the first to show how the bottom topography of the steeply rising Agulhas Plateau could cause northward deflection of an easterly jet, an approximation of the Agulhas Return Current, the exact course of the loop being determined by the velocity structure of the jet. Gründlingh (1978) also modelled this loop successfully using an inertial jet and obtained reasonable correlation of the model with the track of a drifting buoy. As the loop brings the easterly flowing Return Current close to the westerly Agulhas Current, shearing occurs which induces instabilities and eddies over the Plateau (Lutjeharms and Valentine, 1988). Lateral shear between the fast flowing outer loop and water over the centre of the Plateau can also produce cyclonic eddies on the southern edge of the current (Gründlingh, 1982). Both changes in the exact course of the

loop and the occurrence of instabilities are controlled by the topography, explaining the correlation of the observed variability with topography. In some conditions, the Return Current is seen to be deflected south of the Agulhas Plateau (Harris *et al*, 1978) which may explain some of the variability seen here, although eddy formation on the southern edge of the Return (Lutjeharms and Valentine, 1988) seems likely to account for most of it.

The second equatorward deflection of the Return Current, seen at 32°E, occurs immediately west of the southern end of the Mozambique Scarp, but although very similar in form this loop has not been as readily explained. The loop has been recognized in infra-red images (Harris *et al*, 1978) and in the track of a drifting buoy (Gründlingh, 1978) but attempts to model it as an inertial jet have been unsuccessful. The northward deflection of the current can be easily simulated by combining the ridge slope with the direction of the current as it leaves the Agulhas Plateau, however, topography alone seems insufficient to explain the subsequent cyclonic rotation needed to return the current to 40°S. Using sea surface temperature plots Gründlingh (1978) invokes the presence of a periodic southerly incursion of warm water along the eastern edge of the scarp which interacts with the Return Current to cause the rotation observed. The relationship of sea surface height variability to topography is somewhat different from that seen at the Agulhas Plateau, with the northern limit of the variability loop occurring further west relative to the ridge crest, tending to support the theory that a different dynamic regime exists. The height variability does not however lend support to the existence of a southward current along the scarp edge unless it is constant in time (not periodic as suggested by Gründlingh) or of very low velocity, so that the variability signal associated with it is small.

After crossing the Mozambique Basin the next obstruction met by the Agulhas Return Current is the Madagascar-Southwest Indian Ridge where the Return Current passes south of the Madagascar Ridge, via the Discovery II and Indomed Fracture Zones. Between the Fracture Zones the high variability band veers 90° south to run almost parallel to topography contours before again turning northeast, still following depth contours, to produce the southward loop mentioned previously. A similar loop is observed by Gründlingh (1978) in the track of his drifting buoy as being caused by two northward loops, one over the ridge crest to the west and a second to the east. Both these northward loops appear to have variability maxima associated with their western limbs, as was seen in the Agulhas Plateau loop, but the northward deflections are much smaller and occur within the width of the high variability zone. The first loop appears to be caused by the ridge, as for the two previously described, however the second occurs over deepening water and may be the result of a Rossby wave propagating downstream of the ridge (as discussed by Porter and Rattray, 1964).

Once into the Crozet Basin the high rms band still runs almost parallel to the depth contours, following the southern edge of the basin although there is no evidence to suggest that the variability is controlled by the topography.

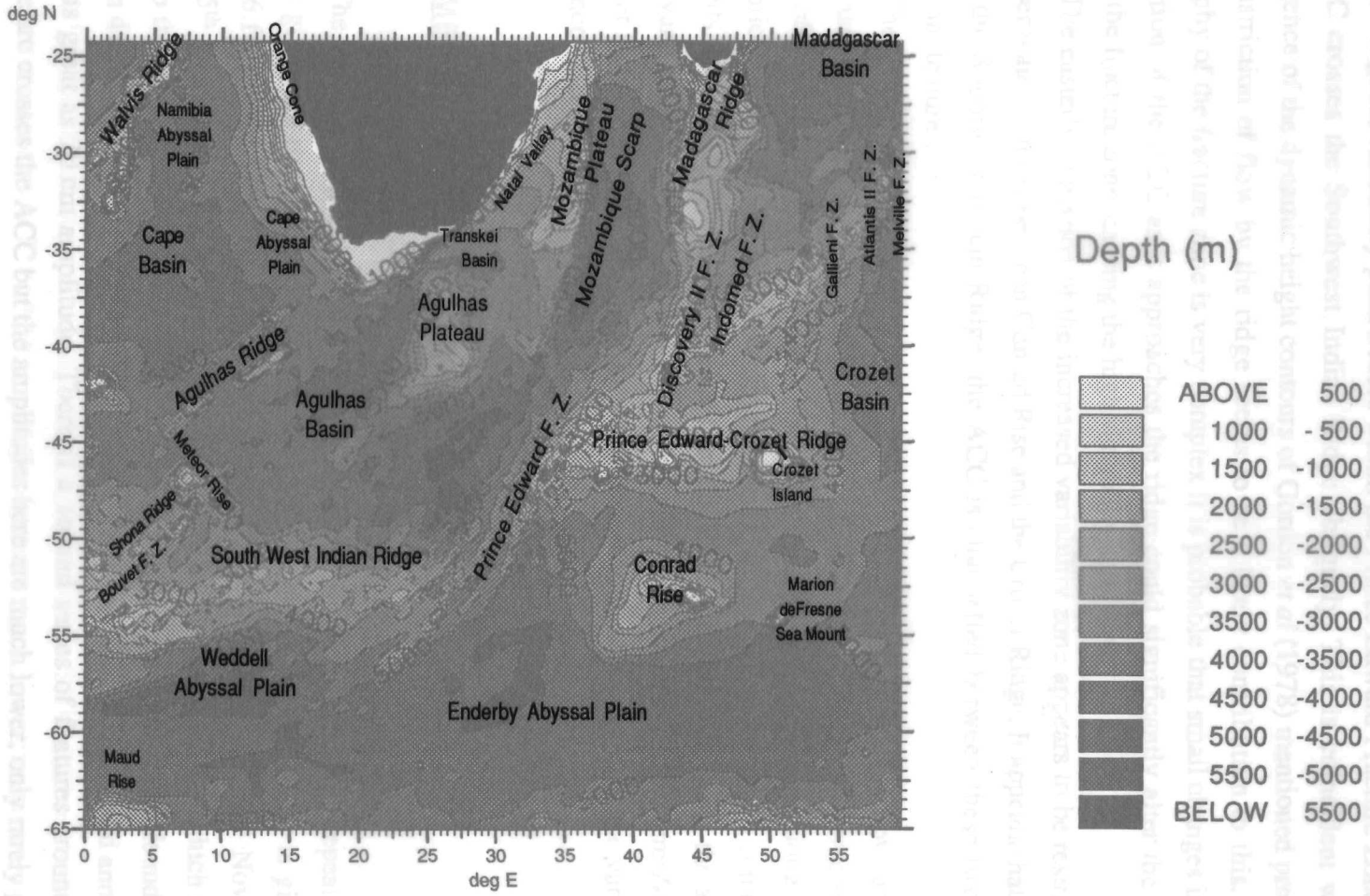

Figure 6.5 The Bottom Topography of the Agulhas Region.

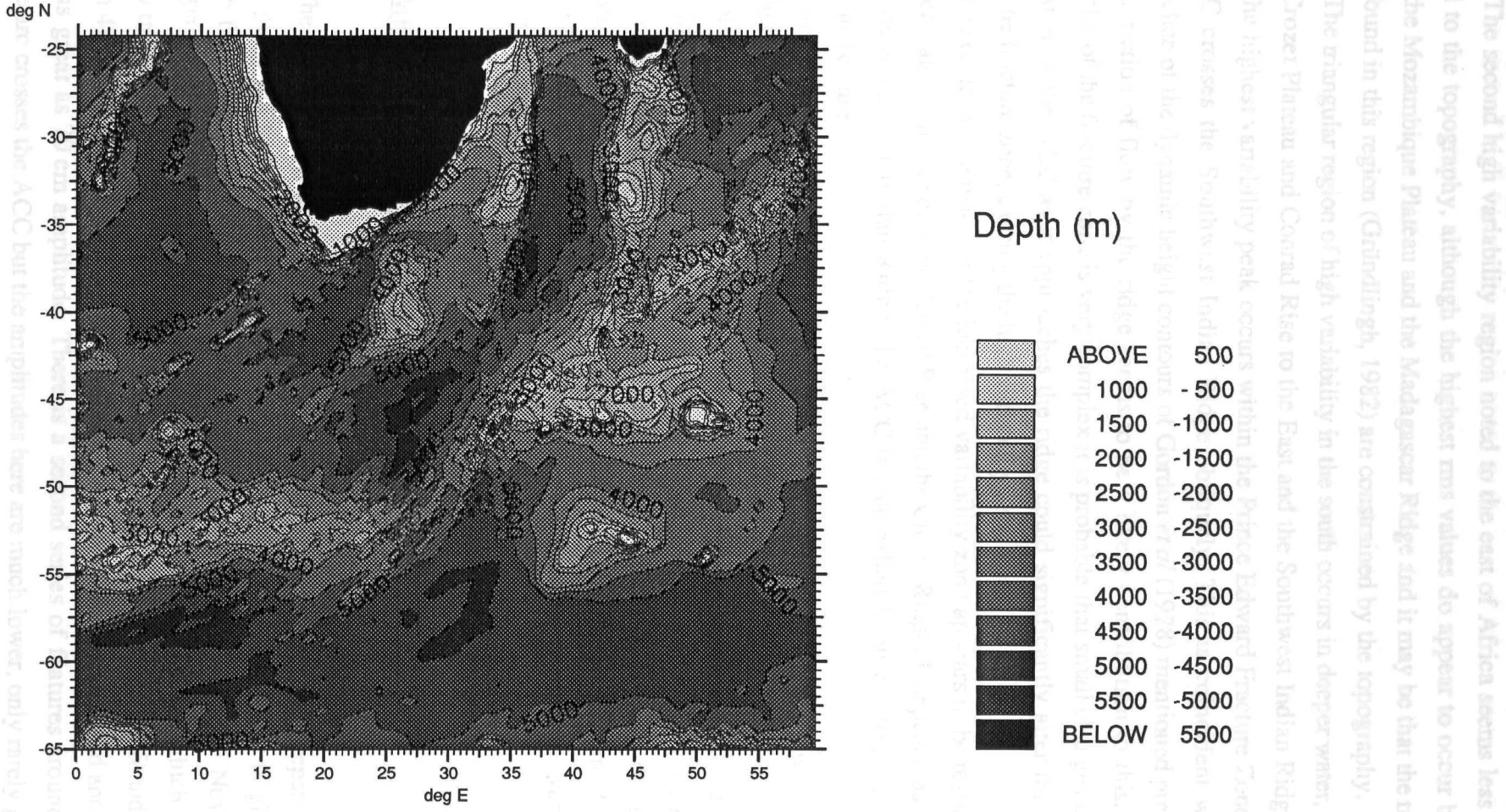

Figure 6.5 The Bottom Topography of the Agulhas Region.

The second high variability region noted to the east of Africa seems less closely coupled to the topography, although the highest rms values do appear to occur between dips in the Mozambique Plateau and the Madagascar Ridge and it may be that the tracks of eddies found in this region (Gründlingh, 1982) are constrained by the topography.

The triangular region of high variability in the south occurs in deeper water, flanked by the Crozet Plateau and Conrad Rise to the East and the Southwest Indian Ridge to the West. The highest variability peak occurs within the Prince Edward Fracture Zone where the ACC crosses the Southwest Indian Ridge obliquely. This is coincident with the convergence of the dynamic height contours of Gordon *et al* (1978) mentioned previously and constriction of flow by the ridge seems to be a likely contribution to this. As the topography of the fracture zone is very complex it is probable that small changes in speed or direction of the ACC as it approaches the ridge could significantly alter the current through the fracture zone, causing the high variability seen here.

The easterly extension of the increased variability zone appears to be restricted to the deeper water channel between Conrad Rise and the Crozet Ridge. It appears that having crossed the Southwest Indian Ridge, the ACC is channelled between these two major topographic features.

Chelton *et al* (1990) note that the separation of regions of high and low variability is often associated with the edges of bathymetric features. This seems to agree with the findings of this study, although Chelton *et al* regard the high variability zone along 38°S as an exception, with no bathymetric steering apparent until 70°E. As has been commented above, this does not appear to be the case with apparent correlation between the areas of greatest variability and the edges of the Agulhas Plateau, the Indomed Fracture Zone and the Crozet Plateau. Only to the west of the region, in the Cape Basin, does the variability appear uncorrelated with depth.

6.4. TIME SERIES OF REPEAT ORBIT ARCS

The height variation from the two year mean for a selected range of repeats of an orbit arc gives the time series of current anomalies. One such time series is given in figure 6.6 for an arc of the ascending pass beginning at 60°S 41°E, for 20th November 1986 to 5th April 1987. This time series shows several variability features which can be related to the velocity field of the region. The largest amplitude features are found in the area from 41° to 37°S where the orbit arc crosses the Agulhas Retroflection and anomalies may be as great as 70 cm amplitude. There is a second series of features around 50°S where the arc crosses the ACC but the amplitudes here are much lower, only rarely greater than 20 cm. Some of the features seen in figure 6.6 will be discussed later.

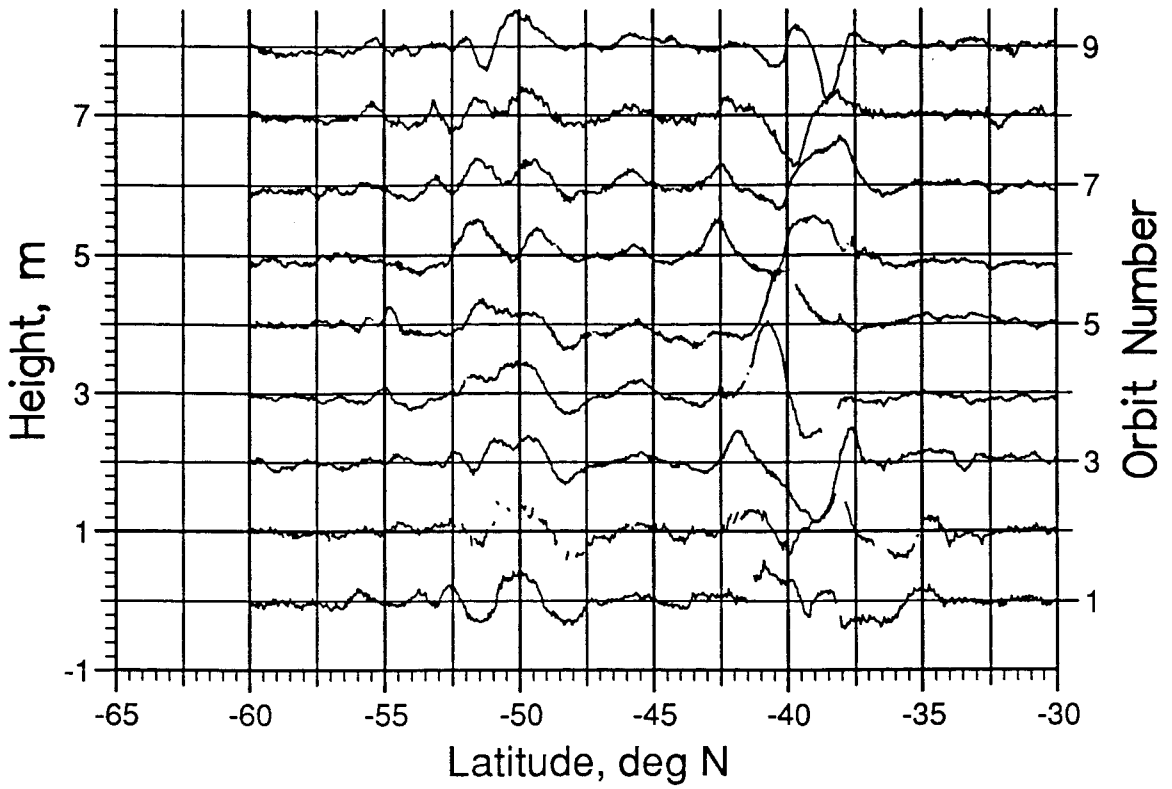

Figure 6.6 Time Series of Sea Surface Height Variation from a Two Year Mean.
Each Successive orbit Repeat is Offset by 1 m.

6.4.a. Mesoscale Features in Individual Profiles

Mesoscale eddies and meanders are the dominant cause of variability in mid-ocean currents and are important in their ability to transport properties such as heat, salt, momentum and nutrients. One of the main obstacles to understanding eddy dynamics has been the difficulty in sampling eddy properties using conventional ship-borne techniques. Recently the availability of infra-red satellite imagery has allowed the mapping of eddy features by their temperature signature, although this process is limited to cloud free conditions. Also no truly quantitative measure of the eddy velocity can be obtained, only the resultant changes in spatial temperature patterns. Use of the all weather altimeter data, from which sea surface slope can be derived, should make the study of eddy dynamics over various space and time scales possible.

The spatial resolution of the altimeter is of the order of 7 km along track over a variable footprint width of 2 to 12 km, whilst the track spacing at the latitudes of the Agulhas current is approximately 100 km. These dimensions make it probable that the altimeter will resolve mesoscale features, although there will be some bias in the resolved

scales as resolution between tracks is much lower than along track. Even a small feature will have several height values sampled if a track passes directly over it, but an eddy of 50 to 100 km which occurs between tracks may not be sampled at all.

For a cyclonic eddy in the Southern hemisphere rotation is clockwise and if the eddy is in approximate geostrophic balance the centre of the eddy will be depressed relative to the rim, as seen in figure 6.7 Similarly for an anticyclonic eddy the centre will be raised, giving a means of identifying the type of feature seen in a height profile.

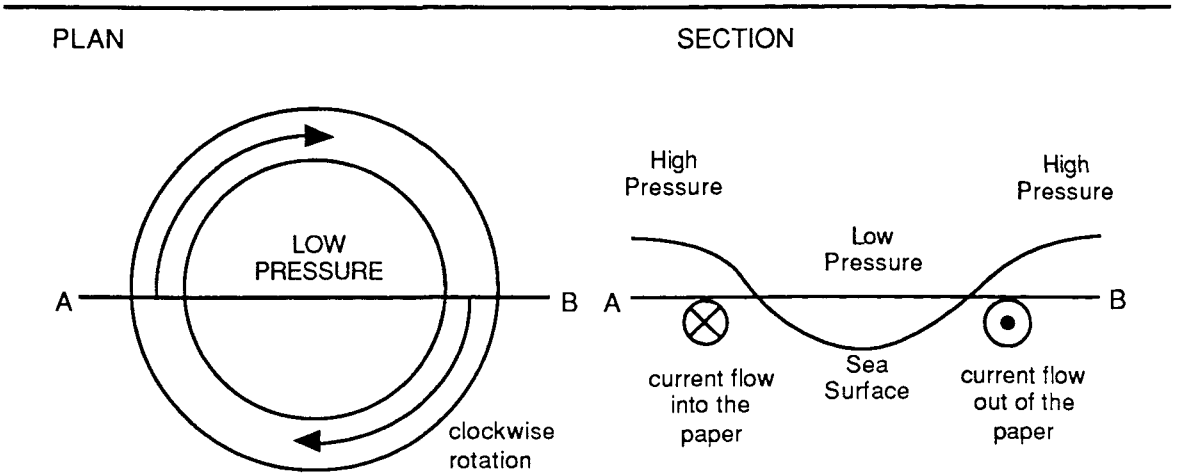

Figure 6.7 The Sea Surface Height Signature of a Cyclonic Eddy in the Southern Hemisphere.

(1) Velocities from Geosat Data

Using the gradient equation (Equation (4.1), page 28) it is possible to calculate the surface velocity relative to the 2 year mean from the Geosat data. This velocity, V', is given by;

$$V' = \frac{g \tan \theta'}{2\Omega \sin \phi} \qquad (6.1)$$

where;

θ' is the sea surface slope relative to the mean slope.

In order to resolve θ' the sea surface slope must be found in at least two directions. A single track yields only the component of slope in the track direction and hence the component of velocity perpendicular to the track direction. From the residual height profiles it is possible to find the along track gradients of the descending and ascending passes ($\tan\theta'_d$ and $\tan\theta'_a$ respectively) and hence the velocities perpendicular to these tracks (V'_d and V'_a). For the feature seen at 49°S on January 10th 1987 in figure 6.6 (the 4th repeat), the sea surface gradient over 200 km is -0.414 cm km^{-1} along the track (taking north distances as positive), giving;

$$\tan\theta'_a = -4.414\times10^{-6}$$

and taking g = 9.8 $m^2\ s^{-1}$ and $\Omega = 7.29\times10^{-5}$ rad s^{-1} equation 6.1 gives;

$$V'_a = \frac{9.8\times-4.14\times10^{-6}}{2\times7.29\times10^{-5}\sin(49°)}$$
$$= -0.36\ ms^{-1}$$

This is the component of surface velocity perpendicular to the track (to the west-south-west approximately) and has a value of 36 cm s^{-1}.

At crossing points between ascending and descending passes both east and north components of velocity can be resolved using;

$$V'_E = \frac{(V'_a + V'_d)}{2\cos\alpha}$$
$$V'_N = \frac{(V'_a - V'_d)}{2\sin\alpha} \qquad (6.2)$$

where

V'_E, V'_N are east and north velocity components
α is the crossing angle of the tracks with north.

If the tracks cross at 90°, which they do at approximately 60°S, α is 45° and the east and north components of the surface velocity are both equally well defined ($\cos\alpha=\sin\alpha$). The value of α increases with latitude until at the southern extreme of the passes α is 90° and both ascending and descending passes will yield only the north velocity component. As $\cos\alpha$ approaches zero any errors in the calculations of V'_d and V'_a will be magnified in the east velocity component which will no longer be well defined and may have to be rejected. Approaching the Equator α decreases, although it never falls below 18° (due to the satellite inclination of 72°), and so $\sin\alpha$ becomes small and the north velocity component will be poorly constrained.

Using the cross-over at 49°S 28°E, the north and east velocity components have been calculated for all orbits in the first six months for which both ascending and descending passes exist. The results are given in table III and show that over this time period the current had speeds of 20 to 40 cm s^{-1} to the west-south-west relative to the mean, as expected by visual analysis of the time series (figure 6.6 shows the time series of the ascending pass).

When comparing Geosat derived velocities with those calculated from *in situ* data, it must be remembered that the Geosat values represent an instantaneous velocity relative to a mean velocity, not an absolute velocity and hence they should be compared with the range of velocities calculated at any one station over time. Unfortunately such repeat measurements are rare, especially at sufficient spatial and temporal resolution for direct

comparison with the altimeter data. Velocity measurements in the ACC are sparse, most of the data being collected in Drake Passage where there are clear limits to the north and south extensions of the flow. Although the ACC may be expected to change velocity characteristics along its path data from around the ACC reported by Bryden (1983) show that surface eddy velocities are typically of the order of 30 cm s^{-1}, comparable with the results in table III, and measurement using current meter moorings in Drake Passage (Bryden and Pillsbury, 1977) also suggest variability in the ACC velocity of the order of 20 cm s^{-1}. The FGGE buoy data for 50°S gives an eddy kinetic eddy value of approximately 1000 cm^2 s^{-2}, corresponding to a velocity of 45 cm s^{-1} (Patterson, 1985) which is somewhat higher than the values found here. This is as expected due to the large grid size used in Patterson's calculations which assigns small spatial scale changes in the mean flow to the eddy field, artificially increasing the apparent eddy kinetic eddy.

Orbit No.	tan θ'_d ($\times 10^{-6}$)	V'_d (m s^{-1})	tan θ'_a ($\times 10^{-6}$)	V'_a (m s^{-1})	V'_N (m s^{-1})	V'_E (m s^{-1})	V' (m s^{-1})	direction (°)
1	-0.65	-0.0580	-3.45	-0.3078	-0.2481	-0.2117	0.3261	220
2	-0.56	-0.0499	-3.62	-0.3230	-0.2711	-0.2158	0.3465	219
3	-1.54	-0.1374	-4.24	-0.3783	-0.2392	-0.2985	0.3825	231
4	-1.33	-0.1187	-4.14	-0.3694	-0.2489	-0.2824	0.3765	229
5	-1.49	-0.1329	-3.21	-0.2864	-0.1524	-0.2427	0.2866	238
6	-1.03	-0.0919	-2.09	-0.1865	-0.0939	-0.1611	0.1865	240
7	-1.60	-0.1428	-3.20	-0.2855	-0.1417	-0.2479	0.2855	240
8	-1.02	-0.0910	-2.92	-0.2605	-0.1683	-0.2034	0.2641	230
9	-0.36	-0.0321	-2.26	-0.2016	-0.1683	-0.1353	0.2160	219

Table III Geostrophic Velocities Calculated at the Cross-over of Two Geosat Tracks at 49°S 28°E.

Similar velocity calculations have been carried out for three other crossing points over the first six months of Geosat data, the first, at 40°S 19.8°E, is at the southern edge of the Agulhas Retroflection whilst the other two, at 40°S 33°E and 39°S 47°E are in the Agulhas Return Current. The current anomalies seen at all three locations are much more variable, in both speed and direction, than those from the ACC given above, as would be expected by the much greater associated sea surface height variability. The maximum velocity anomaly found was 1.38 m s^{-1} in the Agulhas Retroflection, whilst velocity anomalies in the Return Current were up to 65 cm s^{-1} in the west and 66 cm s^{-1} in the east. These values are somewhat lower than the 'instantaneous' drifter speeds found by Gründlingh (1978) in the Agulhas Return at the same locations implying that the mean velocity accounts for a significant portion of absolute current speeds. In all cases the range of values for the northward component was greater than that for the eastward implying a relatively constant eastward flow.

It should also be noted that, although when V'_a and V'_d are calculated at a cross-over they are at the same location, they may be separated by up to 8.5 days in time (half a repeat cycle) and so they are not measuring exactly the same current anomaly. The values used in table III are found at a cross-over where passes are separated by only 1 day, but the anomalies at 40°S were separated by more than 8 days and so linear interpolation of the descending pass velocity anomalies was carried out to find V' at the time of the ascending pass. Such an interpolation assumes that the velocity anomaly changes linearly with time, which is unlikely to be the case, and so further errors are introduced into the velocity calculation. Due to the orbit repeat pattern the time separation of passes for all cross-overs at a given latitude is constant (see chapter 10 for a discussion of the repeat cycle) and so calculations at some latitudes will always give a much better estimate of the true anomaly than at others.

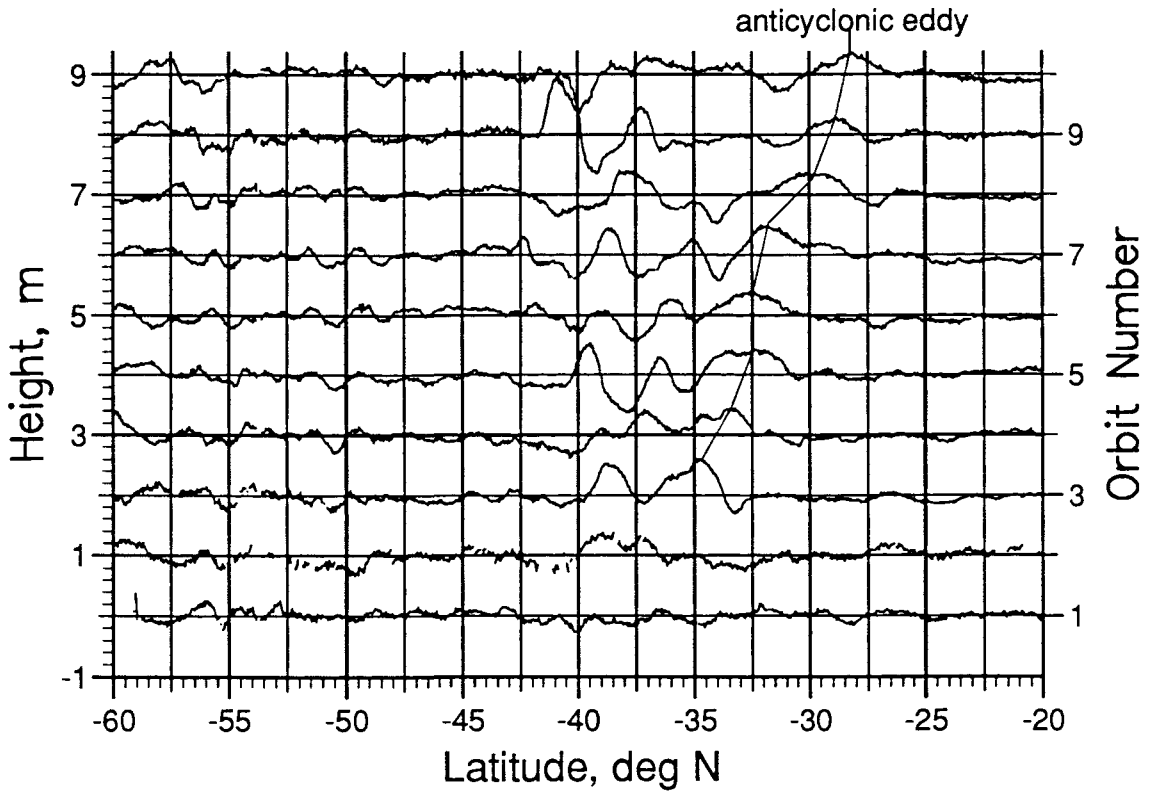

Figure 6.8 A Time Series of Height Residuals from the Ascending Pass Starting at 60°S 35°E Showing an Anticyclonic Eddy Moving Northwest Along the Track from 35° to 27°S.

Direct velocity comparison is possible for one eddy sampled by *Discovery* CTD sections taken from April 24th to May 2nd 1987. This anticyclonic eddy can be seen in several of the Geosat tracks from December 1986 to May 1987 (see figure 6.8) moving to the northwest. Geostrophic velocities calculated relative to the 1500 dbar level from the CTD data, show maximum surface velocities of 43 cm s^{-1} to the south, in the western

limb of the eddy (Gordon and Haxby, 1990). Unfortunately the orbit closest in time to the *Discovery* cruise (orbit 11) is absent for many tracks and at this time the eddy is at approximately 28°S, where only ascending passes have been extracted. Velocity components from two ascending passes on the 10th and 13th April yield speeds of 28 and 45 cm s^{-1} respectively for the southern half of the eddy. As α is small (24°) these values are approximately equal to the east velocity components. The lower value was obtained from near the western limit of the eddy where absolute velocity would be expected to have a lower easterly component. The close agreement of the velocity values from the two data sets is probably due to there being a very low mean current in the area crossed by this eddy and so the Geosat derived relative velocity will be close to the absolute measured velocity.

The eddy kinetic energy (EKE) of a region is another characteristic of the mesoscale current field which can be found from Geosat data using geostrophic calculations. This is a quantity which has been determined in the past from various forms of *in situ* data by observations of current fluctuations about a climatic mean (Patterson, 1985; Wyrtki *et al.*, 1976) and so comparisons are possible between altimeter data and those from other sources. EKE is a measure of the energy of the oceans in changing flow, dominantly mesoscale eddies and meanders, as distinct from that in the mean flow.

EKE is defined as;

$$\mathbf{EKE} = \tfrac{1}{2}\left\{\sigma^2(V_N) + \sigma^2(V_E)\right\} \qquad \text{(Menard, 1983)}$$

where;

$\sigma^2(V_N)$, $\sigma^2(V_E)$ are variances of V_N and V_E

Hence EKE can be determined at all cross-over points where V'_N and V'_E are found since;

$$\sigma^2(V_N) = \tfrac{1}{n}\sum_{i=1}^{n}(V'_N)^2 \quad \textbf{and} \quad \sigma^2(V_E) = \tfrac{1}{n}\sum_{i=1}^{n}(V'_E)^2$$

where;

n is the number of cross-over data pairs available

Most previous altimeter EKE calculations assumed that velocity variance was isotropic, *ie.*;

$$\sigma^2(V_N) = \sigma^2(V_E) = \sigma^2(V_d) = \sigma^2(V_a)$$

and hence that the EKE can be estimated as;

$$\begin{aligned}\mathbf{EKE} &= \sigma^2(V_a) = \sigma^2(V_d) \\ &= \tfrac{1}{n}\sum_{i=1}^{n}(V'_a)^2 = \tfrac{1}{n}\sum_{i=1}^{n}(V'_d)^2 \qquad \text{(Menard, 1983)}\end{aligned}$$

where;

n is the number of repeats tracks for which data is available

In this case the EKE can be estimated for all points where $\tan\theta'_d$ or $\tan\theta'_a$ are available, giving a much greater number of data points. However, recent work by Morrow *et al.*

(1992) has shown that EKE is anisotropic for some regions of the Southern Ocean and that these isotropic estimates will under-estimate the true EKE values.

In order to map EKE the gradient along all tracks must first be calculated and this involves selection of a suitable smoothing method as the gradient is very sensitive to short wavelength noise. The lengthy computation necessary to achieve this was beyond the scope of the present study.

(2) Advective Velocities

The advective velocity of a feature seen in the data can only be determined approximately, and only in the direction of the track. The eddy sampled by Discovery is seen to apparently move to the north-west along the track shown in figure 6.8, from 32.5° to 28°S between February 5th and April 10th (orbits 6 to 10). The motion this implies is of the order of 570 km over 68 days giving an advective velocity of 8.4 cm s^{-1}. This is consistent with Agulhas Ring advective velocities of 4.8 to 8.5 cm s^{-1} to the north-west, determined by Olson and Evans (1986) using satellite tracked drifters. Altimetric advective velocity values must be treated with some caution however as the eddy may be moving obliquely to the track, in which case the speed would be underestimated, and locating the central point of an eddy as it moves is not often possible.

(3) Feature Identification

When attempting to analyze the time series of height residuals from repeat orbit arcs, especially when calculating geostrophic velocities, it becomes difficult to understand these data in terms of oceanographic features. The main problem arises from use of the mean height as an approximation to the geoid, resulting in all height residuals and subsequent velocities being relative to this mean field. If the long term mean of the ocean is known, then absolute values of height and velocity could be found, however this is not the case for the majority of the world's oceans.

Where an oceanographic signal occurs in an area with no 'background' current, then it is relatively simple to interpret the features seen. Figure 6.9a shows a series of simulated height profiles, offset vertically with time, for an anticyclonic eddy moving along a Geosat track, together with the resultant mean profile. Removing this mean gives the series of height residual profiles shown in the right half of the diagram. This type of signal is relatively simple to distinguish, and if there are a large number of additional repeats in which there is no signal, the effect of a single eddy on the mean will be reduced, the residual heights tending towards the true heights. Figure 6.8 shows the eddy which was sampled by *Discovery* in April and May 1987, and the signal structure seen from orbits 5 to 10 between 25° and 35°S is very similar to the simulated residuals of figure 6.9a, the signal being slightly distorted by the change in structure of the eddy with time and some movement across the line of the track. Movement across the track is confirmed by height residuals of the two adjacent tracks, with a similar time series of residuals at similar latitudes being seen first in the arc to the west, and then in that to the east.

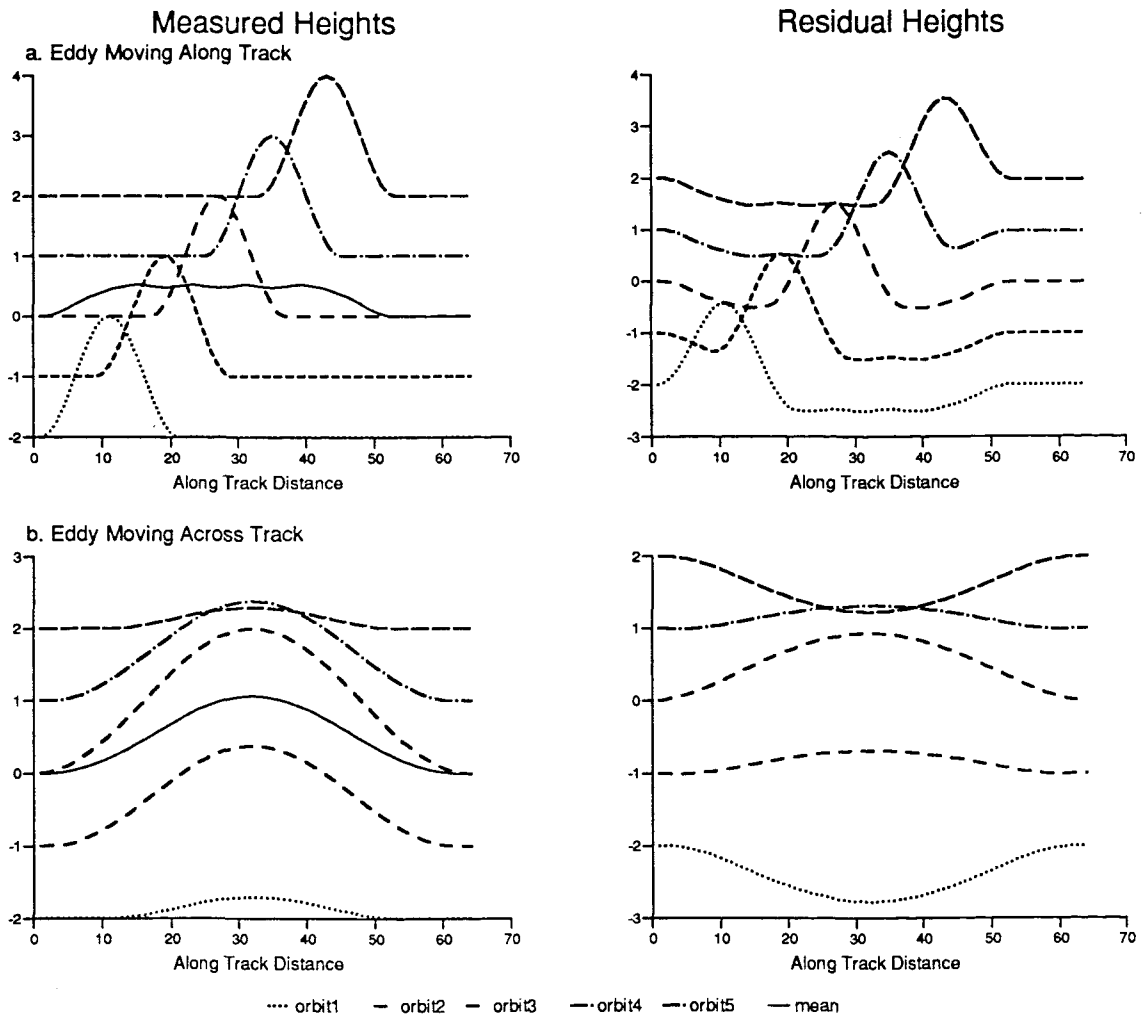

Figure 6.9 Simulated Altimeter Height Profiles and Associated Residuals Calculated by Removal of the Group Mean for an Anticyclonic Eddy Moving Along (a) and Across (b) the Altimeter Track. (Both Height and Distance Scales are in Arbitrary Units).

For a simple eddy moving across the line of a Geosat track there is also a recognizable time series of residual heights (see figure 6.9b) which can be seen if there is no change in structure over time and only a small background signal. Having both ascending and descending satellite passes should aid in interpretation as an eddy moving along one orbit arc should be seen crossing arcs which intercept it. The eddy noted above can be seen to cross three separate descending tracks from east to west, confirming the motion of the eddy along the track in figure 6.8, although the signal is very near the start of the descending orbit arcs and so relatively distorted. A better example is seen in figure 6.6 at 42.5°S from orbits 6 to 8 where a large positive anomaly occurs and then reduces in time implying an anticyclonic eddy moving across the track. A similar time series is seen in two ascending tracks to the west for orbits 7 to 10 and also in the three descending tracks which intercept these at 42.5°S (see figure 6.10). This would imply that this eddy is moving almost due west, against the dominant flow direction.

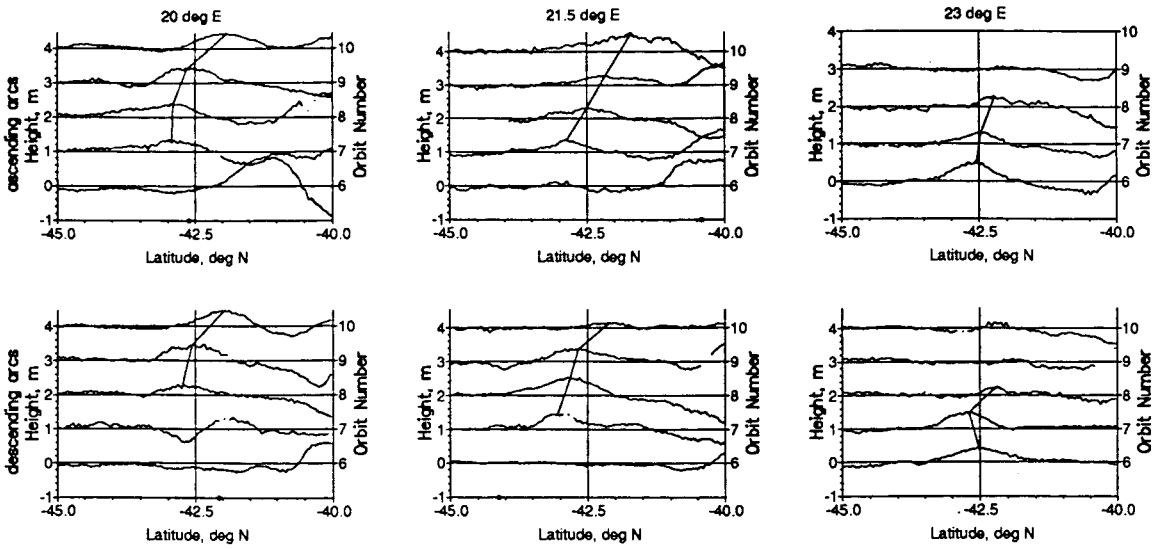

Figure 6.10 Residual Height Profiles for Six Tracks South of the Agulhas Return Current Showing an Anticyclonic Eddy moving from East to West.

Frontal structures, also at mesoscales, can produce very similar height residuals to eddies. A simple ocean front which meanders with time can produce a signal in the height residuals very similar to an eddy moving along the track. Figure 6.11 shows several possible height time series obtainable from an ocean front which moves and alters its velocity profile over time.

In some cases it is possible to distinguish between features by their behaviour. A feature seen to move across several tracks over a relatively short time scale is most likely to be an eddy. The feature seen in figure 6.6 at 49°S (used to calculate the time series of geostrophic velocities given in table III) changes slowly with time and is observed over several parallel tracks, indicating that this is more likely to be caused by a meandering front.

If all mesoscale features were 'classical' circular eddies, the interpretation of the Geosat tracks would be relatively simple. Unfortunately very few such features can be seen in the Geosat height residuals. Dynamic features which change structure or direction can cause much more complicated height residuals, making interpretation more difficult. Also it is rare for the background signal to be small as features tend to be concentrated in limited regions, with several eddies passing along a single track or continuous frontal changes occurring, resulting in a highly complex mean curve.

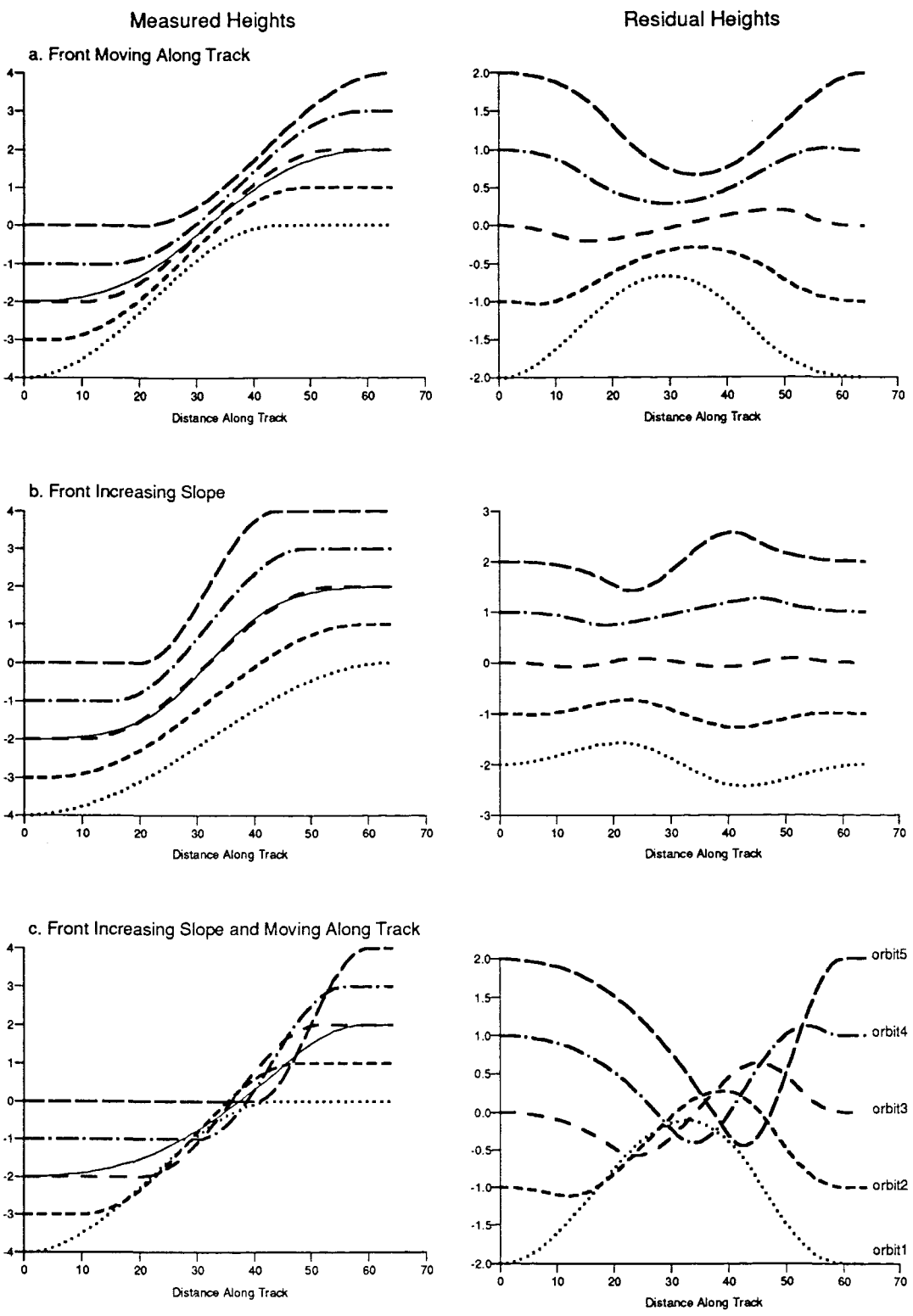

Figure 6.11 Simulated Altimeter Height Profiles and Associated Residuals Calculated by Removal of the Group Mean for an Ocean Front Moving Along the Altimeter Track (a), Increasing Slope with Time (b) and Increasing Slope whilst Moving Along the Altimeter Track (c).
(Both Height and Distance Scales are in Arbitrary Units).

Many of the height features seen in the Geosat data have the sinusoidal shapes noted in the case of a simple eddy, but the sequence of height residuals can rarely be

classified by reference to the simple simulations given in figures 6.9 and 6.11. The time series shown in figures 6.6 and 6.8 illustrate this problem well, both series show large residuals between 37.5 and 42.5°S which change form rapidly with time. Over two adjacent orbits it is sometimes possible to see relationships similar to those of the simulations but it appears that a rapid succession of eddies are passing across these tracks, an explanation supported by past research in this area using both hydrographic data and infra-red radiometry (Lutjeharms and Valentine, 1988). In general the residuals close to cores of high variability regions have the most complicated forms. In quieter regions of the ocean, such as west of the retroflection, between the Agulhas and ACC systems and to the north of the Agulhas Return, the signals are often much simpler to interpret. Even close to the current axes some individual dynamic features have been distinguished (e.g. the anticyclonic eddy seen in figure 6.10) but along the current cores this has not proved possible. It is hoped to use the FRAM data set to help in interpretation of these signals as the time series of height residuals can be referenced to their causal absolute surface dynamic height fields (see § 11.1).

6.4.b. The Autocorrelation Function

In orbit arcs which cross both the ACC and the Agulhas Retroflection or Agulhas Return, there is a marked difference between the amplitude of features seen within the two systems (see § 6.4.a). It also appears that the ACC features have much shorter wavelengths, although this difference may not be significant over time. The autocorrelation function (ACF) provides a method of determining typical length scales over a section of track by assigning a correlation coefficient to a specific value of along track separation or lag. The ACF at lag r is defined as;

$$\mathrm{ACF}(r) = \frac{\mathrm{C}(r)}{\mathrm{C}(0)}$$

where;

C(r) is the autocovariance at lag r given by;

$$\mathrm{C}(r) = \frac{1}{N_r} \sum_1^{N_r} h(x)h(x+r)$$

where;

h is the height residual at location x

N_r is the number of height pairs with separation r

If the value of C(r) is independent of both the location x and the direction of r from x then the field is homogeneous and isotropic with respect to the autocovariance (Dantzler, 1976) and at zero lag (r=0) the autocovariance, C(0), is equal to the variance of the field

(σ^2). The along track autocovariance is strictly only representative of the mesoscale field in the along track direction. Only if the field is homogeneous and isotropic within the region of calculation will the autocovariance be applicable to the entire mesoscale field (Bernstein and White, 1974). As commented previously, some regions of the Southern Ocean show anisotropy in their variability and so the track direction may affect the length scales determined by the ACF analysis. The assumption of homogeneity will also only hold for small regions, as shown by the analysis of the variability field.

If the ACF is calculated for increasing values of r and plotted against lag then a correlogram is created. The ACF will be 1 for perfect correlation, -1 for perfect anti-correlation and zero for non-correlation. Hence the first zero crossing of the correlogram occurs at the first lag for which heights are uncorrelated and the value of r is a correlation length scale for the track. If features in the ACC do have significantly smaller length scales than those for the Agulhas Current systems then the correlation length scale should be smaller.

In order for the ACF calculation to have high statistical confidence a large number of data pairs must be used at each lag. It is difficult to evaluate the errors in ACF calculations as they are a function of the number of independent height measurements available, but it has been shown that the calculated autocovariance tends to have a bias which changes only slowly with r (as the errors are correlated to the lag, Dantzler, 1976), rather than oscillating about the true value. This bias is lowered by increasing the number of data pairs. In order to obtain sufficient pairs at a given lag within a limited region to obtain a statistically significant correlogram, it must also be assumed that the stochastic characteristics of the field do not change significantly with time and so Nr can be increased by including pairs from all repeats of the same track.

A related measure of the spatial characteristics of the height anomalies is the spatial structure function, SSF(r), which is calculated using,

$$\mathrm{SSF}(r) = \frac{1}{N_r} \sum_1^{N_r} \{h(x) - h(x+r)\}^2$$

The spatial structure function is related to the ACF and the standard deviation of the field by

$$\mathrm{ACF}(r) = 1 - \frac{\mathrm{SSF}(r)}{2\sigma^2}$$

For a single data pair the SSF will have a maximum value when r is equal to the distance from the centre of an eddy to the rim, as this will be the largest height difference. Hence if all the eddies within a region have the same, dominant length scale then the structure function will be maximum when r equals half this eddy diameter. If no single scale is dominant then there will be a change of slope in the structure function curve at the smallest scale at which features exist. Due to the relationship between SSF and ACF a peak

in the SSF curve corresponds to a minimum in the ACF curve and if only mesoscale features are present then the minimum should occur near the first zero ACF crossing point as correlation beyond this scale should be small. If features only exist at a single scale within the region to be studied, or small range of scales, then the ACF will decrease to zero at that scale and then remain at zero for all longer scales. If long wavelength features exist in addition to the mesoscale signal, correlations will exist at large lags.

Several studies have attempted to use the ACF or SSF to determine the dominant length scales of a region from hydrographic data. Such data suffer from several problems when undergoing this type of analysis. Station separations are restricted by the size of the area under consideration and the time available for the survey and are rarely less than 50 km, often more than 100 km. From a single cruise, the number of data pairs at any lag, but especially at high separations, is small, limiting the statistical significance of the ACF value. Also the time taken to make a complete survey of a region will mean that the results are not truly synoptic, some station pairs having temporal separations of several days or even weeks, and these data must be eliminated from the ACF analysis, further reducing the ACF statistical significance. In order to increase confidence in the ACF, data pairs are usually grouped within lag ranges, increasing the number of pairs in each range and allowing data from several cruises to be combined. The range size used is generally of the order of 50 to 100 km making resolution at small scales impossible. Geosat data offer a significant improvement in these analyses because such large numbers of data pairs are available that statistical confidence in results is much higher. This is especially important at large scales, as Geosat gives an almost equal number of pairs at all separations up to several hundred kilometres. Also the spatial resolution is equal for all spatial scales from 6.7 km upwards and so the analysis is not restricted at low separations.

Initially correlograms were calculated for individual tracks taking lags up to 600 km (bidirectional), averaged over all repeats of an arc and with the position x limited to a 100 km length of track. The shape of the correlogram obtained was highly dependent on the exact location of x along any given track, changing distinctly for only 0.5° change in x position. The correlograms often showed significant negative lobes in areas where strong signals exist, such as those seen in figure 6.12 at 35°S and 40°S, where the track crosses the Agulhas Retroflection, and at 50°S, from the ACC. If no signal is present, as for the track used in figure 6.12 at 30°S and 45°S, the ACF decreases with lag but never reaches zero and hence no zero crossing length scale can be found.

Unfortunately the ACF is very sensitive to any long wavelength signal which may remain in the data giving correlations over long spatial scales which bias correlations at shorter wavelengths. As a very small change in the slope of the correlogram can produce a large change in the position of the first zero crossing, orbit errors remaining in the tracks can produce significant changes in the calculated length scale. The correlations seen at all scales where no signal exists, implies that there is a long wavelength influence on the ACF, probably due to the residual orbit errors. As the magnitude of orbit errors are track specific

and change along track the correlation due solely to long wavelength effects will also be track dependent and change along track.

In the example shown the zero crossing correlation length scales for the Agulhas Retroflection are 135 and 150 km whilst that for the ACC is 115 km, seeming to support the existence of shorter length scale features in the ACC. Unfortunately most of the tracks do not show such simple ACF curves with many showing the same shape as those of figure 6.12 but with biases which tilt the curves so that no zero crossing is observed.

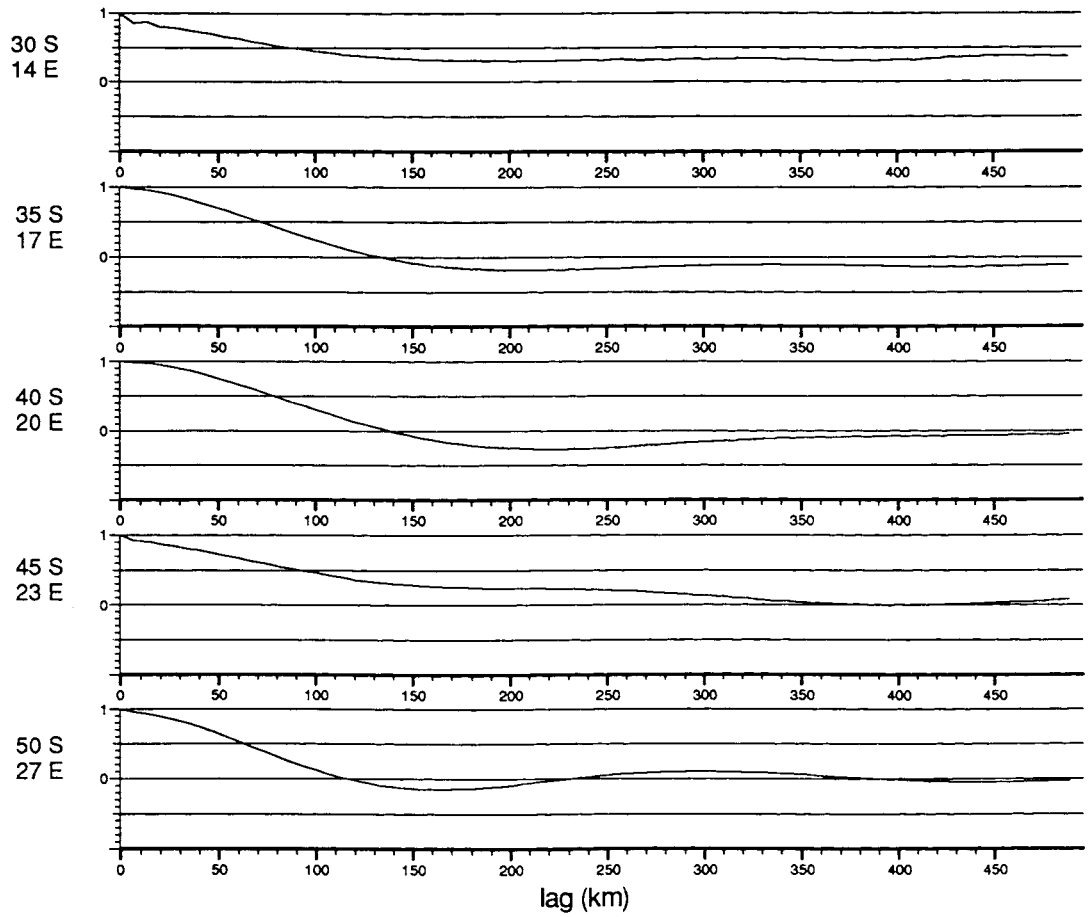

Figure 6.12 Sample Correlograms for an Ascending Orbit Arc Crossing the ACC and the Agulhas Return Current. The Lag is Measured from the Position Given to the Left of each Correlogram.

In order to reduce the effects of track specific long wavelength errors on calculated length scales the ACF was calculated for subdivisions of the Agulhas region consisting of 36 overlapping 15° long by 10° lat boxes. The latitude and longitude ranges of each box are given in figure 6.13, which shows the correlograms calculated using all available repeats of all the tracks within each box (similar to the method used by LeTraon *et al*, 1990). For most boxes there were more that 40,000 data pairs at each lag used, except for the two boxes which include large parts of South Africa (25-35°S and 10-35°E) where 20,000 pairs were found at short lags and less than 100 at long separations and for which results must be treated with some caution.

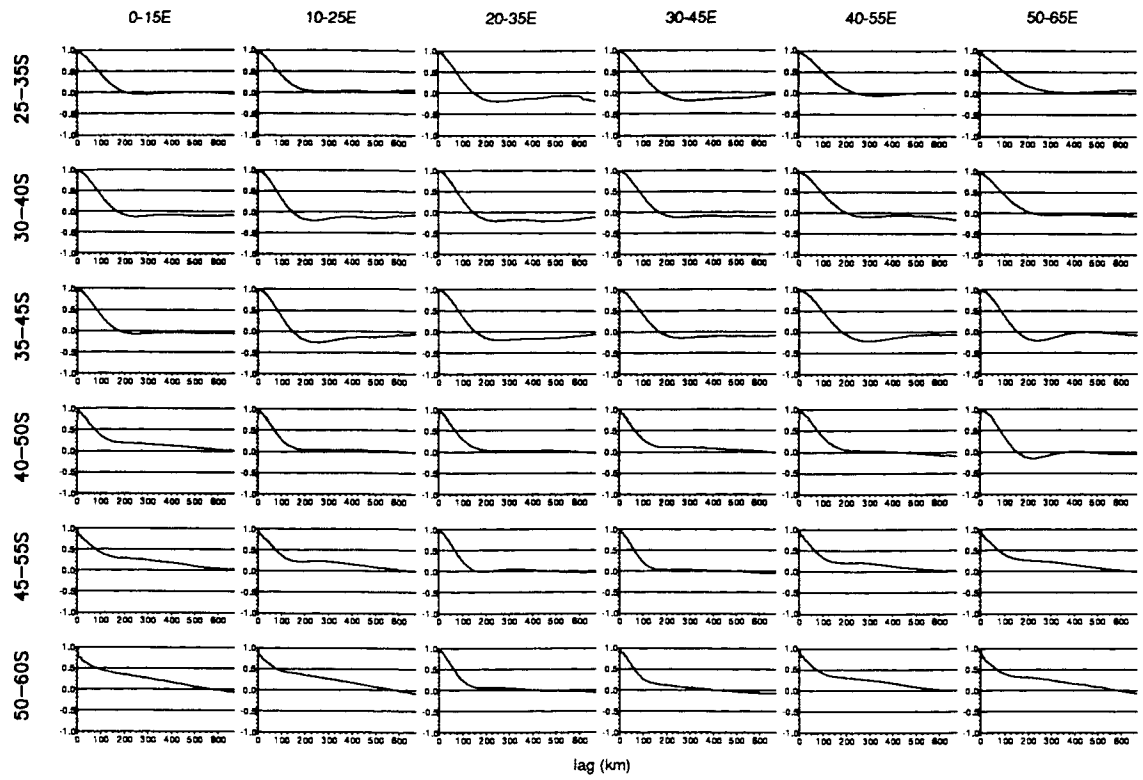

Figure 6.13 Correlograms for 36 Subdivisions of the Agulhas Region.

The first zero crossing correlation length scales, found for each box, appear to be somewhat random due to the long wavelength effects, with values close to the ACC ranging from 163 km to over 600 km and no zero crossing obtained for seven of the boxes. The zero crossing values obtained for the Agulhas Current system appear to be more reliable than those further south and give length scales of 145 to 250 km, although the negative correlations seen at large lags (see figure 6.13) indicate that the lower values may be underestimates.

Lutjeharms (1981) used hydrographic data from the Combined Agulhas Cruise of 1969 to calculate spatial structure functions for the region from 10-40°E and 25-40°S. His calculations gave a minimum scale present of approximately 200 km to the west of the Retroflection and less than 100 km east of this point. Lutjeharms (1981) also reports results of an estimated spatial structure function calculation for the region 40-50°S and 0-40°E which showed a minimum scale present of 150 to 250 km. These results compare well with the zero crossing values obtained above. Lutjeharms and Valentine (1988) used remotely sensed images to study the characteristics of the eddy fields around South Africa and found that most of the features had diameters in excess of 150 km, with their reported eddy statistics giving an average eddy radius of 120 km. This is somewhat lower than the correlation length scale found here but more eddies will have been sampled by the altimeter than by infra-red imagery due to the problems of cloud cover which may have biased the estimates of Lutjeharms and Valentine (1988).

By examination of the correlograms given in figure 6.13 it can be seen that where a large mesoscale signal exists, such as in the Agulhas System, the ACF is dominated by this signal and the first zero crossing length scales obtained give reasonable estimates of the wavelengths of the features. However, where the mesoscale signal is small correlations due to long wavelengths features and errors become proportionally much larger and so the first zero crossing point is no longer a sensible measure of mesoscale feature length scales. By analogy with the SSF it would be possible to find the lag corresponding to either an ACF curve minima, or a change in slope, which would represent the dominant, or minimum, length scales present. Unfortunately this is very time consuming and also highly subjective.

It should be possible to determine the effects of anisotropy on the characteristic length scales by examining the ascending and descending passes within each sub-division separately. This was not carried out due to the problems of long wavelength errors. As many tracks as possible were required within each sub-division to minimize the problem. Also, because of the problem of loss of lock after leaving ice-covered regions there were many more descending passes than ascending for most sub-divisions and differences between the two sets could not be separated from differences in the number of tracks used.

Alternatives to the 'first zero crossing' correlation length have been proposed as 'characteristics' for comparisons between regions. The Integral Scale (IS) of Richman *et al.* (1977) is given as;

$$\mathbf{IS} = \int_0^\infty \mathbf{ACF}(r)\,\mathbf{dr}$$

This length scale suffers from some of the problems of the zero crossing length scale, as negative correlations will reduce the IS. In an attempt to limit this effect Le Traon *et al.* (1990) use the integral of the square of the ACF, L2;

$$\mathbf{L2} = \int_0^\infty \{\mathbf{ACF}(r)\}^2\,\mathbf{dr}$$

In practice the calculation performed is;

$$\mathbf{L2} = \sum_{r=0}^{R} \{\mathbf{ACF}(r)\}^2 \times \Delta r$$

where;

R is the maximum separation used

Δr is the along track sampling distance (6.7 km)

The choice of R proved to have little effect on the value of L2 for R greater than 400 km.

For each of the subdivisions of the region used above the value of L2 was found (see figure 6.14) together with the lag for which the ACF first dropped below 0.5. The distribution of values of L2 show a fairly distinctive trend with the lowest values (less than 50 km) occurring where the ACC variability was seen (see figure 6.3) whilst the

maximum values occur in the region of the Agulhas System. The values of L2 must still be considered with respect to the correlograms as the scale obtained assumes that correlations at long lags are small. This is not the case for areas where the mesoscale signal is small, giving the intermediate values seen in figure 6.14.

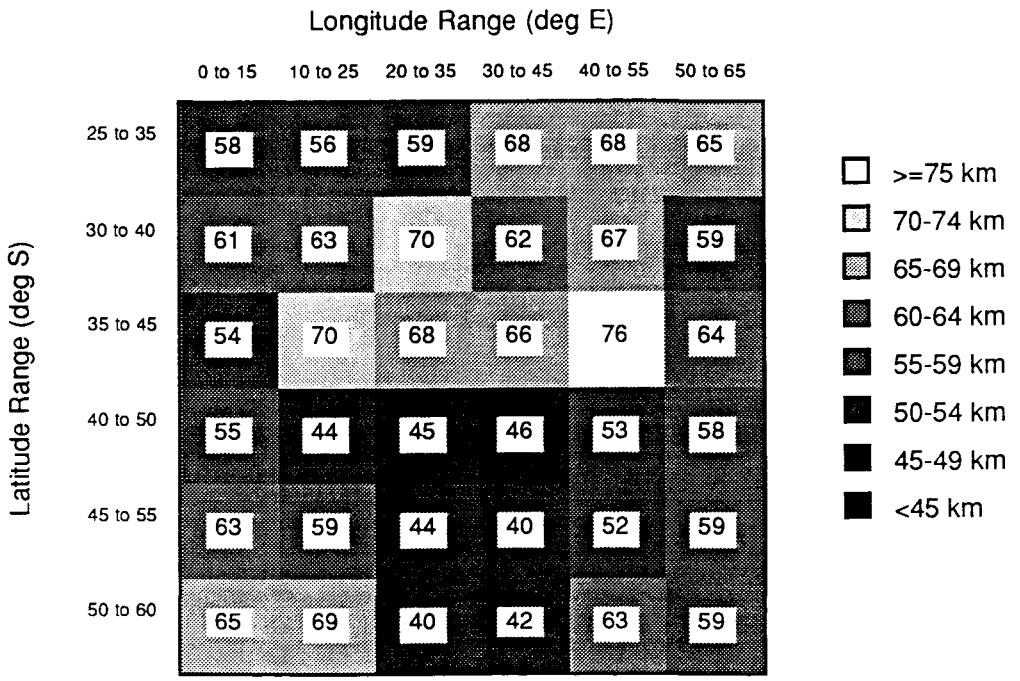

Figure 6.14 The Integral Square Length Scale (L2) for 36 Subdivisions of the Agulhas Region.

The 0.5 crossing lags are more consistent than the zero crossing lags, as the ACF curve is much steeper at shorter lags and so the crossing point is altered less by long wavelength biases. The 0.5 crossing values show a very similar spatial distribution pattern to that found for L2, with values on average 20 km greater than the corresponding L2 values. Figure 6.15 shows the values of L2 plotted against the 0.5 ACF crossing lag (0.5ACF) for all 36 boxes. Although there is a large amount of scatter on the graph there is fairly close correlation to the line L2 = 0.5ACF - 20, implying that L2 gives a reasonable indication of the relative spatial scales of the region and that the apparent difference between spatial scales in the Agulhas and ACC is probably real.

This difference in scale between the two current systems indicates that there are differences between the controlling mechanisms for the mesoscale activity in the ACC and those in the Agulhas System. Within the Agulhas System, the generation of eddies is closely linked to the formation of meanders and instabilities in the mean current (Gründlingh, 1982). The size of these instabilities may be controlled by several factors including bottom topography, volume transport, current velocity structure and wind forcing. The diameter of the large Agulhas Rings, formed by occlusion of the Retroflection, will be controlled by the wavelength of the Retroflection itself, and this has

been shown to be related to changes in planetary vorticity with latitude as well as the factors mentioned above (Boudra and Chassignet, 1988). The dynamics of the ACC in this region have not been as well studied as those of the Agulhas System but it appears that bottom topography again plays a role in the formation of eddies by current instabilities. Differences in the velocity structures of the two current systems, the size and shape of topographic features and the orientation of these features relative to the flow could all affect the length scale of mesoscale features produced. The effect of the African continent on the Agulhas System, both directly as a topographic feature and indirectly by influences on the wind stress, may also be a contributory factor. Obviously further work is required before any conclusions can be drawn as to the causes of this observed difference in scale.

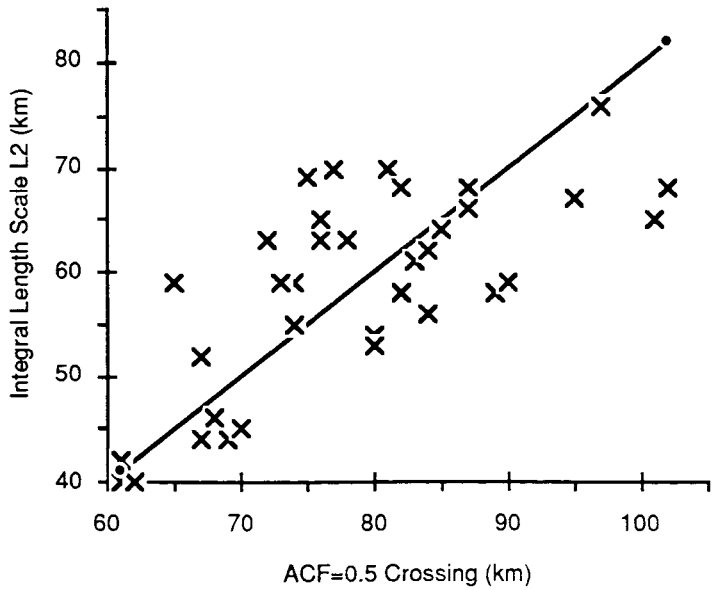

Figure 6.15 The Integral Square Length Scale (L2) against the first ACF 0.5 Crossing Lag for 36 Subdivisions of the Agulhas Region.

The Agulhas region is highly energetic and variable, with the Agulhas Current System and the ACC interacting both with topography and each other, resulting in the altimetric signals obtained being very large and complex. Although the strong currents give altimetric signals which are relatively easy to distinguish from residual noise, the complexity of the data makes interpretation rather difficult. In the following chapter Geosat data will be examined for a region in the Central South Pacific where *in situ* data shows that the current system is rather more simple, although mesoscale signals are expected to be smaller and hence more difficult to isolate.

7 THE CENTRAL SOUTH PACIFIC

The second area chosen for study was the Central South Pacific (the tracks crossing the area are shown in figure 7.1). In this region the ACC crosses the Antarctic Pacific Rise and, as in the Agulhas region, this was an area where the FRAM results seemed to indicate interaction between the ACC and bottom topography.

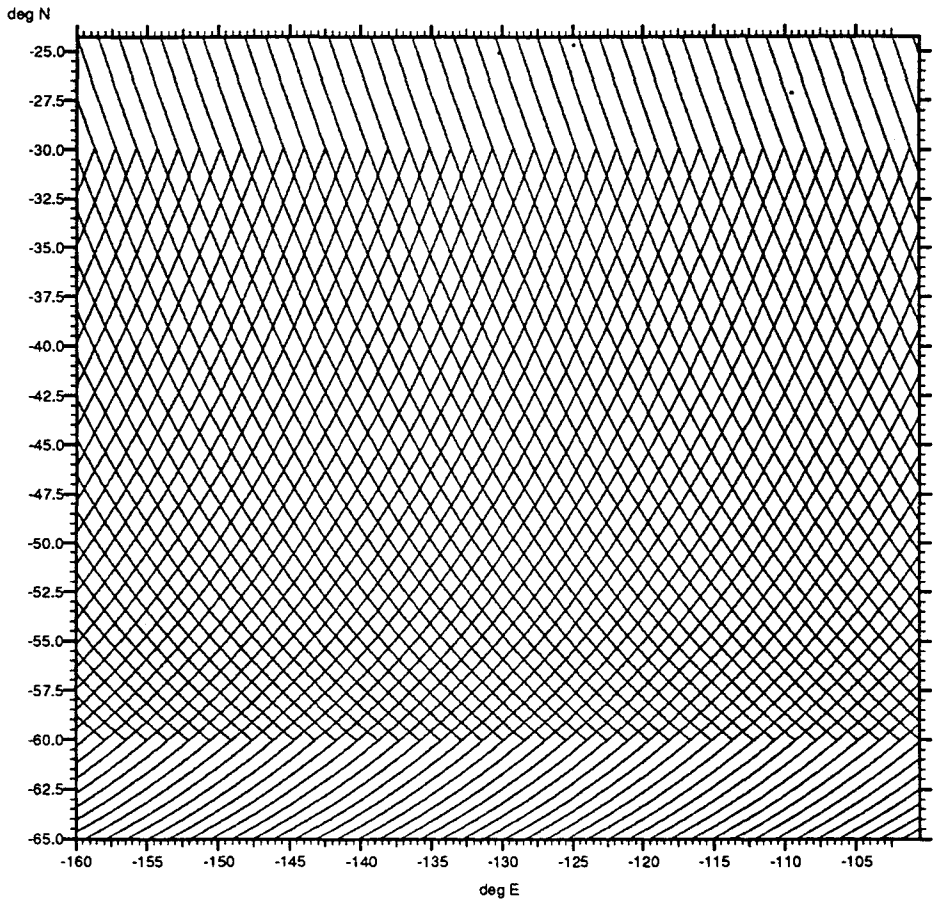

Figure 7.1 A Map of the Central South Pacific Study Area Showing the Location of Geosat Tracks Extracted from the GDR Tapes.

Much of this area is expected to have very low sea surface height variability, as the currents are less intense than those of the Agulhas region (Gordon and Bye, 1972), and so a higher proportion of the observed variability is likely to be due to residual errors, rather than to current activity. Hence, variability here will give a good indication of the noise level remaining in the data after processing.

The current system here has little interaction with the ocean north of the region under investigation, the main current flow being west-east across the area, and there are no western boundary currents to complicate the current structure. Hence the open boundary

conditions of FRAM should have a lesser effect on the model currents making this a good area to test the model's ability to reproduce the effects of topographic steering on the ACC.

As for the Agulhas region, all existing repeats (from the 43 possible) of the orbit arcs shown in figure 7.1 were extracted from the Geosat GDR and processed by the method described in chapter 5. Data coverage is good for almost all repeat cycles, especially for the descending tracks, which enter the region from oceanic areas and so suffer less from data dropout than the ascending tracks, which enter from ice covered areas.

7.1 VARIABILITY FIELD

A variability field was created from the rms curves of all the tracks shown in figure 7.1 using the same interpolation method as for the Agulhas region (see § 6.3) and the resultant field is given in figure 7.2. Variability in the region is generally low, with a background level of around 6 to 7 cm rms existing over much of the region. This is the same level as found in quieter parts of the Agulhas area indicating that the combination of sensor accuracy and processing method has a minimum noise level of around 5 cm rms, assuming that there is a contribution of 1 or 2 cm from true sea surface height variability even in oceanographically quiet areas.

A broad band of higher variability, 5 to 10° wide, exists across the entire region, stretching from 50°S in the west to 60°S in the east, having a maximum signal of less than 21 cm rms. Within this high variability zone is a block of lower variability centred on 55°S 141°W. Chelton *et al* (1990) note the high sea surface height variability west of 140°W. However they do not comment on the continued high variability east of this feature, although this can be seen in their data, nor on the low variability block.

Narrow, linear, high variability bands can be seen south of 60°S in figure 7.2, oriented southwest-northeast, which are not seen in the smoothed 2° plots of Chelton *et al* (1990). Each band is produced by a single descending orbit arc and is probably due to problems in the long wavelength correction applied to these arcs. The study of along-track time series should confirm this (see § 7.2).

North of 30°S there is a second area of increased variability extending eastward to 130°W, although maximum variability here is less than 15 cm. This band of increased height variability can also be seen in the plot of Chelton *et al* (1990) and they attribute at least part of this to problems with the wet tropospheric correction in the tropics, as variability is seen to increase in austral summer when rainfall here is greatest.

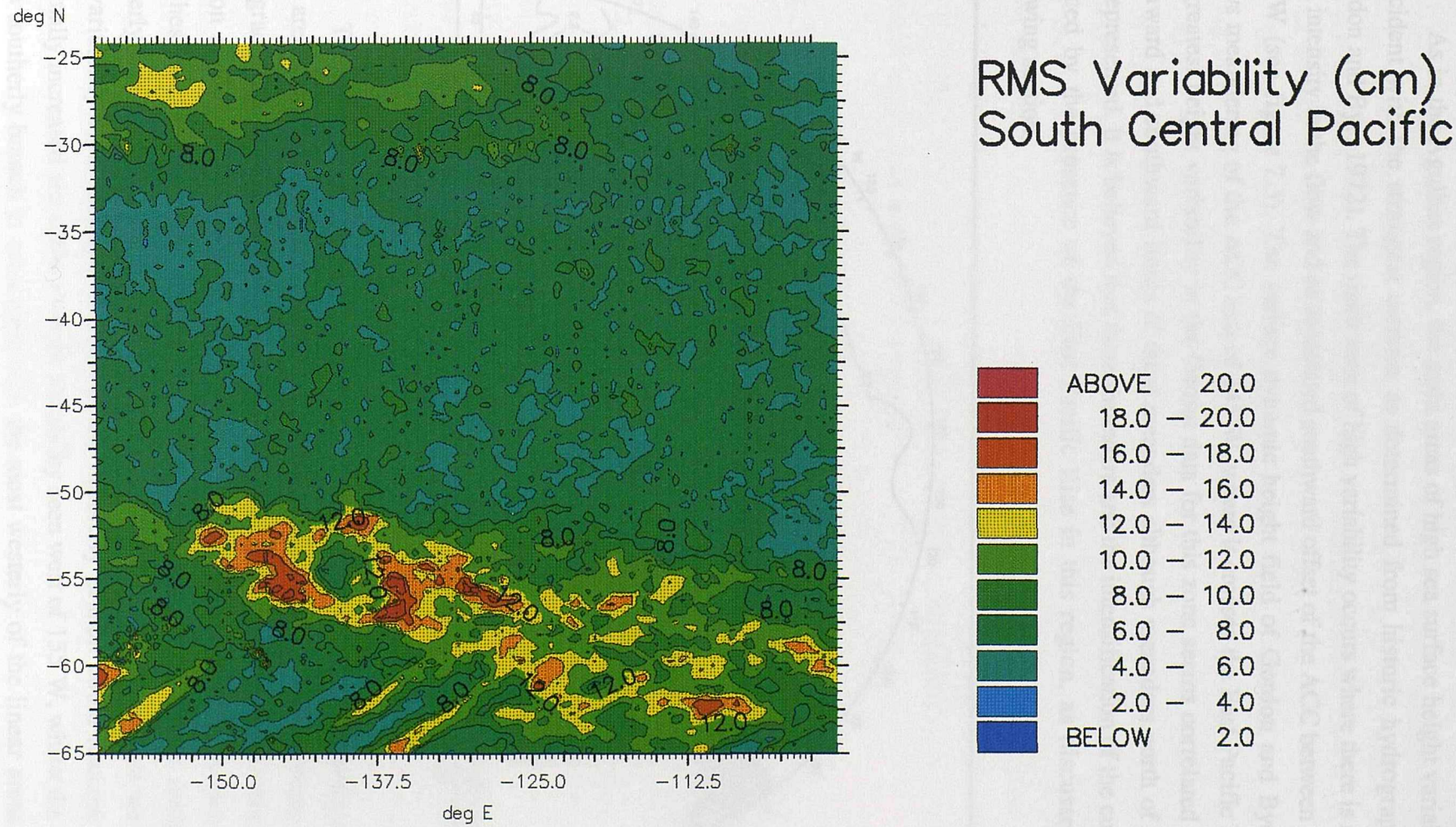

Figure 7.2 RMS Sea Surface Height Variability of the Central South Pacific from Two Years of Geosat Data.

7.1.a Comparison With Historical Current Data

As in the Agulhas region, the main areas of high sea surface height variability are coincident with the strongest currents as determined from historic hydrographic data (Gordon and Bye, 1972). The main zone of high variability occurs where there is a distinct local intensity in the flow and an associated southward offset of the ACC between 150° and 140°W (see figure 7.3). The surface dynamic height field of Gordon and Bye (1972) shows meandering of the ACC east of 145°W, where it crosses the East Pacific Rise and the greatest height variability in the Geosat data for this zone seems correlated with the northward and southward limits of these meanders although meanders north of 55°S are not represented. It is believed that these meanders and the intensification of the current are induced by the presence of the East Pacific Rise in this region, as discussed in the following section.

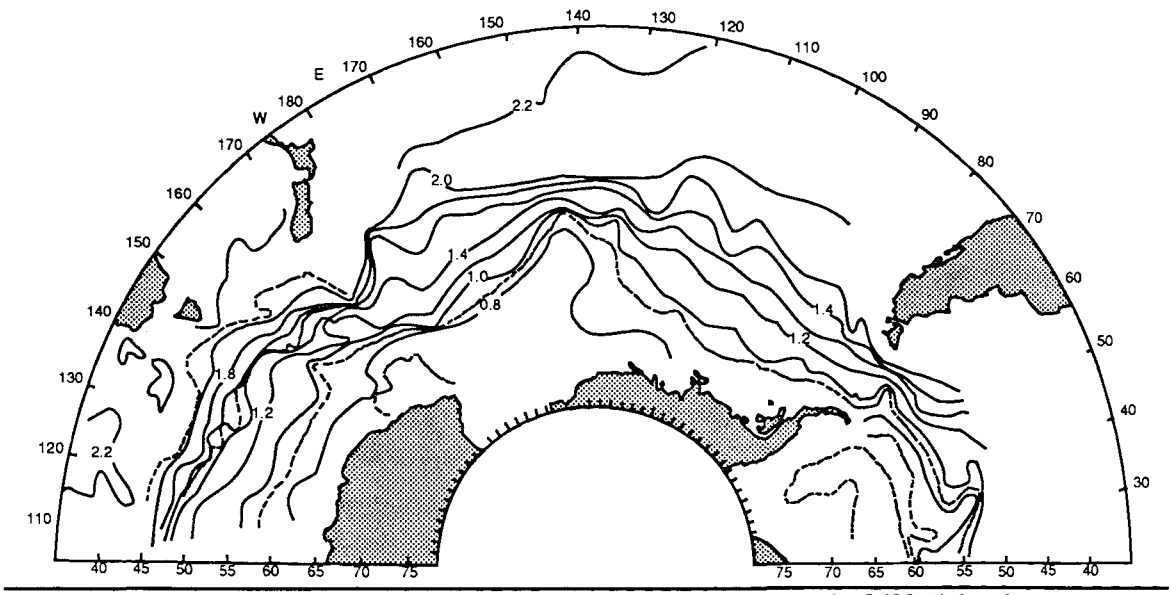

Figure 7.3 Sea surface Dynamic Height Anomaly Relative to the 2500-db level (after Gordon and Bye, 1972).

The block of low sea surface height variability seen in the ACC corresponds to a small area in the historical data where the dynamic height slope is small, the main zones of high gradient passing around the block to north and south. There is also evidence from Gordon and Bye (1972) for the ACC entering the region in the west as two distinct branches, the northerly branch at 52°S flowing almost due east before meeting the southerly branch, which enters the region at 59°S and flows north-east, just west of the low variability area. Changes in flow of the northerly branch could account for the marginally increased sea surface height variability seen west of 155°W, whilst the location of the southerly branch is coincident with the most westerly of the linear areas of high variability noted above, indicating that this may be caused by a real oceanographic signal, not problems with residual orbit errors.

The northerly flow indicated in figure 7.3 along 120°W from 55 to 50°S is not represented in the Geosat variability field. This may indicate that the flow here is particularly steady, but may also reflect the low current speeds, implied by the widely spaced dynamic height contours, which would not produce a large signal even if the current was varying. There is also no variability associated with the southerly flow at 140°W from 58 to 65°S which represents the eastern limit of the Ross Sea Gyre.

Lutjeharms and Baker (1980) highlight the Central South Pacific as an area showing large dynamic height variations at mesoscales in their statistical analysis of historical hydrographic data. Using FGGE drifting buoy data, Patterson (1985) identifies a zone of high eddy kinetic energy between 50 and 60°S extending from 152 to 110°W, corresponding to the zone of greatest sea surface height variability seen in figure 7.2. Patterson also notes high eddy kinetic energy along 25°S from 130 to 180°W, indicating that the variability seen here in the Geosat data is a true representation of current activity, associated with variations in the southern limb of the South Pacific Subtropical Gyre (see Reid, 1986, figure 4). The cause of this feature will be considered further by examination of residual height time series in § 7.2 below.

7.1.b Comparison With Topography

The bottom topography of the Central South Pacific is given in figure 7.4 with the major sea-floor features named. It is obvious from the historical hydrographic data (Gordon and Bye, 1972) that the bottom topography has a great steering effect on the ACC, even though the shallowest depth in the region is still greater than 2000 m, with much of the ridge crest deeper than 2500 m. The coincidence of zones of increased velocities and fracture zones in the ridge was noted by Gordon *et al* (1978). The broad easterly flow of the ACC east of Australia is concentrated into the narrow, high velocity features seen in figure 7.3, which are deflected northwards along the western edge of the Antarctic-Pacific Ridge before crossing the ridge via the Eltanin Fracture Zone (to the north) and the Udintsev Fracture Zone (to the south), into the Amundsen Abyssal Plain. These fracture zones divide the flow into two distinct branches which are separated by the area of low dynamic topography slope noted above.

The Geosat data shows that the location of variability of this current is also strongly correlated to the topography. The highest variability occurs immediately to the west of both the Eltanin and Udintsev fracture zones and east of the ridge between them, extending along the relic fracture zone scarps to the east as two patchy, linear zones of high rms. The low variability block noted in § 7.1 is located just west of a section of the East Pacific Rise isolated between the fracture zones.

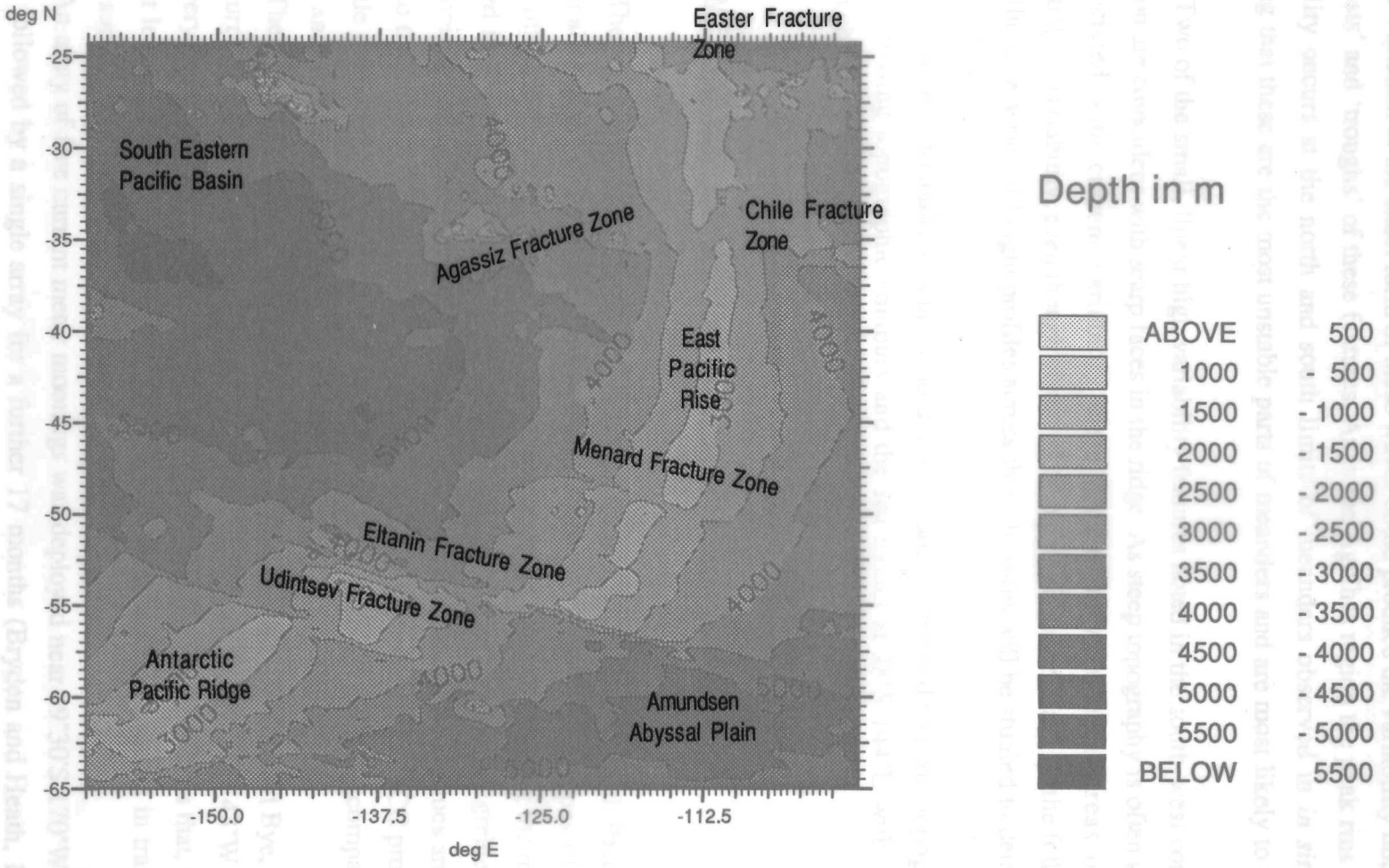

Figure 7.4 The Bottom Topography of the Central South Pacific.

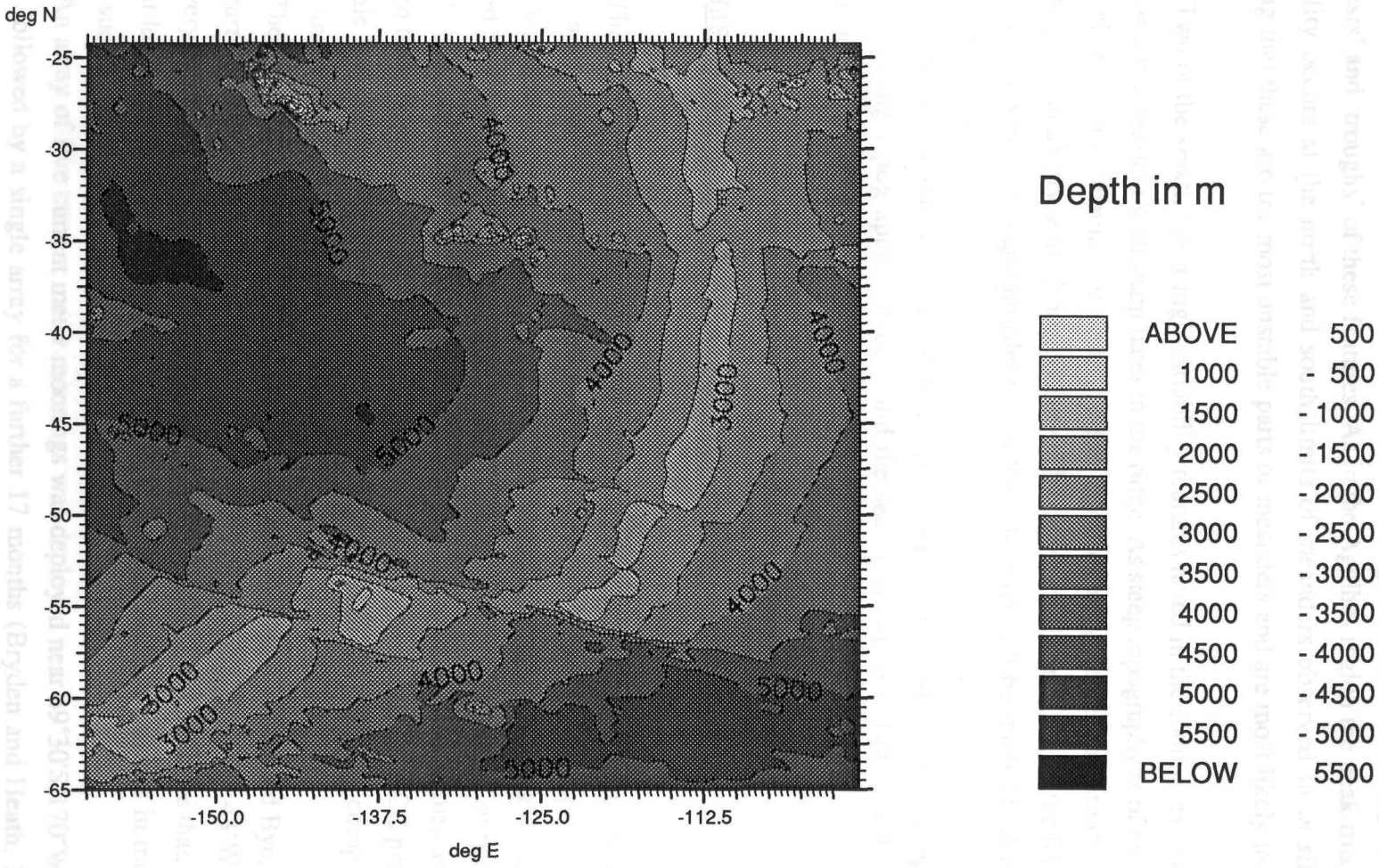

Figure 7.4 The Bottom Topography of the Central South Pacific.

The current flow noted is consistent with the findings of McCartney (1976) who showed that a broad easterly current would be deflected equator-ward on approaching a meridional ridge, with meanders forming downstream. Porter and Rattray (1964) discuss the presence of Rossby waves which may be found in the lee of submarine topographic features. These induced waves migrate westward at a rate equal to the eastward current leading to the formation of standing waves which decay downstream due to the action of friction. Variation in the exact form of these waves could produce the variability noticed at the 'crests' and 'troughs' of these features. As in the Agulhas region the peak rms height variability occurs at the north and south limits of meanders observed in *in situ* data implying that these are the most unstable parts of meanders and are most likely to spawn eddies.

Two of the small, linear high variability features noted in the south-west corner of the region are coincident with scarp faces in the ridge. As steep topography is often seen to be associated with current variability these features may represent areas of true oceanographic variability, even though observed by only a single orbit arc. In the following section the time series of height profiles across these features will be studied to determine the cause of variability.

The higher variability area in the north is not readily correlated with any topographic features, crossing topographic contours and the sea mount at 28°S 144°E without any apparent changes in variability.

7.2 TIME SERIES OF REPEAT ORBIT ARCS

The amplitudes of sea surface height anomalies seen in the Central South Pacific are much smaller than those of the Agulhas Current system, however the slopes of these features may still be large. Velocity anomalies calculated at cross-overs using the method described in § 6.4 yield magnitudes of up to 50 cm s^{-1} within the areas of greatest sea surface height variability, with speeds of 30 cm s^{-1} being frequent. These values are very similar to those found for the ACC in the Agulhas region showing that the ACC produces mesoscale features with similar velocity characteristics at both locations. By comparison, velocity anomalies found in quieter regions rarely rise above 10 cm s^{-1}.

The geostrophic flow calculations from hydrographic data (Gordon and Bye, 1972) give a current velocity of 40 cm s^{-1} across the Udintsev Fracture Zone at 143°W 55°S. This is very close to the values obtained for the velocity anomalies and indicates that, in this region at least, the time averaged current is of similar magnitude to currents in transient features such as eddies or frontal meanders.

An array of five current meter moorings was deployed near 49°30'S 170°W for 7 months, followed by a single array for a further 17 months (Bryden and Heath, 1985).

Data collected on hydrographic surveys from 49 to 50°S, whilst deploying and recovering moorings, gave geostrophic velocities relative to 1000 m of 20 cm s^{-1} to the northeast in April 1978 and 12 cm s^{-1} to the south in November 1978. Drift velocities for five buoys deployed while the moorings were in place gave average current speeds of 21 cm s^{-1} when calculated over 10° longitude, but more than 40 cm s^{-1} when calculated over only one degree. This implies there was a great deal of variation in the buoy trajectories and hence that the current was highly variable. This was confirmed by the current meter data which showed vertically correlated temporal fluctuations at the surface of order 20 cm s^{-1} mean fluctuation at time scales of approximately 20 days. Although slightly west of the area under consideration in this study these data show current variations of similar magnitudes to the velocity anomalies found in the ACC.

7.2.a Feature Identification

Due to the relatively small variability signals of the currents in this region it is rather more difficult to isolate oceanographic signals from residual errors in the variability plot of figure 7.2 than it was for the Agulhas Region. The time series of individual orbit arcs can aid in the identification of noise, however, as the form of height anomalies caused by oceanographic features should be different from those caused by noise.

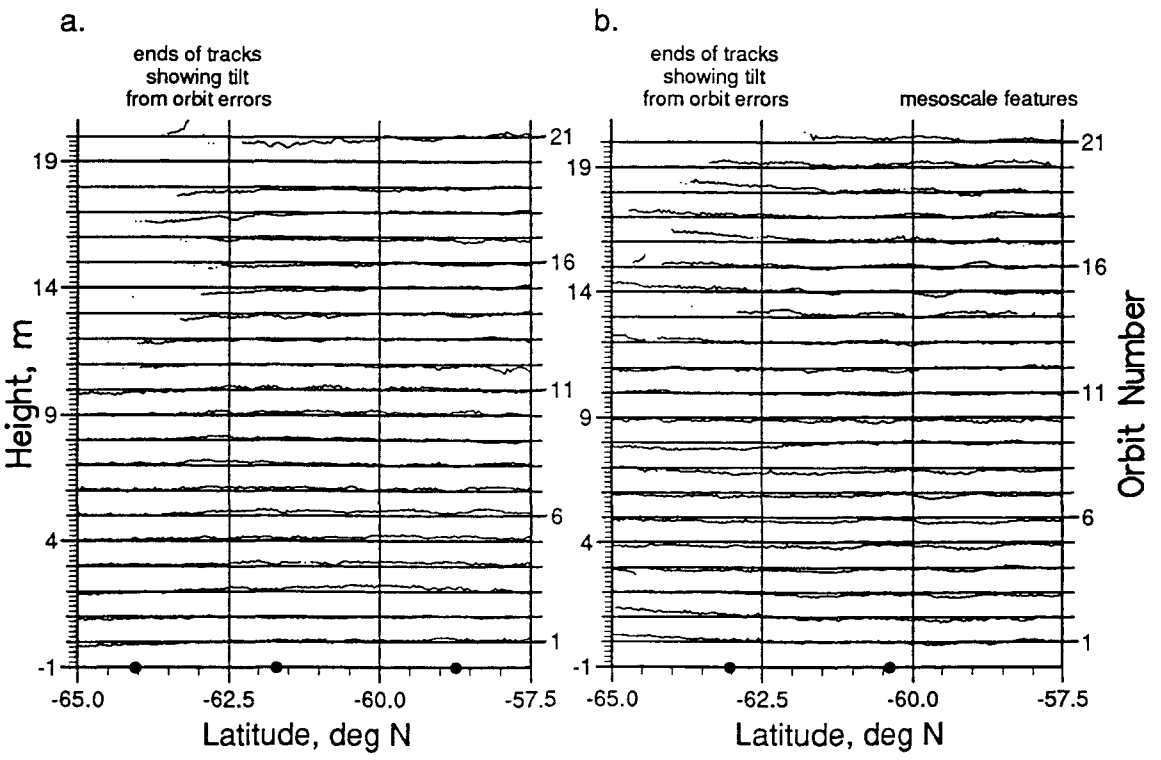

Figure 7.5 Time Series of Height Residuals for Two Descending Orbit Arcs Having Isolated High Variability caused by Orbit Errors Alone (a) and a Combination of Orbit Errors and Mesoscale Oceanographic Signals (b).

The four linear, high variability zones in the SW section of region, noted in section 7.1, are each caused by a single descending orbit arc. The height anomalies for three of these features seem to indicate residual orbit errors as the cause of this variability. Figure 7.5a shows one of these tracks and south of 60°S, where the high variability is seen, there is a long wavelength 'tilt' to the height residuals, especially in the short repeats, which is inverse to the removed quadratic orbit correction. The height anomalies for the most westerly of these features (figure 7.5b) are somewhat different, showing short wavelength features near 60°S which change rapidly over a few orbits, just north of a region where orbit errors can be seen. This would imply that the variability at this location is at least partly due to true mesoscale oceanographic variability, although some contribution from orbit errors may exist. As mentioned previously, the southerly branch of the ACC crosses this area, where there is also a small fracture zone on the Antarctic-Pacific Ridge, and interaction between the current and topography may induce instabilities in the flow.

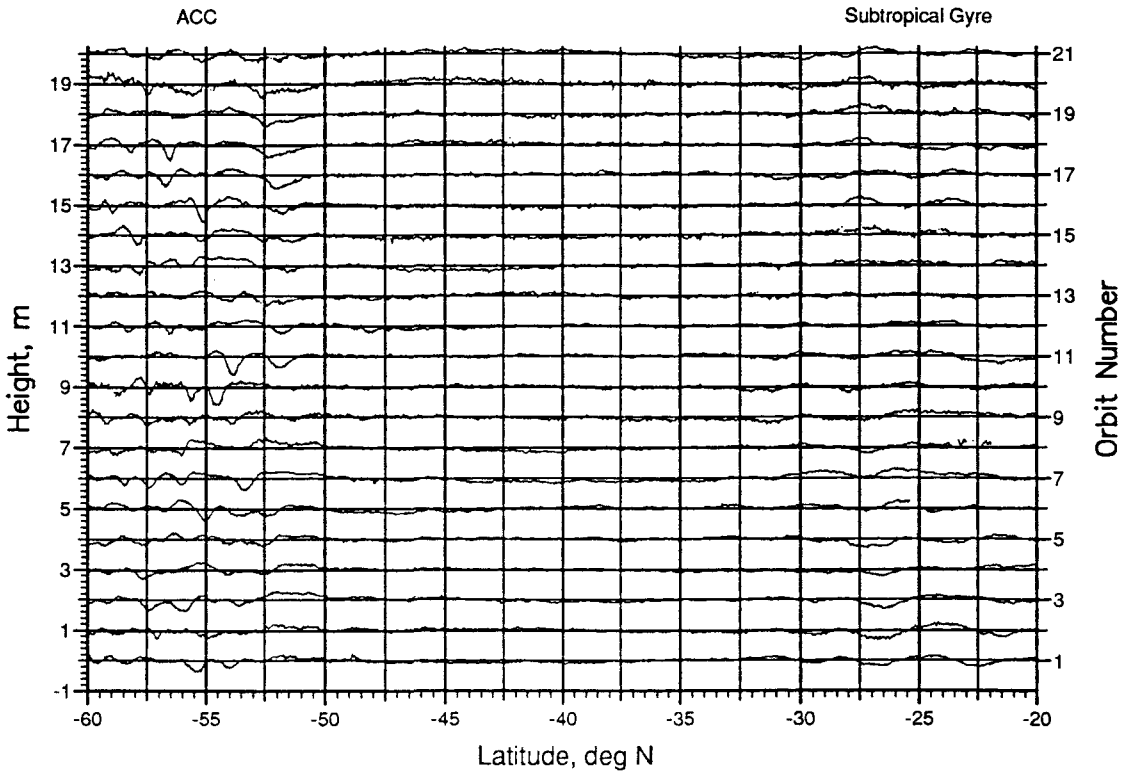

Figure 7.6 A Time Series of Height Residuals for an Ascending Orbit Arc which Crosses the ACC and the Southern Limb of the Subtropical Gyre.

The signals which cause the area of increased variability seen in the north-west of the region are somewhat different to those seen further south, as shown in figure 7.6, having wavelengths of the order of 5° latitude which change over time scales of three months. Chelton *et al* (1990) apportioned at least part of this variability to errors in the

FNOC wet tropospheric range correction. This is supported by water vapour corrections determined from the SSMI (Special Sensor Microwave Imager) and TOVS (TIROS Operational Vertical Sounder) data, interpolated onto Geosat ground points for recent GDR improvements (Cheney *et al*, 1991a). These satellite sensors were operational at the time of the Geosat data and so provide near real time corrections which have been shown to be significantly more reliable than the FNOC values (Cheney *et al*, 1991b). Comparisons of the FNOC corrections used for this study with the SSMI/TOVS correction for a single orbit arc from 30°S 155°W to 24°S 158°W (the arc shown in figure 7.6) have shown that the FNOC correction is in error by up to 12 cm (assuming the SSMI/TOVS value to be correct) and that the error changes over length scales of several degrees latitude. However it must be remembered that the mean error and up to two thirds of the remaining error (Cheney *et al*, 1991b) will be removed by the altimeter processing method and the residual error amplitude will only be of the order of 2 cm. Hence most of the variability seen here is due to oceanic activity.

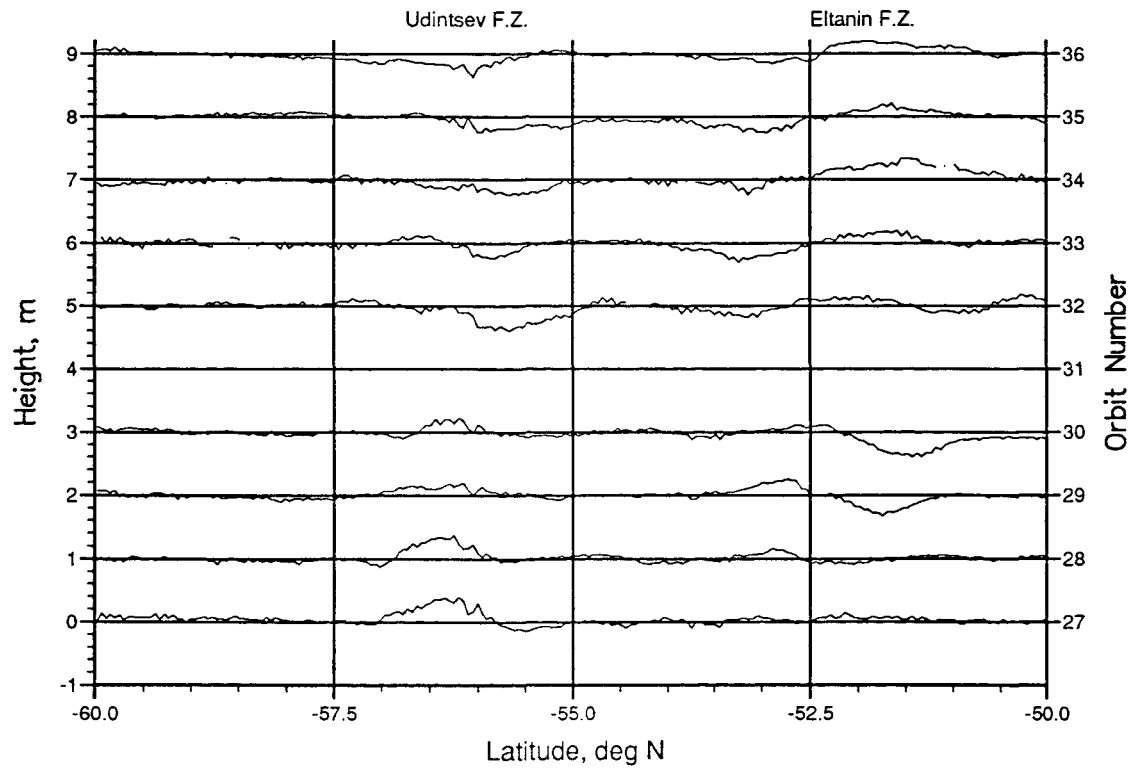

Figure 7.7 A Time Series of Residual Height Profiles for an Orbit Arc which Crosses both the Eltanin and Udintsev Fracture Zones.

Height anomalies for orbit arcs which cross both the Eltanin and Udintsev fracture zones show different features in each of the Fractures. The height anomalies for some tracks in the Eltanin Fracture Zone appear similar to those of figure 6.11b for a front with changing velocity structure but constant location. One such time series is shown in figure 7.7 for orbits 28 to 36, a period of more than four months, and can be interpreted as

a slow increase in the velocity through the northern fracture zone over this time. This may indicate either an increase in the total ACC flow over this period, or that there is transference of the ACC flow between the two fracture zones with corresponding changes in velocity of the flow through the northern fracture zone.

Tracks which cross the area of patchy high variability east of the Ridge crest show rapidly changing height anomalies, with little correlation between adjacent tracks. Mesoscale features are not readily isolated within this higher variability area as the signals change rapidly between repeats, but at the northern edge some individual eddy features can be identified, as was found in the Agulhas region away from the high velocity cores. Most of the features identified appeared to be moving across the tracks, with some along track component, indicating that there is little spreading of eddies north away from the ACC with most eddies moving in the same direction as the mean current. This will have important consequences for the eddy transport of properties such as heat, salt and momentum in the Southern Ocean.

7.2.b The Autocorrelation Function

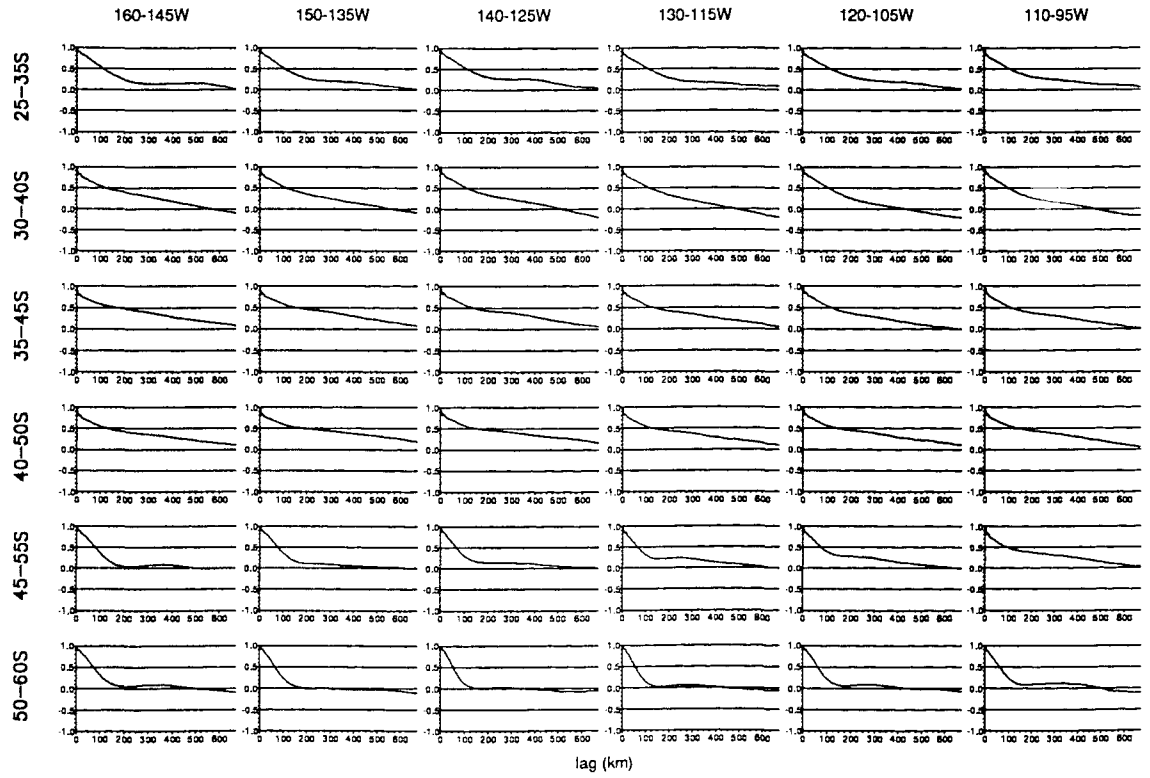

Figure 7.8 Correlograms for 36 Subdivisions of the Central South Pacific Region.

The characteristic length scales for height anomalies in the Central South Pacific were examined using a similar analysis method to that used in the Agulhas Region (see § 6.5). The ACF curves found for each of 36 sub-divisions of the region are given in figure 7.8.

Examination of the correlograms shows that many of the curves have almost constant slope, or gradually decreasing slope, for all lags. Only where there is a significant mesoscale signal (along the ACC and in the north-west corner of the region) can a significant change of slope be seen in the ACF curves, as expected from the study in the Agulhas Region. As the signals here are much lower amplitude than those in the Agulhas region, only one curve shows a zero crossing coincident with this change in slope of the curve, that for the 150-135°W 50-60°S, and the length scale obtained is 185 km. The change in slope for curves in the north-west of the region occurs at lags over 200 km, but is less clearly distinguishable than for slopes in the ACC due to the lower signal amplitude.

The 0.5 crossing lag is fairly consistent for the two latitude bands south of 45°S which have a strong mesoscale signal, varying from 54 km to 78 km. North of these bands values are much longer at 128 to 165 km.

The Integral Length Scale L2 again varies with the 0.5 crossing lag but is lower by approximately 20 km. Values of L2 in the ACC are very similar to those found for the ACC in the Agulhas Region, 35 to 50 km, whilst in the north-west values are 78 to 90 km confirming the apparently longer wavelength of features seen here.

Lutjeharms and Baker (1980) estimated the SSF for the area 160-120°W 50-60°S using dynamic heights from hydrographic data and found a minimum scale present of 150 km but using lag steps of 50 km. All the ACF curves in this area have a change of slope between lags of 150 and 200 km (figure 7.8) which compares well with the findings of Lutjeharms and Baker.

Results from the Geosat data in the Central South Pacific show some very similar conclusions to those found in the Agulhas region despite the much lower levels of sea surface height variability and current speed. Topography has been seen to be a major influence on both the location and intensity of current variability. Major current axes are seen to show the greatest variability with highly complex current anomalies, changing rapidly with time and implying complex eddy shedding and frontal movements. The creation of meanders in the mean flow again appears to be correlated to the formation of eddy features. Away from the current axes variability can more often be associated with specific eddy features due to the less complex mean flow. In the following chapter the extraction of sea surface height data from the FRAM will be discussed and the results for both the Agulhas and Central South Pacific Regions obtained from the FRAM will then be discussed in relation to the results from the Geosat data.

Section III: FRAM DATA

8 MODEL ALTIMETRY

The FRAM project has produced surface pressure fields calculated from the model surface velocities for the entire Southern Ocean. The surface pressure gradient is directly related to the geostrophic surface currents by the geostrophic equation (see section 4.1) and surface dynamic height fields can be calculated from the pressure fields. Once the FRAM dynamic height fields have been created, they can be considered as model sea surfaces relative to the geoid. This gives an opportunity to compare the FRAM data directly with the Geosat data for verification of the model results. By sampling the model fields along lines equivalent to satellite ground tracks it is also possible to treat the FRAM data as 'noise free' altimeter data which can be processed as real altimeter data in order to examine any effects that processing may have on the Geosat height residuals. Height residuals created in this way can also be compared to their causative dynamic fields and may be used to aid in interpretation of the Geosat data.

Equation (4.5) (page 29) gives the difference in geopotential between two isobaric surfaces. If one level is taken as a reference then the geopotential at a height z above this level can be written as;

$$\Phi = -\int_{p_0}^{p_z} \frac{1}{\rho} dp \qquad (8.1)$$

where;

p_0, p_z are pressures of the reference level and a level height z above the reference.

When the sea is at rest, sea level is exactly equal to a geopotential surface defined as $\Phi = 0$ (the geoid) and can be taken as the reference. Geopotential can be measured in units of the geopotential metre (gpm) defined as

$$\mathbf{1\ gpm\ =\ 9.8\ m^2 s^{-2} \equiv\ 9.8\ J\ kg^{-1}}$$

so that geopotential in gpm is numerical approximately equal to the height of the sea surface above the geoid in metres, ie. the geopotential height Z is;

$$Z = \frac{\Phi}{g_c} \qquad (8.2)$$

(Gill, 1982)

where;

$g_c = 9.8$, a dimensionless constant numerically approximately equal to g

Hence by substituting in equation (8.1) we have;

$$Z = -\int_{p_0}^{p_z} \frac{1}{g_c \rho} \mathrm{dp} \qquad (8.3)$$

and integrating gives;

$$Z = \frac{p}{g_c \rho} \qquad (8.4)$$

where;

p is the pressure difference between the surface and the geoid.

The FRAM data set gives the pressure difference between the surface and the geoid for a 1/4° lat by 1/2° long grid for 24° to 79°S (720 by 220 grid points). Taking ρ as a constant of 1000 kg m^{-3} we have;

$$Z = \frac{p(\mathrm{FRAM}) \times 10^{-1}}{9.8 \times 10^{3}} \mathrm{gpm} \qquad (8.5)$$

where;

p(FRAM) is the FRAM output pressure in dyne cm^{-2}

(1 dyne cm^{-2} = 0.1 Pa)

The variation between Z and vertical height z is less than 1% for the sea surface (Gill, 1982) and so the dynamic height field output from FRAM can considered as a sea surface elevation field relative to the geoid and be compared with Geosat sea surface height data as well as hydrographic dynamic height calculations. In most published hydrographic data the dynamic heights are reported in units of dynamic metres (dyn m) where 1 gpm = 0.98 dyn m (see § 4.1.b).

The surface pressure field of the model is calculated from the surface pressure gradients using iterative approximations integrated from the southern ocean boundary. The pressure gradient field is determined from the velocity field, and hence the resultant dynamic height fields are relative to an absolute level of no motion. Unfortunately an error in the pressure calculation program of FRAM led to there being an error at long wavelengths (greater than 1000 km) in the surface pressure fields used in this study, most noticeably from the north to the south boundary. Errors in the iteration should not affect the field at mesoscales but may distort the basin scale features. There is also a bias to each surface pressure field as the pressure at the southern-most ocean grid point for each calculated field is set to a prescribed value during the integration (giving zero variability in the pressure fields here).

8.1 SAMPLING METHOD

The sampling method was kept as simple as possible to minimize the computational time required to extract data from the FRAM grid. A single Geosat orbit arc was sub-sampled every fifth point and plotted onto the FRAM grid. The nearest grid node to each of these Geosat data points was located (as shown in figure 8.1) and the relative x and y (long and lat) locations of the grid nodes were then found. The latitude and longitude of the data points for each FRAM track were found using this list of relative coordinates and a reference point. The longitude of each Geosat orbit arc at 24°S (to the nearest $^1/_2$°) was taken as the reference point for the corresponding FRAM track and data could then be extracted from the dynamic height fields along each required model track. During the extraction procedure, the surface pressure values were converted to dynamic heights using equation (8.5).

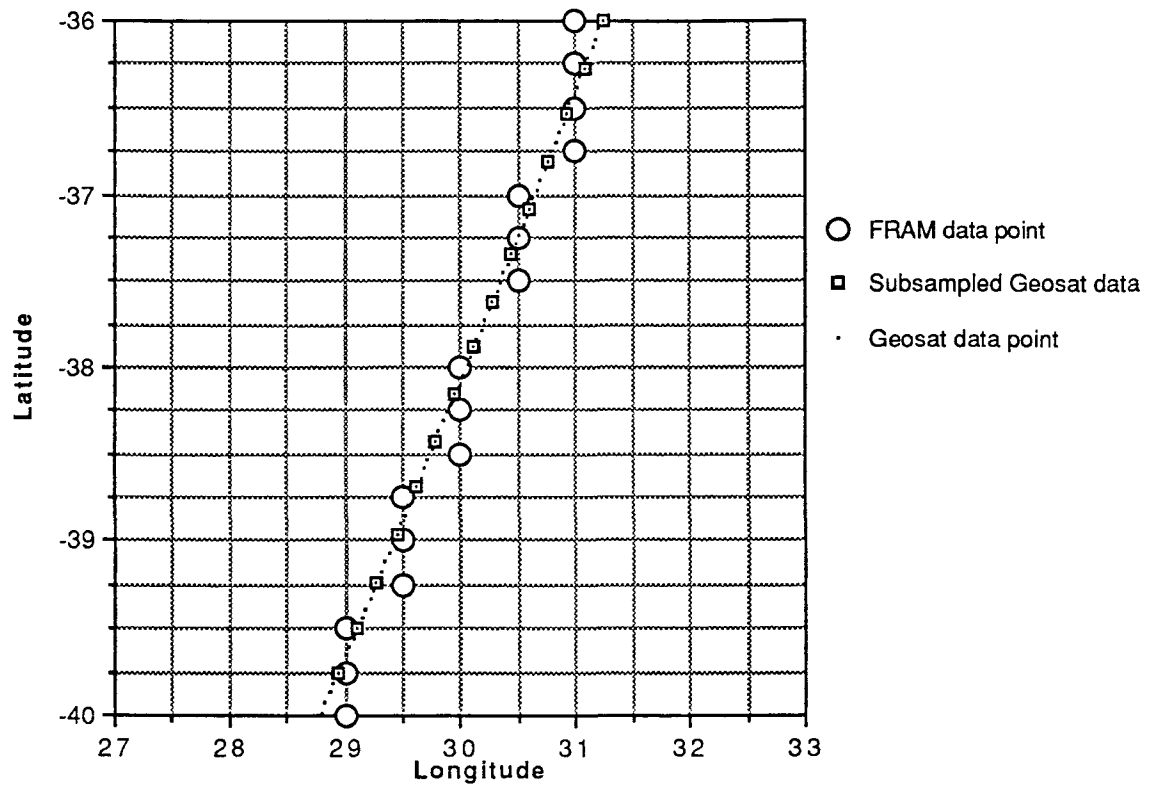

Figure 8.1 A Sample Geosat Orbit Arc and the Corresponding FRAM Data Points.

The FRAM pressure field was available once per calendar month of the model run for 44 months, from model day 3803 (1st June, year 11) to model day 5113 (1st January, year 15). This gave almost four years of data, at a sampling frequency of approximately 30 days, although the exact repeat varied from month to month. Ideally data would have been extracted every 17.05 days to give a sampling frequency as close as possible to that of Geosat, but the extra output from the model that this would have required was not possible.

The difference in sampling frequency and overall time of sampling will create differences between the FRAM and Geosat data sets. Any single mesoscale feature will have a greater influence on the mean under Geosat sampling as it will be sampled almost twice as often as in FRAM sampling. The longer time-scale of data from the model produces a mean which should resolve much longer time-scales of variability than is possible using the Geosat data and should also sample a larger number of mesoscale features. Over the total number of 'orbit repeats' (which is almost the same for both data sets) the overall effect of mesoscale features on the mean should be similar.

8.2 PROCESSING TECHNIQUES

All 'repeats' of a FRAM 'orbit arc' were appended to form a single file, equivalent to the files created from the Geosat GDR (see § 5.2), which was then processed using a collinear technique. As far as possible the FRAM data was processed in exactly the same way as the Geosat data, although some simplification was possible as no data points were ever absent, no quality control had to be carried out and no corrections for transmission path errors, barometric pressure loading or tides had to be applied.

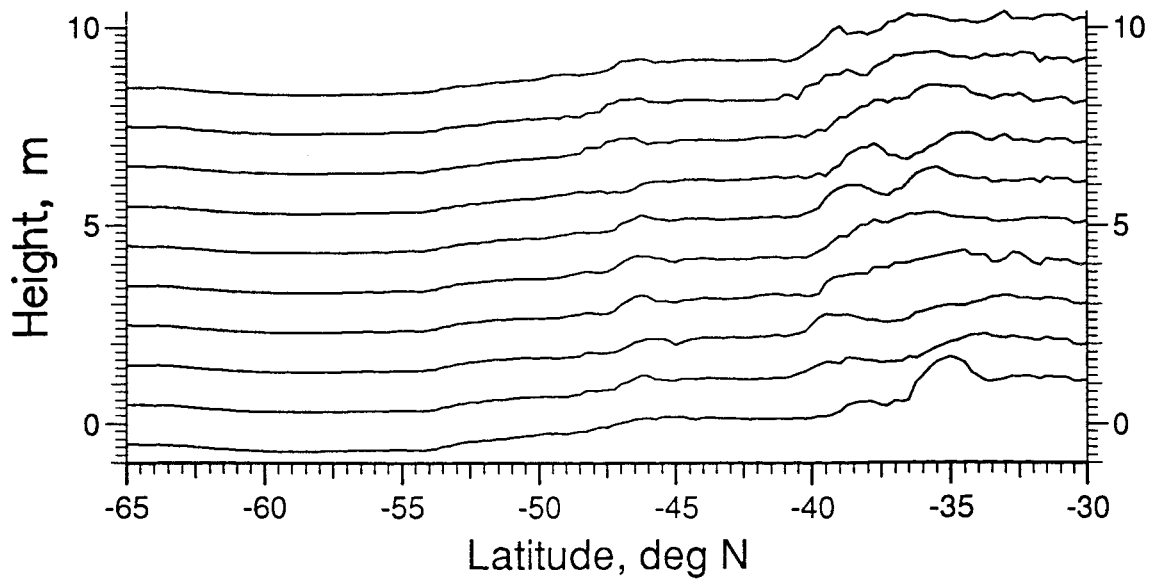

Figure 8.2 Ten Dynamic Height Profiles Along the FRAM Track which Corresponds to the Geosat Track shown in figure 2.6. Successive Repeats are Offset by 1 m.

The FRAM dynamic height fields give sea surface height relative to the geoid, not the reference ellipsoid of the Geosat data, and so the mean of all data tracks has a much smaller magnitude than that of the Geosat data and represents the mean current field. Figure 8.2 shows the raw dynamic heights obtained from one FRAM track. The signal is

caused by sea surface currents, together with the long wavelength error noted previously and with a constant bias introduced by the arbitrary choice of reference pressure level in calculating the surface pressure fields. These heights give an indication of the magnitude of the long wavelength current signal which is removed from Geosat data with the geoid, although this is underestimated due to the error in the FRAM pressure field calculation.

The FRAM data do not contain any orbit errors, but in order to compare the variability of the FRAM data with that from the Geosat data it was decided to carry out the quadratic 'orbit removal' of Geosat processing on each arc repeat to give an indication of the long wavelength errors remaining in the Geosat data due to imperfect orbit modelling. For similar reasons it was decided to include an iteration of the mean in processing the FRAM data.

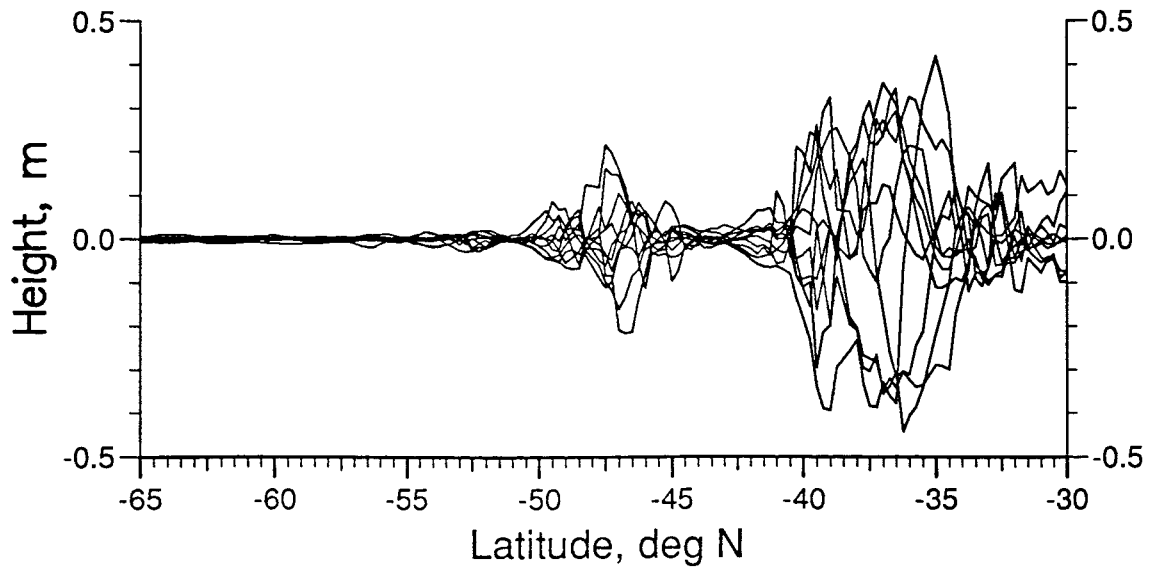

Figure 8.3 The Ten Profiles of Figure 8.2 after Removal of the Group Mean.

The orbit correction applied to FRAM data was found to have a maximum value of 12 cm, the largest change in the correction being of the order of 12 cm over the 5000 km track length. This 'correction' attempts to minimize along track variation of the data and so is modelling the long wavelength changes in surface dynamic height. This long wavelength variation can be seen most clearly in figure 8.3 where the height profiles have been overlain. At the southern end of the arc the dynamic heights have a standard deviation of less than 0.5 cm as all the pressure fields are integrated from the southern boundary where a surface pressure is prescribed. Moving north along the track the heights diverge and even where there appears to be little mesoscale activity the standard deviation of height increases to more than 5 cm. Much of this long wavelength variation is introduced by errors in the pressure field calculations. Removal of the repeat specific quadratic trends decreases the

standard deviation of heights at the northern end of the arc to the order of 2 cm but increases the variation along the rest of the arc by up to 3 cm s.d. (see figure 8.4). The effects of the orbit corrections are seen most clearly at the southern end of the arc where the heights converge at 60°S and then diverge to 65°S as the differences between removed quadratic curves increases at the extremes of the arc.

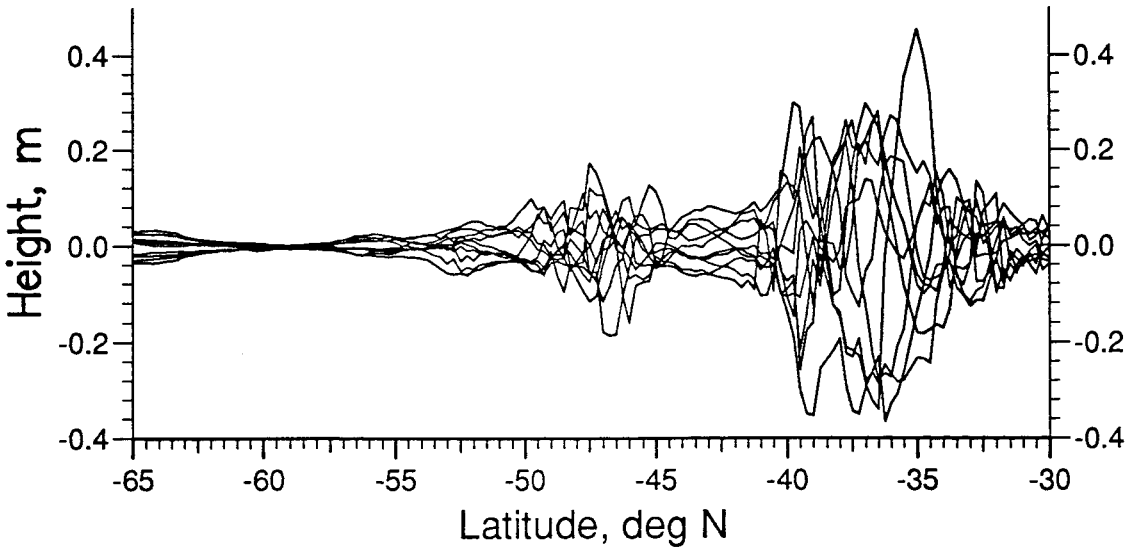

Figure 8.4 The Ten Profiles of Figure 8.3 after Removal of Repeat Specific Orbit Corrections.

Much of the introduced error is due to the effects of short wavelength signals on the quadratic correction. This correction aims to reduce the along track mean to a minimum and is influenced by signals at all length scales. Where mesoscale signals are concentrated in a small area of the track, as is common in the ocean where mesoscale activity is concentrated in areas of high currents, the result is a decrease in the peak variability and an increase in the variability in other sections of the arc. This effect has been calculated theoretically by LeTraon *et al* (1991) as introducing noise of up to 50% of the mesoscale signal when fitting a second degree polynomial to a track 2500 km in length which has homogeneous mesoscale variability along its length. This error is correlated to the mesoscale variability and always reduces the total rms, although as is seen here it may locally increase the variance when mesoscale variability is non-homogeneous along the track. The magnitude of these errors in the rms is not necessarily the same as those in the Geosat data as the model's long wavelength signal is much lower in amplitude than the orbit error of the Geosat data resulting in the orbit correction being more strongly influenced by the relatively large mesoscale signals. It is obvious, however, that the variability observed in the Geosat data will be underestimating the peak values whilst background levels will be artificially enhanced. The effects of the processing method on the model results will be discussed

The difference between the working mean and iterated mean for FRAM tracks was of the order of only 10^{-16} m (the order of the calculation accuracy) and so the iteration process had a negligible effect on the data, as expected. As the iteration was designed to correct for the effects of absent data on the mean curve and no data are absent from the model, no difference is expected between the two mean curves.

9 COMPARISONS OF FRAM DATA WITH OBSERVATIONS

Dynamic height data from the FRAM can be compared with both historical hydrographic data and the results of Geosat data analysis. Hydrographic data are never truly synoptic, usually collected within a region over a period of weeks, and where data from several cruises have been combined to give increased spatial coverage and/or resolution the resultant dynamic height anomaly fields represent a view of the current field of a region smoothed over space and time. The mean surface dynamic heights obtained from FRAM give a similar current field which has been used for comparisons with hydrographic data. It must be remembered that the FRAM data yield absolute surface pressures and hence absolute surface currents, whilst hydrographic data yield geostrophic velocities relative to some reference level. If flow at this reference level is not zero some discrepancy may occur between the two data sets even if the model is accurately predicting the current flow. Geosat data yield the variability of the sea surface elevation and so are compared to the variability of the FRAM surface dynamic height fields. Surface height variability from both data sets are absolute values and so discrepancies should only exist due to noise in the altimeter data or errors in the model currents.

9.1 THE AGULHAS REGION

The Agulhas area is the most eddy energetic region of the FRAM, eddies being shed from the Agulhas Retroflection approximately every 160 days and then drifting north-west into the Atlantic (The FRAM Group, 1991).

The mean FRAM dynamic height field has been calculated directly from the 44 once per month fields (figure 9.1) and shows a general slope from north to south, indicating broad easterly flow across the region. There is some indication of a weak cyclonic gyre across the full east-west extent of the region, the trough being centred along 60°S. The FRAM surface pressure field calculated at the end of year 6 of the model run (Webb *et al.*, 1991) shows this feature extending only as far as 30°E. The eastward extension of this trough seen in figure 9.1 is probably the result of a change in the method of calculating the surface pressure, the field shown in the FRAM Atlas (Webb *et al.*, 1991) being produced by a direct matrix inversion method, not the iterative method used to calculate the fields for this study (see chapter 8).

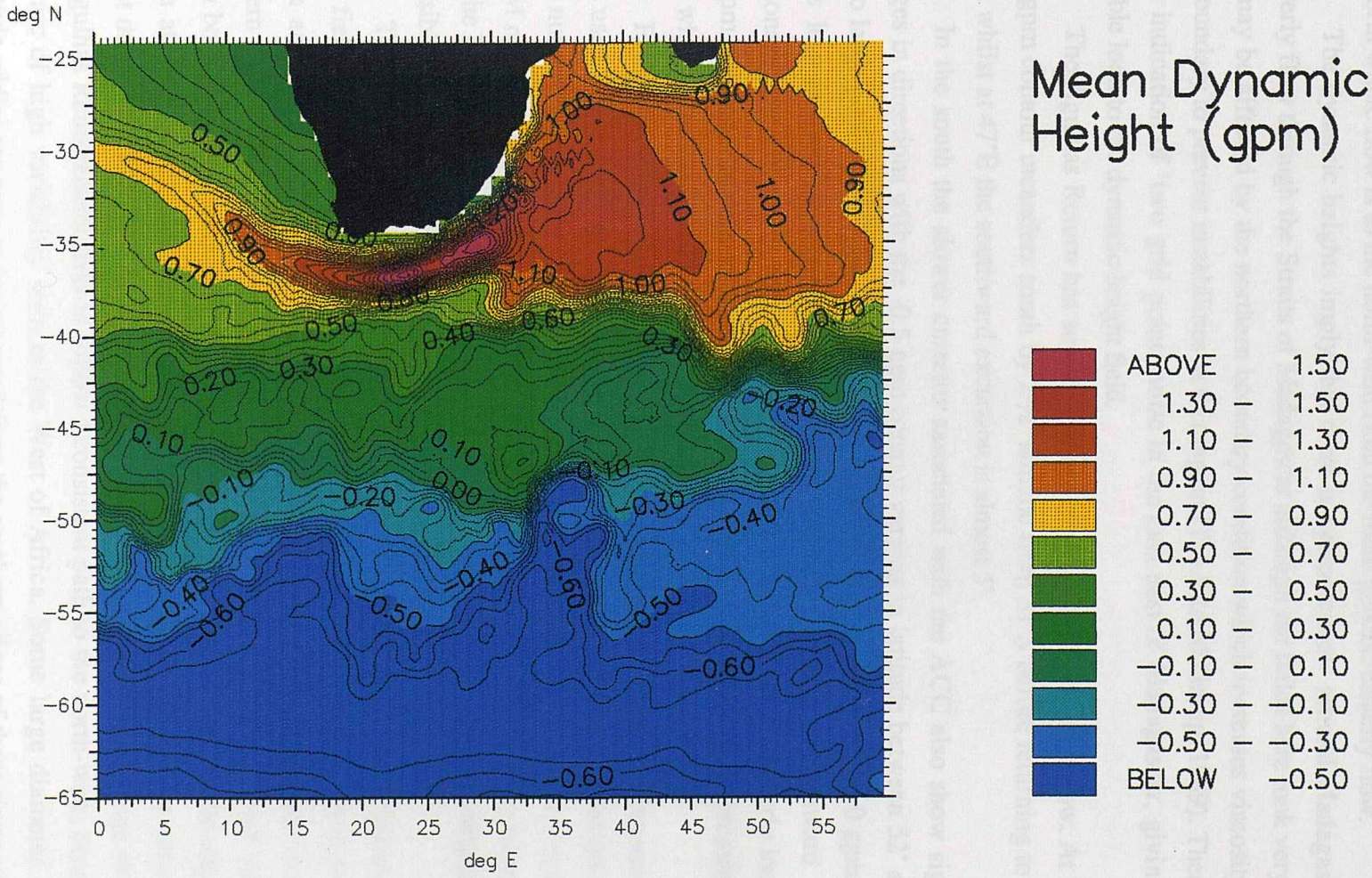

Figure 9.1 Mean Dynamic Height Field of the Agulhas Region from Four Years of FRAM Data.

The Agulhas Retroflection is represented by a narrow anticyclonic system, closed to the east by broad northerly flow, but with a westerly residual in the northern arm implying net surface transport of water from the Indian to the Atlantic Ocean. Currents are strongest in the Agulhas Retroflection, especially from 25° to 30°E, whilst to the west of Africa the area of high dynamic topography is restricted to a very narrow band separating an area to the north where flow is to the north-west from the more general easterly flow.

The dynamic heights imply that there is cyclonic flow around Madagascar with northerly flow through the Straits of Madagascar although the fields here look very smooth and may be affected by the northern boundary condition which increases viscosity near to the boundary to prevent instabilities in this region (The FRAM Group, 1989). There is also some indication of 'two grid point' noise in the data east of Madagascar, giving a very unstable look to the dynamic height field.

The Agulhas Return has several distinct 'meanders' in its mean flow. At 31°E the 0.85 gpm contour meanders south by 2½° latitude from 37°S before returning to 38°S by 35°E, whilst at 47°E the southward excursion is almost 5°.

In the south the slower currents associated with the ACC also show significant changes in directions with the -0.5 gpm contour varying in latitude between 52° and 58°S in two large northward loops. The slightly higher velocity core around the 0 gpm contour varies less in location, generally remaining close to 47°S with a northward velocity component near 7°E. From 40°E eastward, after meeting the second northerly loop of the 0.5 gpm contour, the core of the ACC steps northward, with velocity decreasing in the south whilst it intensifies to the north.

Figure 9.2 shows the rms variability of the four years of FRAM dynamic height fields used in this study (given in cm for ease of comparison with the Geosat data, 1 gpm being numerically equal to 1 m). This field is created from the rms variability found along FRAM model altimetry tracks (after processing as described in chapter 8) by interpolation onto the FRAM grid. By comparisons with the time series of model dynamic height fields it is possible to ascertain the cause of variability within the region.

The variability shows strong correlation with the higher velocity regions of the mean field, especially in the Agulhas Current system. The peak variability is just under 51 cm and occurs at 36.5°S 16°E within a narrow arc of high variability around the southern tip of Africa. To the west this arc bifurcates to form two arms of high variability which both reduce in intensity westward. The first extends north-west to the edge of the region at 30°S, where the variability is still more than 15 cm, whilst the second runs almost due west along 37°S and has reduced to less than 5 cm by 2°E. Rings shed from the Agulhas Retroflection tend to follow a consistent path to the north-west, creating the main arc of high variability seen to the West of Africa. Some large diameter but low amplitude eddies are seen to be spawned form the southern edges of these rings and move west to create the second arm.

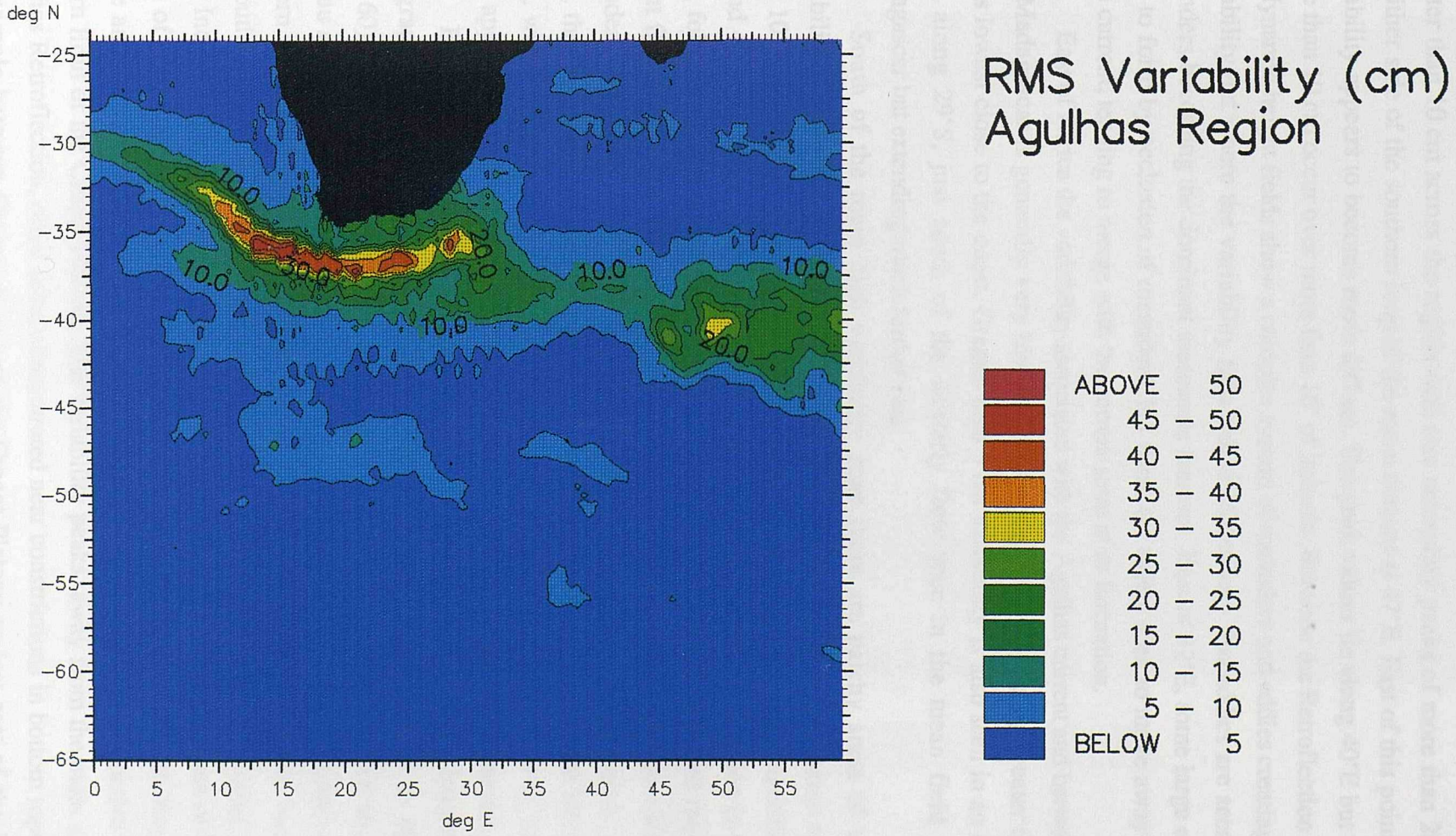

Figure 9.2 RMS Dynamic Height Variability of the Agulhas Region from Four Years of FRAM Data, as Determined Along Altimeter Tracks.

To the east the high variability continues along the axis of greatest mean current, showing the same changes in latitude noted previously for the mean field and remaining greater than 10 cm across the region with two secondary peaks of more than 20 cm rms on either side of the southern loop of the mean current at 47°E. East of this point the high variability appears to become more diffuse. The peak values lie along 40°E but values of more than 10 cm occur over more than 10° of latitude. Between the Retroflection and 33°E the dynamic height fields show a complex system of meanders and eddies creating the high variability but where the variability falls below 15 cm very few eddies are seen, current meanders becoming the dominant mesoscale features. East of 42°E, some large eddies are seen to form by occlusion of meanders, but these are rarely seen to move away from the main current, tending to merge with the current soon after formation.

East of Africa the variability associated with the Agulhas current and between Africa and Madagascar is generally very low and occurs patchily, only rarely greater than 5 cm but is lowest close to the coast. Greater than 5 cm variability is also seen in an east-west strip along 29°S, just south of the westerly flow seen in the mean field south of Madagascar but extending much further east.

South of the main high variability zone there are patchy areas of increased variability, although rarely more than 10 cm. The largest of these areas occurs near 47°S, from 10° to 30°E. At its western limit this area is linked to the main high variability zone around 40°S. This variability seems to be linked to the core of the ACC seen in the mean field, following the southerly bend in the current between 25° and 30°E and the dynamic height fields show that the variability is caused by changes in the exact location of this meander. East of the South West Indian Ridge two smaller patches of increased variability exist, the larger, to the north, is closely linked to the northerly loop of the ACC seen at 36°E, whilst the smaller is at the southern extent of this loop, at 55°S 38°E. These two areas appear to be caused by the formation of small amplitude eddies by the model.

Both the mean and variability fields show a high degree of influence from the model topography (figure 9.3, topographic features are named in the overlay to figure 6.5, page 60). After retroflection the main Agulhas Return Current flows north of the Agulhas Plateau and then turns south along the Plateau edge before being deflected north along the western slope of the Mozambique Plateau to form the loop mentioned above. Further east the southward deflection of the Return Current occurs immediately after crossing the South West Indian Ridge via the Indomed Fracture Zone. Similarly the deflections of the ACC south of 45°S appear to be closely coupled to the topography of the South West Indian Ridge and the northward shift of the ACC east of 45°E seems to be associated with the eastern limit of the Crozet Plateau. The variability peaks, away from the main arc of the Agulhas Retroflection, often seem concentrated near constrictions in bottom topography, for example between Conrad Rise and the Crozet Plateau or just east of the Indomed Fracture Zone.

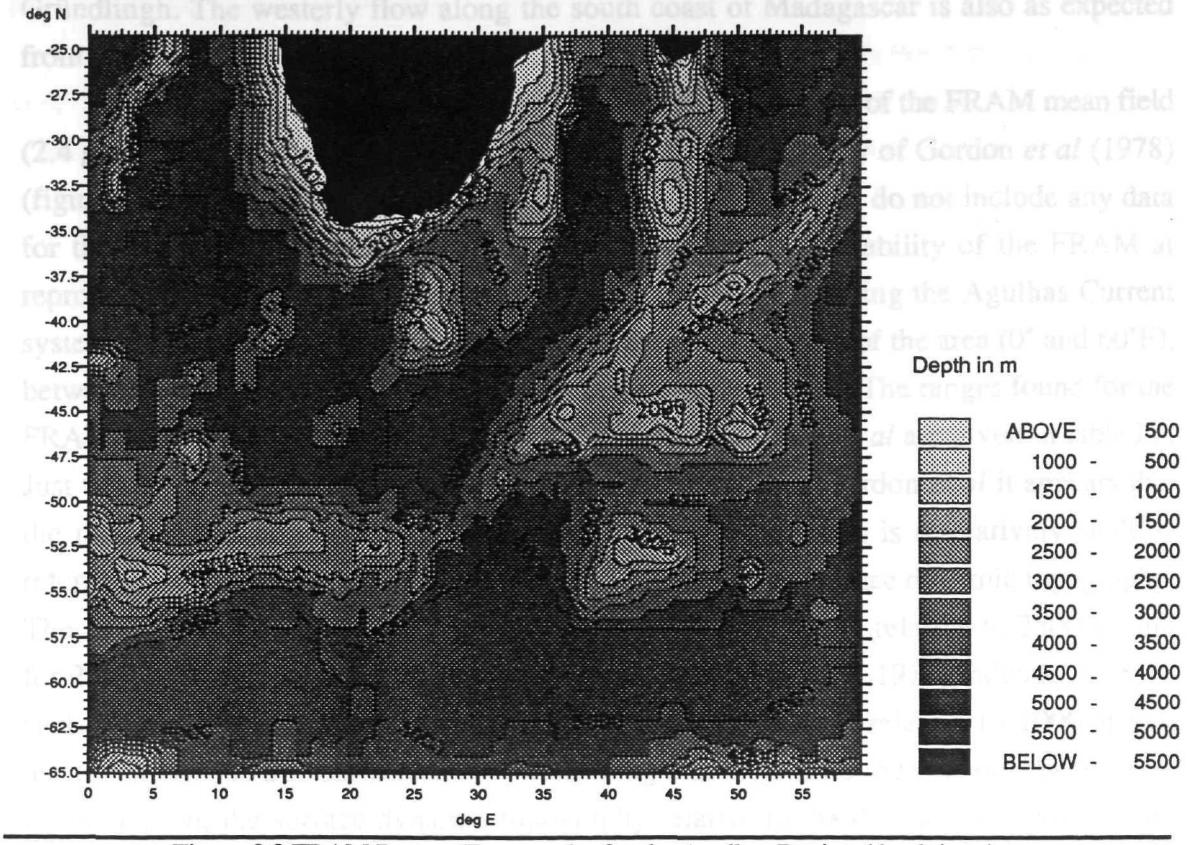

Figure 9.3 FRAM Bottom Topography for the Agulhas Region (depth in m).

9.1.a Comparisons with Ground Truth Data

The general form of the FRAM mean dynamic height field is consistent with historical hydrographic information in the Agulhas region, all the expected current systems being represented in the data. The locations of currents seen within the Agulhas System in the FRAM data are consistent with positions determined by Gründlingh (1978) using satellite-tracked drifting buoys although the extension of high dynamic topography into the Atlantic is not as expected, the Retroflection appearing to be located too far west and south in the mean FRAM field but using the time series of model fields it can be seen that this apparent position of the retroflection is caused by the anticyclonic Agulhas Rings. As mentioned previously these eddies tend to follow a consistent track, around the southern tip of Africa and to the north-west into the Atlantic, and so the mean dynamic height along this track is also high. From the synoptic pressure fields it is apparent that these eddies are being created between 25 and 30°E in the model, which locates the retroflection much further east than observed in nature, as noted by Lutjeharms *et al* (1991).

Within the Agulhas Return Current, the deflection of flow to the north of the Agulhas Plateau with a downstream southerly loop is consistent with the findings of Darbyshire (1972) looking at an easterly flow over the Plateau as well as those of

Gründlingh. The westerly flow along the south coast of Madagascar is also as expected from satellite-tracked drifters (Lutjeharms *et al*, 1981).

The range of dynamic height (maximum height difference) of the FRAM mean field (2.4 gpm) is larger than the range in surface dynamic topography of Gordon *et al* (1978) (figure 4.1) for the same region (1.4 gpm) although Gordon *et al* do not include any data for the Agulhas Retroflection. A much better indicator of the ability of the FRAM at reproducing the average dynamic height field is gained by avoiding the Agulhas Current system and looking at the height range at the west and east limits of the area (0° and 60°E), between 40° and 65° S where there is the best hydrographic data. The ranges found for the FRAM mean field and all the depth intervals given by Gordon *et al* are given in table IV. Just taking the surface to a 1000 m reference level data from Gordon *et al* it appears that the model is slightly over-estimating the easterly current. This is a relatively shallow reference level however and may underestimate the absolute surface dynamic topography. The similarity of the dynamic height anomaly fields for 1000 m relative to 2500 m, and for 2500 m relative to 4000 m, to the surface field (Gordon *et al*, 1978) indicates that the surface currents continue to great depth and the surface field relative to 1000 m will underestimate the true surface current. Assuming that there is no reversal of flow at depth in this region, the surface dynamic topography relative to 4000 m should give a closer estimate of the true surface dynamic height. This poses problems as the 4000 m level is not continuous and also because errors in the dynamic height anomalies increase with the depth of integration, as currents decrease with depth. However from table IV it appears that the model actually under-estimates the true surface dynamic height anomaly by the order of 0.6 gpm over 25° of latitude. This may be explained by the long wavelength error introduced into the pressure field calculation as noted previously.

Longitude	Gordon *et al* (1978) Hydrographic Data				FRAM data
	surface relative to 1000 m	1000 m relative to 2500 m	2500 m relative to 4000 m	surface relative to 4000 m	surface dynamic height
0°E	0.9	0.45	0.3	1.65	1.2
60°E	1.25	0.4	0.2	1.75	1.2

Table IV Dynamic Height Ranges From 40° to 65°S for Historical Hydrographic and FRAM Data (gpm).

9.1.b Comparisons With Geosat Data

The FRAM data can be compared with the results obtained from the Geosat data in two ways. The first is to compare the general distribution of variability within a region by using the rms height variability fields. For a more specific comparison the rms curves for individual tracks can be compared.

(1) RMS Variability Fields

In general the distribution of high and low variability within the Agulhas region is very similar for the two data sets (figures 6.3 and 9.2). For both sets there is an east-west oriented band of high variability south of Africa, high variability east of Africa and south of Madagascar and patchy moderate variability south of 45°S. Figure 9.4 shows the difference between the two variability fields and over much of the region the Geosat value is approximately 5 cm greater than that from FRAM. This is as expected from the Geosat data which appeared to have a noise level of 5 or 6 cm rms. However, there are some marked differences in both the intensity and distribution of the variability between the data sets, as shown by the difference plot (figure 9.4).

The peak variability obtained from the FRAM data is of similar magnitude to that from the Geosat data but occurs some 3° north and 10° west of the Geosat peak. The FRAM peak value exists within a broad band with variability above background level, which extends from the African coast to 41°S. A similar band is seen in the Geosat data, but reaching to almost 43°S and with maximum values occurring further south and over a wider band than in the FRAM data. Within the northern part of this high variability band, west of 35°E, FRAM over-estimates variability by up to 31 cm rms as seen in figure 9.4, but just south, near 40°S, the model underestimates by more than 40 cm rms, much greater than the noise level of the Geosat data. This apparent intensification and constriction of variability is seen most clearly to the west of the region, where FRAM data shows a band of high variability extending to the western edge of the region with only one divergent path, as described previously. The Geosat data yields much lower rms variability but spread in a fan shaped zone to the west and not extending past 5°E. It is possible that much of this difference may be due to differences between the model topography and real topography, as discussed below.

Close to the southern coast of Africa there is an apparent variability over-estimate of almost 15 cm by the model. This is unlikely to represent a true over-estimate, but is more likely to be due to the small number of Geosat data points which exist close to land as the altimeter often lost lock after leaving land. If only a few repeats are present, the resultant rms variability may be artificially decreased. This difference may be enhanced by the effects of the orbit correction at the ends of the FRAM tracks (as discussed in the following chapter).

East of Africa the high variability zones of the two data sets are very similar in location until 50°E where the Geosat variability moves southward whilst the core of FRAM variability continues eastwards. Here however the spread of variability is similar, only the relative location of the highest variability within the band is different, being further south in Geosat data than in FRAM data.

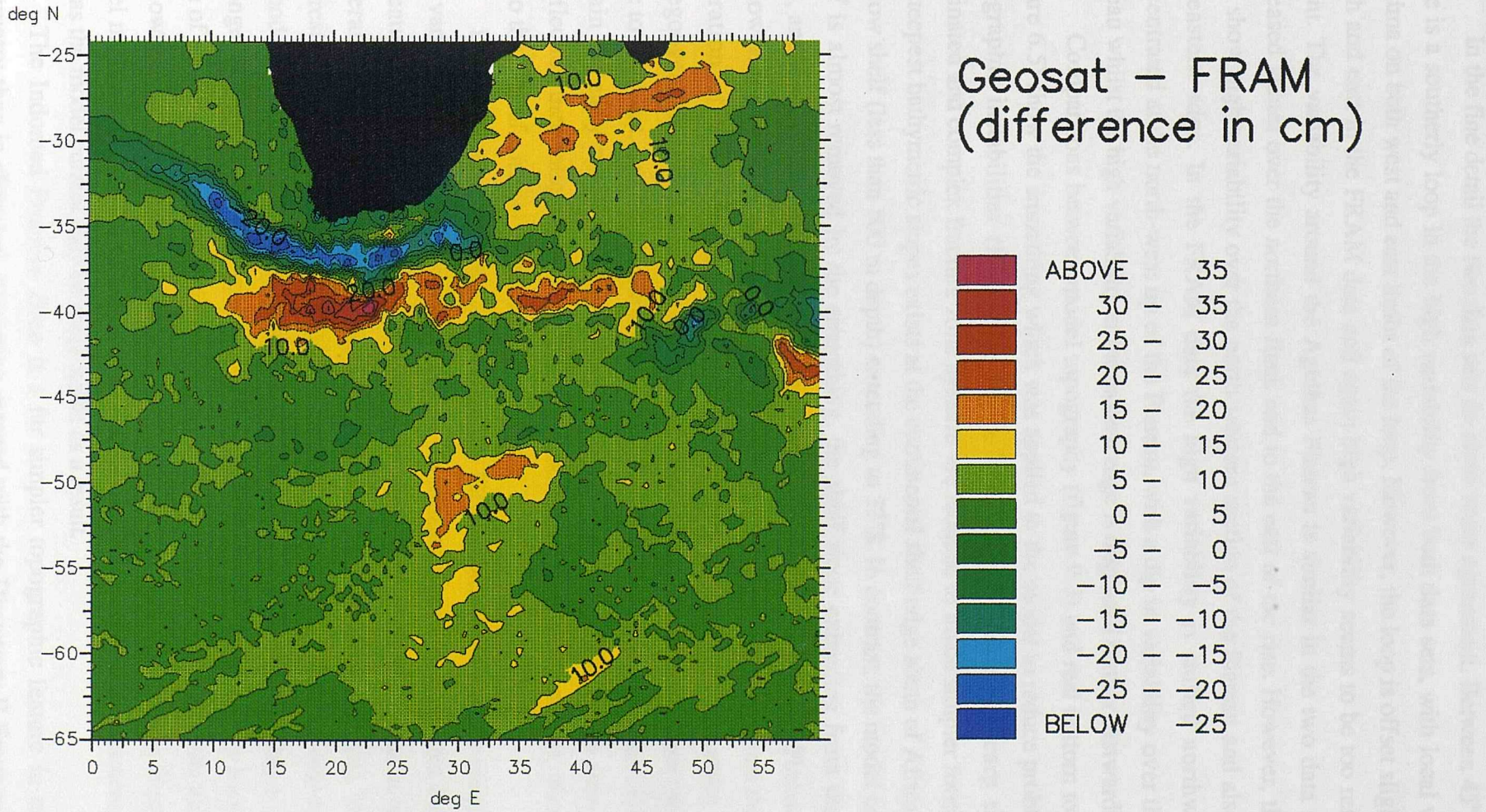

Figure 9.4 The Difference Between Height Variability Obtained from Two Years of Geosat Data and that from Four Years of FRAM Data for the Agulhas Region.

In the fine detail the two data sets do show some agreement. Between 45° and 50°E there is a southerly loop in the high variability from both data sets, with local variability maxima on both west and east limbs of the loop. However, the loop is offset slightly to the south and east in the FRAM data and again high variability seems to be too restricted in extent. The variability around the Agulhas Plateau is similar in the two data sets, with increased values over the northern flank and to the east of the rise. However, the Geosat data show high variability over the north-western section of the Plateau and also close to the eastern edge. In the FRAM data the high variability is shifted northwards and concentrated at the north-west tip of the Plateau, with a dip in variability over the eastern Plateau whilst the high variability at the eastern edge is displaced further eastwards.

Comparisons between model topography (figure 9.3) and real bottom topography (figure 6.5) show the smoothing which was applied to the model to reduce problems with topographic instabilities (Killworth, 1987). The result is that steep scarp slopes are eliminated and complex fracture zone systems are reduced to much simpler forms. One of the steepest bathymetric slopes exists at the continental shelf edge south of Africa, with the shallow shelf (less than 500 m depth) extending to 37°S. In contrast, the model continental shelf is almost removed by the smoothing, the shelf slope extending from the coast to 38°S, and the deep channel between the continental shelf and the Agulhas Plateau is made shallower. It is believed that the shelf edge geometry is a strong influence on the point of separation of the Agulhas Current from the African coast (Lutjeharms and van Ballegooyen, 1984) and hence on the point of retroflection. The much deeper model water close to the coast, combined with the creation of a 'col' north of the Agulhas Plateau, may explain the early retroflection of the model Agulhas Current. The Rings formed at the retroflection then follow a path much further north than observed in reality, possibly also due to the lack of a model continental shelf.

Downstream of the Agulhas Plateau the FRAM data show a fairly simple step of high variability, skirting the southern limit of the Mozambique Plateau. In the Geosat data the features in this area are more complex, showing several peaks of variability within the moderate variability path. Although located in a very similar position, the model underestimates variability determined from Geosat data by up to 20 cm in this area. With the model retroflection occurring further north and east than observed the Return Current is no longer incident on the western flank of the Agulhas Plateau but is already located to the north of the rise and hence no northward deflection of the Return exists across the Plateau. The lower degree of interaction between the Return Current and the Agulhas Plateau in the model may account for the lower surface height variability observed downstream of the Rise as the model current may be more stable as a result.

The Indomed Fracture Zone is a far simpler topographic feature in the model bathymetry than is observed, becoming merged with the Discovery II Fracture Zone to form a broad gap in the South West Indian Ridge near 45°E. This appears to allow the

Return Current to flow too far south in the model resulting in the a more southerly location for variability as noted previously.

More noticeable differences occur in the variability associated with the ACC, the patchy variability of the model being very poorly correlated with that of the Geosat data. West of the Southwest Indian Ridge, the FRAM data shows moderate variability, seeming to connect with the Agulhas variability zone around 12°E. Here Geosat variability is only slightly above background levels, the point of closest connection between the the two high variability zones occurring nearer 25°S, just south of the Agulhas Plateau. Where the peak of Geosat variability occurs, in the Prince Edward Fracture Zone, the FRAM data show little variability and not until 35°E, north-west of Conrad Rise do the two data sets begin to show any similarity.

A simplification of the model topography is seen where the ACC crosses the South West Indian Ridge via the Prince Edward Fracture Zone, with smoothing of the gap and loss of complex topography on the Ridge north of the fracture zone. The much lower variability observed in the model data for this region may be due to this simple topography allowing the ACC to follow a consistent path through the gap, with little interaction to induce instabilities in the flow.

(2) RMS Variability Along Specific Tracks

In order to determine how the distribution of variability differed between the FRAM and Geosat data sets the along track variability of several extracted tracks were compared. One such track, shown in figure 9.5, begins close to the west coast of Africa at 30°S and crosses the high variability area west of the Agulhas Retroflection. Comparison of the two variability curves clearly shows some of the differences noted between the variability fields.

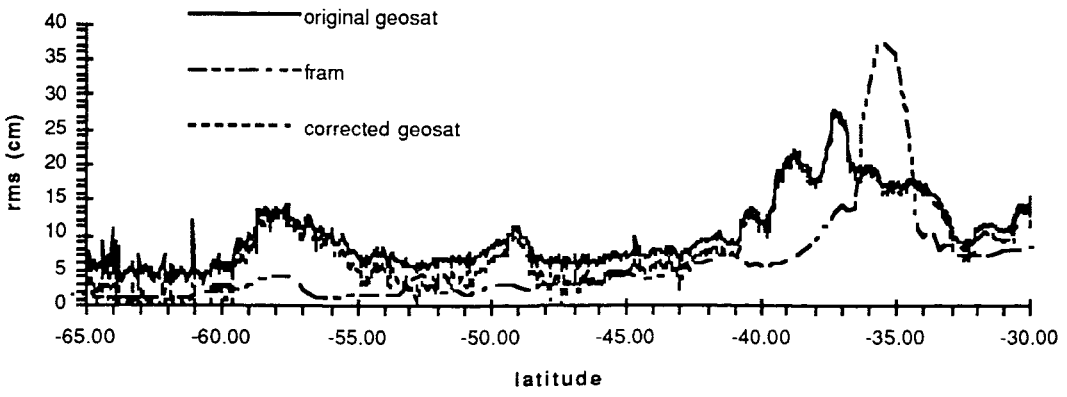

Figure 9.5 RMS Height Variability Along an Altimeter Track as Determined from Geosat and FRAM Data.

South of 41°S the two curves show very good agreement in the location of the the variability peaks, at 58° and 49°S, and the increase in variability from 48° to 41°S is closely

matched. The FRAM variability peaks, however, are of much lower amplitude and shorter wavelength than those seen in the Geosat data and there is a small peak at 53°S in the FRAM data which is more than a degree north of that seen in the Geosat curve. North of 41°S the agreement between the two curves is much poorer. The maximum rms value of the FRAM track is almost 10 cm higher than that of the Geosat data, but there is a much narrower distribution of the variability, which forms a simple peak. Also the location of the maximum value is offset by almost 2° latitude to the north in the FRAM data.

To discover if the FRAM data was over-estimating the total variability in this area, the variances along the two tracks were compared. For the FRAM data the average variance from 30° to 45°S (covering the peak values for both tracks) was 179.5 cm^2 (13.4 cm rms), but for the same section of the Geosat track (the 'original Geosat' curve of figure 9.5) the value obtained was 223 cm^2 (14.9 cm rms) implying a significant under-estimate of variance by the FRAM data. However, for the calmest region along this track (60° to 65°S) Geosat variance was an average of 27 cm^2 (5.2 cm rms) greater than that of FRAM. If this value is assumed to be the noise of the Geosat data and this noise is assumed independant of the signal, then all Geosat variance values can be reduced by this amount to give the corrected curve of figure 9.5. This reduces the average Geosat variance between 30° and 45°S to only 192 cm^2 (13.9 cm rms), much closer to the FRAM value. This estimate of Geosat noise is probably too high, including some true oceanic variability not reproduced by the model.

Similar comparisons were carried out for other tracks in the region with similar results. In general the FRAM data south of 45°S, in the lower variability areas, had variability peaks in the same locations as those of the Geosat data, but with much lower amplitudes and wavelengths. In the highest variability areas the FRAM peaks were usually of a similar magnitude to those of Geosat, or sometimes higher, but with very restricted extent. This would seem to confirm that the FRAM is reproducing the total variance of some more energetic parts of this region to a reasonable degree, but that this variability is being concentrated in limited latitudinal ranges where it becomes intensified beyond levels seen in the real ocean.

9.2 THE CENTRAL SOUTH PACIFIC

The Central South Pacific is a much quieter dynamic region than the Agulhas and surface height signals are much smaller. Figure 9.6 shows the mean dynamic height field from the FRAM data overlain by the model topography contours. The total dynamic height range is just over 1.5 gpm compared to more than 2 gpm for the Agulhas region. There is a general north-south slope in the data indicating eastward flow, but there is a distinct trough along 35°S which implies the presence of a cyclonic gyre. This trough is most pronounced at the eastern and western limits of the area.

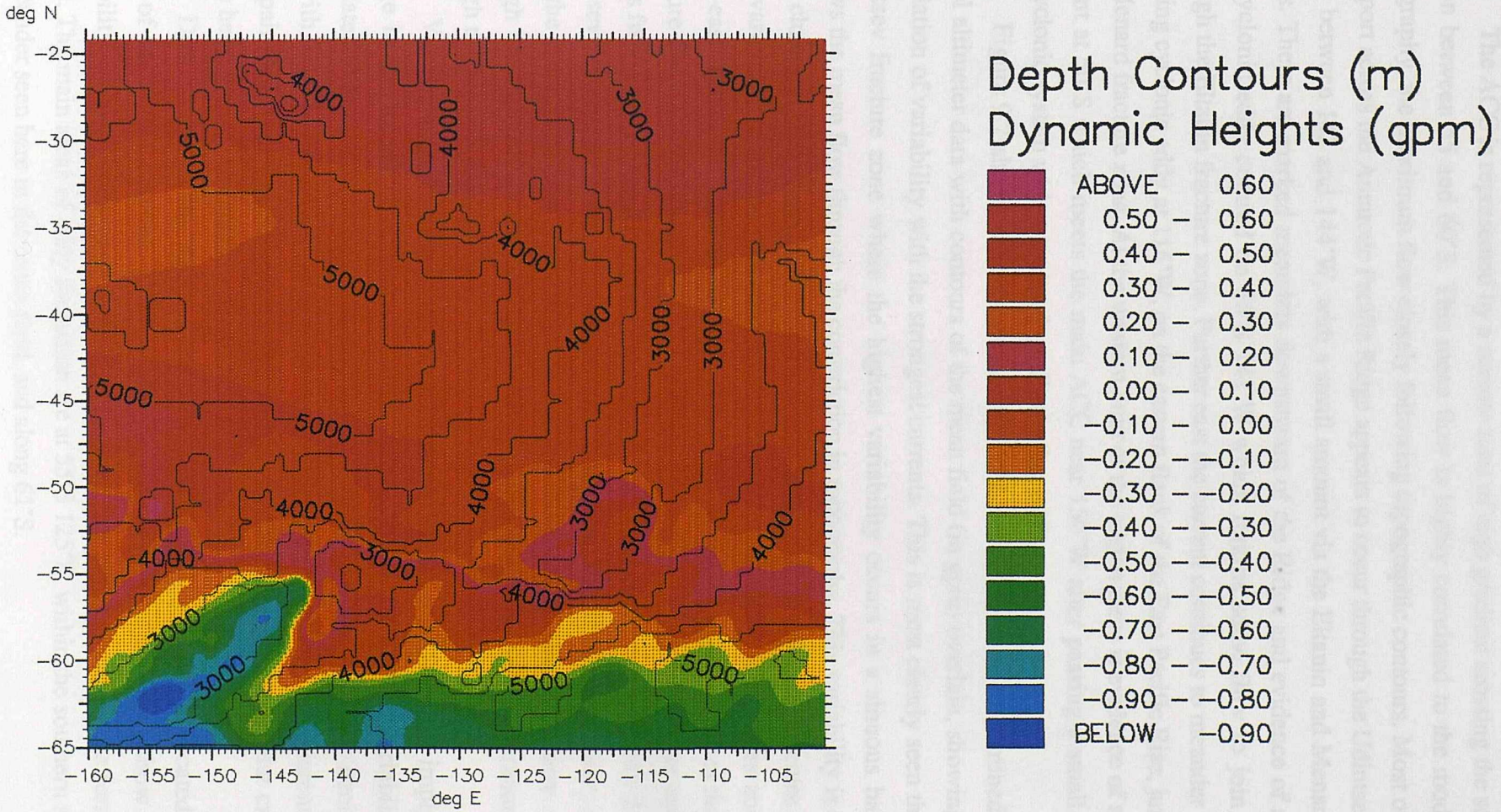

Figure 9.6 Mean Dynamic Height Field of the Central South Pacific from Four Years of FRAM Data with Model Depth Contours.

The ACC is represented by a narrow zone of high gradient crossing the south of the region between 55 and 60°S. This mean flow is highly correlated to the model bottom topography, the maximum flow closely following topographic contours. Most of the ACC transport across the Antarctic Pacific Ridge appears to occur through the Udintsev Fracture Zone between 142 and 144°W, with a small amount via the Eltanin and Menard fracture zones. There are marked meanders downstream of the Ridge and evidence of a standing anticyclonic eddy centred on 56°S 141°W which returns some flow to join with that through the Eltanin fracture zone. Further east the current continues to meander forming a standing cyclonic eddy at 116°W, on the eastern flank of the East Pacific Rise, just south of the Menard fracture zone. At the western limit of the region there is evidence of an easterly current at 50°S which meets the main ACC near 150°W after passing a small cyclonic-anticyclonic system with associated small standing eddies.

Figure 9.7 shows the rms variability field of the region as determined from the model altimeter data with contours of the mean field (in gpm) overlain, showing the high correlation of variability with the strongest currents. This is most clearly seen through the Udintsev fracture zone where the highest variability occurs in a sinuous band which follows the mean flow through the constriction in topography. This variability is caused by small changes in the location of the current core as it passes through the fracture zone. The peak variability of just over 19 cm rms occurs just south-east of the fracture zone, on the south-east limb of the standing eddy mentioned previously. By examination of the synoptic pressure fields it can be seen that this standing eddy spawns many irregular anticyclonic eddies from its southern edge which tend to move away to the east. Variability through the Udintsev fracture zone is much greater than through the Eltanin fracture zone, consistent with the mean flow being much lower through this more northerly fracture zone than through the Udintsev. Very little variability is associated with the small amount of flow through the Menard fracture zone.

Variability to the west of the Eltanin fracture zone is relatively low, implying little change in the location and strength of the current here, the highest variability being associated with the strong current along the western slope of the Antarctic-Pacific Ridge and with loops in the current which joins the ACC from the north. The apparent standing eddy pair observed in this northerly branch of the ACC is due to the regular creation of eddies here, seen in the dynamic height fields.

Downstream of the Ridge, the patchy high variability is still co-located with the areas of maximum current. The dynamic height fields of the region show that this variability is caused both by movement of the main current axes and by the formation of eddies. The main areas of eddy formation are at 55°S 125°E, within the southern section of the meander seen here in the mean field, and along 61°S.

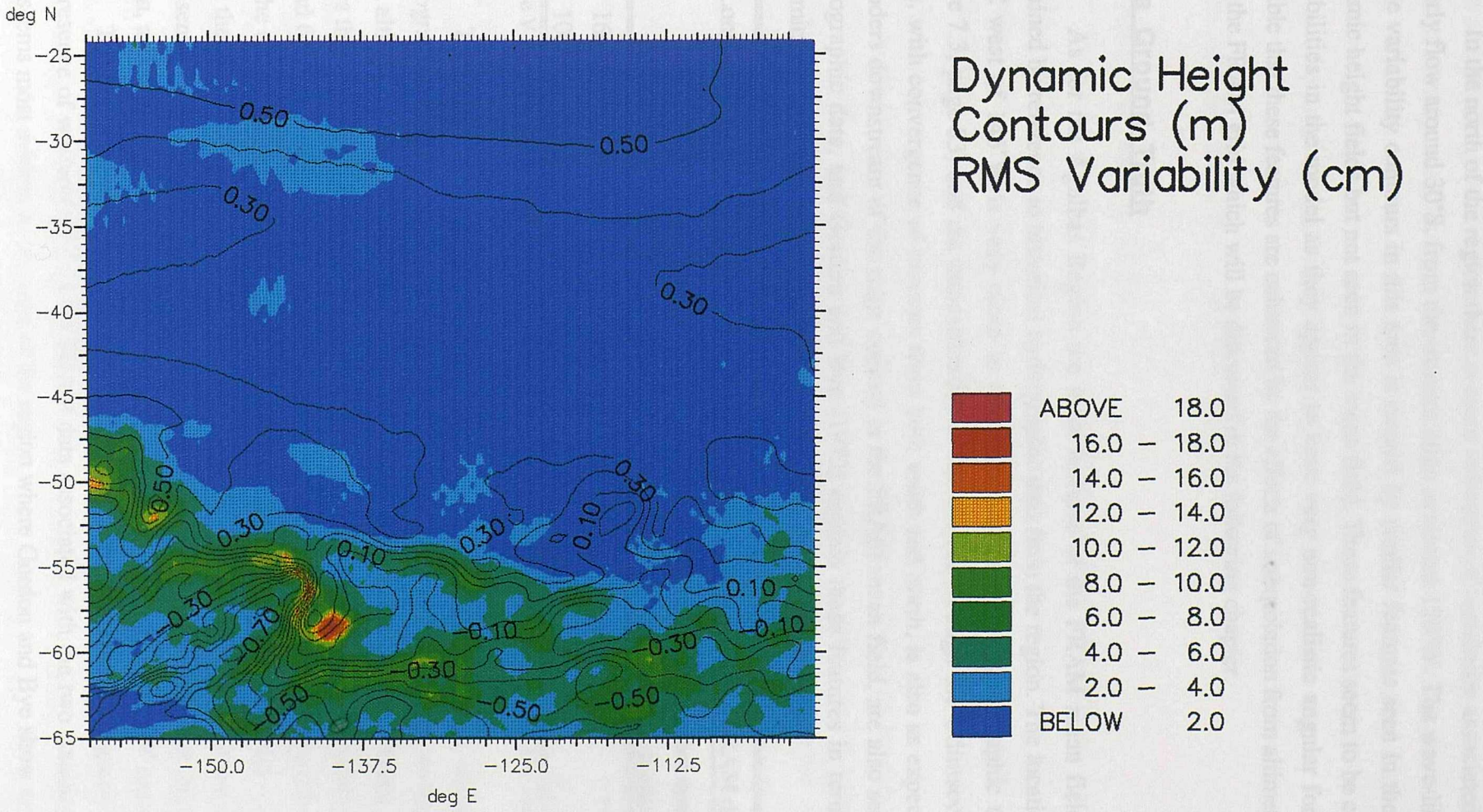

Figure 9.7 RMS Dynamic Height Variability of the Central South Pacific from Four Years of FRAM Data as Determined Along Altimetric Tracks with Mean Dynamic Height Contours.

In the north of the region there is some indication of variability associated with the easterly flow around 30°S, from the western edge to almost 130°W. The wave-like nature of the variability contours in this area is caused by similar features seen in the original dynamic height fields but not seen in the mean field. These features seem to be caused by instabilities in the model as they appear to have very non-realistic angular forms. It is possible that these features are enhanced by the effects of interpolation from altimetry tracks onto the FRAM grid which will be discussed in the following chapter.

9.2.a Ground Truth

As for the Agulhas Region the main features of the FRAM mean field can be explained by reference to historical hydrographic data from the region. The location of the ACC west of 145°W is very close to that expected from the hydrographic data (see figure 7.3, page 83) and the intensification of the current through the Udintsev fracture Zone, with convergence of currents from both south and north, is also as expected. The meanders downstream of the ridge noticed in the FRAM mean field, are also seen in the hydrographic data, and Gordon and Bye (1972) explain these features in terms of the dynamics of flow over topography.

Longitude	Gordon *et al* (1978) Hydrographic Data				FRAM data
	surface relative to 1000 m	1000 m relative to 2500 m	2500 m relative to 4000 m	surface relative to 4000 m	surface dynamic height
160°W	0.95	0.6	0.25	1.8	1.15
100°W	0.7	0.4	0.25	1.55	0.8

Table V Dynamic Height Ranges From 40° to 65°S for Historical Hydrographic and FRAM Data (gpm).

The long wavelength features of the mean FRAM field are not supported by hydrographic data, the dynamic heights of Gordon and Bye (1972) showing no trough near 35°S although they do show very small height gradients north of 50°S. Table V above shows that in this region the FRAM data underestimates the dynamic height slope between 40 and 64°S by a similar value to that obtained in the Agulhas Region. This tends to imply that the underestimate is due to the long wavelength errors in the pressure field calculation. With the much lower current signals in this region it is also possible to see the east-west representation of the error which seems to be greatest at the east and west limits of the region, and least near 130°W, giving a wavelength for the error of at least 60° east-west.

The major difference between the mean FRAM field and the hydrographic field is the presence of westerly flow in the FRAM data associated with the two standing eddies. This seems most evident in the west of the region where Gordon and Bye show continuous easterly transport with a very small northward current component forming the meanders, but the FRAM shows much greater north-south excursions in the flow. This may be the

result of the hydrographic data being smoothed spatially in comparison to that from FRAM and hence losing detail. In the FRAM data, flow through the Menard fracture zone appears to be very weak and this may explain the occurrence of the standing eddy, with the westward flow which occurs in the lee of the topography being only weakly opposed by eastward flow through gaps in the topography.

9.2.b Comparison with Geosat Data

(1) RMS Variability Field

Figure 9.8 shows the difference between the variability obtained from four years of FRAM data (figure 9.7) and that from two years of Geosat data (figure 7.2). Over the majority of the region, the difference in rms variability is between 4 and 6 cm indicating that the Geosat data has the same level of background noise in this region as in the Agulhas region.

As in the Agulhas region there are some large discrepancies between the two variability fields, although the magnitude of the differences is much smaller, reflecting the much lower signals of this region. The greatest differences occur where the variability values found in the two data sets are highest, and as in the Agulhas region the areas of over-estimate and under-estimate by the FRAM data form distinct regions.

The peak variability observed in the FRAM data is more than 10 cm greater than variability of the Geosat data at the same location and the model over-estimates variability for most of the area immediately south of the Udintsev fracture zone. East and north of the fracture zone, where Geosat shows high variability, the model under-estimates this variability by up to 16 cm. There is evidence of increased variability in the Geosat data along the western flank of the Antarctic-Pacific Ridge and to the north of the ridge near 50°S, as seen in the FRAM data, but this is over-estimated by the model, whilst variability near the entrance of the Udintsev fracture zone (145°W) is under-estimated.

The differences in the variability fields can be correlated with the differences noted between the mean FRAM field and hydrographic data. The strong model variability associated with the standing eddy and large southward meander east of the Udintsev fracture zone is much greater than that seen in the Geosat data and may be caused by erroneously large velocities in this area.

A comparison between the model topography (figure 9.6) and real topography (figure 7.2) for the region shows that there is significant smoothing of the fracture zones in the model field, especially around the 3500 m depth contour. The Udintsev fracture zone is made broader and smoother whilst the Eltanin fracture zone is changed such that the deepest part of the fracture is oriented north-south rather than east-west. The interaction of flow through the two fracture zone systems, especially just before and after crossing the ridge crest, and possible changes in the division of flow with time may explain the

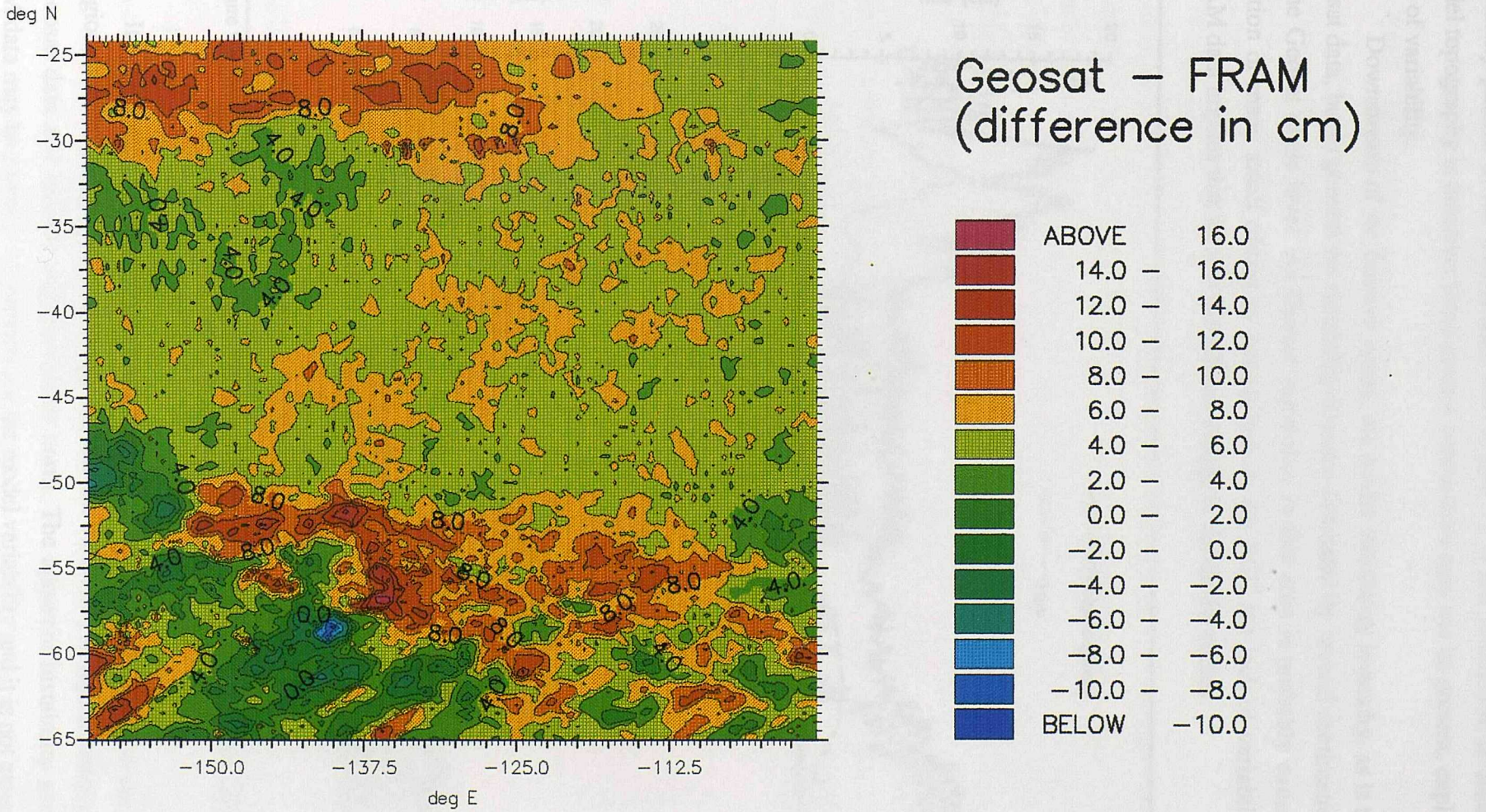

Figure 9.8 The Difference Between Height Variability Obtained from Two Years of Geosat Data and that from Four Years of FRAM Data for the Central South Pacific.

variability pattern of the Geosat data (see chapter 7). If the interaction of flow with the model topography is incorrect these current interactions may not be present, explaining the lack of variability.

Downstream of the fracture zones, the model variability is patchy, as is that of the Geosat data, but in general the variability is under-estimated by several centimetres relative to the Geosat noise level. As Geosat variability in this area is probably caused by the creation of many small eddies by instabilities in the ACC the lack of variability in the FRAM data implies that there is insufficient energy in the model eddies.

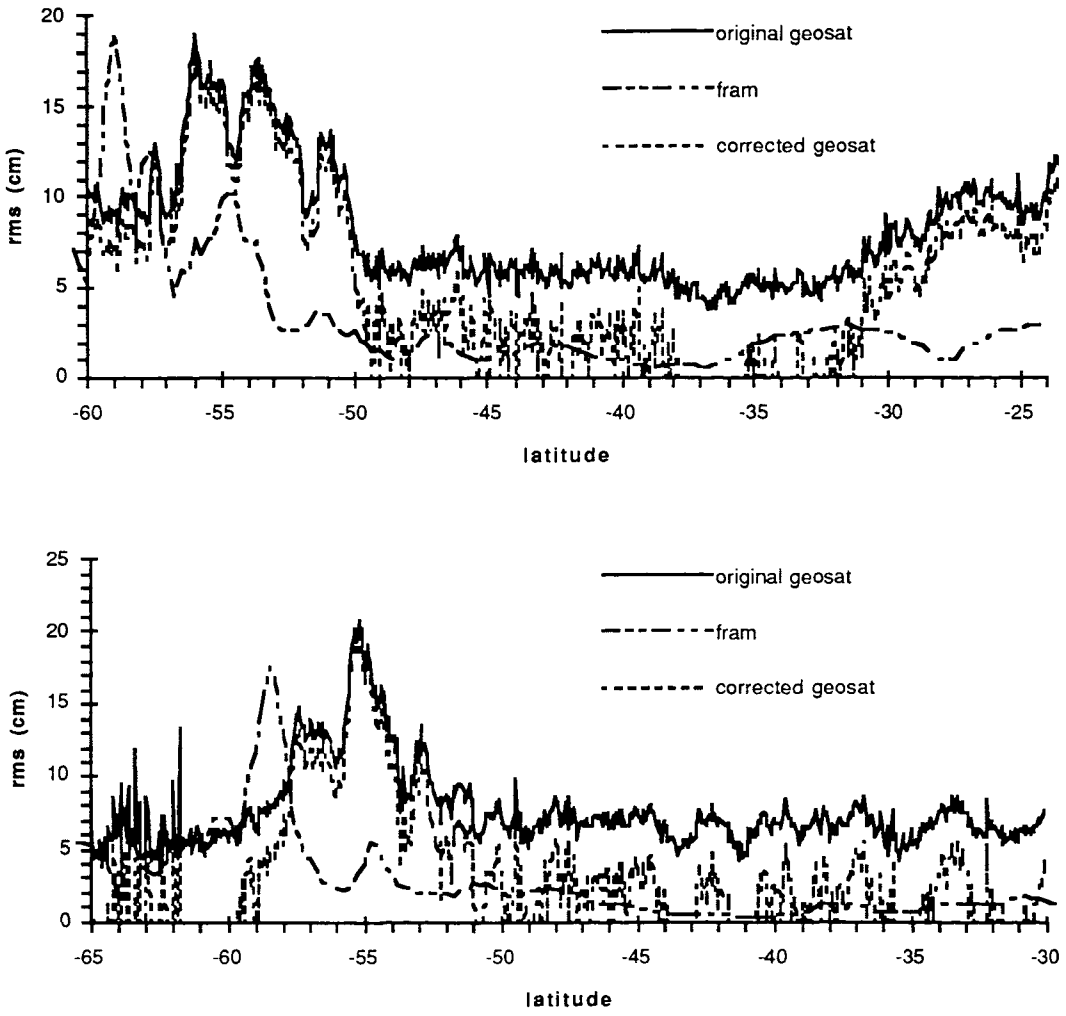

Figure 9.9 The RMS Height Variability Along Two Altimeter Tracks as Determined from Geosat and FRAM Data, an Ascending Track (above) and Descending Track (below).

It was noticed in both data sets that there was increased variability in the north of the region, but comparison of the fields shows that this variability is significantly greater in the Geosat data and located slightly further north. The apparent instability seen in the FRAM data may be partially responsible for the model variability and it is not expected that

the model would accurately recreate the ocean currents within a few degrees of the open northern boundary.

(2) RMS Variability Along Specific Tracks

Using selected tracks across the region, a similar analysis to those given above for the Agulhas region was carried out. As the main signal was towards the southern edge of the region the latitude range of 35° to 45°S was chosen to find the noise level of the Geosat data and this noise then removed to give a corrected Geosat rms variability curve.

Two examples are given in figure 9.9, one of an ascending pass and the other from a descending pass, both of which cross the peak FRAM variability area near 140°W. These curves show that once again the model is locating local variability peaks at the same latitudes as seen in the Geosat data but that these peaks have much reduced magnitudes and tend to exist as simple single peaks. The highest variabilities in the FRAM data are occurring too far south in this region but again have similar magnitudes to the highest Geosat variabilities.

North of 35°S the FRAM data do not show good agreement with Geosat curves. The high variability region seen around 27°S in most of the ascending Geosat tracks is absent in the FRAM data.

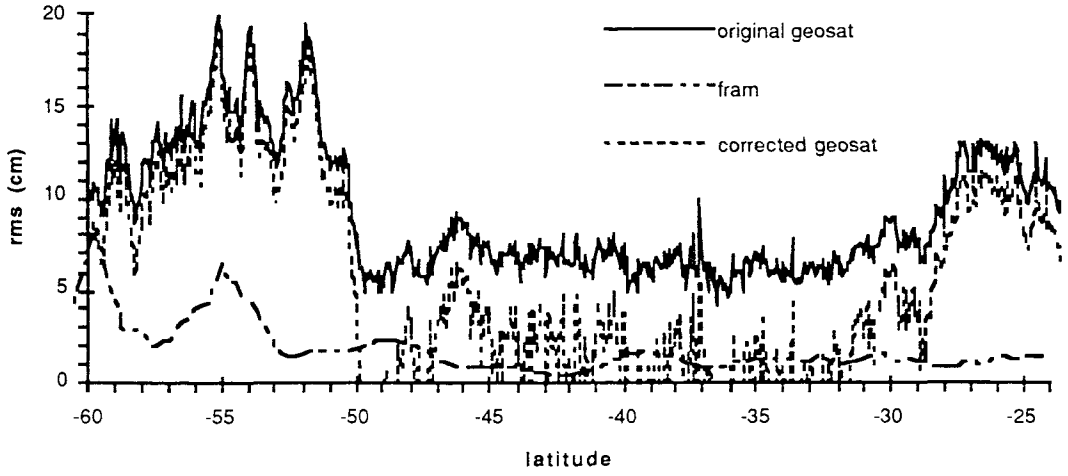

Figure 9.10 The RMS Height Variability Along an Ascending Altimeter Track Through the Eltanin Fracture Zone as Determined from Geosat and FRAM Data.

For most of the tracks examined the FRAM variability under-estimated that from Geosat by several centimetres across the area of main variability. One of the worst discrepancies occurs along an ascending track which passes through the Eltanin fracture zone (figure 9.10). Here the average variability from 50 to 60°S is under-estimated by more than a factor of two (3.8 cm rms compared with 12.3 cm rms from Geosat).

It would appear that in this region the model is not only mis-locating the variability but is not allowing sufficient variability to occur.

9.3 SUMMARY OF COMPARISONS

The comparisons given above show that the model is not accurately reproducing the variability signals of the two regions under consideration at specific locations. There are also some discrepancies with the hydrographic data although here the differences are much smaller. Many of these differences may be explained by the smoothing applied to the model topography which simplifies many of the complex topographic features which appear to be linked to the distribution of ocean variability observed by Geosat. The topography does produce deflections in the model mean currents and induces some variability by meandering of these currents but the flow appears more stable in the model than is observed. Where the model does produce very high variability it appears to be limited to very small areas, producing narrow peaks in the rms field.

Despite these differences, the general distribution and form of the variability and current flow are reasonably close to those of the real ocean. Given this it was felt that the results were sufficiently similar to enable the model to be used in examining the effects of altimeter sampling and processing on the variability results and also to aid in improving the interpretation of altimeter residual height profiles.

10 THE EFFECTS OF ALTIMETRY SAMPLING AND PROCESSING ON FRAM DATA

Whilst analysing the FRAM data set, it was noticed that there were significant differences between the variability fields obtained by direct calculation from the dynamic height grids and those obtained by interpolation of the model altimeter track rms curves. There are several possible causes for these differences, concerned with the sampling and processing of altimetric data. Using the model data it is possible to study these effects to see what errors they may introduce into real satellite altimeter data.

10.1 ALTIMETRIC SAMPLING

The ground sampling pattern of a satellite altimeter may affect the final variability fields through one of two processes;

1. interpolation of fields from discrete tracks.
2. temporal sampling frequency of the satellite.

These two processes are discussed below and may combine to produce fields significantly different from the true field. For these investigations a 'true' model mean field was found by calculating the mean of the dynamic height fields for each region on a grid-point-by-grid-point basis. The rms variation from this mean was then found at each grid-point to give a 'true' model variability field.

10.1.a Interpolation Effects

In order to examine the effects of the interpolation scheme used on the variability fields produced it was decided to process the model altimeter data by simply removing a group mean before finding the rms variability at each data point. These along track mean and variability values were then interpolated onto the FRAM grid and the resultant fields compared with the true mean and true variability fields. As the model altimeter data are extracted at grid points, with no interpolation or smoothing along the tracks, a perfect interpolation from the discrete tracks to the grid will result in the two fields being identical.

The comparisons showed that the interpolation method was good at reproducing the mean field where gradients were small or constant. In the Agulhas region, the largest discrepancy was 0.09 gpm, with only a limited number of places where the difference was more than 0.03 gpm. These differences occur where the mean dynamic height field has a strong gradient which changes direction, as in meanders of the Agulhas Return Current

(see figure 9.1), or where the gradient changes rapidly over a small distance, as in the peak height in the Agulhas Retroflection which is 'flattened' in the altimetric field. In the Central South Pacific, with its smaller dynamic height signal, the differences are even smaller having a maximum discrepancy of only 0.06 gpm. In this region, the effects of steep and rapidly changing height gradients are seen more readily. North of 45°S, where the dynamic height gradients are all very low (see figure 9.6), the difference between the two fields is everywhere less than 0.01 gpm. South of here the largest differences all occur at the edges of the steepest gradients and where the main currents change direction.

The interpolation method is not as good at reproducing the variability fields as the mean fields. This is due to the more patchy nature of these fields, gradients of variability tending to be less regular than dynamic height gradients, combined with the problems of interpolating over changing gradients noted above. Again the Central South Pacific field is better reproduced than the Agulhas field. In the Agulhas region the maximum difference between the altimetric and true variability fields was 6.6 cm with the peak value reduced from 62 to 56 cm. In the Central South Pacific the greatest difference was less than 3 cm but the peak value was only reduced from 20.8 to 20 cm. The better result for the Pacific is in part due to the smaller variability signal than in the Agulhas, but is also due to the more southerly location of the main signal. The satellite track spacing is much closer near the poles than near the equator and so signals in the south of the regions of investigation will be better resolved than those in the north and the interpolation will introduce less smoothing.

From the above analysis it was seen that at the scale of the track spacing the interpolation method (described in § 6.3.b) correctly reproduces the surface fields, but it should be remembered that this scale decreases with increasing latitude. The exact form of features at scales less than the track spacing, especially the field gradient, should not be considered accurate, in particular where the field is patchy or the gradient changes rapidly.

10.1.b Satellite Sampling Frequency

The ground trace of the Geosat satellite repeated exactly every 17.05 days (245 orbits). Each orbit the satellite ground track moved west by 25.15° so that from a reference orbit (orbit 1) orbit number 15 will be 8.8° east of orbit 1 and occur almost 1 day later. This orbit pattern produces a coarse grid coverage of any region every day, the grid for successive days being offset by approximately 17° westward, filling in the spaces as shown in figure 10.1. This orbit repeat pattern is such that for any arc, the track in the same sense (ascending or descending) immediately east will be sampled approximately 3 days later and the track immediately west 3 days previously, giving a three day sub-cycle as well as the main 17 day repeat cycle. This orbit configuration was chosen so that the ground tracks were within the Seasat orbits constraints in order that the data could be freely available (Born *et al.*, 1987).

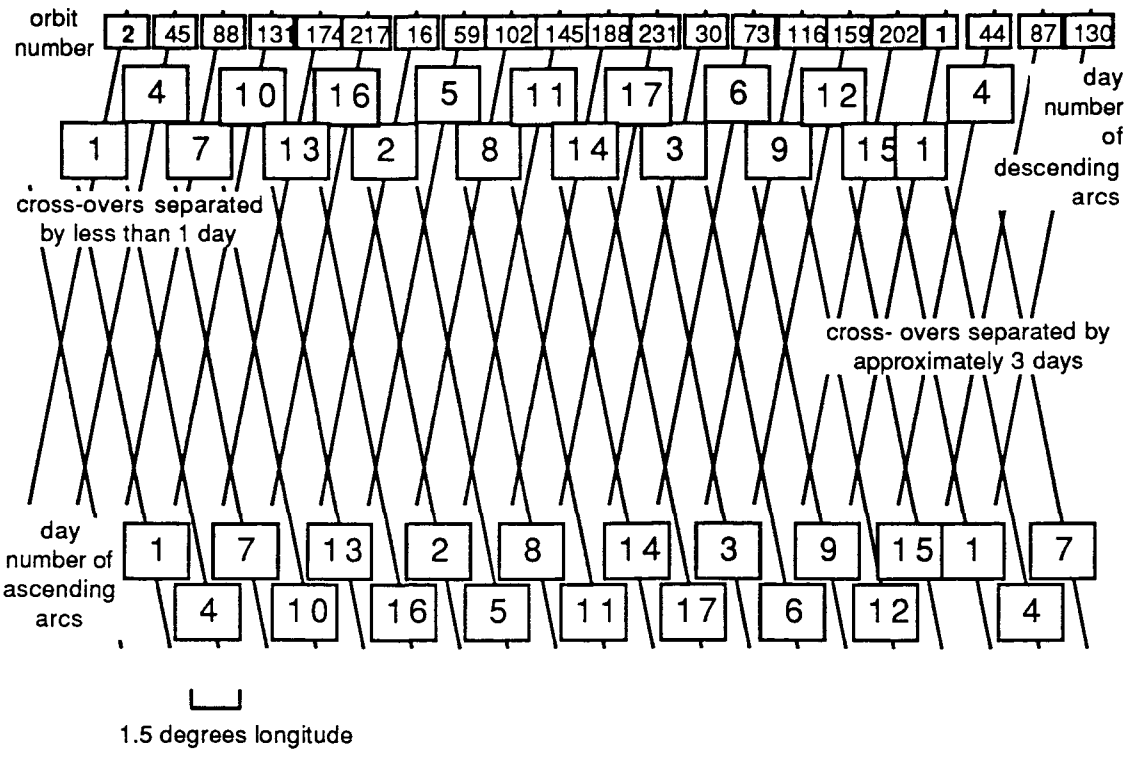

Figure 10.1 A Representation of the Ground Sampling Pattern of Geosat.

As a result of the sampling pattern, cross-overs between ascending and descending passes can be separated by as little as a few hours, or up to 17 days. All cross-overs which have the same temporal separation occur at the same latitude (see figure 10.1), eg. all cross-overs at 45.5°S are separated by 10.635 days whilst at 46.25°S the separation is 7.632 days.

For one model month, from day 5083 to day 5113 of the FRAM run, surface pressure fields were output once per day. Using this data set the FRAM tracks (located by the method given in § 8.1) were extracted in a similar temporal and spatial sequence to the Geosat data. The mean dynamic height calculated at each grid point from the four year data set was used as a climatic mean and removed from each of the dynamic height fields to obtain synoptic dynamic height anomaly fields for each day of this month. The height anomaly relative to the four year mean was also found along each of the sampled tracks and these data were interpolated onto the FRAM grid to produce 17-day composite height anomaly fields corresponding to two orbit repeat cycles of Geosat. As only 32 sequential surface pressure fields were available it was only possible to extract data for one complete 17 day cycle, but a second cycle was created using an overlap of 2 days of data.

(1) Effect on Variability

In order to determine the effect of the sampling pattern on the measurement of variability by a satellite altimeter, the rms values obtained from synoptic fields could be compared with those from composite fields. As only one month of data were available for

this analysis it was not possible to make such a comparison, the statistical significance of variability calculated over a month being very low, especially from just two composite fields, and the changes in current fields over this time are very small and non-representative of the changes over several years. Hence no conclusions can be made on the effects of the Geosat sampling pattern on the variability fields produced.

(2) Effect on Height Anomaly Fields

The composite fields obtained from altimetric data can be used as synoptic height anomaly fields for comparisons with *in situ* data, as has been done by Chelton *et al* (1990), Willebrand *et al* (1990) and Gordon and Haxby (1990). Comparisons of the composite height anomaly fields with the mean synoptic surfaces for each orbit cycle should give an indication of the errors of these composites.

For the Pacific the mean difference between the composite field and the mean synoptic fields was less than 0.1 mm, with a standard deviation of less than 3/4 cm. Figure 10.2 shows the difference between the mean synoptic height anomaly and the composite anomaly for the first 'orbit' cycle. The effects of the sampling pattern can be seen in the diamond shapes evident in the errors. The small diamonds (of order 1°) are caused by the temporal separation of adjacent tracks, whilst the large (order 10°) diamonds are the result of the three day sub-cycle. At any cross-over point the error is a function of the temporal separation of tracks at the cross-over and the relative time of the track sampling within the orbit cycle. For a track sampled near the beginning or end of an orbit cycle, errors will be reduced if the temporal separation of the cross-overs is large as some smoothing in time will result. The largest discrepancies, of up to 14 cm, occur in isolated patches, less than the orbit spacing in size, which are in part due to the spatial interpolation.

For the Agulhas region (figure 10.2b), the effect over most of the area is very similar to that seen in the Pacific, except to the west of the retroflection where errors of up to 45 cm are seen over two or more tracks. These errors are introduced by the westward moving anticyclonic eddies in this area. Consider a large, westward moving, anticyclonic eddy which is sampled on the first day of an orbit cycle by a track across its centre. On subsequent days the eddy will be sampled by tracks to the east of this first track but as the eddy is moving west the heights measured by these tracks will be lower than if sampled on the first day. Similarly, the tracks immediately west (sampled up to 16 days later) will give larger heights than if sampled on the first day. This can introduce large biases in the data, which are dependent on the rate of advection of an eddy and its location relative to track cross-overs, which may either exaggerate or minimize the error depending on the temporal separation of the tracks involved.

Obviously, use of composite fields for comparisons with *in situ* data must involve a method of reducing or evaluating these biases. The use of a time-dependent term in the interpolation weighting scheme, as well as the distance weighting used for all the fields in

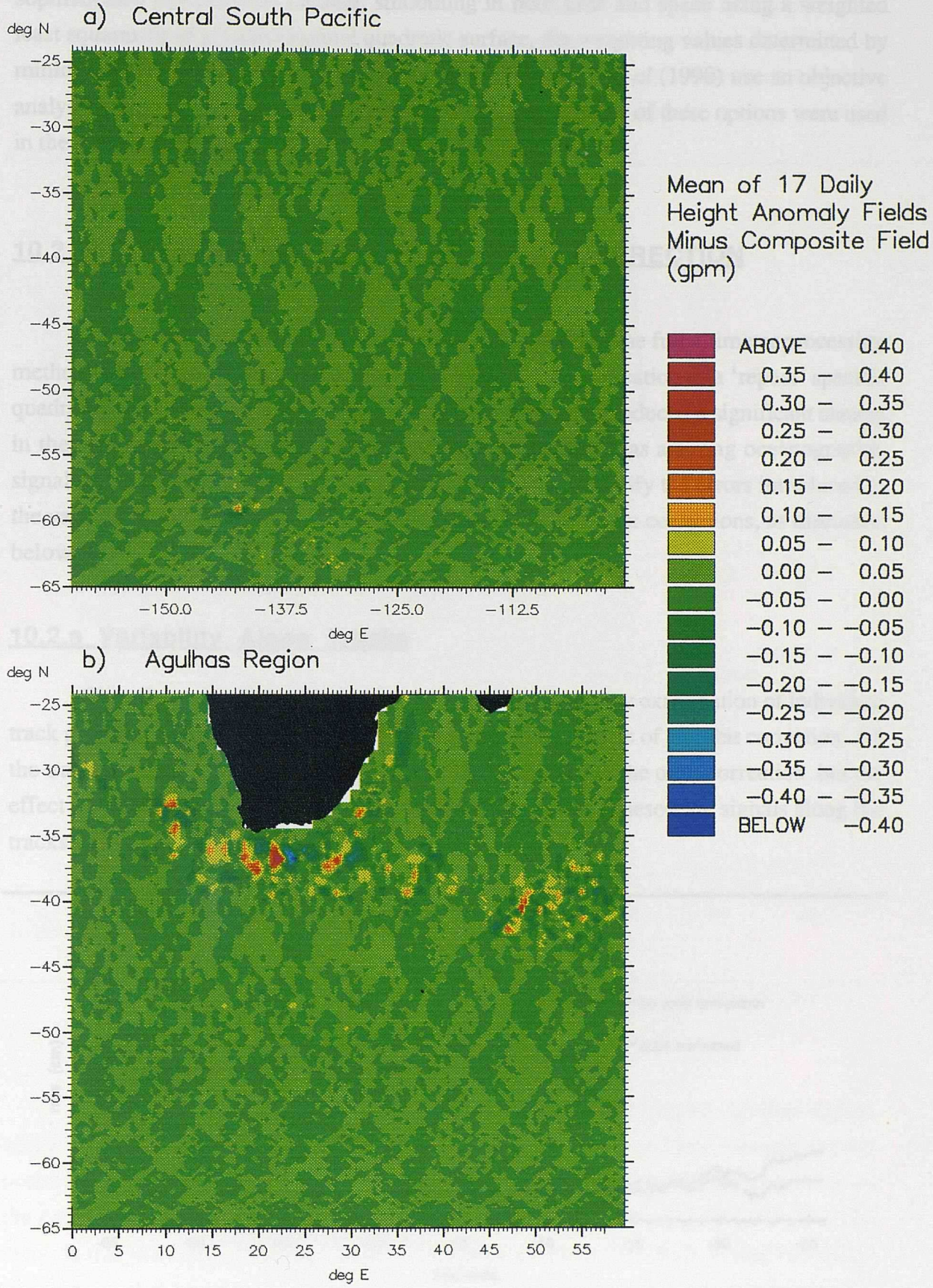

Figure 10.2 The Difference Between the Mean of 17 Daily FRAM Synoptic Height Anomaly Fields and an Altimetrically Sampled Composite for (a) the Central South Pacific and (b) the Agulhas Region.

this study, would probably reduce some of this bias. Chelton *et al* (1990) use a more sophisticated interpolation method, smoothing in both time and space using a weighted least squares fit of a 3-dimensional quadratic surface, the weighting values determined by minimizing the weighted sum of squares errors. Willebrand *et al* (1990) use an objective analysis scheme to obtain a similar temporal weighting. Neither of these options were used in the present study due to computational and time restraints.

10.2 PROCESSING EFFECTS: THE ORBIT CORRECTION

The above analyses were carried out without applying the full altimeter processing method to the FRAM data. As was noted in chapter 8 the application of a 'repeat' specific quadratic 'orbit' correction to the FRAM altimeter track data produced a significant change in the along track variability curves, especially where there was a strong oceanographic signal on the track. Using the FRAM data it is possible to quantify the errors introduced to the variability and time series of sea-surface heights by the orbit corrections, as discussed below.

10.2.a Variability Along Tracks

The effects of orbit correction can be seen most clearly by examination of individual track profiles and the changes in variability introduced by the use of an orbit correction. All the tracks examined showed some change in variability due to the orbit correction, but the effect varied according to the relative size and position of the mesoscale signals along the tracks.

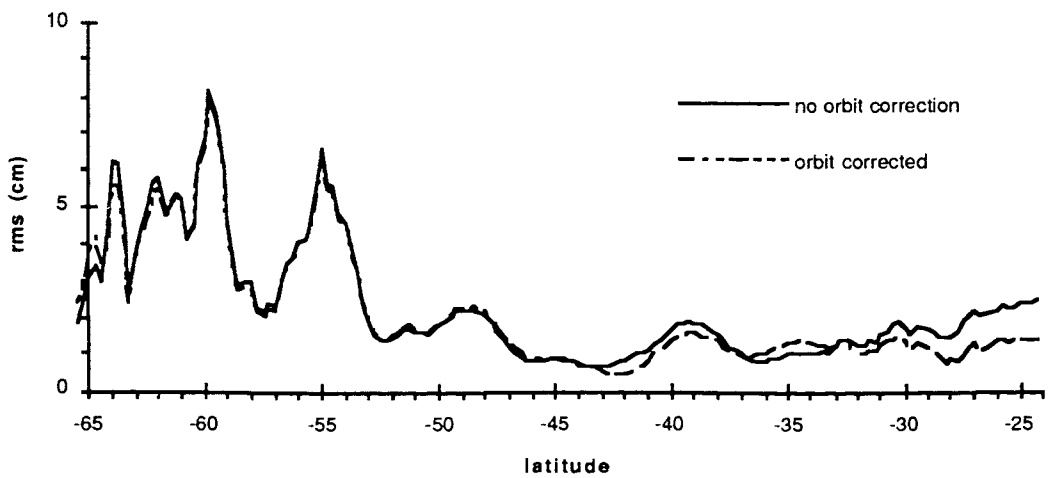

Figure 10.3 Comparison of RMS Variability Along a Track in the Central South Pacific Before and After Orbit Correction.

Figure 10.3 shows a track in the Central South Pacific where there has been very little change in variability, at most 1 cm in the oceanographically quiet sections and less than 3/4 cm in active sections. This track shows some of the smallest changes in variability observed, but even here the uneven distribution of the error can be seen, with the errors much larger towards the ends of the track.

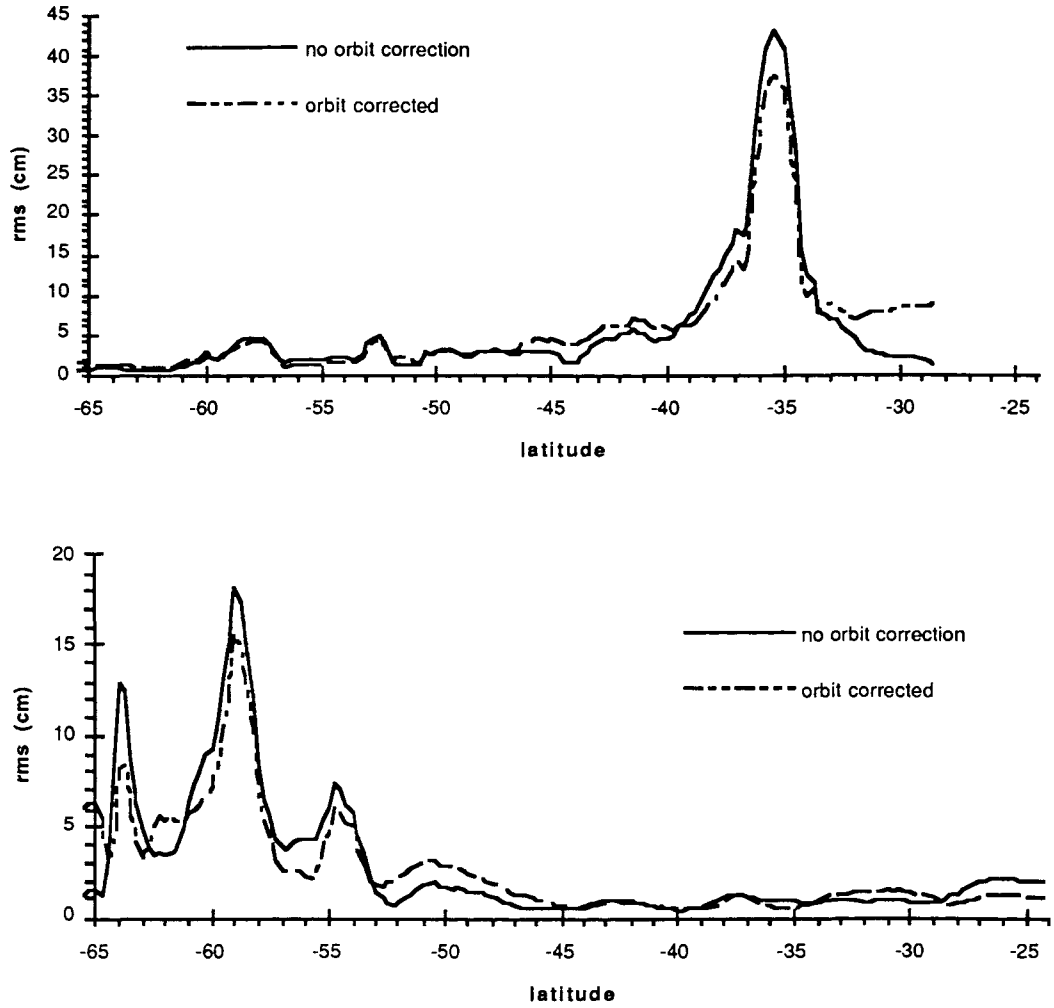

Figure 10.4 Comparison of Along Track RMS Variability Before and After Orbit Correction for a Descending Track in the Agulhas Region (above) and an Ascending Track in the Central South Pacific (below).

The upper half of figure 10.4 shows a descending pass from the Agulhas region, where the dominant variability feature is a single, narrow peak caused by mesoscale activity occurring very close to the northern end of the track. This activity is the major control on the quadratic orbit correction, other, smaller, signals having only a minor influence. The result is that the peak variability at 35°S is reduced by more than 5 cm whilst variability along most of the rest of the track is increased slightly, promoting the importance of a secondary peak at 41.5°S and causing very large errors of almost 10 cm close to the African coast at 28.5°S. This increase in importance of secondary areas of high variability

and increase in variability near the end of tracks is noted in a large number of the passes examined, especially where a single large mesoscale signal occurs along the track, close to the end of the track.

An ascending pass in the Central South Pacific shows a more complex effect (seen in the lower half of figure 10.4) as the signal is spread over a greater length of the track. The result is that the secondary peak at the southern end of the track is reduced by 30% and there is introduction of a narrow peak at the southern limit of the track.

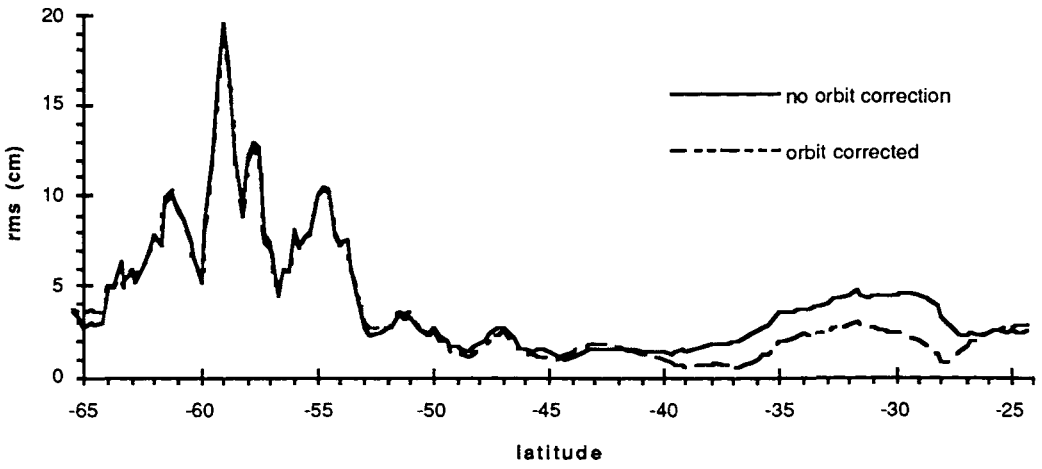

Figure 10.5 Comparison of Along Track RMS Variability Before and After Orbit Correction for an Ascending Track in the Central South Pacific.

The final example of an ascending pass in the Central South Pacific (figure 10.5) shows how strong the effect of orbit corrections is in very quiet sections of tracks. The largest variability signal is concentrated south of 50°S but is spread over a long section of track and the orbit correction has little effect on the variability observed here. In the Northern half of the track, however, a small increase in variability between 28 and 37°S is increased by almost 50% after orbit correction.

The effect on a single track will be modified by the variability of crossing tracks after interpolation onto a field, which may produce even more varied results discussed in the following section.

10.2.b Variability Fields

The altimetric track data for each of the two study regions were processed twice, first using the full processing scheme described in chapter 8, then by simply removing the working mean along each track. The rms variabilities calculated along each track by the two methods were then interpolated onto the FRAM grid to obtain two sets of variability fields, the first are those used in chapter 9 whilst the second are those used for § 10.1.a above.

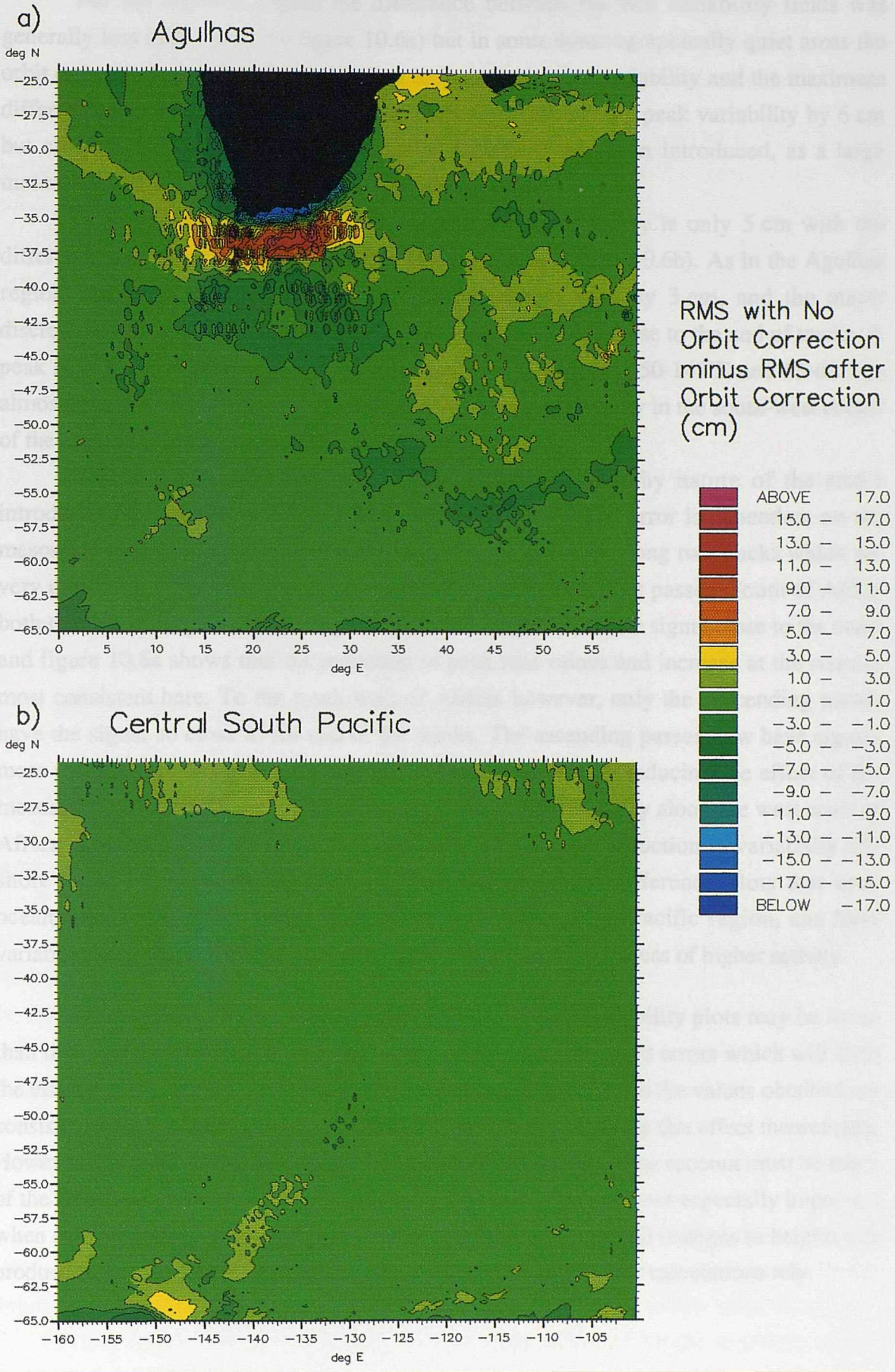

Figure 10.6 The Difference Between the RMS Variability Field With No Orbit Correction and that With an Orbit Correction Applied Obtained from Four Years of FRAM Altimetric data for (a) the Agulhas Region and (b) the Central South Pacific.

For the Agulhas region the difference between the two variability fields was generally less than 1 cm (see figure 10.6a) but in some oceanographically quiet areas the orbit correction caused an increase of up to 5 cm in the rms variability and the maximum difference was 20 cm. Applying an orbit correction reduces the peak variability by 6 cm but close to the coast more than 18 cm of variability has been introduced, as a large mesoscale signal occurs very near the end of the tracks.

In the Central South Pacific the maximum discrepancy is only 5 cm with the difference over most of the region again less than 1 cm (figure 10.6b). As in the Agulhas region, the peak variability value is reduced, in this case by 3 cm, and the major discrepancies occur where a large mesoscale signal is located close to the end of tracks. A peak in variability seen in the 'non-orbit corrected' field from 150-147°E and 63-65°S is almost absent in the 'altimetric' field (figure 9.6) whilst variability in the south-west corner of the region is greatly increased by the processing.

The two difference plots (figure 10.6) show the patchy nature of the errors introduced by the orbit correction procedure. The introduced error is dependent on the mesoscale signals of specific tracks and can be very different along two tracks which are very close and especially between the ascending and descending passes. South of Africa both the descending and ascending passes have a large mesoscale signal close to the coast and figure 10.6a shows that the reduction in peak rms values and increase at the coast is most consistent here. To the south-west of Africa, however, only the descending passes have the signal so close to the end of the tracks. The ascending passes now have signals more centrally as they extend along the west coast of Africa, reducing the effect of the mesoscale signal on the orbit correction. As a result the variability along the west coast of Africa is not increased as much as it is further east, and the reduction in variability off-shore is rather more patchy. It should be noted from the difference plots that even oceanographically quiet areas, such as the north-east of the Pacific region, can have variability altered by several centimetres if the tracks extend into areas of higher activity.

The magnitude of the errors introduced into Geosat variability plots may be lower than those seen in the FRAM data due to the existence of real orbit errors which will limit the effects of mesoscale signals on the correction applied, although the values obtained are consistent with the findings of Le Traon *et al* (1991) when studying this effect theoretically However it is obvious that when examining real altimeter data, some account must be taken of the effects of processing on the observed variability. This becomes especially important when considering velocity calculations from altimeter data as small changes in heights can produce large changes in the height gradients on which geostrophic calculations rely.

11 FRAM TIME SERIES

After processing of model altimeter tracks by the method given in § 8.1 a time series of height anomaly profiles is obtained for each track, just as for Geosat data. These time series can be treated in the same manner as Geosat residuals for identification of mesoscale features and calculation of auto-correlations can also be carried out using the same methods as used for the Geosat data.

11.1 FEATURE IDENTIFICATION

Unlike real altimeter data, the time series of dynamic height fields from which the FRAM anomaly profiles were produced are also available, making it possible to compare height residuals with the fields in order to determine the source of a signal. If anomaly profiles are found in the FRAM data which are similar to those seen in the Geosat data then this analysis may aid in interpretation of the real data.

11.1.a The Agulhas Current System

(1) Agulhas Rings

The height residuals from tracks which pass to the south and west of Africa show very simple features associated with the anticyclonic Agulhas Rings which are seen to move west along the south coast of Africa and then northwest into the Atlantic. This sequence of eddies is seen most clearly in the height profiles of an ascending track, shown in figure 11.1, which passes to the west of Africa. In this time series, several eddies can be seen moving southeast to northwest along the track from 40 to 30°S, each showing a series of residuals very similar to those of figure 6.9a. Comparison with the time series of height residuals for the corresponding Geosat track (figure 6.8, page 66) shows the relatively simple form of the model rings and their regularity, although the rate of advection for the model rings along this track (7.2 to 7.4 cm^{-1}) is close to that calculated for the ring seen in figure 6.8 (8.4 cm^{-1}).

Slightly further east of the track given in figure 11.1 the Agulhas Rings are still seen to move dominantly along track, but with a small cross-track component and so the height residual signals are slightly distorted. All ascending tracks which cross the path of the Agulhas Rings show very regular, simple time series of height residuals which highlight the extreme regularity of spawning of Rings in the model and their uniformity of

size, path and rate of advection. This is in contrast to the Rings seen in the Geosat data, which were highly irregular in form and seen only rarely along any single track.

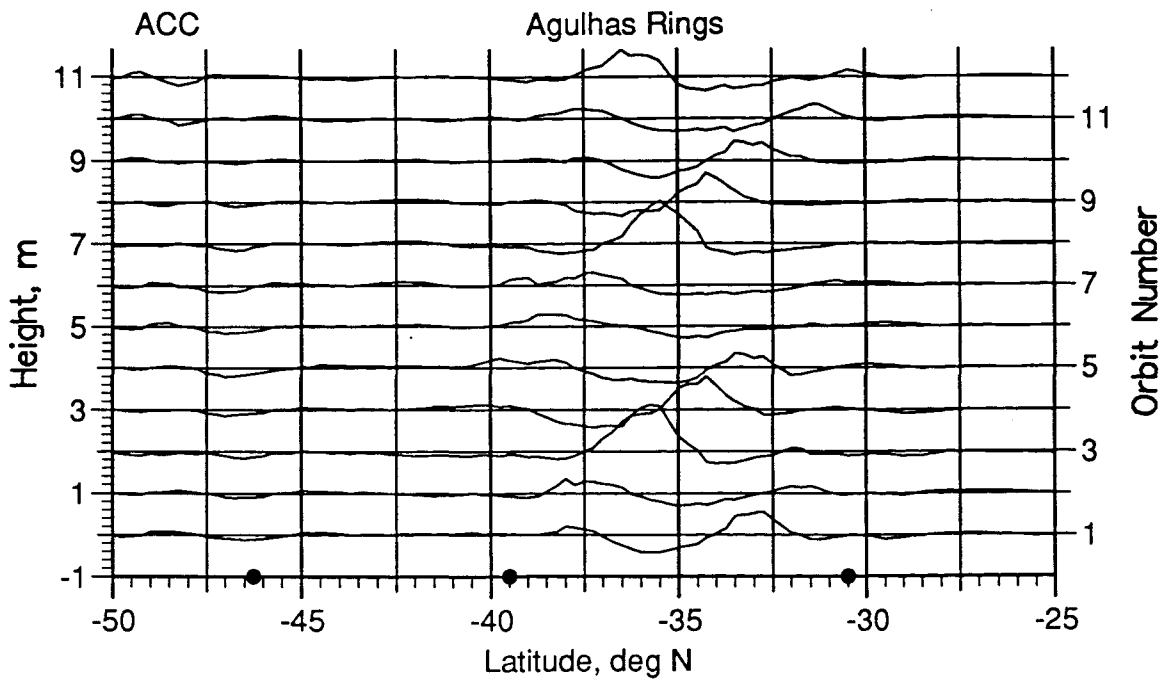

Figure 11.1 Time Series of FRAM Height Residuals for an Ascending Track Showing Agulhas Rings Moving Northwest Along the Track.

Descending tracks which cross the Agulhas Rings are almost orthogonal to the Ring paths and so show eddies crossing the tracks. Figure 11.2 shows a descending track in the west of the region and between 30 and 35°S the profiles show large amplitude signals, generally greater than 50 cm maximum amplitude, which oscillate from low to high as expected for rings crossing the track (see figure 6.9b). To the south, between 35 and 37.5°S, there is a series of smaller signals, of the order of 20 cm amplitude, which appear to be related to the ring residuals and give a complex appearance to the profiles. This series is in fact due to the second set of anticyclonic eddies, noted in § 9.1, spawned from the southern edges of Agulhas Rings. These eddies move along a more westerly path and with a slightly faster rate of advection than the rings so that by 10°E they are almost 180° out of phase with the rings giving the sinusoidal shape of the profiles.

Closer to the point of separation of these eddies (to the east) they appear as a single large, anticyclonic eddy which is non-symmetrical in form but still easily recognizable in the height residuals. Similar effects may explain some of the more complex Geosat height profiles in which a sinusoidal signal is seen but cannot be associated with an eddy moving along the track as the time-series is not as would be expected (see § 6.4).

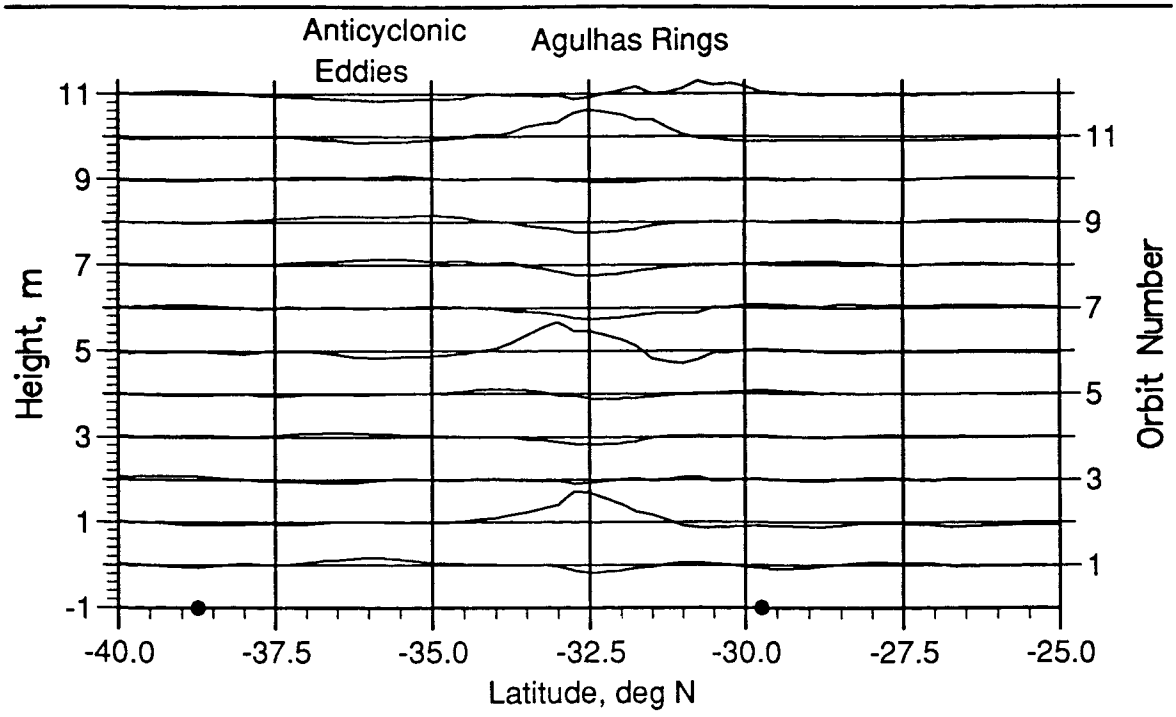

Figure 11.2 Time Series of FRAM Height Residuals for a Descending Track Showing Agulhas Rings and Associated Anticyclonic Eddies Moving Across the Track.

(2) The Retroflection and Return Current

At the point of retroflection, the height residuals apparently show an anticyclonic eddy moving across both ascending and descending tracks, with an associated increasing amplitude signal, but instead of the signal then slowly decreasing again in amplitude, the change is very abrupt as the ring separates and the retroflection point retreats eastwards. If similar time series could be found in the Geosat data then the point of retroflection could be located and monitored over time. As this point is important in terms of the properties transported by the resultant ring, such as heat, salt and momentum, into the Atlantic, such monitoring could aid in understanding fluxes between the ocean basins.

Signals in the height profiles of tracks which cross the Return Current appear almost as complex as those from Geosat data in the same area and their cause can only be determined by careful examination of the dynamic height fields. Meanders are frequently formed in the Return Current and then move downstream, giving very similar residuals to those for an eddy crossing the tracks. Eddies are occasionally formed by break off of these meanders, similar to the formation of an Agulhas Ring but on a much smaller scale, and this separation causes very complex height signals which are dependant on the sampling in both time and space relative to the eddy formation. Differentiation of eddies and meanders is important as meanders will transport water along the main current whilst eddies provide a mechanism for mixing and transporting water away from its source. Comparisons of the model height residuals with those from Geosat have so far not enabled identification of any features in the latter additional to those isolated in § 6.4.

11.1.b The ACC

(1) The Agulhas Region

Compared to the Agulhas Current System the model ACC shows a high degree of stability with many areas of strong currents remaining very constant with time. Where height residual features are seen they tend to be very low amplitude (less than 20 cm) and often also short wavelength. As in the Return Current, meanders are seen to form and then move along the current giving very similar height residual signals to those of eddies.

Many small eddies are seen to form in the dynamic height fields close to the Prince Edward fracture Zone in the South West Indian Ridge, but the evidence for them in height residual profiles is sparse as they are small and short lived and so not as frequently sampled as the larger eddies of the Agulhas System. They also tend to coalesce with the mean current close to their point of formation making sampling even less likely. If this is also true of the real ocean then the Geosat data is probably also 'missing' small eddies spawned by the ACC.

Several tracks cross a region east of the Prince Edward Fracture Zone where the ACC front changes location to the north and then south again. The corresponding height residuals (see figure 11.1) can be rather complex but change slowly over time, as observed for the Geosat height residuals of figure 6.6, tending to confirm that these signals are due to changes in the front.

Interaction of mesoscale features between the ACC and Agulhas Current System is noted in the height profiles north of the Prince Edward Fracture Zone, but elsewhere activity is restricted to south of the main ACC front. The eddies that are seen to be created rarely exist for more than a few months and seldom move far from the main current. This may explain why the variability of the model is too concentrated in narrow bands, although the reason why eddies should not be radiated from the model currents is unclear.

(2) The Central South Pacific

Even where the dynamic height fields appear to show a simple series of features, *eg* a series of small anticyclonic eddies which move to the east near 54°S 143°E, this is not clear in the height residuals. Many of the event sequences seen in the model create time series of height residuals which are not identifiable from simple models.

As in the Agulhas Region, little activity is seen north of the main front but is concentrated to the south, even close to the Ridge crest, comparable to the Prince Edward Fracture Zone in the Agulhas Region. This is probably because there is no current to the north of ridge to induce interaction. Again few eddies are seen to migrate away from ACC core, explaining the localized nature of the variability which is only seen where meanders occur and short lived eddies are formed.

Although few eddies could be identified in the Geosat data, variability away from the main currents was associated with rapidly changing signals most likely to be caused by smal eddies. The FRAM appears to recreate meanders in the main currents and associated features such as the Agulhas Rings, producing variability close to the main currents similar to that observed in reality. However, very little activity is seen in the model height profiles away from the current cores which implies that the model does not create sufficient eddies which can tranfer energy away from the currents.

11.1.c The Effect of Orbit Corrections

The quadratic 'orbit correction' applied to the FRAM data not only affects the variability found along each track, but also has a very large and variable effect on the residual height profiles. These effects are seen most clearly in tracks where a large signal exists close to the end of the track, where the effect on the rms was also found to be greatest (see § 10.2) and signal amlitudes in the Agulhas Current System are reduced by up to 20 cm in some cases.

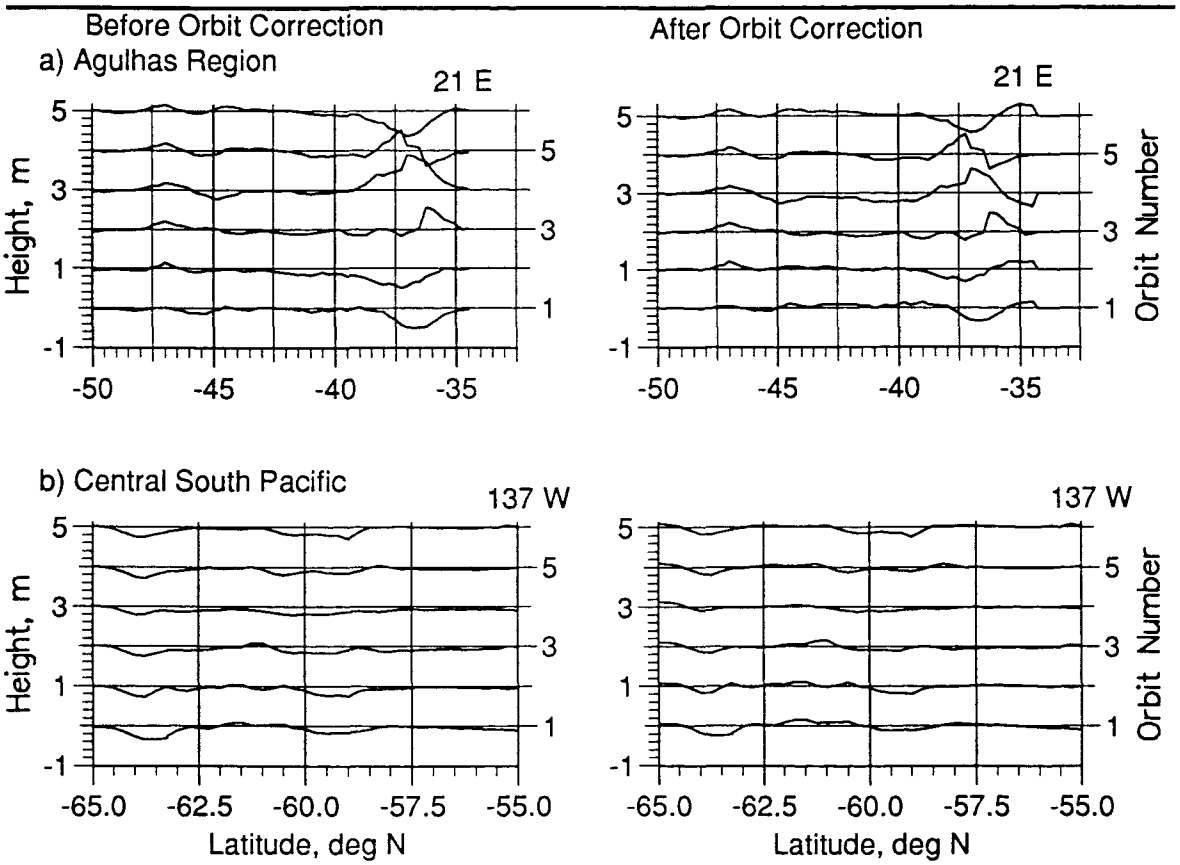

Figure 11.3 Time Series of FRAM Height Residuals Before and After Orbit Correction for Two Descending Tracks in the Agulhas Region (a) and the Central South Pacific (b).

Figure 11.3a shows the height residuals for a track which crosses the Agulhas Retroflection area south of Africa, the left hand diagram showing the residuals before an

orbit correction is made, and the right hand diagram the same residuals after an orbit correction has been applied. The short wavelength signal seen near to the coast in some of the orbit corrected height profiles is purely an artefact of the processing which has created a very complex signal from one which was originally simple. The height profiles in figure 11.3b show a similar effect for a track in the Central South Pacific. Although the magnitude of the errors is much smaller, the relative effect on the smaller mesoscale signal is very large.

As was commented in § 10.2, the effect of quadratic orbit corrections on the FRAM data is exaggerated compared to that on the Geosat data, but similar effects are occurring in the Geosat data and an orbit correction which is less influenced by the mesoscale signal could make interpretation of the height residuals more straightforward. It should be recognized that the effect on the height gradients is greater than on the heights themselves. This will have important consequences for the calculation of geostrophic velocities from altimeter data, with the gradients even being reversed in some locations (see figure 11.3).

11.2 THE AUTOCORRELATION FUNCTION

Calculation of the autocorrelation function for the FRAM height residuals has been carried out in the same manner as for the Geosat height residuals (see § 6.4.b). This allows a comparison of the scale of features shown by FRAM with scales seen in the Geosat data. It is expected that very short wavelengths will not be correctly represented as the model is unable to accurately resolve features smaller than a few grid points in size. It should also be noted that the value of Δr (the lag increment) used in the calculations is 33.5 km, five times the value for Geosat of 6.7 km. This may affect the shape of the correlograms, especially at short lags.

11.2.a The Agulhas Region

Correlograms can be calculated for individual tracks as they were for Geosat data and they show many of the same features, including large negative lobes where there is a strong mesoscale signal and high correlations at long lags where there is a very weak mesoscale signal. Both ascending and descending tracks which cross the path of Agulhas Rings to the south-west of Africa show high correlations at mesoscales. Typical zero crossing length scales are 175-200 km whilst curve minima are found from 250-300 km, as seen in figure 11.4. These values are somewhat greater than typical values found from the Geosat data.

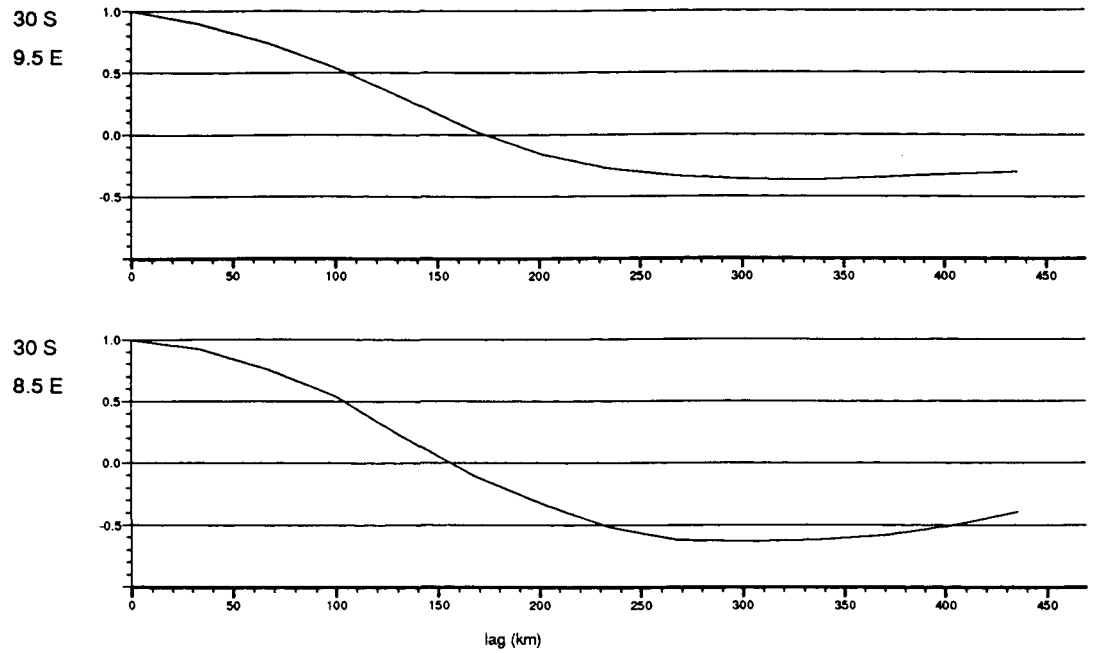

Figure 11.4 Correlograms for an Ascending Track (above) and a Descending Track (below) which Cross the Path of Agulhas Rings. The Starting Location for Each Correlogram is Given to the Left of the Graph.

East of the Retroflection correlograms are very similar to those seen further west, but typical zero-crossing and minima length scales are some 50 km smaller. Further east along the Return Current, the correlograms become more variable and no curve break or minima are observed making determination of a length scale impossible.

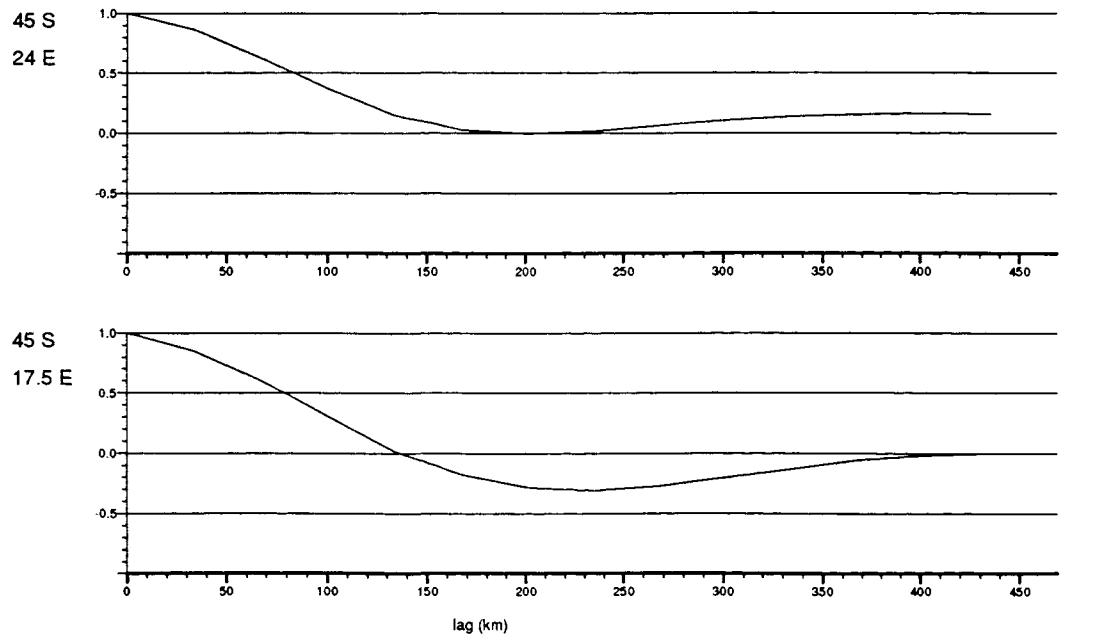

Figure 11.5 Correlograms for an Ascending Track (above) and a Descending Track (below) which Cross the ACC. The Starting Location for Each Correlogram is Given to the Left of the Graph.

Correlograms calculated where tracks cross the ACC tend to show much simpler forms than the corresponding Geosat correlograms. Both ascending and descending passes give significantly shorter length scales than seen in the Retroflection and Agulhas Ring areas, zero-crossings typically occurring near 130 km when present, with curve minima at 160-170 km (figure 11.5). This is slightly shorter than the values of about 190 km for the curve minima lags seen in Geosat data.

Correlograms were also calculated for the 36 subdivisions of the region used in § 6.4.b (figure 11.6) and these show very similar forms to those obtained for Geosat (figure 6.13). Where mesoscale signals exist, the negative lobes recognized in the Geosat data appear more pronounced in the FRAM curves. This may be due to the increased effect of the quadratic orbit corrections on the FRAM height profiles as noted in § 10.2. Further evidence for this lies in the much greater correlations which exist at long wavelengths and which severely affect the zero crossing and integral length scale values obtained. For the Geosat data it was found that the integral length scale (L2) changed very little with the value of the maximum separation used in calculation for maximum lags greater than 400 km. This was not the case for the model data with increases of up to 60 km in L2 introduced by increasing the maximum lag from 600 km to 1000 km.

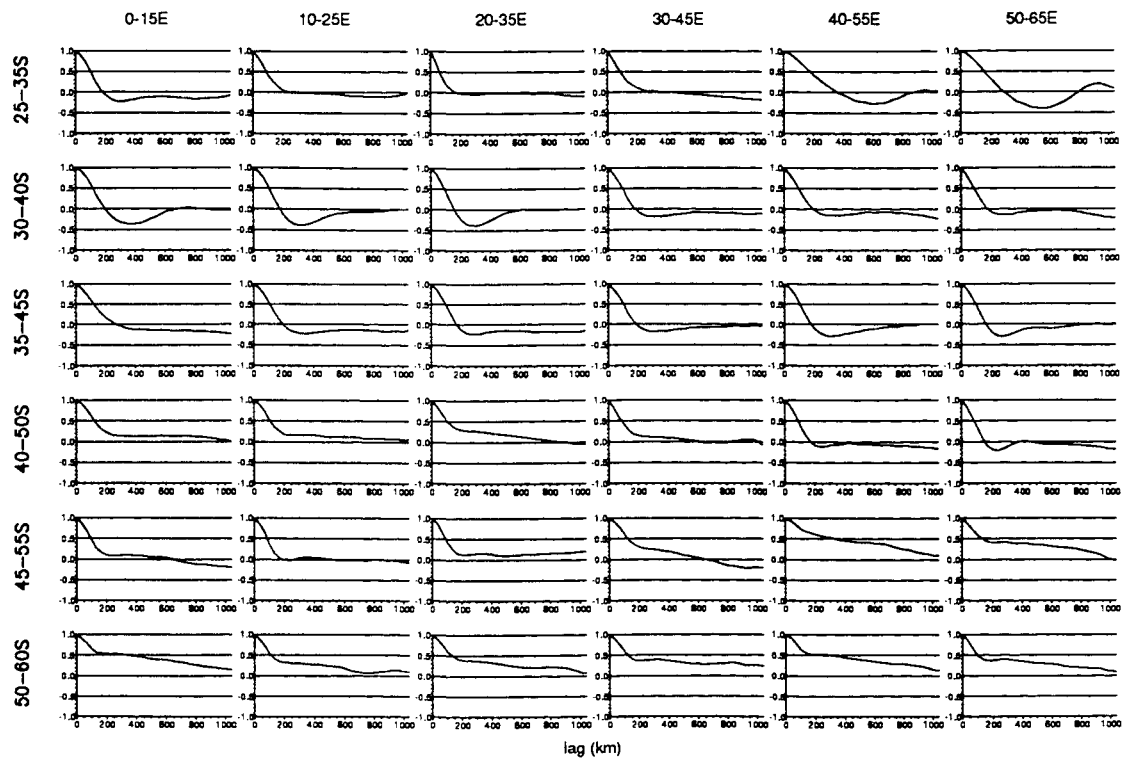

Figure 11.6 Correlograms for 36 Sub-divisions of the Agulhas Region from FRAM Data.

The integral lengths scales calculated for the subdivisions are all much larger than the corresponding values from the Geosat data due to the high correlations at long lags, as shown in figure 11.7, a plot of the values of L2 calculated from model data against those

from Geosat data for the sub-divisions of the Agulhas Region. This diagram also shows the poor correlation of these two sets of values. Although inspection of the model correlograms shows shorter length scales for the ACC than for the Agulhas Current System, as observed in the Geosat data, this is not evident in the integral length scales.

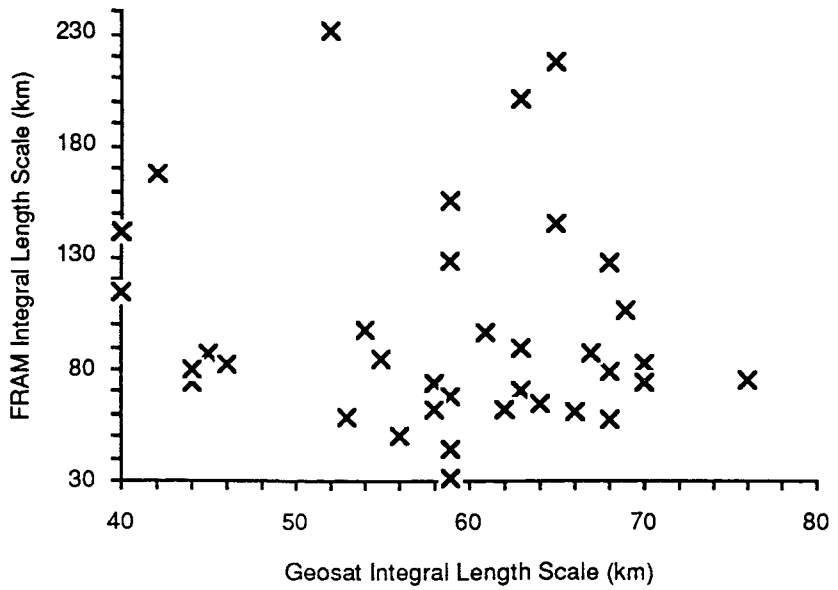

Figure 11.7 The Integral Length Scale of the FRAM Data Against that from Geosat Data for 36 Subdivisions of the Agulhas Region.

11.2.b The Central South Pacific

The correlograms calculated along individual tracks within small areas do not show the same degree of similarity as was seen in the Agulhas region and ascending and descending passes can give significantly different results for auto-correlation functions found near their cross-over points. The descending track which passes through the Udintsev fracture zone has a simple correlogram which decreases to zero at 250 km, but the ascending track has a zero-crossing at 110 km and a large negative lobe having a minimum at 170 km. This may be an indication of the non-isotropy of dynamic height anomalies within the model.

North of the ACC, none of the correlograms examined had a break of slope indicative of a dominant length scale for mesoscale features, but south of the Antarctic-Pacific Ridge zero-crossings and curve minima were often found close to 100 km and 170 km respectively which would indicate similar length scales to those observed in the Agulhas Region for the model ACC.

The correlograms for the 36 sub-divisions of the region used in § 7.2.b are given in figure 11.8. When compared to the results from Geosat (figure 7.8) the correlograms for the southern half of the region show a high degree of similarity. As was observed in the Agulhas region the negative lobes, where strong mesoscale signals are apparent, are somewhat more pronounced in the model curves, probably due to the orbit correction. Only in one sub-division (40-50°S 160-145°W) does the model data show a strong mesoscale signal not evident in the Geosat data.

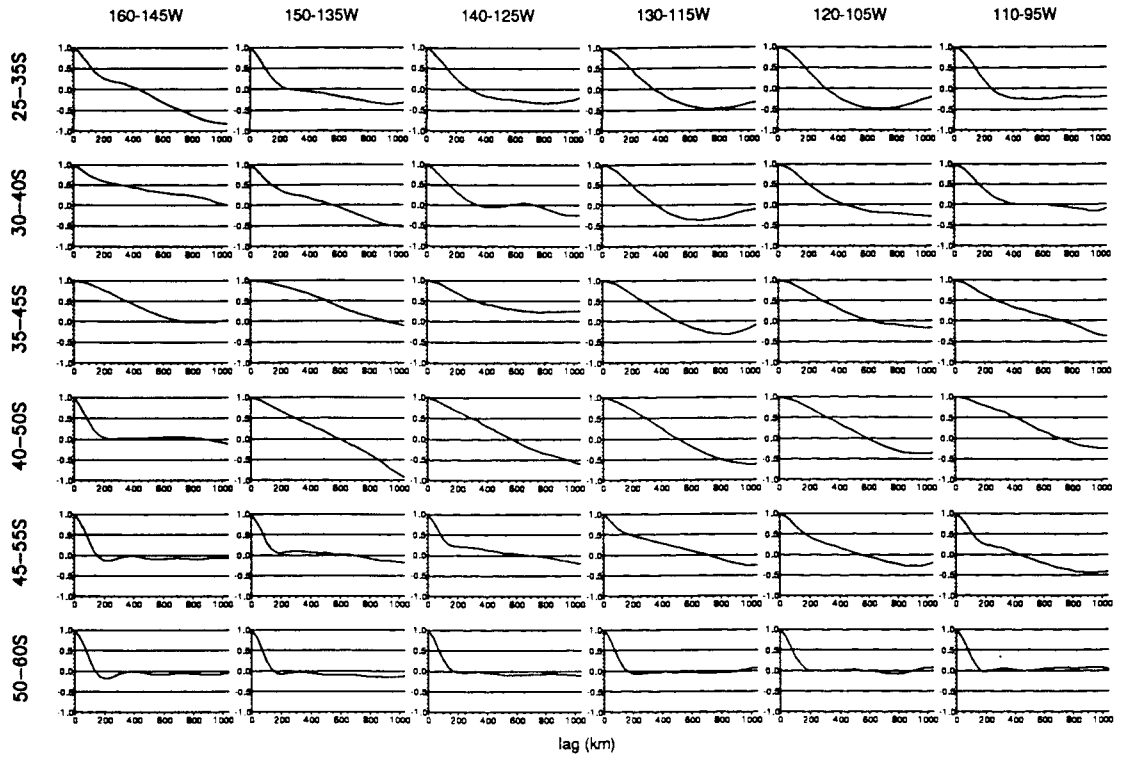

Figure 11.8 Correlograms for 36 Sub-divisions of the Central South Pacific from FRAM Data.

The correlograms for the three northern bands used in the analysis show a much weaker similarity to the Geosat data. Here very strong correlations exist at long wavelengths, not observed in the Geosat data. This is also believed to be due to problems with the long wavelength 'orbit error' of the model data.

The integral length scales calculated for the regional sub-divisions show similar general trends to those seen in the Geosat data. Although model values are again much greater than Geosat values (see figure 11.9) there is much greater correlation between the two. The correlation is even closer if a maximum lag of 600 km is used in the calculation of L2 from the FRAM data, with values of 35 to 57 being obtained for the ACC features, very similar to those found from the Geosat data.

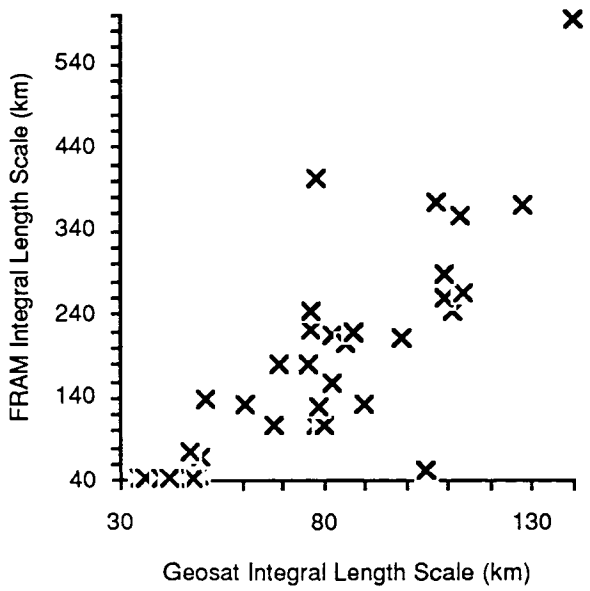

Figure 11.9 The Integral Length Scale of the FRAM Data Against that from Geosat Data for 36 Subdivisions of the Central South Pacific Region.

For both the Agulhas and Central South Pacific regions the major difficulty in determining the ACF from model data appears to be the application of a quadratic orbit correction which produces very large correlations at long wavelengths. This seems to have a major effect on the integral length scale calculations which become critically dependent on the maximum lag chosen. The location of curve minima and changes of slope seem more reliable indicators of the dominant length scales present, but their interpretation requires a high degree of subjectivity which makes comparisons between the model and Geosat results less reliable.

Section IV: CONCLUSIONS

12. CONCLUSIONS

For this study satellite altimeter and model data have both been used to aid in understanding of the current systems and especially the mesoscale activity in the Southern Ocean, where *in situ* data collection is expensive and hazardous. The Southern Ocean is an important region as it provides the only link between the other major ocean basins and fluxes of heat, salt and momentum here are influential in global climate control. Mesoscale eddies are believed to be important in controlling the distribution and mixing of water masses in the ocean and conventional *in situ* data collection methods do not allow long term monitoring of large ocean areas at small spatial scales. Two regions of the Southern Ocean were selected for this study, the Agulhas Region (south of Africa) and the Central South Pacific.

12.1 SUMMARY OF RESULTS

The variability fields obtained from Geosat data show the main areas of high mesoscale activity within the two regions studied. Results are similar to those from altimetry in published literature except in small details which may be explained by differences in sampling frequency and scale (Seasat) or spatial resolution of the presented fields (Geosat). The similarity of the Geosat fields to Seasat fields implies that the location and intensity of mesoscale activity in the Southern Ocean have remained fairly constant for at least the last decade. The similarity of the variability fields obtained in this study and those produced from Geosat data using different processing methods (Chelton *et al*, 1990, Wakker *et al*, 1990) indicates that determination of mesoscale variability is largely independent of the processing technique used.

The Geosat mesoscale variability fields show strong correlation with historical hydrographic information, the areas of greatest variability coinciding with the strongest currents, implying baroclinic instability in these currents as the cause of the variability. Variability also appears to be strongly correlated to bottom topography, possibly due to topographic control of the currents. Areas of steep topographic slope are often coincident with the maximum observed variability which seems to indicate that interaction between the current and topography may induce instabilities.

Comparisons of the FRAM data with results from both *in situ* and Geosat data show that the model recreates the coarse structure of the circulation correctly in both regions studied. Some discrepancies do occur, especially in the exact location and extent of variability which tends to be too constrained within narrow limits. In the Agulhas Region,

eddies are constrained to follow a single, narrow track which results in locally increased variability with similar total variances. The location of variability is important in determining how water masses are distributed and it is likely that transport of water from the Indian Ocean to the Atlantic is too high in the model due to these regular eddy tracks. In the Central South Pacific it is the mean current which appears to be too constrained and so total variability is under-estimated. In both regions there appears to be insufficient energy released away from the main currents.

In both the Agulhas and Pacific regions the FRAM data show correlation between the location of high variability areas and bottom topography, similar to that observed in the Geosat data. However, the model uses a smoothed version of the real topography (for numerical stability) which reduces slope gradients and makes narrow, deep fractures broader and shallower so changing the absolute position of variability and often reducing its intensity. Both the Geosat and the FRAM data highlight the strong influence of bottom topography on current location and the formation of instabilities, even where bathymetric features are several kilometres deep.

Using time series of individual orbit arc repeats it was possible to calculate geostrophic current velocities from the Geosat data which show reasonable agreement with *in situ* current data in both study regions. These velocities, which are relative to an unknown mean velocity, are very similar in magnitude to the *in situ* current measurements for both the Agulhas Current System and the ACC, which implies that the variable part of the current contains much of the energy of the system.

It was attempted to use the time series of Geosat height residuals to determine the cause of variability and hence to differentiate between features such as eddies and fronts. This proved to be very difficult in all but a few, limited situations as the systems involved appeared to be too complex. There was some indication that isolated eddies could be recognised away from the cores of the main currents and that flow through the Eltanin Fracture Zone increased over time, but interactions between the mean flow and mesoscale features seem to occur. This is confirmed by similar studies using the FRAM 'model altimeter' data which showed that determining the cause of a height residual signal was still difficult, even when the dynamic height fields were also available for comparison.

The high spatial resolution of the height residual profiles allowed the calculation of autocorrelation functions with high statistical significance. Using these autocorrelation functions the characteristic length scales of height anomalies were determined within sub-divisions of the regions examined. These scales are only relevant to mesoscale features that are the dominant source of variability. In the Agulhas Region, length scales determined from the Geosat data within the ACC were found to be smaller than those within the Agulhas Current System. When comparing the Agulhas Region with the Central South Pacific, scales determined for the ACC (*ie* south of 45°S) were fairly consistent. This implies that although the controlling dynamics of the ACC and the Agulhas Systems must be different, those for the ACC may be consistent, at least between the two regions studied.

Similar autocorrelation function calculations using the FRAM data proved inconclusive, the major control on length scales obtained being the orbit correction applied.

12.2 ORBIT ERRORS AND FRAM DATA

Processing of the model altimetry data allowed the determination of errors which may exist in altimeter height residuals after processing. Strong mesoscale signals that affect the quadratic orbit correction proved the greatest problem, decreasing total variability along track, especially where peak values occur, but increasing background variability levels. The model results are not strictly applicable to the real altimeter data because there is a different number of points along a model track (161) than a Geosat track (1000) and the tracks are slightly shorter in length (5400 km compared to 6700 km) but this is thought to introduce only small differences. The model results may also exaggerate the effect as there is no orbit error in the data and the orbit correction will thus be more closely tied to the mesoscale signal than is the case for Geosat data, where there is a large amplitude, long wavelength signal. The results do show the need for caution in comparisons between results for different data sources and highlight the need to understand fully the implications of error correction methods on the signal of interest.

The model height residual profiles show the effect of orbit errors on the height slopes obtained, which is greater than on the height residuals themselves. This has important implications when calculating geostrophic velocity anomalies from the data as the velocity magnitudes and even the direction can be affected by the orbit correction applied.

12.3 SUGGESTIONS FOR FUTURE WORK

Since this study was carried out, an improved set of Geosat GDRs has been produced (Cheney *et al*, 1991a) for the sensor life span. These data incorporate the TOVS/SMMI wet tropospheric corrections described in § 7.2, the altered tidal model used for the later GDRs (see § 5.2) and a much improved orbit based on improved geoidal information. The improved corrections should limit the noise introduced into the data whilst the higher accuracy orbit allows a lower order curve to be applied to the data to correct residual orbit errors (Cheney *et al*, 1991b), which will retain a greater amount of oceanographic information in the height residuals. It is recommended that any further analysis of the Geosat results is performed using these new data.

Improvements to the method of residual orbit error removal in Geosat data processing method are indicated by the results of this study and the use of FRAM data in evaluating these changes is suggested. In order to model the Geosat altimetric sampling

more closely, data should be extracted from the FRAM at exact Geosat points by interpolation from the grid nodes. This will result in over-sampling of the data but should give much smoother height profiles and a better indication of the true effects of sampling and processing on altimeter results.

In order to better understand the magnitude of the effects of orbit correction on variability fields, it should be possible to introduce a model orbit error of the magnitude of that in the new GDR (0.5 m) to the FRAM data, which should give the true magnitude of error residuals. As the improved GDR data require lower order polynomials to correct for the residual orbit errors, it should be possible to compare results from these 'orbit error inclusive' FRAM data after application of either a quadratic or linear orbit correction to ascertain the amount of oceanic variability which will be lost by the processing. It was noticed in the FRAM data that the greatest errors were introduced by the orbit correction where a large mesoscale signal existed close to the end of a track. A possible solution to this problem would be to attempt to fit an orbit correction to a limited number of sub-sampled points, distributed along the track but selected so that large mesoscale signals were avoided.

During this study the FRAM data were used to determine the effects of the interpolation scheme used to map discrete track data onto a grid. It should be possible to extend this study to determine the most appropriate interpolation method to use. Results from the ACF length scale determination could be incorporated into the scheme as suitable interpolation distances.

12.4 CONCLUSIONS

Altimeter data from Geosat have provided the oceanographic community with the first global, all weather data set from which mesoscale currents can be monitored over long time periods. The lack of supporting data, especially from laser tracking for orbit determination, and lack of an atmospheric sounder for tropospheric range delay, have limited the accuracy of the data. This study has shown how the impact of some of the data errors can be limited by careful selection of quality controls and the use of a simple, computationally efficient processing method.

The FRAM is the first attempt to model the effects of mesoscale activity for the entire Southern Ocean. Verification of the results is difficult due to the lack of comparable *in situ* data for much of the Southern Ocean but the Geosat data allow verification of the important mesoscale portion of the model velocity fields. Although discrepancies were found between the model variability and that determined from Geosat, the main areas of high and low variability were reproduced by the model confirming that the model dynamics created mesoscale activity in the correct locations and of the correct order of intensity.

It was noted during the analysis that both Geosat and FRAM height variability appeared strongly correlated to the appropriate bottom topography but that differences between the real and model bathymetry appeared to explain the discrepancies in location and intensity of the model variability. Although previous studies have commented on the correlation of altimeter derived variability and steep topographic slopes, the detail of variability and its relation to the observed currents and topography have not previously been reported for the two study regions. The ability of the FRAM to reproduce topographically induced instabilities is the first such observation for a wind-driven ocean circulation model. The similarity between the relationship in the model and that from Geosat confirms the observations from the model that surface current patterns can be seen to extend to great depth (Webb *et al.*, 1991), providing mechanisms by which deep topography could influence surface currents.

The FRAM data also provide a model ocean from which model altimeter data can be produced. These data are of much greater complexity, and provide a more realistic model ocean, than those produced by other simulation methods. These data have been used in evaluating the effects of altimeter processing on the variability fields in a way not previously possible.

The very high spatial resolution of time series of height residuals makes them valuable for gaining further information on mesoscale features than is possible from the variability or height anomaly fields alone. This study showed how the complex height residual signals obtained from altimeter data can be related to a variety of mesoscale features, giving extra information on the cause of variability and its distribution. The separation of noise and error induced variability from that caused by mesoscale activity is an additional benefit of examining the height profiles. The along track height profiles also provided the input for ACF calculations that showed a smaller dominant length scale for mesoscale features in the ACC than existed in the Agulhas Current System, a result not previously observed.

The use of remote-sensed and numerical model data provide the only methods of understanding the dynamics of large areas of the worlds' ocean at small spatial scales over long time periods. The comparisons of Geosat and FRAM data presented in this study show how complex the dynamics of the Southern Ocean are and highlight the importance of bathymetry in the control of both major ocean currents and their associated mesoscale variability. Although the FRAM is the best model of its type currently available for the Southern Ocean, discrepancies in the variability field from that observed by Geosat indicate that the effect of mesoscale features in dispersing energy away from major current cores is still not fully represented, making further study of these spatial scales of great importance in improving our understanding of the dynamics of ocean circulation.

REFERENCES

Bernstein, R.L. and W.B. White (1974). Time and Length Scales of Baroclinic Eddies in the Central North Pacific Ocean. J.Phys.Oceanogr., 4: 613-624.

Born, G.H., F.G. Lemoine and M.J. Crawford (1988). Geosat ERM- Orbit Determination. Adv. Astronautical Sci., 65: 65-81.

Born, G.H., J.L. Mitchell and G.A. Heyler (1987). Geosat ERM- Mission Design. J.Astronaut.Sci., 35: 119-134.

Born, G.H., M.A. Richards and G.W. Rosborough (1982). An Empirical Determination of the Effects of Sea-State Bias on SEASAT Altimetry. J.Geophys.Res., 87(C5): 3221-3226.

Boudra, D.B. and E.P. Chassignet (1988). Dynamics of the Agulhas Retroflection and Ring Formation in a Numerical Model. Part I: The Vorticity Balance. J.Phys.Oceanogr., 18(2): 280-303.

Bowen, J.L. and H. Stommel (1974). How Variable is the Antarctic Circumpolar Current? In: Research in the Antarctic, Quam, L.O. (Ed.). 645-650.

Brenner, A.C., C.J. Koblinsky and B.D. Beckley (1990). A Preliminary Estimate of Geoid Induced Variations in Repeat Orbit Satellite Altimeter Observations. J.Geophys.Res., 95(C3): 3033-3040.

Brown, R.D. (1983). M2 Ocean Tide at Cobb Seamount from SEASAT Altimeter Data. J.Geophys.Res., 88(C3): 1637-1646.

Bryan, F.O. and W.R. Holland (1989). A High Resolution Simulation of the Wind- and Thermohaline- driven Circulation of the North Atlantic Ocean. Parameterization of Small-Scale Processes, Proceedings of the Hawaiian Winter Workshop, Manoa, Hawaii, University of Hawaii.

Bryan, K. (1969). A Numerical Method for the Study of the Circulation of the World Ocean. J.Computational Phys., 4(3): 347- 375.

Bryan, K. and M.D. Cox (1967). A Numerical Investigation of the Oceanic General Circulation. Tellus, 19: 54-80.

Bryden, H. (1983). The Southern Ocean. In: Eddies in Marine Science, Robinson, A.R. (Ed.). Berlin Heidelberg, Springer-Verlag. 265-277.

Bryden, H.L. and R.A. Heath (1985). Energetic Eddies at the Northern Edge of the Antarctic Circumpolar Current in the Southwest Pacific. Prog. Oceanog., 14: 65-87.

Bryden, H.L. and R.D. Pillsbury (1977). Variability of Deep Flow in the Drake Passage from Year Long Current Measurements. J.Phys.Oceanogr., 7(11): 803-810.

Callahan, P.S. (1984). Ionospheric Variations Affecting Altimeter Measurements: A Brief Synopsis. Mar.Geodesy, 8(1-4): 249-263.

Cartwright, D.E. and R.D. Ray (1989). New Estimates of Oceanic Tidal Energy Dissipation from Satellite Altimetry. Geophys.Res.Lett., 16(1): 73-76.

Cartwright, D.E. and R.D. Ray (1990a). Observations of the Mf Ocean Tide from Geosat Altimetry. Geophys.Res.Lett., 17(5): 619-622.

Cartwright, D.E. and R.D. Ray (1990b). Oceanic Tides from Geosat Altimetry. J.Geophys.Res., 95(C3): 3069-3090.

Cartwright, D.E. and R.D. Ray (1991). Energetics of Global Ocean Tides from Geosat Altimetry. J.Geophys.Res., 96(C9): 16,897-16,912.

Challenor, P.G., S. Foale and D.J. Webb (1990). Seasonal Changes in the Global Wave Climate Measured by the Geosat Altimeter. Intl.J.Rem.Sens., 11(12): 2205-2213.

Chelton, D.B., M.G. Schlax, D.L. Witter and J.G. Richman (1990). Geosat Altimeter Observations of the Surface Circulation of the Southern Ocean. J.Geophys.Res., 95(C10): 17,877-17,904.

Chelton, D.B., E.J. Walsh and J.L. MacArthur (1989). Pulse Compression and Sea Level Tracking in Satellite Altimetry. J.Atmos.Oceanic Tech., 7(3): 407-438.

Cheney, R.E., B.C. Douglas, R.W. Agreen, L. Miller and N.S. Doyle (1988). The NOAA Geosat Geophysical Data Records: Summary of the First Year of the Exact Repeat Mission. NOAA Tech.Memo., NOS NGS 48. 20 pp.. National Ocean Service/NOAA, Rockville, Md.

Cheney, R.E., B.C. Douglas, R.W. Agreen, L. Miller, D.L. Porter and N.S. Doyle (1987). Geosat Altimeter Geophysical Data Record (GDR) User Handbook. NOAA Tech.Memo, NOS NGS 46. 32 pp.. National Ocean Service/NOAA, Rockville, Md.

Cheney, R.E., N.S. Doyle, B.C. Douglas, R.W. Agreen, L. Miller, E.L. Timmerman and D.C. McAdoo (1991a). The Complete Geosat Altimeter GDR Handbook. NOAA Manual, NOS NGS 7. 25 pp.. National Ocean Service/NOAA, Rockville, Md.

Cheney, R.E., W.J. Emery, B.J. Haines and F. Wentz (1991b). Recent Improvements in Geosat Altimeter Data. EOS Trans.AGU, 71(51): 577-580.

Cheney, R.E. and J.G. Marsh (1981a). Oceanic Eddy Variability as Measured by GEOS-3 Altimeter Cross-over Differences. EOS Trans.AGU, 62(45): 737-752.

Cheney, R.E. and J.G. Marsh (1981b). SEASAT Altimeter Observations of Dynamic Topography in the Gulf Stream Region. J.Geophys.Res., 86(C1): 473-483.

Cheney, R.E., J.G. Marsh and B.D. Beckley (1983). Global Mesoscale Variability from Collinear Tracks of SEASAT Altimeter Data. J.Geophys.Res., 88(C7): 4343-4354.

Choy, L.W., D.L. Hammond and E.A. Uliana (1984). The Electromagnetic Bias of Altimeter Measurements of Mean Sea Level as Determined by an Airborne 10 GHz Radar. Mar.Geodesy, 8(1-4): 297-312.

Choy, L.W. and E.A. Uliana (1980). Backscattering of Narrow Laser Pulses from a Non-Gaussian Sea. Terrain and Sea-Scatter Workshop Proc.GWU, Wash. D.C,

Colton, M.T. and R.R.P. Chase (1983). Interaction of the Antarctic Circumpolar Current with Bottom Topography: An Investigation Using Satellite Altimetry. J.Geophys.Res., 88(C3): 1825-1843.

Cox, M.D. (1984). A Primitive Equation, Three-dimensional Model of the Ocean. GFDL Ocean Group Tech.Rep., 1. Geophysical Fluid Dynamics Lab., Princeton Univ., N.J.

Dantzler, H.L.J. (1976). Geographic Variations in Intensity of the North Altantic and North Pacific Oceanic Eddy Fields. Deep Sea Res., 23: 783-794.

Darbyshire, J. (1964). A Hydrological Investigation of the Agulhas Current Area. Deep Sea Res., 11: 781-815.

Darbyshire, J. (1972). The Effect of Bottom Topography on the Agulhas Current. Rev.Appl.Geophys., 101(9): 208-220.

Deacon, G.E.R. (1937). The Hydrology of the Southern Ocean. Discovery Reports, 15: 1-124.

Dobson, E., F. Monaldo, J. Goldhirsh and J. Wilkerson (1987). Validation of Geosat Altimeter-derived Wind Speeds and Significant Wave Heights Using Buoy Data. J.Geophys.Res., 92(C10): 10,719-10,731.

Douglas, B.C., R.W. Agreen and D.T. Sandwell (1984). Observing Global Ocean Circulation with SEASAT Altimeter Data. Mar.Geodesy, 8(1-4): 67-83.

Douglas, B.C. and P.D. Gaborski (1979). Observation of Sea Surface Topography with GEOS-3 Altimeter Data. J.Geophys.Res., 84(B8): 3893-3896.

Doyle, N.S., R.E. Cheney, B.C. Douglas, R.W. Agreen, L. Miller and E.L. Timmerman (1989). The NOAA Geosat Geophysical Data Records: Summary of the Second Year of the Exact Repeat Mission. NOAA Tech.Memo., NOS NGS 49. 15 pp.. National Ocean Service/NOAA, Rockville, M.D.

Emery, W.J., G.H. Born, D.G. Baldwin and C.L. Norris (1990). Satellite-derived Water Vapour Corrections for Geosat Altimetry. J.Geophys.Res., 95(C3): 2953-2964.

Foster, L.A. (1972). Current Measurements in the Drake Passage. 61 pp.. M.S. thesis, Dalhousie University.

Frey, E.J., J.V. Harrington and W.S. von Arx (1966). A Study of Satellite Altimetry for Geophysical and Oceanographic Measurements. Proceedings of the 16th International Astronautical Congress, New York, Gordon and Breach.

Fu, L.-L. and D.B. Chelton (1985). Observing Large Scale Temporal Variability of Ocean Currents by Satellite Altimetry: with Application to the Antarctic Circumpolar Current. J.Geophys.Res., 90(C3): 4721-4737.

Fu, L.-L., D.B. Chelton and V. Zlotnicki (1988). Satellite Altimetry: Observing Ocean Variability from Space. Oceanography Magazine, 1(2): 4-11.

Fu, L.-L. and R. Glazman (1991). The Effect of the Degree of Wave Development on the Sea State Bias in Radar Altimetry Measurement. J.Geophys.Res., 96(C1): 829-834.

Gill, A.E. (1982). Atmosphere-Ocean Dynamics. Academic Press.

Gordon, A.L. (1972). On the Interaction of the Antarctic Circumpolar Current and the Macquarie Ridge. In: Antarctic Oceanology II: The Australasian-New Zealand Section, Hayes, D.E. (Ed.). Washington DC., AGU. 71-78.

Gordon, A.L. and J.A.T. Bye (1972). Surface Dynamic Topography of Antarctic Waters. J.Geophys.Res., 77(30): 5993-5999.

Gordon, A.L. and W.F. Haxby (1990). Agulhas Eddies Invade the South Atlantic: Evidence from Geosat Altimeter and Shipboard Conductivity-Temperature-Depth Survey. J.Geophys.Res., 95(C3): 3117-3125.

Gordon, A.L. and E. Molinelli (1982). Southern Ocean Atlas. New York, Columbia, University Press.

Gordon, A.L., E. Molinelli and T. Baker (1978). Large Scale Relative Dynamic Topography of the Southern Ocean. J.Geophys.Res., 83(C6): 3023-3032.

Gormatyuk, Y.K. and A.S. Sarkisyan (1965). Results of 4-level Model Calculations of North Atlantic Currents. Izv.Acad.Nauk (USSR) Atmos.Ocean Physics, 1: 313-326.

Gründlingh, M.L. (1977). Drift Observations from Nimbus VI Satellite-tracked Buoys in the Southwestern Indian Ocean. Deep Sea Res., 24(10): 903-913.

Gründlingh, M.L. (1978). Drift of Satellite-tracked Buoy in the Southern Agulhas Current and Agulhas Return Current. Deep Sea Res., 25(12): 1209-1224.

Gründlingh, M.L. (1979). Observation of a Large Meander in the Agulhas Current. J.Geophys.Res., 84(C7): 3776-3778.

Gründlingh, M.L. (1982). Eddies in the Southern Indian Ocean and Agulhas Current. In: Eddies in Marine Science, Robinson, A.R. (Ed.). Berlin Heidelberg, Springer-Verlag. 245-264.

Haines, B., G. Born, G.W. Rosborough, J.G. Marsh and R.G. Williamson (1990). Precise Orbit Computation for the Geosat Exact Repeat Mission. J.Geophys.Res., 95(C3): 2871-2885.

Harris, T.F.W. and N.D. Bang (1974). Topographic Rossby Waves in the Agulhas Current. South African Journal of Science, 70(7): 212-213.

Harris, T.F.W., R. Legeckis and D. Van Foreest (1978). Satellite Infra-red Images in the Agulhas Current System. Deep Sea Res., 25(6): 549-561.

Hayne, G.S. and D.W. Hancock (1990). Corrections for the Effects of Significant Wave Height and Attitude on Geosat Radar Altimeter Measurements. J.Geophys.Res., 95(C3): 2837-2842.

Hellerman, S. and M. Rosenstein (1983). Normal Monthly Wind Stress Over the World Ocean with Error Estimates. J.Phys.Oceanogr., 13: 1093.

Khimitsa, V.A. (1976). Study of Geostrophic Currents in Antarctic Zone of Indian Ocean. Okeanologiy (USSR), 16(2): 234-238.

Killworth, P.J. (1987). Topographic Instabilities in Level Model OGCMs. Ocean Modelling, 75: 9.

Killworth, P.J. (1991). Mean and Eddy Features in FRAM. FRAM News, 1991(1): 3-5. The FRAM Team, IOSDL

Le Traon, P.Y., C. Boissier and P. Gaspar (1991). Analysis of Errors Due to Polynomial Adjustment of Altimeter Profiles. J.Atmos.Oceanic Tech., 8(6): 385-396.

Le Traon, P.Y., M.C. Rouquet and C. Boissier (1990). Spatial Scales of Mesoscale Variability in the North Atlantic as Deduced from Geosat Data. J.Geophys.Res., 95(C11): 202647-20285.

Leitao, C.D. and J.T. McGoogan (1974). Skylab Radar Altimeter:- Short Wavelength Perturbations Detected in Ocean Surface Profiles. Science, 186: 1208-1209.

Lerch, F.J., S.M. Klosko, R.E. Laubscher and C.A. Wagner (1979). Gravity Model Improvements Using GEOS-3 (GEM 9 and 10). J.Geophys.Res., 84(B8): 3897-3916.

Levitus, S. (1982). Climatological Atlas of the World Ocean. NOAA Professional Paper, 13. 173 pp.. US Dep.of Commer., Wash. DC

Lorell, J., E. Colquitt and R.L. Anderle (1982). Ionospheric Correction for SEASAT Altimeter Height Measurement. J.Geophys.Res., 87(C5): 3207-3212.

Lutjeharms, J.R.E. (1972). A Quantitative Assessment of Year to Year Variability in Water Movement in the Southwest Indian Ocean. Nature, 239(91): 59-60.

Lutjeharms, J.R.E. (1981). Spatial Scales and Intensities of Circulation in the Ocean Areas Adjacent to South Africa. Deep Sea Res., 28(11): 1289-1302.

Lutjeharms, J.R.E. (1991). Modelling the Ocean: Report of a Period Spent at IOSDL. FRAM News, 1991(1): 7. The Fram Group, IOSDL

Lutjeharms, J.R.E. and D.J. Baker (1980). A Statistical Analysis of the Mesoscale Dynamics of the Southern Ocean. Deep Sea Res., 27(A2): 145-159.

Lutjeharms, J.R.E., N.D. Bang and C.P. Duncan (1981). Characteristics of the Currents East and South of Madagascar. Deep Sea Res., 28(3): 879-899.

Lutjeharms, J.R.E. and H.R. Valentine (1988). Eddies in the Subtropical Convergence South of Africa. J.Phys.Oceanogr., 18(5): 761-774.

Lutjeharms, J.R.E. and R.C. van Ballegooyen (1984). Topographic Control in the Agulhas Current System. Deep Sea Res., 31(11): 1321-1337.

Lutjeharms, J.R.E., D.J. Webb and B.A. de Cuevas (1991). Applying the Fine Resolution Antarctic Model (FRAM) to the Ocean Circulation around Southern Africa. South African Journal of Sciences, 87(8): 346-349.

Marsh, J.G., F.J. Lerch, B.H. Putney, D.C. Christodoulidis, D.E. Smith, T.L. Felsentreger, B.V. Sanchez, S.M. Klosko, E.C. Pavlis, T.V. Martin, J.W. Robbins, R.G. Williamson, O.C. Colombo, D.D. Rowlands, W.F. Eddy, N.L. Chandler, K.E. Rachlin, G.B. Patel, S. Bhati and D.S. Chinn (1989). The GEM-T2 Gravitational Model. NASA Tech.Memo., 100746. 94 pp.. Goddard Space Flight Center, Grennbelt, MD

Marsh, J.G., T.V. Martin and J.J. McCarthy (1982). Global Mean Sea-Surface Computation Using GEOS-3 Altimeter Data. J.Geophys.Res., 87(B13): 955-964.

Marsh, J.G. and R.G. Williamson (1982). SEASAT Altimeter Timing Bias Estimation. J.Geophys.Res., 87(C5): 3232-3238.

McCartney, M.S. (1976). The Interaction of Zonal Currents with Topography with Applications to the Southern Ocean. Deep Sea Res., 23(5): 413-427.

McConathy, D.R. and C.C. Kilgus (1987). The Navy Geosat Mission: An Overview. John Hopkins APL Technical Digest, 8(2): 170-175.

McGoogan, J.T. (1975). Satellite Altimetry Applications. IEEE Trans.Microwave Theory Tech., MTT-23(12): 970-978.

Menard, Y. (1983). Observations of Eddy Fields in the Northwest Atlantic and Northwest Pacific by SEASAT Altimeter Data. J.Geophys.Res., 88(C3): 1853-1866.

Mognard, N.M. (1983). Swell Propagation in the North Atlantic Ocean Using SEASAT Altimeter. In: Satellite Microwave Remote-Sensing, Allan, T.D. (Ed.). Chichester, Ellis Horwood. 425-437.

Mognard, N.M. (1984). Swell in the Pacific Ocean Observed by SEASAT Radar Altimeter. Mar.Geodesy, 8(1-4): 183-210.

Mognard, N.M., W.J. Campbell and C. Brossier (1984). World Ocean Mean Monthly Waves, Swell and Surface Winds for July through October 1978 from SEASAT Radar Altimeter Data. Mar.Geodesy, 8(1-4): 159-181.

Mognard, N.M., W.J. Campbell, R.E. Cheney and J.G. Marsh (1983). Southern Ocean Mean Monthly Waves and Surface Winds for Winter 1978 by SEASAT Radar Altimeter. J.Geophys.Res., 88(C3): 1736-1744.

Monaldo, F.M., J. Goldhirsh and E.J. Walsh (1986). Altimeter Height Measurement Error Introduced by the Presence of Variable Cloud and Rain Attenuation. J.Geophys.Res., 91(C2): 2345-2350.

Morrow, R., J. Church, R. Coleman, D. Chelton and N. White (1992). Eddy Momentum Flux and its Contribution to the Southern Ocean Momentum Balance. Nature, 357: 482-484.

Nowlin, W.D. and J.M. Klink (1986). The Physics of the Antarctic Circumpolar Current. Rev.Geophys.Space Phys., 24(3): 469-491.

Nowlin, W.D., T. Whitworth and R.D. Pillsbury (1977). Structure and Transport of the Antarctic Circumpolar Current from Short-term Measurements. J.Phys.Oceanogr., 7(11): 788-802.

Olson, D.B. and R.H. Evans (1986). Rings of the Agulhas Current. Deep Sea Res., 33(1): 27-42.

Parke, M.E., R.H. Stewart, D.L. Farless and D.E. Cartwright (1987). On the Choice of Orbits for an Altimetric Satellite to Study Ocean Circulation and Tides. J.Geophys.Res., 92(C11): 11,693-11,708.

Patterson, S.L. (1985). Surface Circulation and Kinetic Energy Distributions in the Southern Hemisphere from FGGE Drifting Buoys. J.Phys.Oceanogr., 15(7): 865-884.

Pearce, A.F. (1977). Some Features of the Upper 500 m of the Agulhas Current. J.Mar.Res., 35(4): 731-753.

Pearce, A.F. and M.L. Gründlingh (1982). Is there a Seasonal Variation in the Agulhas Current? J.Mar.Res., 40(1): 177-184.

Pearce, A.F., E.H. Schumann and G.S.H. Lundie (1978). Features of the Shelf Circulation off the Natal Coast. South African Journal of Science, 74(9): 328-331.

Pickard, G.L. and W.J. Emery (1990). Descriptive Physical Oceanography: An Introduction. Fifth Enlarged Edition (in S.I. Units). 319 pp.. Pergammon Press.

Pond, S. and G.L. Pickard (1983). Introductory Dynamical Oceanography. Second Edition. 241 pp.. Pergammon Press.

Porter, G.H. and M. Rattray (1964). The Influence of Variable Depth on Steady Barotropic Flow. Deut.Hydrogr.Z., 17(4): 164.

Prabhakara, C., D.A. Short and B.E. Vollmer (1985). El Niño and Atmospheric Water Vapour: Observations from NIMBUS-7 SMMR. J.Clim.Appl.Met., 24(12): 1311-1324.

Queffeulou, P. (1983). SEASAT Wave Height Measurement: A Comparison with Sea-Truth Data and a Wave Forecasting Model- Application to the Geographic Distribution of Strong Sea States in Storms. J.Geophys.Res., 88(C3): 1779-1788.

Rapley, C.G. (1990). Satellite Radar Altimeters. In: Microwave Remote Sensing for Oceanographic and Marine Weather-Forecast Models, Vaughan, R.A. (Ed.). Dordrecht, Boston and London, Kluwer Academic Publishers. 45-63.

Rapp, R.H. (1983). The Determination of Geoid Undulations and Gravity Anomalies from SEASAT Altimeter Data. J.Geophys.Res., 88(C3): 1552-1562.

Ray, R.D., C.J. Koblinsky and B.D. Beckley (1991). On the Effectiveness of Geosat Altimeter Corrections. Intl.J.Rem.Sens., 12(9): 1979-1984.

Reid, J.L. (1986). On the Total Geostrophic Circulation of the South Pacific Ocean: Flow Patterns, Tracers and Transports. Progress in Oceanography, 16(1): 1-61.

Reid, J.L. and W.D.J. Nowlin (1971). Transport of Water through the Drake Passage. Deep Sea Res., 18: 51-64.

Richman, J.G., C. Wunsch and N.G. Hogg (1977). Space and Time Scales of Mesoscale Motion in the Western North Atlantic. Rev.Geophys.Space Phys., 15(4): 385-420.

Robinson, A.R., N.E. Huang, D.C. Leitao and C.G. Parra (1983). A Study of the Variability of Ocean Currents in the Northwestern Atlantic using Satellite Altimetry. J.Phys.Oceanogr., 13(4): 565-585.

Robinson, I.S. (1985). Satellite Oceanography: An Introduction for Oceanographers and Remote-Sensing Scientists. 526 pp.. Chichester, Ellis Horwood.

Saastamoinen, J. (1972). Atmospheric Correction for the Troposphere and Stratosphere in Radio Ranging of Satellites. In: The Use of Artificial Satellites for Geodesy, Heriksen, S.W., A. Mansini and B.H. Chovitz (Ed.). Washington DC, AGU. 247-251.

Sandwell, D.T. and B. Zhang (1989). Global Mesoscale Variability from the Geosat Exact Repeat Mission: Correlation with Ocean Depth. J.Geophys.Res., 94(C12): 17,971-17,984.

Sarkisyan, A.S. (1962). On the Dynamics of the Origin of Wind Currents in the Baroclinic Ocean. Okeanologia, 11: 393-409.

Schutz, B.E., B.D. Tapley and C.K. Shum (1982). Evaluation of the SEASAT Altimeter Time Tag Bias. J.Geophys.Res., 87(C5): 3239-3245.

Semtner, A.J. (1974). An Oceanic General Circulation Model with Bottom Topography. UCLA Dept.of Meteorology Tech.Rep., 9. 99 pp..

Semtner, A.J. and R.M. Chervin (1988). A Simulation of the Global Ocean Circulation with Resolved Eddies. J.Geophys.Res., 93(C12): 15,502-15,522.

Smagorinsky, J. (1963). General Circulation Experiments with the Primitive Equations. Mon.Wea.Rev.USWB, 91: 99-164.

Stevens, D.P. (1990). On Open Boundary Conditions for Three Dimensional Primitive Equation Ocean Circulation Models. Geophys.Astrophys.Fluid Dyn., 51(1-4): 103.

Stommel, H. and J. Webster (1962). Some Properties of Thermocline Equations in a Subtropical Gyre. J.Mar.Res., 20: 42-56.

Sverdrup, H.U. (1953). The Currents off the Coast of Queen Maud Land. Nor.Geogr.Tidsskr., 14: 239-249.

Swithinbank, C., P. McLain and P. Little (1977). Drift Tracks of Antarctic Icebergs. Polar Rec., 18(161): 495-501.

Tai, C.-K. (1988). Geosat Cross-over Analysis in the Tropical Pacific 1: Constrained Sinusoidal Cross-over Adjustment. J.Geophys.Res., 93(C9): 10,621-10,629.

Tai, C.-K. and L.-L. Fu (1986). On Crossover Adjustment in Satellite Altimetry and its Oceanographic Implications. J.Geophys.Res., 91(C2): 2549-2554.

Tapley, B.D., J.B. Lundberg and G.H. Born (1982). The SEASAT Wet Tropospheric Range Correction. J.Geophys.Res., 87(C5): 3213-3220.

Tapley, B.D., B.E. Schutz, J.G. Marsh, W.F. Townsend and G.H. Born (Ed.) (1979). Accuracy Assessment of the SEASAT Orbit and Altimeter Height Measurement. Rep., IASOM TR 79-5. Inst. for Adv. Stud. in Orbital Mech., Univ. Texas, Austin

Tchernia, P. (1974). Etude de la Dérive Antarctique est-quest au Moyen d'Icebergs Suivis par la Satellite Eole. C.R.Acad.Sci. Ser.B, 278: 667-670.

The FRAM Group (1989). An Instability near the Open Boundary. FRAM news, 1 Sep 1989. The FRAM Team, IOSDL

The FRAM Group (1991). An Eddy Resolving Model of the Southern Ocean. EOS Trans.AGU, 72(15): 169.

Thomas, J.P. and P.L. Woodworth (1990). The Influence of Ocean Tide Model Corrections on Geosat Mesoscale Variability Maps of the North East Atlantic. Geophys.Res.Lett., 17(13): 2389-2392.

U.S. Naval Oceanographic Office and the U.S. Naval Ocean Research and Development Activity (1983). DBDB5 (Digital Bathymetric Data base - 5 minute Grid). USNOO, Bay S^{t} Louis, Mississippi

Wakker, K.F., R.C.A. Zandbergen, M.C. Naeije and B.A.C. Ambrosius (1990). Geosat Altimeter Data Analysis for the Oceans Around South Africa. J.Geophys.Res., 95(C3): 2991-3006.

Walsh, E.J., D.W. Hancock III, D.E. Hines and J.E. Kenney (1984a). Electromagnetic Bias of 36-GHz Radar Altimeter Measurements of MSL. Mar.Geodesy, 8(1-4): 265-296.

Walsh, E.J., F.M. Monaldo and J. Goldhirsh (1984b). Rain and Cloud Effects on a Satellite Dual-Frequency Radar Altimeter System Operating at 13.5 and 35 GHz. IEEE Trans.Geosci.Rem.Sens., GE-22(6): 615-622.

Walsh, E.J., E.A. Uliana and B.S. Yaplee (1978). Ocean Wave Height Measured by a High-resolution Pulse-limited Radar. Bound-Lay.Meteorol., 13(1-4): 263-276.

Webb, D.J. (1983). Wave Measurements with the SEASAT Radar Altimeter: A Review. In: Satellite Microwave Remote-Sensing, Allan, T.D. (Ed.). Chichester, Ellis Horwood. 419-424.

Webb, D.J., P.D. Killworth, A.C. Coward and S.R. Thompson (1991). The FRAM Atlas of the Southern Ocean. 647 pp.. Swindon, Natural Environment Research Council.

Wellander, P. (1959). An Advective Model of the Ocean Thermocline. Tellus, 11: 309-318.

Whitworth, T., W.D. Nowlin and S.J. Worsley (1982). The Net Transport of the Antarctic Circumpolar Current through Drake Passage. J.Phys.Oceanogr., 12: 960.

Whitworth, T. and R.G. Peterson (1985). The Volume Transport of the Antarctic Circumpolar Current from Bottom Pressure Measurements. J.Phys.Oceanogr., 15(6): 810-816.

Willebrand, J., R.H. Käse, D. Stammer, H.-H. Hinrichsen and W. Krauss (1990). Verification of Geosat Sea Surface Topography in the Gulf Stream Extension With Surface Drifting Buoys and Hydrographic Measurements. J.Geophys.Res., 95(C3): 3007-3014.

Witter, D.L. and D.B. Chelton (1991). An Apparent Wave Height Dependence in the Sea-state Bias in Geosat Altimeter Range. J.Geophys.Res., 96(C5): 8861-8868.

Won, I.J. and L.S. Miller (1979). Oceanic Geoid and Tides Derived from GEOS-3 Satellite Data in the Northwestern Atlantic Ocean. J.Geophys.Res., 84(B8): 3833-3842.

Wyrtki, K., L. Magaard and J. Hager (1976). Eddy Energy in the Oceans. J.Geophys.Res., 81(15): 2641-2646.

Yaplee, B.S., A. Shapiro, D.L. Hammond, B.B. Au and E.A. Uliana (1971). Nano-second Radar Observation of the Ocean Surface from a Stable Platform. IEEE Trans.Geosci.Electron., GE-9(3): 170-174.

Yunck, T.P., W.G. Melbourne and C.L. Thornton (1985). GPS Based Satellite Tracking System for Precise Positioning. IEEE Trans.Geosci.Rem.Sens., GE-23(4): 450-457.

Zlotnicki, V., L.-L. Fu and W. Patzert (1989). Seasonal Variability in Global Sea Level Observed with Geosat Altimetry. J.Geophys.Res., 94(C12): 17,959-17,969.